Transport and Deposition of Fine Particulates in Turbulence: Numerical Modeling and Uncertainty Quantification

by

Yuan Yao

A dissertation submitted in partial fulfillment
of the requirement for the degree of
Doctor of Philosophy
(Mechanical Engineering and Scientific Computing)
in the University of Michigan
2021

Doctoral Committee:

Assistant Professor Jesse Capecelatro, Chair
Assistant Professor Xun Huan
Associate Professor Eric Johnsen
Professor Venkat Raman

Yuan Yao

yyaoaa@umich.edu

ORCID iD: 0000-0002-4180-1811

To my beloved parents and wife.

ACKNOWLEDGEMENTS

The last five years have been a challenging but fruitful journey for me. There are many people whom I am extremely grateful to have encountered, collaborated with, and received advice from. I would like to begin by thanking my advisor Prof. Jesse Capecelatro. He is very knowledgable and inspiring as an advisor, and at the same time very approachable and easygoing as a person. His high standards and intrinsic curiosity toward fluid dynamics and science in general have enabled me to thrive at my best and have shaped who I want to be for the years to come.

I extend my gratitude to the committee members, Prof. Xun Huan, Prof. Venkat Raman and Prof. Eric Johnsen for their availability and interest in my work. Their deep understanding of the fundamental nature of turbulent flows and uncertainty quantification have provided me constant support via valuable discussions and courses they taught. I would also like to thank Prof. Jeffery Bons, Prof. Houssem Kasbaoui, Prof. John Palmore, Prof. Rui Ni for sharing their knowledges and professional opinions with me during meetings, conferences, and collaborations. I am sincerely grateful for Prof. Shuhuai Yao, Prof. Shawn Shadden, and Prof. Craig Arnold for their previous mentorship and recommendations before me joining the University of Michigan.

In addition, I would like to thank all the people and friends I have met at the University of Michigan who made this journey full of joy and fun, some of which include Ali Kord, Gregory Shallcross, Sarah Beetham, Meet Patel, Aaron Lattanzi, Kalvin Monroe, Kazuya Murakami, Minki Kim, Shaowu Pan, Yihao Tang, Xiaoyi Zhang, Lei Guo, Yuhao

Ding, Chen Di, Cai Ting, Yongzhao Wang. I still vividly remember the days and nights we spent debugging coding assignments, debating about research ideas, or simply exchanging visions and outlooks on life. Beyond the University of Michigan, I am extremely fortunate to have met many talented students and scholars with whom I share the same passion in CFD related research, some of which include Yuanhang Zhu, Xiaomeng Zhai, Guangchen Shen, Yixing Li, Lam Vu, Pedram Pakseresht, Guang Chen, Saurabh Pargal, Sai Mangavelli, Jincheng Lou. It is the interaction with these people during conferences and summer schools that constantly reminds me of an old saying in Chinese: "*Never forget why you started, and you can accomplish your mission.*"

Last but not least, I owe great thanks to my parents, Xiuan Yao and Yanyun Yuan, for their unconditional support, encouragement, and understanding especially during the past five years. I cannot express my gratitude enough to my wife, Tingjun Man, for her unfailing love and care in my pursuit of science. I am also lucky to have two adorable kittens, Peep and Legrand, from whom I can always seek emotional comfort and calm.

This work has been supported in part by the Office of Naval Research under Award No. N00014-19-1-2202. Computational resources provided by the Advanced Research Computing at the University of Michigan, Ann Arbor, are gratefully acknowledged.

TABLE OF CONTENTS

LIST OF FIGURES

Figure

LIST OF TABLES

Table

LIST OF APPENDICES

Appendix

ABSTRACT

In recent years, public awareness of the impact caused by micron-sized particles such as infectious aerosols or dust has increased drastically, ranging from severe public health concerns to various environmental issues. In addition, airborne dust and volcanic ash ingested by aircraft engines compromise the durability, performance, and safety of engine turbine components. The transport and deposition of fine ($\lesssim \mathcal{O}(10\,\mu\text{m})$) particulates in turbulence (e.g., dust or powder) is largely controlled by cohesive forces such as electrostatics and van der Waals. Due to their small size and cohesive nature, tracking individual particles in turbulence is challenging, and is further complicated by significant uncertainties in material properties. Although computational methods with varying levels of complexity have been developed over past decades, accurate predictive models of cohesive particle transport and deposition do not yet exist for large-scale simulations.

The main objective of this work is to develop a numerical framework tailored for resolving cohesive particle interactions in turbulence. Efficient algorithms are developed to optimally resolve particle contact forces in a direct numerical simulation (DNS) framework. The framework is then used to study the effect of electrostatics on particle transport in turbulence. It is found that the short-range electric potential plays a key role in particle clustering even in dilute suspensions. A follow-up study of charged aerosols in ionized air identifies a feedback mechanism capable of generating atmospheric turbulence via an electrohydrodynamic body force.

Turbulence-induced breakup of an aggregate of solid particles subject to van der Waals is also investigated. A phenomenological model of the breakup process is developed that acts as a granular counterpart to the Taylor analogy breakup (TAB) model commonly

used for droplet breakup. Such a model is capable of predicting the onset of aggregate breakup in the absence of a resolved turbulent flow field. Finally, particle deposition in a turbulent pipe flow is studied in the presence of van der Waals and electrostatics. The sensitivity of deposition rate to uncertainties in cohesive forces is efficiently quantified using a multi-fidelity framework. Deposition is found more sensitive to electrostatics than van der Waals across all particle sizes and exhibits largest uncertainty for mid-sized particles.

CHAPTER I

Introduction

1.1 Fine particulates in turbulent flows

In this dissertation, solid particles or liquid droplets of size below 20 μm are considered fine particulates, which generally refer to dust, powder, pollen, soot, smoke and aerosols suspended in air. The transport and deposition of fine particulates in turbulent flows play important roles in many engineering, environmental and medical systems. For example, pathogen-laden aerosols can transmit infectious diseases during inhalation, which results in long-range transmission and pose severe challenges to public disease control [115]. Various solid particulates emitted from combustion processes have been shown to contribute to global warming [20] and cause cardiovascular diseases [86]. Other examples include dry powder inhalers for drug delivery [12, 267, 268], dust ingestion in gas turbine engines [9, 56, 21, 202] and fluidized bed reactors [165, 242, 146, 175], where particles are commonly observed to form long chains and aggregates due to inter-particle attractive forces such as electrostatics and van der Waals (see Fig. 1.1). In past decades, tremendous efforts have been made to understand and predict the behavior of fine particle transport and deposition in turbulent environments, which is crucial for the design and improvement of the aforementioned systems.

Solid particles are typically classified into four groups based on solid-fluid density differ-

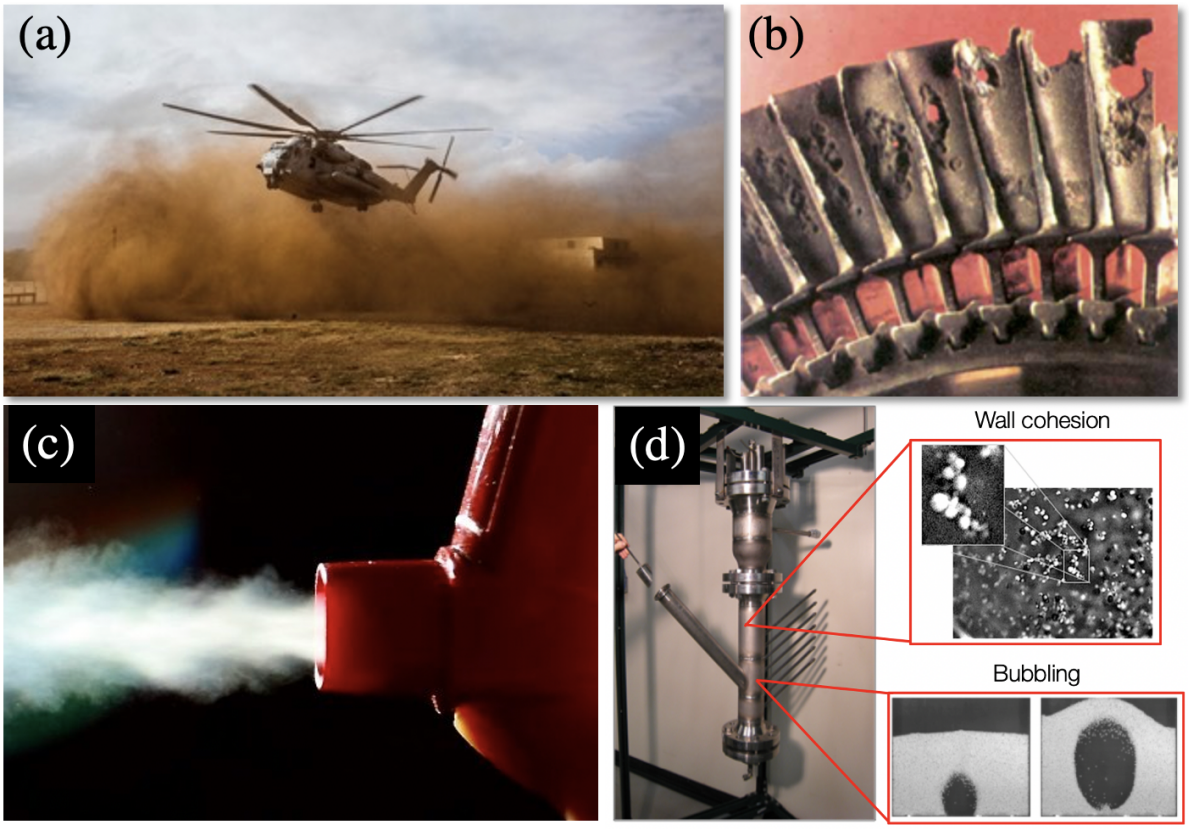

Figure 1.1: Examples of fine particulates in turbulent flows. (a) Aircraft engines are susceptible to sand and dust ingestion at takeoff, while other airborne particulates (e.g., volcanic ash and pollutants) can contaminate the intake at higher altitudes (photo credit: Tim Grabert). (b) Severe corrosion of turbine blades by ingested particles [263]. (c) Particle clumping due to van der Waals significantly deteriorates the delivery efficiency of drug particles in dry powder inhalers (Photo credit: Dan Stanton). (d) Triboelectrical charging of particles at the walls of fluidized bed reactors alter bubble dynamics and increase wall deposition [37].

ence and particle size according to the classic Geldart classification [80] shown in Fig. 1.2. The focus of this dissertation is on Geldart C-type particles (e.g. dust or powder in air) in which inter-particle attractive forces (cohesion) are important [160, 251]. The dynamical evolution and morphology of cohesive particles involve a complex interplay between turbulent stresses and inter-particle attractive forces, both long-range (e.g., electrostatic forces) and short-range (e.g., van der Waals forces). As a result, particle clumping can arise under various circumstances, which is known to compromise the performance of the aforementioned systems. For example, agglomeration has been shown to significantly

deteriorate the delivery efficiency of drug particles [12], accelerate turbine blade erosion in gas turbine engines [87, 97] and defluidize two-phase reactors [165, 37]. Due to the small size and opaque nature of these particles, however, experimental investigations are limited to either a small number of particles under well-controlled conditions [95] or measurements of quantities that do not require optical access [97, 40]. When particles agglomerate into larger clumps, tracking a large number of tiny particles becomes intractable experimentally. The remainder of the introduction will summarize the physical processes associated with particle-laden turbulence, highlight key simulation challenges, followed by the objectives and outlines of this dissertation.

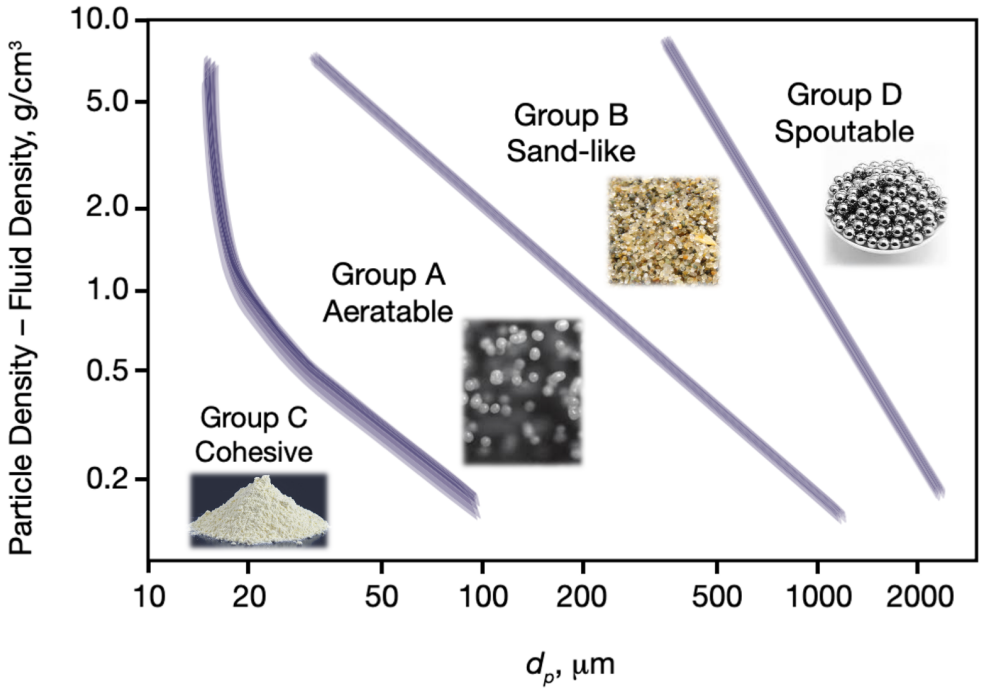

Figure 1.2: Particle classification according to Geldart [80]. Transport of Group C-type particles such as dust or powder with size ranging from 1 to 20 μm are dominated by cohesive forces. Figure adapted from Cocco et al. [38].

1.2 Introduction to particle-laden turbulence

1.2.1 Particle transport in turbulence

Particle transport and dispersion in turbulent flows is a key aspect of a large number of important processes, including cloud formation in the atmosphere [280], transmission of infectious diseases [23, 22, 166], and various combustion and emission processes [123, 33]. Momentum coupling between the phases is primarily characterized by the particle volume fraction ϕ_p, defined as the volume occupied by the particle phase over the entire volume of consideration, as shown in Fig. 1.3. When $\phi_p < 10^{-6}$, particles have very little effect on each other or the fluid phase due to their low concentration (i.e., one-way coupled). As the particle concentration increases ($10^{-6} \leq \phi_p \lesssim 10^{-3}$), the momentum source of the dispersed phase on the carrier-phase via drag becomes important such that particles also modify the fluid dynamics (i.e., two-way coupled). At higher loading ($\phi_p \gtrsim 10^{-3}$), particle-particle interactions such as collisions become non-negligible and the particle-fluid system is considered four-way coupled. For instance, droplet collision in a cloud plays a key role in coalescence between water droplets, which dictates the onset of rainfall [280].

One of the key features of particle distribution in turbulent flows is the phenomenon of preferential concentration [159, 60, 57]. Heavy particles tend to accumulate in regions of high strain rate and avoid regions of high vorticity. This phenomenon is characterized by the Stokes number St, defined as the ratio of particle-to-fluid inertia. For very small St, particles follow fluid streamlines and act as tracer particles, whereas particles with large St are inertial and less responsive to the carrier phase. At intermediate St, particle inertia is comparable to the fluid such that particles are effectively ejected by the turbulent eddies and cluster in high strain-rate regions. Preferential concentration is found to be most profound when St is close to unity (see Fig. 1.4).

When particles carry electrical charge, such coupling between particles and the underly-

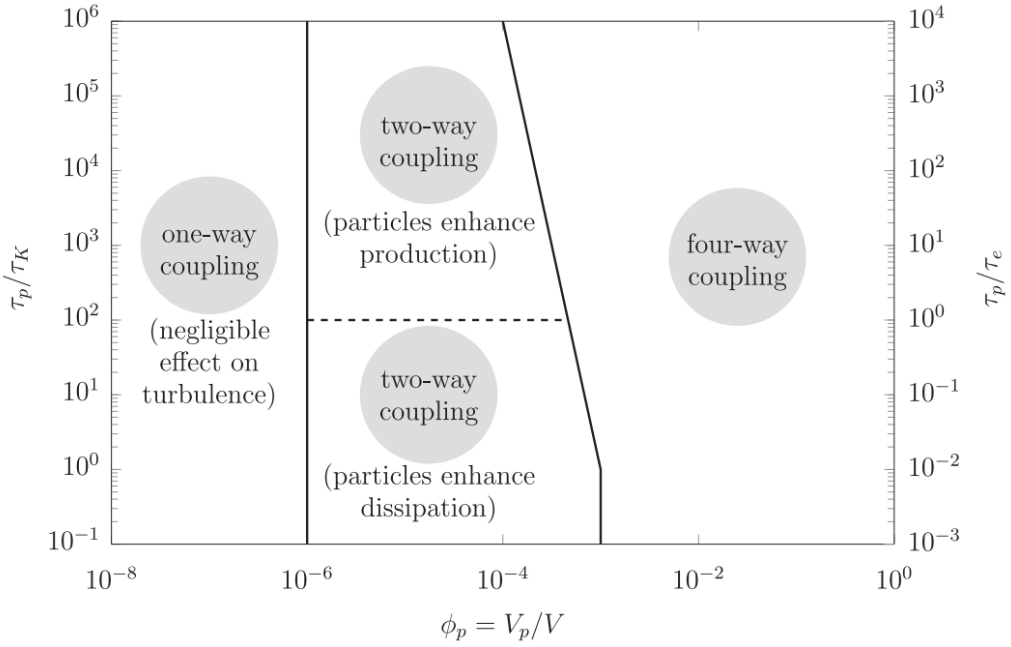

Figure 1.3: Phase coupling regimes for particle-laden turbulence proposed by Elghobashi [59]. ϕ_p is the particle volume fraction defined as volume occupied by the particle phase V_p over the entire volume of the domain V. τ_p, τ_e, and τ_K are particle response time, turbulence eddy turnover time, and Kolmogorov time scale respectively. Figure adapted from Kasper et al. [121].

ing carrier phase can lead to significant spatial segregation in charge density that induces, or amplifies, an electric field. A recent study of the Sahara dessert showed that electric fields contribute to an increase of up to ten times the amount of particles emitted into the atmosphere [62]. A positive feedback was observed whereby the electric field increases shear-induced dust lifting, which in turn introduces increased charges to the atmosphere resulting in a stronger electric field [125]. Meanwhile, the relative importance between fluid forces (i.e., drag) and electrostatic forces in turbulent flows remain elusive. When drag is dominant, we expect the particles to preferentially concentrate in high strain rate regions of the flow, with the level of clustering determined by the Reynolds number and Stokes number [222]. With increasing charge magnitude, eventually Coulomb interactions will have an order-one effect on the spatial distribution of particles. Note that due to the long-range nature of electrostatics, particle-particle interactions become important even

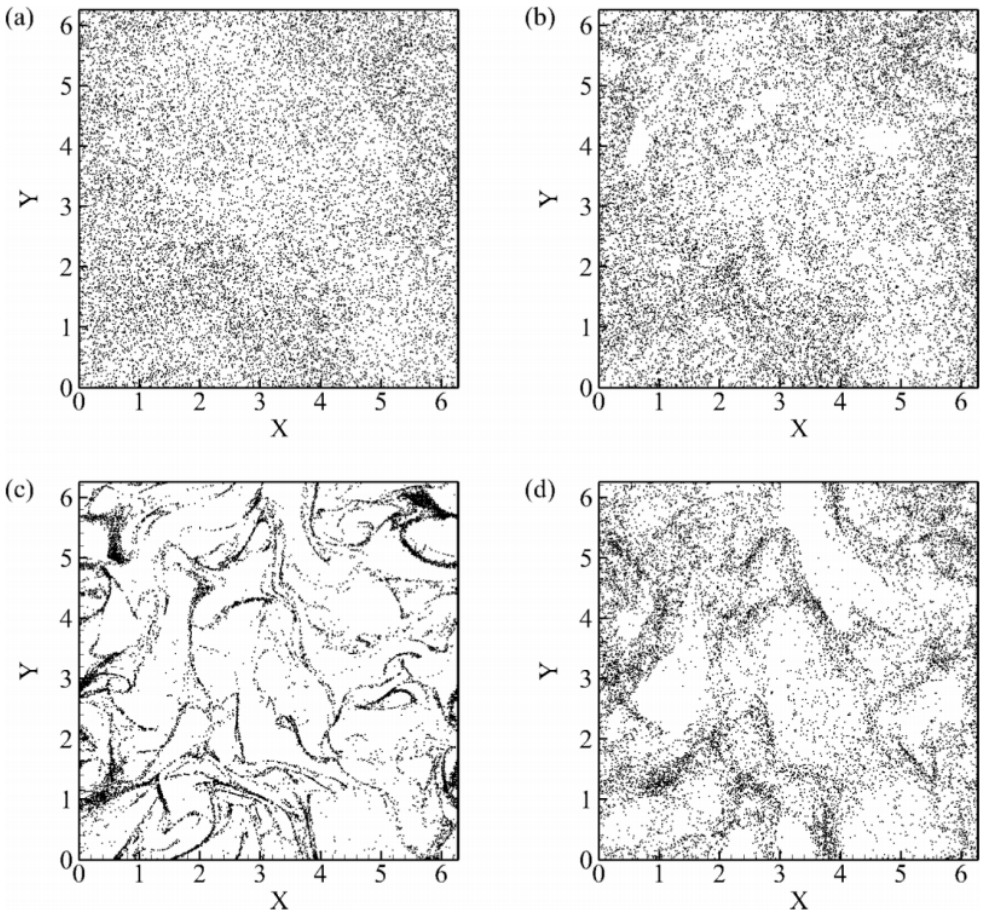

Figure 1.4: Instantaneous particle distribution in homogeneous isotropic turbulence with Taylor microscale Reynolds number $\mathrm{Re}_\lambda = 100$ and different Stokes numbers. (a) $\mathrm{St} = 0$ (Tracer), (b) $\mathrm{St} = 0.1$, (c) $\mathrm{St} = 1$, and (d) $\mathrm{St} = 5$. Figure adapted from Zhang et al. [278].

in dilute suspensions (one-way coupling regime).

Particle transport in turbulence is further complicated by the presence of other cohesive forces such as van der Waals. Development of aggregates of cohesive particles in turbulent flows is affected by the turbulence in two different ways. The inertia imparted on the particles by the turbulent fluctuations leads to enhanced collision rate, and hence increases the rate of agglomerate formation. On the other hand, various fluid stress fluctuations associated with the turbulent flow such as shear and rotation can tear apart the agglomerates if sufficiently strong. Transport of cohesive particles is therefore particularly responsive to local fluctuations in particle concentration and fluid velocities. As a result,

the small time- and length-scales need to be resolved simultaneously in order to accurately capture the physics associated with particle-particle interactions. Furthermore, particles can modify the fluid phase due to high local particle volume fraction if agglomerates are formed, and two-way coupling is therefore important even for systems with small ϕ_p on average. Due to the complex interplay between cohesive particles and turbulence, the formation and breakup of cohesive aggregates in turbulence is still an active area of research and will be discussed in the following chapters.

As shown in Fig. 1.3, particles can in return modulate turbulence at large ϕ_p via two-way coupling. Depending on the particle size and density, velocity fluctuations in the carrier phase can be either augmented or attenuated by the presence of particles [8]. The focus of this dissertation is on dilute suspension of fine particulates, for which turbulence modulation due to momentum coupling is often negligible. However, charged particles can affect turbulent kinetic energy through a different mechanism when the carrier phase is ionized. The gradients in the electric potential induce molecular motions of the ionized fluid, which is known as the electrohydrodynamic (EHD) force. One example is the atmosphere for which the EHD force can be amplified by more than three orders of magnitude in extreme conditions, such as thunderstorms, compared to typical fair weather conditions [201, 214]. While the EHD force is known to induce turbulence in ionized fluids, such as electrolytic cells [28], liquid films [232], and electrostatic precipitators [5], and similar instabilities due to magnetohydrodynamics exist in plasmas [136, 229, 76], the effect of self-induced electric field by charged particles on turbulence augmentation via EHD force is less established.

1.2.2 Particle deposition in wall-bounded flows

Particles suspended in a fluid are commonly observed to be deposited on solid walls. Measuring, predicting, and understanding the deposition rate are important in many

medical and engineering applications such as dry powder inhalers [12, 267, 268], dust ingestion in gas turbine engines [9, 56, 21, 202] and fluidized bed reactors [165, 242, 146, 175]. Similar physical processes take place in the atmospheric dispersal of pollutants [262, 109], the determination of indoor air quality [132, 131], the sedimentation of various substances in rivers [164, 265], and heat transfer equipments [255]. For example, particles sticking to heat exchanger surfaces can cause severe performance degradation of the device. Deposition is known to be driven by either gravity for large particles (sedimentation) or adhesive forces such as van der Waals attraction and electrostatics for Geldart-C particles. Tremendous experimental and numerical efforts have been made toward understanding and predicting particle deposition rates.

Many previous studies provide experimental measurements of the deposition velocity V_{dep} defined as the particle mass transfer rate on the wall normalized by the bulk density of particles [137, 73, 210, 257, 211]. The results fall into three distinct regimes in which particle deposition is governed by different physics (see Fig. 1.5). For sub-micron particles, the brownian motion becomes important, particles primarily deposit on the wall driven by turbulent diffusion, this regime is called turbulent diffusion regime. As the particle size increases, the deposition rate increases dramatically as the result of the interaction between inertial particles and fluid turbulent eddies. These particles are preferentially concentrated in high strain rate regions and ejected from turbulent eddies to the wall at a relatively high velocity. This regime is named diffusion-impaction regime. The third regime is known as the inertia-moderated regime where ballistic particles acquire sufficient momentum from turbulent eddies to impact the wall directly. The deposition rate reduces with increasing particle size due to the fact that larger particle inertia results in a delayed response to the turbulence.

The complex and multi-physical nature of the particle deposition process make the

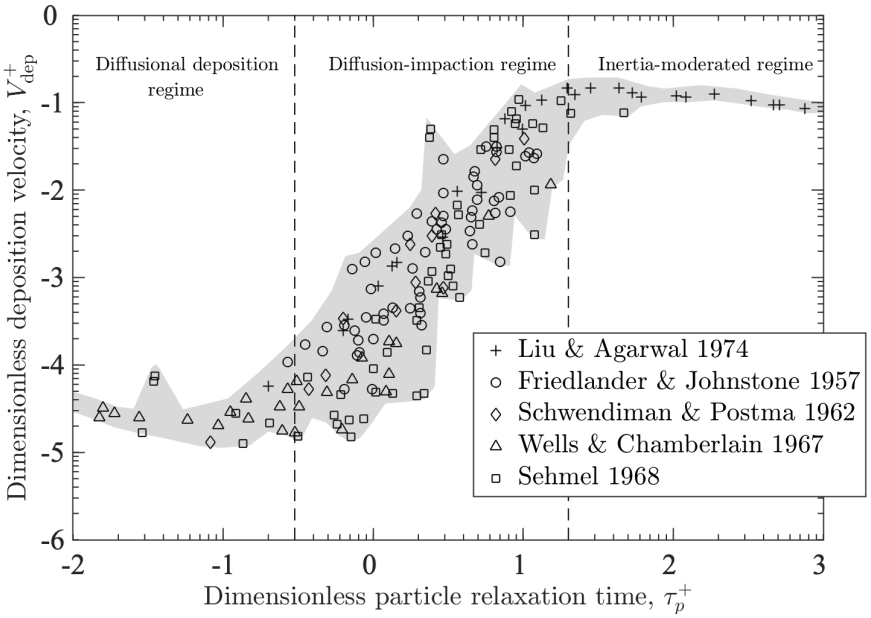

Figure 1.5: Summary of experimental data for particle deposition in fully developed turbulent pipe flow. Shaded region highlights the range of experimental measurements with significant uncertainties. Figure adapted from Young and Leeming [274].

modeling extremely challenging. The most well-known theory is the 'free-flight' or 'stop-distance' model proposed by Friedlander and Johnstone [73], which assumes particles can directly deposit on the wall once they diffuse to one 'stop-distance' from the wall. However, it requires the particle velocity to be on the same order of the friction velocity at the stop distance, which is a significant over-prediction [274]. The model has been improved by many others [43, 10, 264, 178], but all require tuning of free-flight velocity and only work for the diffusion-impaction regime. More recently, Lagrangian particle tracking is adopted for deposition predictions. The fluid phase fluctuation can be obtained by numerically solving the Navier-Stokes equations [173, 26, 254], estimated by empirical correlations [116], or simulated using random walk models [84, 44, 83]. Depending on how resolved the fluid phase is, the accuracies and computational costs of these simulations vary significantly. Alternatively, Eulerian calculations provides an efficient way to predict deposition. Johansen [112] found good agreement with experiment by solving

particle continuity and momentum equations with empirical closure models for the particle turbulence terms. More recently, Guha [93, 94] proposed a one-dimensional Eulerian model which is derived purely from conservation laws in the wall-normal direction and has decent predictions for all three regimes.

These models of different fidelities, Eulerian or Lagrangian, are all based on the assumption that particle cohesion is negligible comparing to other effects such as turbulent dispersion due to drag. However as mentioned previously, cohesion plays an important role in particle transport especially for the turbulent diffusion regime (Geldart-C particles). Furthermore, there are large uncertainties in particle charge amount and cohesion strength whose effects on particle deposition models remain elusive. Guha [94] demonstrated electrostatics, temperature gradients, and surface roughness can all cause orders of magnitude variations in the deposition rate using the aforementioned 1D Eulerian model (see Fig. 1.6). While incredibly valuable, the model only accounts for particle-wall electrostatic interactions and the particle distribution is assumed to be only a function of wall distance. In reality, however, particle clustering can be significantly modified by particle-particle electrostatic interactions [50, 51, 118]. In addition, particles are known to accumulate along low-speed streaks, defined as regions of lower-than-mean streamwise velocity [244, 282, 151]. These spatial inhomogeneities can alter particle near-wall deposition and are yet to be fully understood.

1.3 Challenges in simulating fine particulates in turbulence

Development of accurate predictive models for fine particle-laden flows is hindered by the current incomplete understanding of how cohesive forces depend on the experimental conditions and property uncertainties. Numerical investigations have attempted to tackle this issue by employing computational approaches with varying levels of resolution. How-

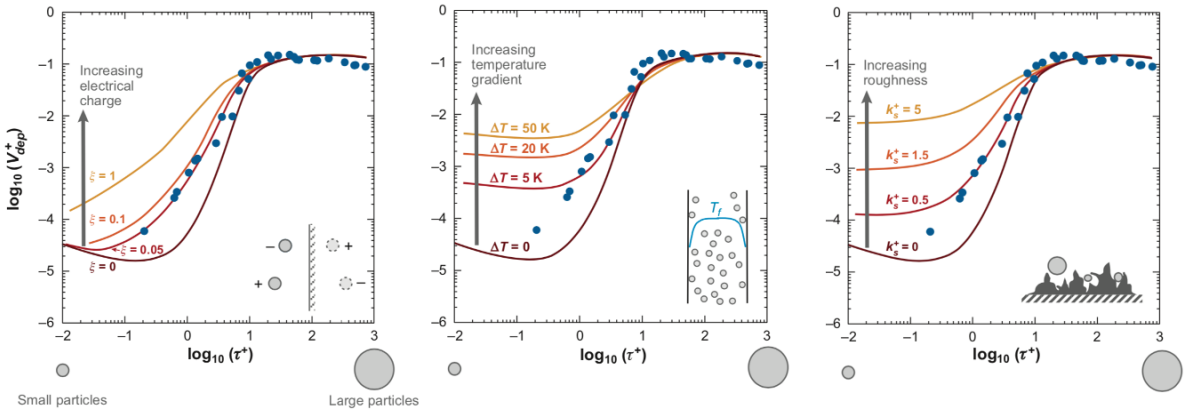

Figure 1.6: Effects of charge, temperature gradients, and surface roughness on the predicted deposition rate using the 1D Eulerian deposition model proposed by Guha [94]. Parameter ranges are chosen to be relevant to typical particle-laden turbulent pipe flows. Figure adapted from Guha [94].

ever, the multi-scale and multi-physics nature of cohesive particle flows present a few outstanding numerical challenges.

1.3.1 A question of scales

The major challenge in numerically investigating cohesive particles in turbulence is properly resolving the wide range of length- and time-scales at play. Consider a typical application that involves dust suspended in an air flow with Reynolds number $\mathrm{Re} = \mathcal{O}(10^4)$, a particle diameter $d_p = \mathcal{O}(10^{-5})\,\mathrm{m}$, the characteristic fluid length $L_f = \mathcal{O}(10^{-3})\,\mathrm{m}$, and velocity scales in both phase $u_f = u_p = \mathcal{O}(1)\,\mathrm{m/s}$. The advection time scale of the fluid phase is therefore $\tau_f = L_f/u_f = \mathcal{O}(10^{-3})$ whereas $\tau_p = d_p/u_p = \mathcal{O}(10^{-5})$ for the particle phase. When two particles collide, a contact time scale arises with $\tau_{\mathrm{col}} = L_{\mathrm{col}}/u_p = \mathcal{O}(10^{-8})$ given that most short-range cohesive forces are only active in $L_{\mathrm{col}} = \mathcal{O}(10^{-8})\,\mathrm{m}$ [153]. Therefore, the physical length- and time-scales of such systems can vary five orders of magnitude, and is often further complicated by the large number of particles involved with $N = \mathcal{O}(10^8)$. Special attention should be given when numerically resolving both phases simultaneously to capture multi-scale physics and at the same time avoid prohibitive computational costs.

A number of modeling approaches have been developed to simulate particle-laden flows at different scales. One common approach is to couple Lagrangian particle tracking with a mean flow field obtained from Reynolds-averaged Navior-Stokes (RANS). This approach has been widely used for particle ingestion in gas turbine engines [87, 97, 21]. Despite its low computational cost, it has been shown to significantly under-predict turbulent dispersion [260] as the micro-scale particle-fluid interactions are not resolved. Particle-resolved direct numerical simulation (PR–DNS) fully resolves the fluid phase with exact boundary conditions imposed at each particle surface [227] and has been applied to study particle cohesion in turbulence [239, 248, 249]. While PR–DNS is highly accurate, it is limited to small systems due to its high computational cost and therefore agnostic to macro-scale physics.

Eulerian–Eulerian (EE) methods solve both the fluid and particle phase on a common Eulerian grid. In the small Knudsen number (highly collisional) limit with an underlying assumption that the flow is nearly at equilibrium, the particle velocity distribution is close to Maxwellian and a Chapman–Enskog expansion can be used to derive a two-fluid model (TFM) using ensemble or volume averaging [4, 81, 277]. This approach leads to particle-phase transport equations that closely resemble the Navier–Stokes equations using moment closures obtained from kinetic theory. While cohesion models have been coupled with TFM in the past [195, 196], it is typically only valid in dense granular regimes and are unable to capture important features of particulate flows when the particle phase is far from equilibrium [49].

Eulerian–Lagrangian (EL) methods provide an alternative framework that explicitly captures particle-particle interactions (e.g., collisions, short- and long-range interactions, etc.). In this approach, each particle is tracked individually and coupled to the fluid via interphase exchange terms [238, 30], which has been widely applied to study cohe-

sive particles in turbulence [103, 128, 25, 221, 139, 270]. However, most existing studies consider one-way coupling without taking into account influences of drag or volume displacement by particles on the fluid. Such an approach is not appropriate when modeling large particle aggregates as it over-predicts the interphase slip velocity in the vicinity of the particles [53]. Another known deficiency of this method when dealing with cohesive particles is the restrictive time step.

1.3.2 Long-range vs. short-range interactions

Cohesive forces between particles are present in various forms that are active across different scales, some of which include electrostatics, van der Waals, protein binding, liquid bridging, sintering, etc. Long-range interactions, such as electrostatics, decays with the square of the particle separation distance and typically results in non-negligible interactions even with particles far away. Short-range forces, such as van der Waals, are only active at a sub-micron length scale but can lead to numerically stiff gradients for particles in contact.

Due to the long-range nature of electrostatic forces, properly accounting for Coulomb interactions in systems with many particles must be handled carefully for accurate predictions that avoid $\mathcal{O}(N^2)$ computations, with N the number of charged particles. The particle-mesh (PM) method is typically employed in numerical simulations of both homogeneous (e.g., Karnik and Shrimpton [117]) and wall-bounded (e.g., Ceresiat et al. [32]) flows as it avoids computing direct pairwise sums. Instead, the charge is projected on the computational grid, and the electric potential is solved via a Poisson equation. While computationally efficient, PM fails to capture short-range interactions that are anticipated to be important when particles cluster. The particle-particle particle-mesh (P^3M) method introduced by Hockney and Eastwood [104] improves upon PM method by explicitly adding a short-range contribution within a cut-off radius. It requires modifying

the long-range potential in Fourier space to avoid double counting the short-range and long-range contributions, and scales with $\mathcal{O}(N \log N)$. P^3M has been applied to simulations of ionic liquids [2], molecular dynamics [250, 77, 212], and cosmology [39], yet to date has not been applied to particle-laden flows. The major drawback of P^3M is that the correction to the long-range potential is typically handled in Fourier space and consequently limited to cubic periodic domains, which prevents its application in studying particle deposition in wall-bounded flows.

The effect of van der Waals attraction during collision of two particles can be illustrated by different mechanics. When two particles come into contact, the contact region can either be approximated as two flattened surfaces or retain their original shape, depending on the properties of the particles and the strength of adhesive forces. These two assumptions are the basis for two widely applied contact mechanics models, the JKR approach by Johnson et al. [114] and the DMT approach by Derjaguin et al. [45] respectively. Both assume elastic contact based on Hertzian theory and are therefore limited to small deformations in the absence of other particle forces such as electrostatics. Alternatively, the van der Waals force can be modeled independent of the contact model and simply treated as another external force. The magnitude of the van der Waals force between two particles was given by Hamaker [96] in 1937 as a function of particle separation s and the Hamaker constant A. However, one outstanding challenge of directly resolving van der Waals forces is that a brute-force implementation would require excessively small time steps to resolve inter-particle contact time scales. To this end, the spring stiffness of simulated particles is typically reduced from its realistic values, resulting in artificially 'soft' particles to enable larger time steps. It is therefore important to ensure the overall effect of cohesion is insensitive to the choice of particle stiffness and consequently the results remain unchanged as simulation time step is adjusted.

1.3.3 Underlying uncertainties

Another outstanding modeling challenge is the significant uncertainties associated with cohesive force measurements as well as particle material properties. For example, typical dust is composed of fine mineral particulates for which the measurement of the Hamaker constant, which dictates the strength of van der Waals attraction, can span five orders of magnitudes [249]. It remains an ongoing debate in the literature about how to parametrize and measure cohesive forces accurately [103, 135, 25]. Another key uncertainty of dust ingestion in gas turbine engines is the constitution of the ingested particles, which varies significantly with geographic locations [219]. For example, Fig. 1.7 summarizes the mineral and chemical components of dust from different sites of the Middle East [61], from which large variation can be seen in the mass percentage of each constituent. In addition, the composition of the same dust sample varies at different size ranges [217], which are becoming more relevant for modern helicopter turboshaft engines where large particles are filtered out during engine intakes by inertial particle separators [41].

Particle types	d_p [μm]	Hamaker constant [1e-20 J]		Electric charge [C]	CoR
		A_{11}	A_{12}		
SiO_2 (Silica)	$0.1 - 100$	6.5	$5.37 - 13.7$	8.0e-18 – 4.0e-16	$0.62 - 0.77$
SiO_2 (Quartz)	$0.5 - 15$	8.86	$7.59 - 12.1$	8.0e-18 – 4.0e-16	0.19
Al_2O_3 (Alumina)	$0.2 - 34$	15.2	$7.90 - 21.1$	1.4e-18 – 2.4e-16	0.62
$CaSO_4$ (Gypsum)	$0.7 - 20$	–	–	–	0.10
Dolomite	$2 - 40$	$7.34 - 13.75$	–	–	0.15
NaCl (Salt)	–	6.48	$6.45 - 10.3$	–	0.11
Fe_2O_3	–	$6.8 - 25$	–	–	–
MgO	–	$10.6 - 12.1$	$8.84 - 14.2$	–	–
CaO	–	12.4	–	–	–
TiO_2	–	15.3	$9.46 - 15.4$	–	–
ARD	$1 - 40$	$1.76 - 125$	N/A	1.08e-17 – 5.2e-16	$0.34 - 0.76$
Fly ash	$1.5 - 80$	$0.25 - 1.9$	N/A	8.7e-17 – 2.2e-16	$0.16 - 0.75$
Fine soil	$2 - 20$	$1.05 - 513$	N/A	2.3e-17 – 2.5e-16	$0.38 - 0.92$

Table 1.1: Size, Hamaker constant, charge and coefficient of restitution (CoR) reported in the literature of common natural particulates and dust constituents. Upper and lower bounds are chosen to be within 10 to 90 percentile when distributions are given. ARD denotes Arizona road dust. References: [237, 241, 130, 16, 65, 52, 71, 69, 40, 75, 224, 172, 82, 41, 215, 134, 55, 236, 19, 127, 85, 225, 133, 269, 193, 206, 191, 168].

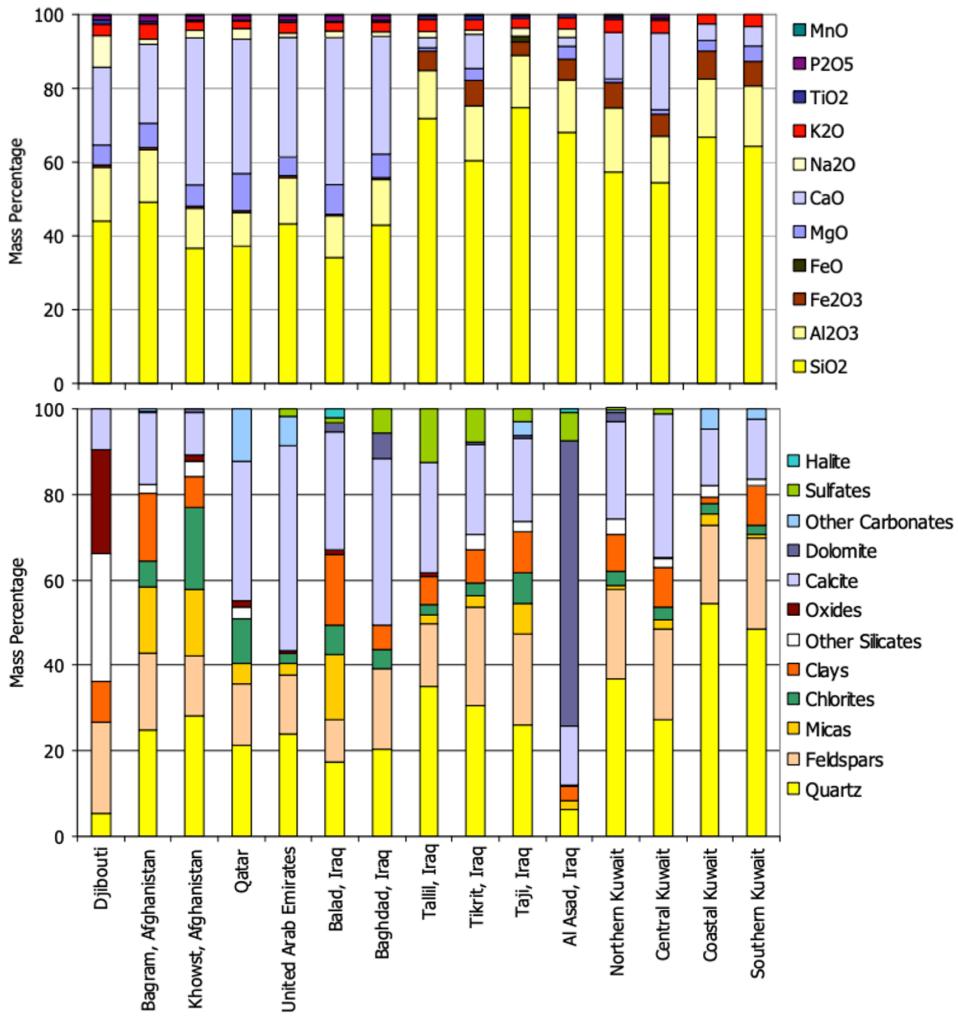

Figure 1.7: Particulates composition of dust samples from different sites around the Middle East in terms of mineral components (top) and metal oxides (bottom). Figure adapted from Engelbrecht et al. [61].

Table 1.1 summarizes typical size, charge, and Hamaker constant ranges for these common particulates of dust constituents. It can be seen that particle properties exhibit large variations even at standard atmospheric conditions. Other effects such as temperature gradients or surface roughness may further contribute to these uncertainties [94]. The variations in particulate constitutions, physical properties and flow conditions introduce inevitable measurement errors for experimental deposition studies as shown in Fig. 1.5, demonstrating the importance of quantifying how sensitive the particle deposition rate is to these uncertainties.

Nevertheless, most of the existing studies on cohesive particles consider monodisperse particles with single valued charge [143, 144] and Hamaker constant [103, 99]. The effect of uncertainties in these parameters on particle dynamics remains elusive, especially when the carrier phase is turbulent. Accurately quantifying these uncertainties requires many expensive simulations. An efficient framework for uncertainty quantification and sensitivity analysis is needed to investigate the effects of particle uncertainties on deposition in a tractable manner.

1.4 Objectives of this work

To alleviate previous numerical constraints, the overarching goal of this work is to establish a physics-based numerical modeling approach to understand and accurately predict transport and deposition of cohesive particles. To date, coarse-grained turbulence models such as RANS coupled with Lagrangian particle tracking remain the workhorse for the simulations of large-scale applications such as turbomachinery and fluidized bed reactors. Reliable, physics-based models for the transport and deposition of fine particles in turbulent flows are a key step towards enabling next generation energy conversion process and gas turbine engines. In the present work, physical insights provided by high-fidelity simulations will be used to understand the effect of cohesion on particle dynamics and inform reduced-order models in coarse-grained simulation frameworks, where relevant spatial- and temporal-scales are not resolved. The effects of underlying uncertainties on particle deposition will be quantified. The specific objectives of this dissertation include:

1. Develop an efficient numerical framework capable of accurately predicting particle transport and deposition of Geldart-C type particles in turbulence.
2. Characterize the effect of cohesive forces (electrostatics and van der Waals) on particle dynamics in both homogeneous and wall-bounded turbulent flows.

3. Quantify the uncertainties in particle deposition due to variations in particle material properties and cohesion strength.
4. Advance reduced-order models capable of predicting particle transport and deposition phenomena in turbulence using data from high-fidelity simulations.

1.5 Thesis overview

This dissertation is divided into seven chapters. Chapters II - VI are reorganized preprints of manuscripts that have been published or are in preparation for submission to a journal.

Chapter II [270, 273, 272] describes in detail the Eulerian–Lagrangian numerical framework tailored for fine particulates in turbulence. Specifically, the details on numerical algorithms of particle-particle and particle-fluid forces as well as two-way coupling treatment are provided. A multi-scale time stepping algorithm is presented to alleviate restrictive time steps. The framework acts as a foundation for the following chapters in which several detailed studies of cohesive particle-laden flows will be presented.

The effects of cohesive forces (electrostatics and van der Waals) on particle transport are provided in Chapter III - V. In Chapter III [270, 272], an efficient electrostatic algorithm (P^3M) is coupled with a soft-sphere collision models for the first time to accurately capture particle interactions. The accuracy of the approach is compared to other existing methods and then applied to a Taylor-Green vortex and homogeneous isotropic turbulence to quantify the relative importance of electrostatics and drag. Chapter IV [271] presents a followup study on turbulence augmentation due to charged particles via electrohydrodynamic forces. A feedback mechanism of turbulence generation is identified through linear stability analysis and direct simulation of ionized air with charged aerosols.

A detailed study of turbulence-induced breakup of a particle clump subject to van der

Waals attraction is presented in Chapter V [273]. The breakup rate is found to scale with cohesion strength and turbulence intensity. A phenomenological model is proposed to predict aggregate breakup based on a granular counterpart of Taylor-analogy breakup model developed for liquid droplets.

In Chapter VI, particle deposition is investigated in a turbulent pipe flow where the effects of charge and van der Waals attraction are quantified. The relative importance of cohesive forces are compared for particles of different sizes using both DNS and a 1D Eulerian model. The sensitivity of particle deposition to uncertainties in these cohesive forces are efficiently assessed by leveraging deposition models of different fidelities.

Finally, Chapter VII summarizes the major findings, contributions and suggestions for future work.

CHAPTER II

A Multi-scale Euler–Lagrange framework

In this work, we consider Geldart-C type particles such as dust or powder suspended in air with diameter d_p ranging from 1 μm to 20 μm. Cohesion due to electrostatics and van der Waals is important for this size range. The long range nature of the electrostatic force requires special numerical treatment to avoid $\mathcal{O}(N^2)$ computation. Although the van der Waals interaction is short ranged, it introduces small time-scales during particle contact that need to be resolved. In addition, when particles aggregate, momentum coupling between particles and the fluid must be taken into account. In this chapter, a multi-scale Eulerian–Lagrangian numerical framework is introduced that specifically addresses these issues by simultaneously resolving the wide range of time- and length-scales at play. Efficient and scalable algorithms are developed to accurately handle electrostatics and van der Waals interactions in periodic and wall-bounded flows.

2.1 Introduction

Numerical simulations can provide the space–time information needed to shed light on the complex interactions that occur in turbulent suspensions of fine cohesive particles. Due to the long-range nature of electrostatic forces, properly accounting for Coulomb interactions in systems with many particles must be handled carefully for accurate predictions that avoid $\mathcal{O}(N^2)$ computations, with N the number of charged particles. The

particle-mesh (PM) method is typically employed in numerical simulations of both homogeneous (e.g., Karnik and Shrimpton [117]) and wall-bounded (e.g., Ceresiat et al. [32]) flows as it avoids computing direct pairwise sums. Instead, the charge is projected on the computational grid, and the electric potential is solved via a Poisson equation. This method implicitly assumes that the electrostatic force between neighboring particles is small compared to the net effect of all other particles. While computationally efficient, PM fails to capture short-range interactions that are anticipated to be important when particles preferentially concentrate in regions of the flow [270]. An alternative approach is to apply a screen function, or cutoff radius, such that a limited range of particle interactions are considered, and the far field influence is ignored. In order to limit the computational burden, Lu and Shaw [143] summed the Coulomb contribution within the Debye screening radius. Such a truncated method is only valid for relatively low levels of charge density, and is not applicable to particle-laden flows in general.

Ewald summations methods were developed to handle long-range potentials accurately in periodic boxes. This approach splits the slowly-converging Coulomb potential into long-range and short-range contributions, each of which converges exponentially fast [64, 182]. The short-range potential is evaluated using direct pairwise sums over the set of nearest neighbors within a cutoff radius, and the long-range contribution is solved in reciprocal space. However, this approach remains computationally demanding as the long-range contribution requires several Fourier transforms, and the total scheme scales like $\mathcal{O}(N^{3/2})$ with an optimized cutoff radius [46, 47]. The particle-particle particle-mesh (P^3M) method introduced by Hockney and Eastwood [104] is a Fourier-based Ewald summation approach that makes use of an underlying grid to speed up the evaluation of the long-range potential. The P^3M method requires modifying the long-range potential in Fourier space to avoid double counting the short-range and long-range contributions, and

scales with $\mathcal{O}(N \log N)$ [183]. P^3M has been applied to simulations of ionic liquids [2], molecular dynamics [250, 77, 212], and cosmology [39], yet to date has not been applied to particle-laden flows.

The major drawback of P^3M is that the correction to the long-range potential is typically handled in Fourier space and consequently limited to cubic periodic domains. A few efforts have been made to extend P^3M to non-periodic domains but at the expense of computational efficiency. Beams et al. [11] avoided using FFTs by solving the long-range force using a finite element method by reconstructing the screened potentials with specially designed polynomial bases. An alternative approach is to evaluate the Gaussian convolution (Eq. (2.20)) in real space [140]. While both modifications were found to retain the high accuracy of P^3M, the resulting computational cost is increased.

In the present study, an efficient Eulerian–Lagrangian framework coupled with P^3M is developed to alleviate these computational constrains. The governing equations and numerical implementation are presented in § 2.2 and 2.3. An overview of the PM, P^3M, and other methods are discussed in § 2.4 and the accuracy of each are compared for a simple periodic box. The classic P^3M approach is then extended to simulate charged particles in wall-bounded flows while retaining the same accuracy and cost savings in § 2.5. The solution to the electric Poisson equation is performed agnostic to the presence of any walls, allowing for the use of FFT. The contribution from periodic images are removed by exploiting the linearity of the Poisson equation and strategically mapping the particle charge to the grid. A signed-distance levelset function is used to enforce appropriate boundary conditions. The accuracy of the proposed approach is compared against PM and the classic P^3M algorithms for a cylindrical pipe configuration. In addition, the van der Waals force model is modified to allow for soft-sphere contact in § 2.6. Two-way coupling is accounted for via drag and volume displacement effects in § 2.7. A multi-scale

time stepping algorithm is introduced to minimize the computational cost in § 2.8.

2.2 Fluid-phase equations

Despite the relatively small size of the particles considered in this work, two-way coupling between the phases must be taken into account when particle aggregates are larger than the Kolmogorov length scale. To account for the presence of particles without requiring a resolution sufficient to resolve the boundary layers at the surface of each particle, a volume filter is applied to the constant-density Navier–Stokes equations [4], thereby replacing the point variables (fluid velocity, pressure, etc.) by smoother, locally filtered fields. The volume-filtered conservation equations for a constant-density fluid are given by

$$\frac{\partial \alpha}{\partial t} + \nabla \cdot (\alpha \boldsymbol{u}) = 0, \tag{2.1}$$

and

$$\frac{\partial \alpha \boldsymbol{u}}{\partial t} + \nabla \cdot (\alpha \boldsymbol{u} \otimes \boldsymbol{u}) = \nabla \cdot \boldsymbol{\tau} + \boldsymbol{F}_{\text{inter}}, \tag{2.2}$$

where $\boldsymbol{u}$ is the fluid velocity, α is the fluid volume fraction, and $\boldsymbol{\tau} = -p/\rho \mathbf{I} + \nu\big(\nabla \boldsymbol{u} + \nabla \boldsymbol{u}^{\top} - \frac{2}{3}(\nabla \cdot \boldsymbol{u})\mathbf{I}\big)$ is the stress tensor with p the fluid-phase pressure, ν the kinematic viscosity, ρ the fluid density, and $\mathbf{I}$ the identity matrix. $\boldsymbol{F}_{\text{inter}}$ is the interphase exchange term due to particles that will be defined in § 2.7. In this work, the equations are implemented in the framework of NGA [48], a fully conservative solver tailored for turbulent flow computations. The Navier–Stokes equations are solved on a staggered grid with second-order spatial accuracy for both the convective and viscous terms, and the second-order accurate semi-implicit Crank–Nicolson scheme of Pierce [186] is used for time advancement. The pressure Poisson equation that enforces continuity is solved using a multi-grid precondi-

tioned conjugate gradient method [66, 243].

2.3 Particle-phase equations

Particles are treated in a Lagrangian manner according to Newton's second law of motion where the translational and rotational motion of an individual particle i is given by

$$\frac{d\boldsymbol{x}_p^{(i)}}{dt} = \boldsymbol{v}_p^{(i)}, \tag{2.3}$$

$$m_p \frac{d\boldsymbol{v}_p^{(i)}}{dt} = \boldsymbol{f}_{\text{inter}}^{(i)} + \boldsymbol{f}_{\text{col}}^{(i)} + \boldsymbol{f}_{\text{vw}}^{(i)} + \boldsymbol{f}_{\text{coulomb}}^{(i)}, \tag{2.4}$$

and

$$I_p \frac{d\boldsymbol{\omega}_p^{(i)}}{dt} = \sum_j \frac{d_p}{2} \boldsymbol{n}_{ij} \times \boldsymbol{f}_{t,j\to i}^{\text{col}}, \tag{2.5}$$

where $\boldsymbol{x}_p^{(i)}$, $\boldsymbol{v}_p^{(i)}$ and $\boldsymbol{\omega}_p^{(i)}$ are the instantaneous particle position, velocity and angular velocity, respectively, $m_p = \rho_p \pi d_p^3/6$ is the particle mass, $I_p = m_p d_p^2/10$ is the moment of inertia for a sphere, and $\boldsymbol{n}_{ij}$ is the unit normal vector outward from particle i to particle j. The translational motion of each particle is determined by momentum exchange with the fluid phase, $\boldsymbol{f}_{\text{inter}}^{(i)}$, which will be defined in § 2.7, in addition to inter-particle collision $\boldsymbol{f}_{\text{col}}^{(i)}$, van der Waals attraction $\boldsymbol{f}_{\text{vw}}^{(i)}$, and electrostatic force $\boldsymbol{f}_{\text{coulomb}}^{(i)}$. Particle rotation is a consequence of the tangential component of the collision force, $\boldsymbol{f}_{t,j\to i}^{\text{col}}$. The effects of $\boldsymbol{f}_{\text{coulomb}}^{(i)}$ and $\boldsymbol{f}_{\text{vw}}^{(i)}$ on particle dynamics will be discussed in details in Chapters III and V, respectively.

2.3.1 Particle collisions

Particle collisions are needed to prevent unphysical overlap that may arise when attractive inter-particle forces are present [270]. In this work, normal and tangential collisions are modeled using a soft-sphere approach originally proposed by Cundall and Strack [42]. When two particles come into contact, a repulsive force is created as

$$\boldsymbol{f}^{\text{col}}_{n,j\to i} = \begin{cases} -k\delta_{ij}\boldsymbol{n}_{ij} - \eta\boldsymbol{v}_{ij,n} & \text{if } \ s < 0, \\ 0 \quad \text{else,} \end{cases} \tag{2.6}$$

where s is the distance between the particle surfaces, δ_{ij} is the overlap between the particles, $\boldsymbol{n}_{ij}$ is the unit normal vector from particle i to particle j and $\boldsymbol{v}_{ij,n}$ is the normal relative velocity between particles i and j. The spring stiffness and damping parameter are given by k and η, respectively. A model for the damping parameter [42] uses a coefficient of restitution $0 < \mathrm{e} < 1$ such that

$$\eta = -2\ln \mathrm{e}\frac{\sqrt{km_p/2}}{\sqrt{\pi^2 + (\ln \mathrm{e})^2}}. \tag{2.7}$$

The spring stiffness is related to the collision time, τ_{col}, according to

$$k = m_p/2\tau_{\text{col}}^2\left(\pi^2 + (\ln \mathrm{e})^2\right). \tag{2.8}$$

Collisions are treated as inelastic with a coefficient of restitution e=0.9, representative of many solid spherical objects in dry air. To properly resolve the collisions without requiring an excessively small timestep, τ_{col} is set to be 20 times the simulation time step Δt for all simulations presented in this work. To account for friction between particles and thus particle rotation, the static friction model is employed for the tangential component of the collision force, given by

$$\boldsymbol{f}^{\text{col}}_{t,j\to i} = -\mu_f \left|\boldsymbol{f}^{\text{col}}_{n,j\to i}\right| \boldsymbol{t}_{ij}, \tag{2.9}$$

where $\mu_f = 0.1$ is the coefficient of friction and $\boldsymbol{t}_{ij}$ is the tangential unit vector. Once each individual collision force is computed, the full collision force that particle i experiences can be expressed as

$$\boldsymbol{f}_{\text{col}}^{(i)} = \sum_{j \neq i} \left(\boldsymbol{f}_{n,j\to i}^{\text{col}} + \boldsymbol{f}_{t,j\to i}^{\text{col}} \right). \tag{2.10}$$

The particles are distributed among the processors based on the underlying domain decomposition of the fluid phase. A second-order Runge–Kutta scheme is used for updating each particle's position, velocity, and angular velocity. To avoid $\mathcal{O}(N^2)$ calculations of the collision force, a nearest neighbor detection algorithm is employed, such that collisions are only considered between particles in adjacent grid cells [30].

The cohesive forces, i.e., van der Waals attraction $\boldsymbol{f}_{\text{vw}}^{(i)}$ and electrostatic force $\boldsymbol{f}_{\text{coulomb}}^{(i)}$ require special numerical treatment to be computed efficiently and accurately, which are made explicit in the following sections.

2.4 Accurate Particle-Mesh methods for simulating charged particles

The last term in Eq. (2.4) is the electrostatic force governed by Coulomb's law, given by

$$\boldsymbol{f}_{\text{coulomb}}^{(i)} = \frac{q_p^{(i)}}{4\pi\epsilon_0} \sum_{j \neq i} q_p^{(j)} \frac{\boldsymbol{n}_{ij}}{\left| \boldsymbol{x}_p^{(j)} - \boldsymbol{x}_p^{(i)} \right|^2}, \tag{2.11}$$

where $q_p^{(i)}$ and $q_p^{(j)}$ are the charges belonging to particles i and j, respectively, and $\epsilon_0 = 8.854 \times 10^{-12}\ \text{F} \cdot \text{m}^{-1}$ is the vacuum permittivity. For the simulations considered in this work, the permittivity is assumed constant and taken to be ϵ_0. The force of interaction between the particles is attractive if their charges have opposite signs and repulsive if like-signed. As shown in Eq. (2.11), a direct summation will result in $\mathcal{O}(N^2)$ computations, which becomes computationally prohibitive for systems that involve a large number of

charged particles. In the following, efficient algorithms for computing electrostatics are presented in details.

2.4.1 Particle-Mesh (PM) method

To avoid the $\mathcal{O}(N^2)$ calculation involved with solving Eq. (2.11) via a direct summation, the particle mesh (PM) method approximates the force according to

$$\boldsymbol{f}^{(i)}_{\text{coulomb}} = q_p^{(i)} \boldsymbol{E}[\boldsymbol{x}_p^{(i)}], \tag{2.12}$$

where $\boldsymbol{E}[\boldsymbol{x}_p^{(i)}]$ is the electric field interpolated to the position of particle i. The electric field is obtained by taking the gradient of the electric potential via

$$\boldsymbol{E}(\boldsymbol{x}, t) = -\nabla\phi(\boldsymbol{x}, t), \tag{2.13}$$

where $\boldsymbol{x}$ is the Eulerian coordinate system, and the electric potential ϕ is calculated by solving the following Poisson equation

$$\nabla^2\phi(\boldsymbol{x}, t) = -\frac{\rho_m(\boldsymbol{x}, t)}{\epsilon_0}. \tag{2.14}$$

The charge density, ρ_m, is obtained by interpolating the particle charge using the following convolution product

$$\rho_m(\boldsymbol{x}, t) = \sum_{i=1}^{N} q_p^{(i)} \mathcal{W}(\boldsymbol{x} - \boldsymbol{x}_p^{(i)}(t)), \tag{2.15}$$

where $\mathcal{W}$ is a polynomial weighting function that projects the particle charge to the mesh. In the following sections, different orders of weighting functions will be considered to asses its effect on the overall order of accuracy.

2.4.2 Particle-Particle Particle-Mesh (P^3M) method

While the PM approach avoids $\mathcal{O}(N^2)$ calculations, it requires that the length scale used to resolve the spatial gradients of the electric potential are greater than the spacing

between adjacent particles. In turbulent flows, particles may preferentially concentrate in certain regions, and thus in general this assumption does not hold. The particle-particle particle-mesh (P^3M) method, introduced by Hockney and Eastwood [104], improves upon PM by separating long-range and short-range contributions by a cutoff radius $r_{\max}$. The long-range field is solved using Fast Fourier Transform (FFT) [189] on an underlying mesh. With a well-chosen cutoff radius and mesh size, P^3M has been shown to have an overall computational cost of $\mathcal{O}(N \log N)$ when $N \gtrsim 10^4$ [183]. When $N < 10^4$, the majority of the cost comes from solving the elctric Poisson equation which scales with the number of grid points.

Instead of using a point charge, P^3M reconstructs the charges by using a Gaussian charge distribution given by

$$G(\boldsymbol{r};\beta) = \frac{\beta^3}{\pi^{3/2}} e^{-\beta^2 r^2}, \tag{2.16}$$

whose Fourier transform can be easily obtained via

$$\hat{G}(\boldsymbol{k};\beta) = \int d^3 r G(\boldsymbol{r};\beta) e^{-i\boldsymbol{k}\cdot\boldsymbol{r}} = e^{-k^2/(2\beta)^2}. \tag{2.17}$$

Here, $\boldsymbol{k}$ is the wave number and the constant β tunes the standard deviation of the Gaussian distribution, commonly referred to as the P^3M constant, and $i = \sqrt{-1}$. Applying Gauss's law to Eq. (2.16), the resulting electric field located at the center of particle i is

$$\boldsymbol{E}_s^{(i)} = \sum_j \frac{q_p^{(j)} \boldsymbol{n}_{ij}}{2\epsilon_0 \pi^{3/2}} \Big[\frac{\sqrt{\pi}}{2 r_{ij}^2} \mathrm{erf}(r_{ij}\beta) - \frac{\beta}{r_{ij}} e^{-\beta^2 r_{ij}^2} \Big]. \tag{2.18}$$

Since the field from a point particle and the field produced by the Gaussian function are

both known analytically, the corrected short-range force can be expressed exactly as

$$\boldsymbol{f}_s^{(i)} = \begin{cases} \sum_j q_p^{(i)} q_p^{(j)} \left(\frac{\boldsymbol{n}_{ij}}{4\pi\epsilon_0 r_{ij}^2} - \frac{\boldsymbol{n}_{ij}}{2\epsilon_0 \pi^{3/2}} \left[\frac{\sqrt{\pi}}{2r_{ij}^2} \mathrm{erf}(r_{ij}\beta) - \frac{\beta}{r_{ij}} e^{-\beta^2 r_{ij}^2} \right] \right), & \text{if } r_{ij} < r_{\max} \\ 0, & \text{otherwise.} \end{cases} \tag{2.19}$$

The P^{3}M method handles the long-range force by sending the particle charge to the mesh and multiplying the resulting charge density by an influence function. This step optimizes the solution by minimizing the overall discretization error. The particle charges are first weighted to the underlying mesh to obtain the charge density, $\rho_m(\boldsymbol{x})$. An FFT is then applied to transform the charge density to Fourier space $\hat{\rho}_m(\boldsymbol{k})$. The resulting charge density is convolved with the Gaussian screen function via

$$\hat{\rho}_l(\boldsymbol{k}) = \hat{\rho}_m(\boldsymbol{k}) \hat{G}(\boldsymbol{k}) \tag{2.20}$$

to obtain the screened density field. To minimize the force error introduced by the screen function $\hat{G}(\boldsymbol{k})$, we use the optimized influence function derived by Hockney and Eastwood [104] that replaces $\hat{G}(\boldsymbol{k})$ by

$$\hat{G}_{\mathrm{opt}}(\boldsymbol{k}) = \frac{\hat{\boldsymbol{D}}(\boldsymbol{k}) \cdot \sum_{\boldsymbol{m} \in \boldsymbol{Z}} \hat{U}^2(\boldsymbol{k} + \frac{2\pi}{\Delta x}\boldsymbol{m}) \hat{\boldsymbol{R}}^2(\boldsymbol{k} + \frac{2\pi}{\Delta x}\boldsymbol{m})}{|\hat{\boldsymbol{D}}(\boldsymbol{k})|^2 \Big[\sum_{\boldsymbol{m} \in \boldsymbol{Z}} \hat{U}^2(\boldsymbol{k} + \frac{2\pi}{\Delta x}\boldsymbol{m}) \Big]^2}, \tag{2.21}$$

where

$$\hat{\boldsymbol{R}}(\boldsymbol{k}) = -i\boldsymbol{k} \frac{\hat{G}(\boldsymbol{k})}{k^2}, \tag{2.22}$$

$$\hat{U}(\boldsymbol{k}) = \left(\frac{\sin \frac{k_x \Delta x}{2}}{\frac{k_x \Delta x}{2}} \frac{\sin \frac{k_y \Delta x}{2}}{\frac{k_y \Delta x}{2}} \frac{\sin \frac{k_z \Delta x}{2}}{\frac{k_z \Delta x}{2}} \right)^{p+1}, \tag{2.23}$$

and

$$\hat{D}_j = \begin{cases} i\frac{\sin k_j \Delta x}{\Delta x}, & \text{for finite differences,} \\ i\boldsymbol{k}, & \text{for spectral integration,} \end{cases} \tag{2.24}$$

with Δx being the mesh spacing that is assumed uniform in all directions. Next, the potential field is calculated by solving the Poisson equation

$$k^2 \hat{\phi}_l(\boldsymbol{k}) = \frac{\hat{\rho}_l(\boldsymbol{k})}{\epsilon_0} \tag{2.25}$$

for $\hat{\phi}_l(\boldsymbol{k})$. An inverse Fourier transform is then applied to convert $\hat{\phi}_l(\boldsymbol{k})$ to real space $\phi_l(\boldsymbol{x})$. The electric field is then obtained by

$$\boldsymbol{E}_l(\boldsymbol{x}, t) = -\nabla \phi_l(\boldsymbol{x}, t) \tag{2.26}$$

on the mesh and interpolated to the particle position. Once the short-range field is calculated via Eq. (2.18), the total electric field can be obtained by

$$\boldsymbol{E}[\boldsymbol{x}_p^{(i)}] = \boldsymbol{E}_l[\boldsymbol{x}_p^{(i)}] + \boldsymbol{E}_s^{(i)}, \tag{2.27}$$

where $\boldsymbol{E}_l[\boldsymbol{x}_p^{(i)}]$ is the long-range electric field interpolated to the position of particle i. The total force can then be calculated via Eq. (2.12) and used to update the velocity of each particle.

2.4.3 A comparison of methods

Inspired by P^{3}M, Kolehmainen et al. [126] recently proposed a hybrid method that computes the short-range force using direct truncated pairwise summation within a cutoff radius and evaluates the cell-centered long-range force in a finite-volume framework (see Appendix A). Here we assess the accuracy of PM, P^{3}M, and the hybrid method. We consider the system given by Deserno and Holm [47], where $N = 100$ oppositely-charged

particles (50 with positive unit charge and 50 negative) are randomly placed within a triply-periodic box of length $L = 10$ m in the absence of a fluid. All cases are solved on a grid of size $N_g = 32$ in each direction, with a cutoff radius $r_{\max} = 4$ m. The L_2 norm of the force error, given by

$$L_2 = \sqrt{\frac{1}{N}\sum_{i=1}^{N}\left(\boldsymbol{f}^{(i)}_{\text{coulomb}} - \boldsymbol{f}^{(i)}_{\text{exact}}\right)^2}, \tag{2.28}$$

is shown in Fig. 2.1 as a function of the Ewald constant. $\boldsymbol{f}_{\text{exact}}$ is the Coulomb force obtained from a well-converged Ewald summation (see Appendix. A), which gives the exact solution for an electrostatic field with periodic boundary conditions. For comparison, the electric field is computed using both spectral difference and finite difference schemes. Results from PM were obtained by projecting the particle charge to the mesh and sending the resulting electric field to the particle location using second-order interpolation. It was found that changing the order of accuracy for interpolation when computing PM had negligible effect on its L_2 error.

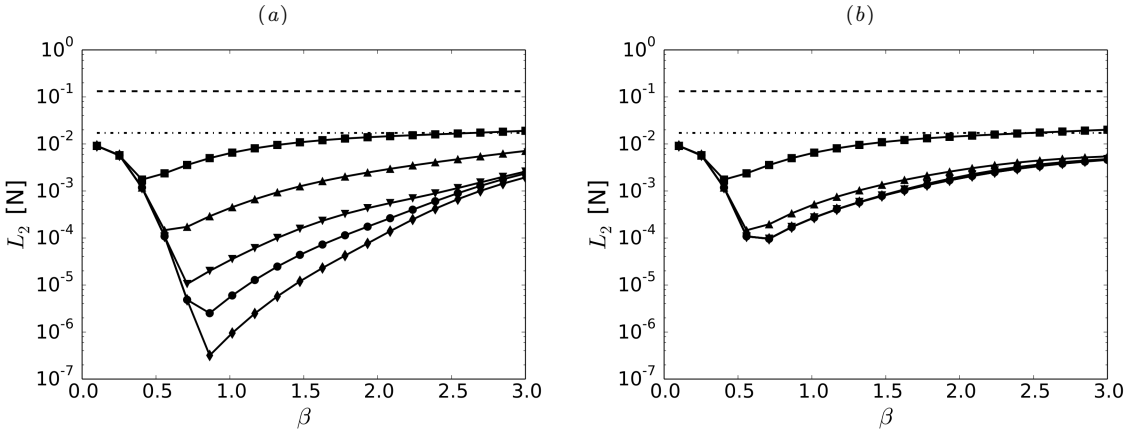

Figure 2.1: L_2 norm of the electrostatic force with the electric field computed as a function of the P^{3}M constant β that appears in Eq. (2.16). P^{3}M is solved using (a) spectral difference and (b) finite difference. PM ($--$), Hybrid method ($\cdots$) and P^{3}M (symbols) with interpolation order 0 to 4 from top to bottom, respectively.

P^{3}M shows accuracy that is approximately five orders of magnitude higher than PM

and the Hybrid method with a set of well-chosen parameters (i.e., in this case $\beta \approx 0.8$ and $r_{\max} = 4$ m). The Hybrid method shows improvement over PM, though it does not outperform P^{3}M for the parameters under consideration for both the spectral and finite difference scheme. As shown in Fig. 2.1(b), when the electric field is evaluated via finite difference, the errors associated with P^{3}M collapse for different orders of interpolation since finite difference introduces truncation errors that cannot be eliminated by increasing the interpolation order. Since P^{3}M directly takes the differentiating scheme into account when constructing the optimized screen function $\hat{G}(\boldsymbol{k})$ in Eq. (2.24), increased accuracy is obtained when the spectral scheme is employed for P^{3}M. PM and the Hybrid method, however, do not show improvement when using spectral differences. In the remaining chapters of this dissertation, only second-order finite difference operators will be considered when computing the gradient of the electric potential to be consistent with the difference operators employed in the EL framework as described in § 2.2. P^{3}M and PM will be considered to access the added benefits of capturing the short-range interactions.

2.5 A modified P^{3}M approach to handle non-periodic geometries

Despite being highly accurate and computationally efficient, the original formulation of P^{3}M relies on solving FFTs and is therefore restricted to periodic boundaries. A few efforts have been made to extend P^{3}M to non-periodic domains [11, 140] but at the expense of computational efficiency. One example is the aforementioned hybrid method proposed by Kolehmainen et al. [126]. Grosshans and Papalexandris [88] also proposed a similar hybrid scheme in which the short-range force is directly evaluated via Coulomb's law and the long-range contribution is estimated using Gauss' law instead. As with P^{3}M, these methods scale like $\mathcal{O}(N \log N)$, yet they are not restricted to periodic domains. However, the double-counting term is either neglected or not computed as precisely as with P^{3}M,

which impacts their overall accuracy.

In this section, the classic P^{3}M approach is extended to simulate charged particles in wall-bounded flows while retaining the same accuracy and cost savings. For demonstration purpose, we consider $N = 1000$ charged particles randomly distributed inside a cylindrical pipe of diameter D embedded in a domain of size $L \times H \times H$ (see Fig. 2.2(a)). For reproducibility, particle locations are determined using the random number generator by Deserno and Holm [46]. Particles are fixed in space and the fluid phase is absent to allow for direct error measurements of the electrostatic force. The pipe only admits longitudinal periodicity. The domain is discretized using a uniform Cartesian mesh with 32 grid points across D and uniform grid spacing $\Delta x = \Delta y = \Delta z$. Note that the proposed method is generally applicable to other non-periodic domains of arbitrary geometry where D would be replaced by other relevant length scales.

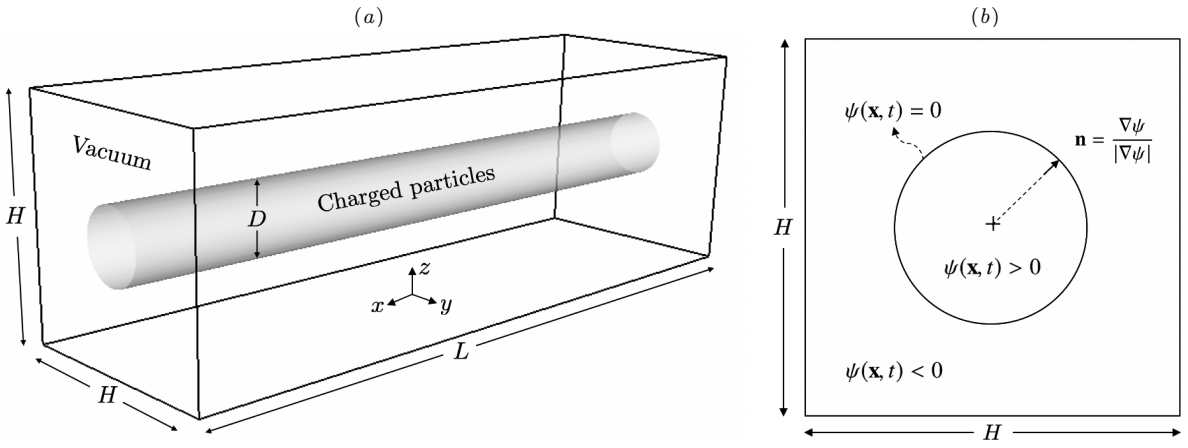

Figure 2.2: Schematic of the numerical configuration used for demonstrating the modified P^{3}M approach. (a) Charged particles are located within the grey cylindrical region, surrounded by a vacuum (white region). (b) Signed distance levelset function used to obtain distance and normal information from the boundary. Fluid and particles reside within the cylinder ($\psi > 0$). A pure vacuum exists outside the cylinder ($\psi < 0$).

A signed distance levelset function $\psi(\boldsymbol{x}, t)$ is employed to represent the closest distance to the wall such that $\psi(\boldsymbol{x}, t) > 0$ inside and $\psi(\boldsymbol{x}, t) < 0$ outside. The wall corresponds to

$\psi(\boldsymbol{x}, t) = 0$. The unit normal vector pointing into the domain is defined as

$$\mathbf{n} = \frac{\nabla\psi}{|\nabla\psi|}, \tag{2.29}$$

which will be used in § 2.5.3 to enforce appropriate boundary conditions. Note that the same levelset information is used by a cut-cell immersed boundary method when imposing boundary conditions for the fluid phase.

2.5.1 Effect of domain size on the accuracy of classic P^{3}M

As a first attempt to extend P^{3}M to non-periodic geometries, the computational domain remains triply periodic which allows for FFT evaluations. Instead, the spanwise domain length H is increased to mimic a pseudo periodic boundary condition. However, errors will be introduced to the Coulomb force due to the periodic images. To quantify this error associated with the classic P^{3}M approach, the L_2 norm of the relative error in the Coulomb force is computed according to

$$L_2 = \sqrt{\frac{1}{N}\sum_{i=1}^{N}\left(\boldsymbol{f}^{(i)}_{\text{coulomb}} - \boldsymbol{f}^{(i)}_{\text{exact}}\right)^2} \Bigg/ \sqrt{\frac{1}{N}\sum_{i=1}^{N}\left(\boldsymbol{f}^{(i)}_{\text{exact}}\right)^2}, \tag{2.30}$$

where $\boldsymbol{f}_{\text{exact}}$ is the Coulomb force obtained from a well-converged Ewald summation that only admits streamwise periodicity. For comparison, the electric field is computed using both likely-charged and oppositely-charged particles.

The error of the classic P^{3}M approach is plotted as a function of the non-dimensional domain size H/D in Fig. 2.3. In this case, $\beta = 8$ is the optimal value that minimizes the L_2 error, which is determined by performing a parameter sweep. In practice, the optimal value of β can be easily estimated using an analytical approximation derived by Deserno and Holm [47]. $r_{\max} = 6.4\Delta x$, which is the minimum value that the L_2 errors are insensitive to and satisfies the lower bound ($r_{\max} \gtrsim 3\Delta x$) suggested by Hockney and Eastwood [104]. The error decreases with the lateral domain size H due to the decay of

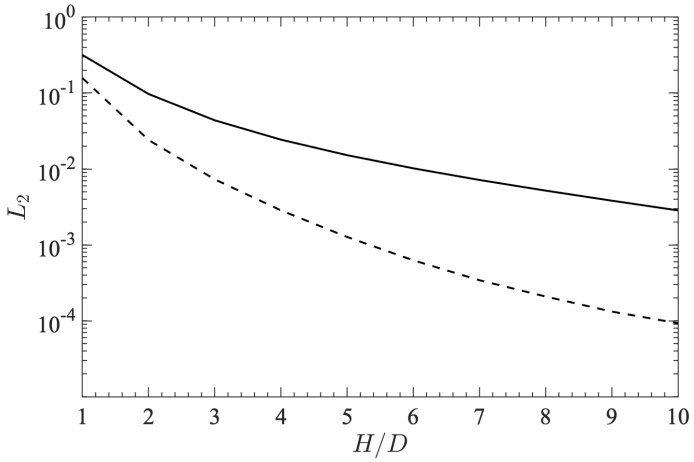

Figure 2.3: L_2 norm of the error in Coulomb force using the classic P^{3}M approach as a function of domain size H/D. 1000 likely-charged (–) and oppositely-charged (- -) particles within a pipe of diameter D are considered. The exact solution is computed using a well-converged Ewald-summation ($\boldsymbol{m} = 10$) with periodicity only in the axial direction.

the electric field. For likely-charged particles, H must be at least $7D$ to obtain a relative error below 1%. For oppositely-charged particles, the error decays more rapidly and therefore $H \geq 3D$ is required. Nevertheless, this indicates that naively applying P^{3}M to non-periodic geometries requires much larger domain sizes and consequently significantly higher computational cost. For example, P^{3}M has been applied to non-periodic molecular dynamics calculations by inserting empty volumes between atom slabs [1]. The treatment is found to be computationally inefficient when the domain size $H > 3D$. Note that since P^{3}M involves FFT evaluations with uniform grid spacing in each direction, grid stretching is also not applicable without significant modification.

2.5.2 Scaled-mapping treatment to handle non-periodic geometries

Here we propose an alternative way to solve electrostatics on the mesh such that P^{3}M can be accurately evaluated without artificially increasing the domain size in non-periodic directions. The physical domain size is set to $H = D$ and we define $\mathcal{L}$ as the target lateral domain length required to remove periodic images. Instead of increasing the domain size

to $\mathcal{L}$ as was done in the previous section, the particle positions are linearly scaled down by a ratio $\gamma = \mathcal{L}/D$ when extrapolating the particle charge onto the mesh (see Fig. 2.4(a)), referred to herein as 'scaled-mapping,' according to

$$\rho'_m(\boldsymbol{x}, t) = \sum_{i=1}^{N} q_p^{(i)} \mathcal{W}(\boldsymbol{x} - \boldsymbol{\mathcal{X}}_p^{(i)}(t)), \tag{2.31}$$

where $\boldsymbol{\mathcal{X}}_p^{(i)} = \boldsymbol{x}_p^{(i)} \otimes (1, 1/\gamma, 1/\gamma)$ is a fictitious particle located at the scaled position of particle i and $\rho'_m(\boldsymbol{x}, t)$ denotes the corresponding charge density. Due to the linear nature of the electric Poisson equation, this will result in the same electric field as if the domain size was increased to $\mathcal{L}$ (see Fig. 2.4(b)) given that the interpolation, extrapolation, and gradient operators are scaled accordingly, which will be made explicit later. The resulting electric field at the scaled particle positions are then assigned back to their original locations (i.e., $\boldsymbol{E}_l[\boldsymbol{x}_p^{(i)}] = \boldsymbol{E}_l[\boldsymbol{\mathcal{X}}_p^{(i)}]$, see Fig. 2.4(c)). This modified P^{3}M approach allows for accurate evaluations of the electric Poisson equation without sacrificing computational efficiency, and is generally applicable to any non-periodic geometries other than cylindrical pipes. For complex geometries with large curvatures, sufficient grid resolution is required to accurately represent the distance function on the grid.

Let $\boldsymbol{k}'$ and $\boldsymbol{E}'_l(\boldsymbol{x}, t)$ denote the wavenumber and long-range electric field computed at the location of the fictitious particles. To obtain the correct solution to the electric Poisson equation at physical locations, these quantities must be scaled linearly according to

$$\rho_m(\boldsymbol{x}, t) = \rho'_m(\boldsymbol{x}, t)/\gamma^2, \tag{2.32}$$

$$\boldsymbol{k} = (k'_x, k'_y/\gamma, k'_z/\gamma) \equiv \boldsymbol{k}' \otimes (1, 1/\gamma, 1/\gamma), \tag{2.33}$$

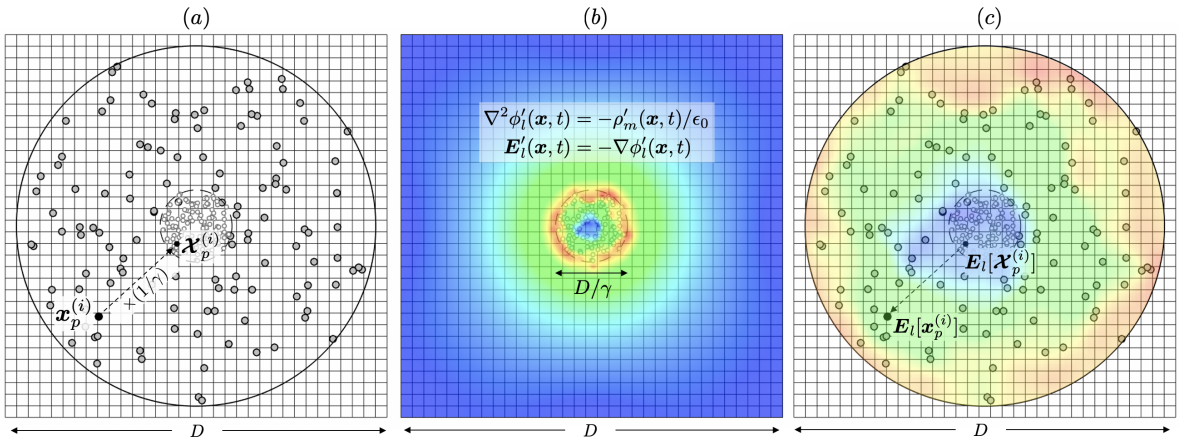

Figure 2.4: Proposed treatment to solve the P^{3}M long-range contribution in non-periodic geometries. Physical particles at $\boldsymbol{x}_p^{(i)}$ are shown in grey. Fictitious particles after linearly scaling their positions at $\boldsymbol{\mathcal{X}}_p^{(i)}$ are shown as hollow (not to scale). A black particle before and after mapping is highlighted to illustrate the proposed procedure. The physical boundary and the fictitious boundary after mapping are shown as solid and dashed circles, respectively. Color indicates the corresponding electric field (blue: low; red: high). (a) Step 1: particle locations $\boldsymbol{x}_p^{(i)}$ are scaled down by a factor of $\gamma = \mathcal{L}/D$ to $\boldsymbol{\mathcal{X}}_p^{(i)}$. (b) Step 2: particle charges at $\boldsymbol{\mathcal{X}}_p^{(i)}$ are extrapolated onto the mesh to obtain ρ_m' and $\boldsymbol{E}_l'$, which are then rescaled to ρ_m and $\boldsymbol{E}_l$. (c) Step 3: $\boldsymbol{E}_l$ is interpolated to the location of the fictitious particles to obtain $\boldsymbol{E}_l[\boldsymbol{\mathcal{X}}_p^{(i)}]$, which is then directly assigned back to its original location as $\boldsymbol{E}_l[\boldsymbol{x}_p^{(i)}]$.

$$\boldsymbol{E}_l(\boldsymbol{x},t) = (E_{l,x}', E_{l,y}'/\gamma, E_{l,z}'/\gamma) \equiv \boldsymbol{E}_l'(\boldsymbol{x},t) \otimes (1, 1/\gamma, 1/\gamma). \tag{2.34}$$

The detailed solution procedure is summarized in § 2.5.4.

2.5.3 Boundary conditions

In the presence of walls, the net electric field of particle i can be decomposed into two components as $\boldsymbol{E}[\boldsymbol{x}_p^{(i)}]_{\text{tot}} = \boldsymbol{E}[\boldsymbol{x}_p^{(i)}] + \boldsymbol{E}[\boldsymbol{x}_p^{(i)}]_{\text{wall}}$, where $\boldsymbol{E}[\boldsymbol{x}_p^{(i)}]_{\text{wall}}$ is an additional term that imposes appropriate boundary conditions at the walls. This term can be obtained by integrating Gauss law $\nabla^2\phi_{\text{wall}} = 0$ in the computational domain [51]. If the wall is iso-potential it is an electrical conductor, which yields a Dirichlet boundary condition for the potential (i.e., ϕ_{wall} is a constant). As a result, $\boldsymbol{E}[\boldsymbol{x}_p^{(i)}]_{\text{wall}} = -\nabla\phi_{\text{wall}}|\boldsymbol{x}=\boldsymbol{x}_p = 0$, and thus the Coulomb forces experienced by the particles are not affected by the boundary if

the pipe wall is assumed to conduct electrical charge. Note that such additive treatment of particle-particle and particle-wall contributions generally holds for most inner regions of wall-bounded flows, however for regions very close to the boundary, the local electrical field is modified by the presence of the wall such that the iso-potential line is aligned with the wall boundary. Such localized wall effects often play a negligible role on the particle dynamics unless particles are located within the wall buffer region. In that case, additional models are required to correctly capture particle-wall interactions.

In this study, the method of image charging is employed. The electrostatic force on a particle at distance $\psi(\boldsymbol{x}_p)$ from the wall can be found by placing an image particle of opposite charge mirrored across the boundary at a distance $-\psi(\boldsymbol{x}_p)$ from the wall. The particle-wall attractive force of particle i can be calculated using Coulomb's law given by

$$\boldsymbol{f}^{(i)}_{\text{image}} = \frac{q_p(-q_p)}{4\pi\epsilon_0} \frac{\boldsymbol{n}_i}{\left|\psi(\boldsymbol{x}_p^{(i)}) - (-\psi(\boldsymbol{x}_p^{(i)}))\right|^2} = -\frac{q_p^2 \boldsymbol{n}_i}{16\pi\epsilon_0 \psi(\boldsymbol{x}_p^{(i)})^2}, \tag{2.35}$$

where $\mathbf{n}_i = \nabla\psi(\boldsymbol{x}_p^{(i)})/|\nabla\psi(\boldsymbol{x}_p^{(i)})|$ is the normal vector pointing from particle i to the closest point on the wall. Note that traditionally $\boldsymbol{f}^{(i)}_{\text{image}}$ only accounts for the image of particle i and neglects contributions from its neighbors [94]. In this study, all particles are imaged across the boundary and their electrostatic forces are computed using direct summation within the same cut-off radius used in P^3M. The truncated direct summation has been shown to be capable of accurately computing electrostatic interactions [143]. A comparison of the modified image charging procedure using a truncated direct summation and the traditional image charging of a single particle will be presented in the following sections.

As shown in Fig. 2.5, the spatial location of the imaged particles can be found using

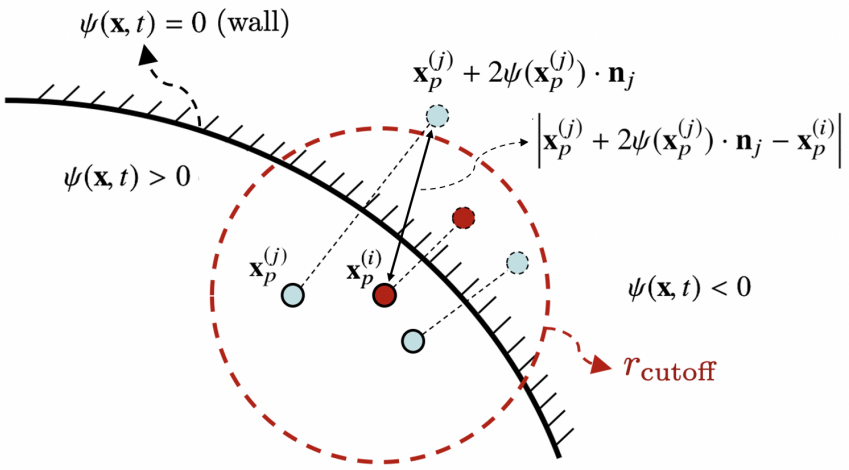

Figure 2.5: Schematic of the wall image charging approach that leverages the signed distance levelset function and its normal to account for electrostatic interactions due to neighboring particles within a prescribed cutoff radius.

the levelset normal and distance information given by

$$\boldsymbol{x}_p^{(j)}{}_{\text{image}} = \boldsymbol{x}_p^{(j)} + 2\psi(\boldsymbol{x}_p^{(j)}) \cdot \mathbf{n}_j. \tag{2.36}$$

A truncated direct summation method is then employed to compute the electrostatic force due to all image particles via

$$\boldsymbol{f}_{\text{image}}^{(i)} = \frac{q_p^{(i)}}{4\pi\epsilon_0} \sum_{j \neq i} q_p^{(j)} \frac{\boldsymbol{n}_{ij}}{\left|\boldsymbol{x}_p^{(j)}{}_{\text{image}} - \boldsymbol{x}_p^{(i)}\right|^2}, \text{ if } \left|\boldsymbol{x}_p^{(j)}{}_{\text{image}} - \boldsymbol{x}_p^{(i)}\right| \leq r_{\text{cutoff}}, \tag{2.37}$$

which is added to Eq. (2.12) as an additional wall-correction term giving rise to the total electrostatic force as

$$\boldsymbol{f}_{\text{coulomb}}^{(i)} = q_p^{(i)} \boldsymbol{E}[\boldsymbol{x}_p^{(i)}] + \boldsymbol{f}_{\text{image}}^{(i)}. \tag{2.38}$$

This is performed after $\boldsymbol{E}[\boldsymbol{x}_p^{(i)}]$ is obtained using the extended P^{3}M procedure by following the steps described in § 2.5.4.

If the wall is made of non-conducting materials (e.g., acrylic), charges will accumulate on the surface and remain localized. As a result, the boundary is no longer iso-potential

and the current image charging method requires modification [216, 140]. Although such modification is not necessary in this study as we only consider conducting walls, the current approach can be readily extended to insulating wall-bounded flows.

2.5.4 Solution procedure

The solution procedure for the modified P^3M algorithm is summarized here. Additional steps compared to the original P^3M approach are shown in italic.

1. Initialization
   - Initialize the complex FFT routine
   - Read in the P^3M cutoff radius and P^3M constant β
   - *Read in the fictitious domain length $\mathcal{L}$ and determine the scaling ratio $\gamma = \mathcal{L}/D$*
   - Populate the Gaussian screen function in reciprocal space $\hat{G}(\boldsymbol{k})$ according to Eq. (2.21)
   - *Scale the wavenumber in $\hat{G}(\boldsymbol{k})$ using Eq.* (2.33)
2. Compute the long-range contribution of the electric field
   - *Map the particles to their fictitious locations: $\boldsymbol{\mathcal{X}}^{(i)} = \boldsymbol{x}_p^{(i)} \otimes (1, 1/\gamma, 1/\gamma)$*
   - Extrapolate the particle charge at $\boldsymbol{\mathcal{X}}_p^{(i)}$ onto the mesh using Eq. (2.31) to obtain $\rho'_m(\boldsymbol{x}, t)$
   - *Linearly scale $\rho'_m(\boldsymbol{x}, t)$ according to Eq.* (2.32) *to obtain $\rho_m(\boldsymbol{x})$*
   - Solve the electric Poisson equation (Eqs. (2.20) and (2.25)) using FFTs to obtain ϕ_l
   - Obtain the long-range electric field $\boldsymbol{E}'_l(\boldsymbol{x}, t)$ according to Eq. (2.26)
   - *Scale $\boldsymbol{E}'_l(\boldsymbol{x}, t)$ according to Eq.* (2.34) *to obtain $\boldsymbol{E}_l(\boldsymbol{x}, t)$*
   - Interpolate the electric field onto the fictitious particles at $\boldsymbol{\mathcal{X}}_p^{(i)}$ as $\boldsymbol{E}_l[\boldsymbol{\mathcal{X}}_p^{(i)}]$

- *Assign the electric field at* $\boldsymbol{\mathcal{X}}_p^{(i)}$ *back to* $\boldsymbol{x}_p^{(i)}$ *via* $\boldsymbol{E}_l[\boldsymbol{x}_p^{(i)}] = \boldsymbol{E}_l[\boldsymbol{\mathcal{X}}_p^{(i)}]$

3. Compute the short-range contribution of the electric field

   - Check if particle j is within a cutoff radius of particle i using near neighbor detection (e.g., see [30])
   - Calculate the short-range electric field according to Eq. (2.18)

4. Compute the total electrostatic force

   - Compute the total electric field using Eq. (2.27)
   - Apply Eq. (2.12) to obtain the net electrostatic force on particle i

5. *Apply appropriate boundary conditions*

   - *Compute the electrostatic force due to image particles at the wall using Eq.* (2.37)
   - *Apply Eq.* (2.38) *to correct the electrostatic force on particle i due to boundaries*

Since all additional steps compared to the classic P^{3}M method (denoted by italic text above) are of cost of either $\mathcal{O}(1)$ or $\mathcal{O}(N)$, the modified P^{3}M retains its original cost of $\mathcal{O}\left(N \log N\right)$. It should be noted that for systems that are not charge neutral, the Poisson equation used to solve the electric potential (Eq. (2.25)) is ill-defined. To that end, a uniform charge density is added to the background flow such that the domain-averaged charge density is zero in step 2.

2.5.5 Verification

Here we assess the accuracy of the extended P^{3}M approach as well as PM and the classic P^{3}M methods where the contribution from periodic images of particles are not removed. We consider $N = 1000$ oppositely-charged particles (500 with positive unit charge and 500 negative) and a domain size of $H = D = 1$ and $L = 10$ in the absence of a fluid. All cases are solved on a Cartesian mesh, with a cutoff radius $r_{\max} = 0.2$, scaling

ratio $\gamma = 10$, and the number of grid points per direction $N_{\mathrm{g}} = 128$. The L_2 norm of the force error as defined in Eq. (2.30) is shown in Fig. 2.6(a) as a function of the P^{3}M constant. Results from PM were obtained by projecting the particle charge to the mesh and solving the Poisson equation using a multi-grid solver. The resulting electric field is then sent to the particle location using second-order interpolation. It was found that changing the order of accuracy for interpolation when computing PM had negligible effect on its L_2 error.

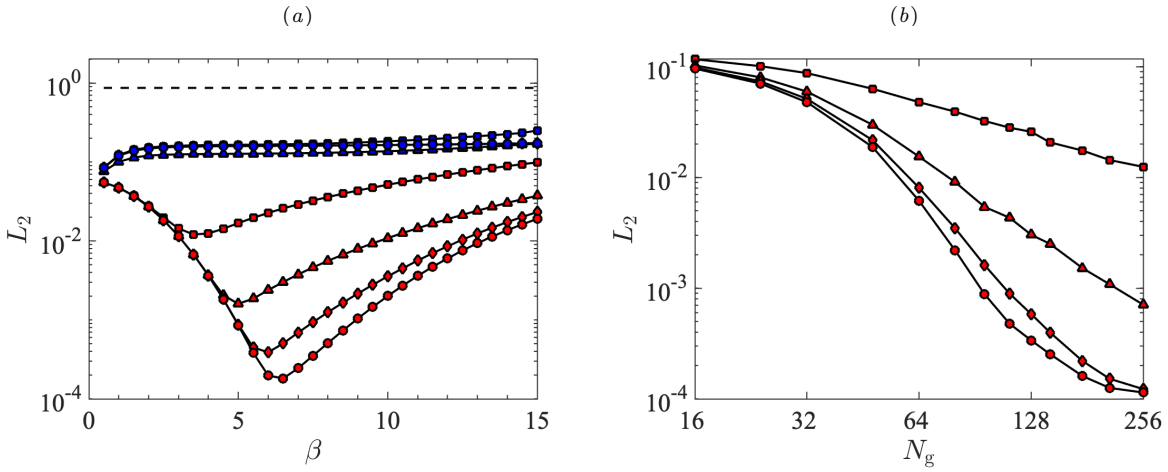

Figure 2.6: The L_2-norm of the relative error of the electrostatic force for PM (dashed line), classic P^{3}M (blue symbols), and extended P^{3}M (red symbols). Interpolation order 1 to 4 are shown as $\square$, $\triangle$, $\diamond$ and $\circ$, respectively. The error is plotted as a function of (a) the P^{3}M constant β that appears in Eqs. (2.16) and (2.18) with $N_g = 128$ and (b) the number of grid point per direction with $\beta = 6.5$.

The extended P^{3}M approach exhibits errors that are approximately four orders of magnitude smaller than PM with a set of well-chosen parameters (i.e., in this case $\beta \approx 6.5$ and $r_{\max} = 0.2$). The error of the classic P^{3}M approach, however, is only approximately an order of magnitude smaller than PM and remains insensitive to the interpolation order or β. This suggests the errors introduced by the periodic images of charged particles can not be eliminated by increasing the interpolation order or β. PM exhibits large error primarily due to cancellation of opposite charges on the mesh. Note in this study, spectral difference operators are considered when computing the gradient of the electric potential

since it exhibits higher accuracy compared to other difference operators such as finite difference [270].

The grid convergence study for the extended P^{3}M is shown in Fig. 2.6(b). The error decays monotonically with increasing grid resolution and interpolation order. For interpolation order 3 and 4, the convergence rate slows down when $N_\mathrm{g} \geq 128$, which indicates that the error is no longer bounded by the truncation error but instead due to periodic images. For example, when $N_\mathrm{g} = 256$, the error approaches $\mathcal{O}(10^{-4})$, which is consistent with the error due to periodic images for $\gamma = 10$ as shown in Fig. 2.3.

2.6 Van der Waals models compatible with soft-sphere collisions

The magnitude of the van der Waals force between two particles i and j of the same size, F_{ij}^{vw}, is modeled as [96]

$$F_{ij}^{\mathrm{vw}}(A,s) = \frac{A}{6}\frac{d_p^2\,(d_p+s)}{s^2(2d_p+s)^2}\left[\frac{s\,(2d_p+s)}{(d_p+s)^2}-1\right]^2, \tag{2.39}$$

where A is the Hamaker constant. Due to the short range nature of the van der Waals force, it is assumed that the force saturates at a minimum separation, $s_\mathrm{min} = 1\times10^{-9}$ m and is cut off at $s_\mathrm{max} = d_p/4$. For particle-wall interactions, Eq. (2.39) is reduced to

$$F_{i,\,\mathrm{wall}}^{\mathrm{vw}}(A,s) = \frac{A\,d_p}{12\,s^2}. \tag{2.40}$$

As described in § 2.3.1, the spring stiffness k used in the soft-sphere collision model is determined based on the collision time τ_col according to Eq. (2.8), resulting in artificially 'soft' particles to enable larger time steps. A modified van der Waals model was recently proposed to be compatible with the soft-sphere collision model outlined in § 2.3 [91]. The modification ensures the work done by the van der Waals force remains unchanged when particles overlap, such that its overall effect is insensitive to the choice of k and

consequently the results remain unchanged as Δt is adjusted. This is accomplished by modifying the saturation distance and Hamaker constant when two particles are in direct contact, according to

$$\boldsymbol{f}_{\mathrm{vw}}^{(i)} = -F_{\mathrm{vw}}^{(i)}\boldsymbol{n}_{ij} = \begin{cases} -F_{ij}^{\mathrm{vw}}(A, s - s_0)\boldsymbol{n}_{ij} & \text{for} \quad s_{\min}^s < s < s_{\max} \\ -F_{ij}^{\mathrm{vw}}\left(A^s, s_{\min}\right)\boldsymbol{n}_{ij} & \text{for} \quad s \leq s_{\min}^s, \end{cases} \tag{2.41}$$

with $A^s = A\left(k/k_r\right)^{1/2}$ where k_r is the "real" spring stiffness of the particle that would result in negligible overlap during collisions. A value of $k_r = 7000$ N/m is used and the simulation spring stiffness k is chosen such that $k_r/k = 700$ as described in [91]. The offset s_0 and shifted saturation distance $s_{\min}^s$ can be obtained by solving the following nonlinear equations

$$F_{\mathrm{vw}}\left(\theta, s_{\min}^R\right) = F_{\mathrm{vw}}\left(1, s_{\min}^s - s_0\right), \tag{2.42}$$

and

$$F_{\mathrm{vw}}\left(1, s_{\min}\right) \cdot s_{\min} + \int_{s_{\min}}^{s_{\max}} F_{\mathrm{vw}}(1, s)\mathrm{d}s = F_{\mathrm{vw}}\left(\theta, s_{\min}\right) \cdot s_{\min}^s + \int_{s_{\min}^s}^{s_{\max}} F_{\mathrm{vw}}\left(1, s - s_0\right)\mathrm{d}s. \tag{2.43}$$

A bisection method is used to solve the nonlinear system of equations as a preprocessing step prior to simulation runtime. Note that the same treatment (Eq. (2.41)-(2.43)) is applied to particle-wall interactions.

2.7 Two-way coupling

Particle information is projected to the mesh using a Gaussian filtering kernel $\mathcal{G}$ with a characteristic length δ_f. The local volume fraction and momentum exchange term appearing in the fluid-phase equations (2.1)–(2.2) are evaluated as

$$\alpha = 1 - \sum_{i=1}^{N} \mathcal{G}\left(\left|\boldsymbol{x} - \boldsymbol{x}_p^{(i)}\right|\right) V_p, \tag{2.44}$$

and

$$\boldsymbol{F}_{\text{inter}} = -\frac{1}{\rho}\sum_{i=1}^{N}\mathcal{G}\left(\left|\boldsymbol{x}-\boldsymbol{x}_p^{(i)}\right|\right)\boldsymbol{f}_{\text{inter}}\,, \tag{2.45}$$

where $V_p = \pi d_p^3/6$ is the particle volume, and the momentum exchange term for particle i is given by

$$\boldsymbol{f}_{\text{inter}}^{(i)} = \boldsymbol{f}_{\text{drag}}^{(i)} + \rho V_p \nabla\cdot\boldsymbol{\tau}[\boldsymbol{x}_p^{(i)}], \tag{2.46}$$

which contains contributions of resolved fluid stresses at the particle location ($\boldsymbol{\tau}[\boldsymbol{x}_p^{(i)}]$) and unresolved stresses (i.e. drag) modeled according to

$$\frac{\boldsymbol{f}_{\text{drag}}^{(i)}}{m_p} = \frac{F\left(\alpha,\text{Re}_p\right)}{\tau_p}\alpha\left(\boldsymbol{u}[\boldsymbol{x}_p^{(i)}]-\boldsymbol{v}_p^{(i)}\right), \tag{2.47}$$

where $\boldsymbol{u}[\boldsymbol{x}_p^{(i)}]$ is the fluid velocity at the location of particle i, $\text{Re}_p = \alpha\|\boldsymbol{u}[\boldsymbol{x}_p^{(i)}]-\boldsymbol{v}_p^{(i)}\|d_p/\nu$ is the particle Reynolds number, and $\tau_p = \rho_p d_p^2/(18\rho\nu)$ is the particle response time. In this work, $F\left(\alpha,\text{Re}_p\right)$ is modeled according to the dimensionless drag coefficient of Tenneti et al. [228] to take into account finite Reynolds number and volume fraction effects on the drag force.

In order to project the particle data to the grid in an efficient manner and ensure numerical stability, the two-step filtering approach of Capecelatro and Desjardins [30] is employed. First the particle data is sent to the neighboring grid points via trilinear extrapolation, the solution is then diffused such that the projection resembles a Gaussian with characteristic size of δ_f. To avoid restrictive time step constraints in the diffusion process, the latter step is solved implicitly via approximate factorization with a second order alternating direction implicit (ADI) scheme. In this work, the filter size $\delta_f = 8\,d_p$. Such an approach has been demonstrated to accurately predict the characteristics of particle clustering in turbulent flows [31].

2.8 Multi-scale time stepping

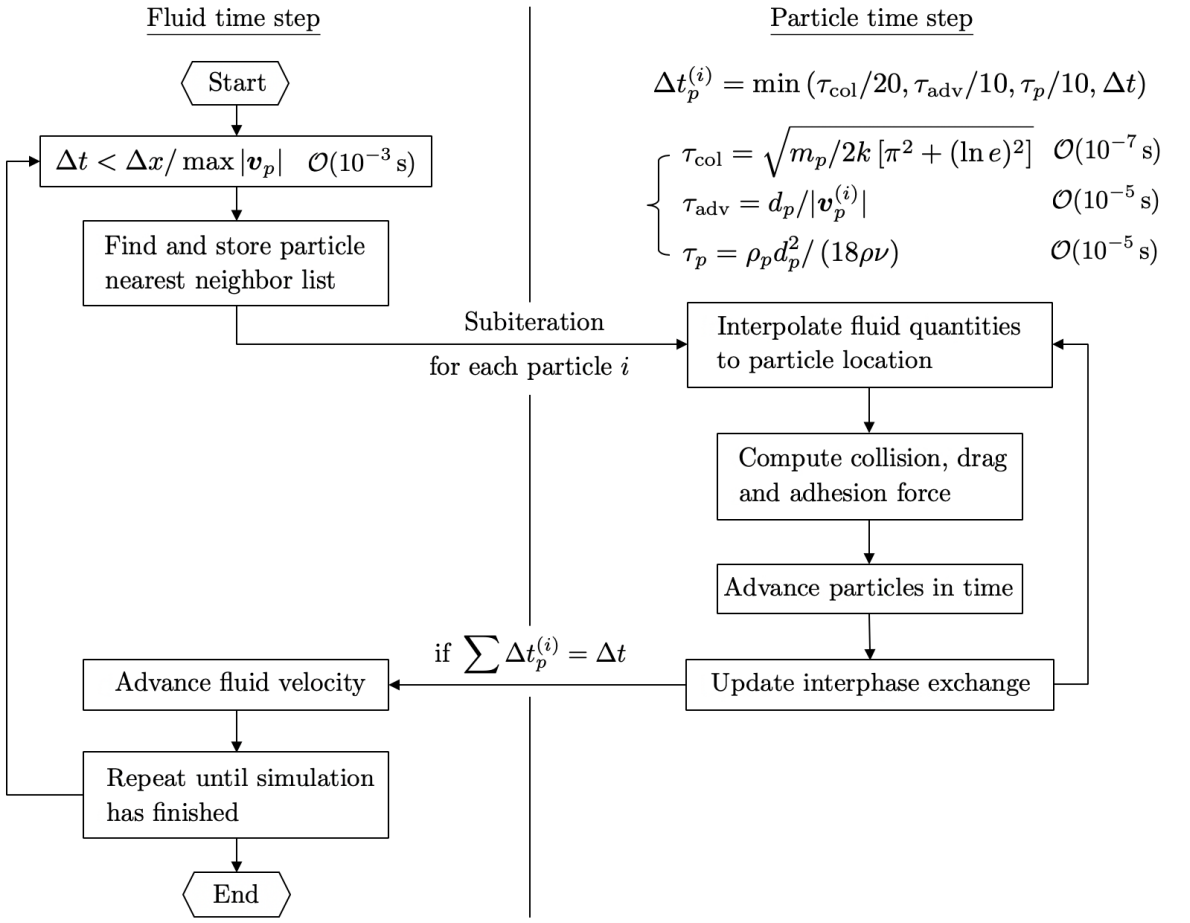

Figure 2.7: Multi-scale time stepping algorithm used in the simulations. For each fluid time step Δt, particles are sub-iterated at a smaller time step Δt_p until they are in sync with the fluid.

The wide range of time scales associated with cohesive particles in turbulent flows presents a significant challenge in numerical simulations. In typical incompressible flow applications, the fluid time scale $\tau_f = (\nu/\varepsilon)^{1/2}$ is $\mathcal{O}(10^{-3}\,\mathrm{s})$, while the particle response time $\tau_p = \mathcal{O}(10^{-5}\,\mathrm{s})$ and the collision time scale $\tau_{\mathrm{col}} = \mathcal{O}(10^{-7}\,\mathrm{s})$, even with the artificially softened particles and modified van der Waals model. In order to properly resolve the time scales at play in a tractable manner, a multi-scale time stepping framework based on the method proposed by Marshall [152] is employed (see Fig. 2.7). In this approach, the fluid equations are solved on a separate time scale from the particles. To avoid $\mathcal{O}(N^2)$ calcula-

tions of the inter-particle forces, a nearest neighbor detection algorithm is employed, such that interactions via collisions and van der Waals are only considered between particles in adjacent grid cells [30]. The fluid time step, Δt, is limited by the convective time scale dictated by the Courant–Friedrichs–Lewy (CFL) number. To simplify the implementation of the two-way coupling described in § 2.7, the fluid time step is further constrained to prevent particles from moving more than one grid cell, i.e. $\Delta t < \Delta x / \max |\boldsymbol{v}_p|$. This ensures that the particle nearest-neighbor list only needs to be updated once per fluid time step. The particle advection time scale, $\tau_{\text{adv}} = d_p/|\boldsymbol{v}_p|$, must be small enough to prevent significant overlap between particles. To ensure the particle dynamics are well resolved, particles are sub-iterated each fluid time step based on a time scale that is one order of magnitude smaller than the minimum of the collision time, particle response time, and particle advection time. Finally, a second-order Runge–Kutta scheme is used for updating each particle's position, velocity and angular velocity.

2.9 Conclusions

In this chapter, an efficient and tractable Eulerian–Lagrangian framework capable of accurately resolving particle interactions in the presence of attractive forces was developed. Two-way coupling is accounted for via drag and volume displacement effects. The van der Waals force model is modified to allow for soft-sphere contact. A multiscale time-stepping algorithm is introduced to minimize the computational cost when resolving the wide range of time scales. Due to the long-range nature of the Coulomb potential, special attention was paid to treating the electrostatic force. We reviewed several methods, including the particle mesh, Ewald summation, particle-particle-particle–mesh, and hybrid approaches. We showed that the P^3M method admits several orders of magnitude higher accuracy for simple configurations of oppositely charged particles in periodic boxes.

Despite being highly accurate and computationally efficient, the original formulation of P^3M involves FFT evaluations and is therefore restricted to periodic boundaries. In this work, we extend the P^3M method to accurately compute electrostatic interactions in wall-bounded flows. The domain is discretized using a uniform Cartesian mesh coupled with a levelset distance function to provide wall normal information when enforcing appropriate boundary conditions for particle charge. The electric field is solved using FFTs agnostic to the presence of walls. To remove the contribution of periodic images from the resulting electric field, particle positions are scaled down when computing the long-range electrostatic potential. This is in contrast to increasing the domain size, which allows for the same electric field to be obtained without sacrificing grid resolution or computational efficiency. The modified P^3M approach is shown to be orders of magnitude more accurate than PM and the classic P^3M for non-periodic geometries.

CHAPTER III

Transport of Charged Particles in Turbulent Flows

In this chapter, different algorithms to compute electrostatics are compared and tested for different flow configurations. One-point and two-point particle statistics are computed to understand the effect of electrostatics on particle transport.

3.1 Introduction

Non-trivial interactions between electrically charged particles and turbulence play an important role in many engineering and environmental flows, including atmospheric clouds [280], fluidized bed reactors [100, 195, 196], charged hydrocarbon sprays [13, 14, 213], dusty plasmas [192, 125], and wind-blown dust [125, 62]. Throughout the atmosphere for example, ion pairs are produced by cosmic rays that attach to aerosol particles and droplets. Ionization of atmospheric air together with the potential difference that exists between the upper atmosphere and the earth's surface generates a non-negligible vertical electric field that can potentially affect the collision rate and coalescence between charged droplets, which dictates the onset of rainfall [280]. Dilute suspensions of inertial (heavy) particles in isotropic turbulence will preferentially concentrate in regions of high strain rate and low vorticity [57]. Such coupling between particles and the underlying carrier phase can lead to significant spatial segregation in charge density that induces, or amplifies, an electric field. A recent study of the Sahara dessert showed that electric

fields contribute to an increase of up to ten times the amount of particles emitted into the atmosphere [62]. A positive feedback was observed whereby the electric field increases shear-induced dust lifting, which in turn introduces increased charges to the atmosphere resulting in a stronger electric field [125].

Meanwhile, the relative importance between fluid forces (i.e., drag) and electrostatic forces in turbulent flows remain elusive. When fluid-particle coupling is dominant, we expect the particles to preferentially concentrate in high strain rate regions of the flow, with the level of clustering determined by the Reynolds number and Stokes number [222]. With increasing charge magnitude, eventually Coulomb interactions will have an order-one effect on the spatial distribution of particles. Thus, the primary interest of the current work is to investigate the competition between drag and Coulomb interactions on the particle distribution and to determine to what extent particles segregate as a function of the Reynolds number, Stokes number, and charge magnitude.

In the present study, PM and P^3M methods coupled with an Eulerian–Lagrangian framework is employed to simulate charged particles in homogeneous turbulence. The governing equations and numerical implementation were presented in Chapter II. The proposed EL–P^3M method is applied to a Taylor–Green vortex in § 3.2 and homogeneous isotropic turbulence in § 3.3 to assess the competition between particle transport due to fluid coupling and Coulomb interactions. One-point and two-point statistics obtained using PM and P^3M are compared to assess the effect of added accuracy on collision rate and clustering. Finally, the extended P^3M is employed to demonstrate its utility in modeling charged particles in a turbulent pipe flow. Simulations of a turbulent pipe flow are performed in § 3.4 where the effect of charge on particle distribution and statistics are characterized.

3.2 Charged particles in a Taylor–Green vortex

The Taylor–Green vortex flow is investigated as an example of demonstrating the competition between particle transport due to fluid coupling and electrostatics, and highlight the importance of computing the short-range interaction correctly. We consider a pseudo two-dimensional flow field given by

(3.1)
$$u_f = V_0 \cos\left(\frac{2\pi x}{L}\right) \sin\left(\frac{2\pi y}{L}\right), \quad v_f \ = -V_0 \sin\left(\frac{2\pi x}{L}\right) \cos\left(\frac{2\pi y}{L}\right), \quad \text{and} \quad w_f = 0,$$

that remains constant throughout the simulation. Here, the domain length L and characteristic velocity V_0 are chosen such that the Reynolds number $\mathrm{Re} = \rho_f V_0 L/\mu = 40$. It should be noted that the two-dimensional electric Poisson equation yields an electrostatic force that scales like $1/r$, which would require modifying the PM and P^{3}M formulation. To avoid this added complexity, a pseudo two-dimensional domain is considered, discretized using $N_g = 32$ grid points in the x- and y-direction, and 4 grid points in the z-direction. Uniform grid spacing of L/N_g is employed in each direction. Particles are initially randomly distributed throughout the domain, half assigned with a positive charge and the other half a negative charge with a mean volume fraction $\langle \alpha_p \rangle = 1.0 \times 10^{-3}$. Different inertial regimes are considered by varying the Stokes number, $\mathrm{St} = \tau_p/\tau_f$, where $\tau_f = L/V_0$ is the characteristic fluid time scale. For uncharged flows with a Stokes number below a critical value $\mathrm{St_{cr}} = 1/(8\pi)$, particles will closely follow fluid streamlines [154]. Above $\mathrm{St_{cr}}$, particle inertia is high enough such that they cross fluid streamlines, giving rise to particle-trajectory crossing [49]. For $\mathrm{St} = \mathrm{St_{cr}}$, particles will collapse between the vortices.

Following Karnik and Shrimpton [117], we introduce a dimensionless number v_c^* to characterize the relative magnitude of the electric field by first defining the electric settling

velocity as

$$v_c = \tau_p \frac{E_{\text{rms}} |q_p|}{m_p}, \tag{3.2}$$

where E_{rms} is the root-mean-square (rms) magnitude of the electric field and $|q_p|$ is the charge magnitude. The electric settling velocity represents the terminal velocity that a particle would attain due to the influence of a specified electric field in a quiescent flow. With this, the corresponding non-dimensional electric settling velocity is

$$v_c^* = \frac{v_c}{u_{\text{rms}}}, \tag{3.3}$$

where u_{rms} is the rms fluid velocity magnitude.

Figures 3.1–3.3 show oppositely-charged particles in the Taylor–Green vortex using PM and P^{3}M as a function of v_c^* and St, with contours showing the vortex streamlines. The gray scale represents the self-induced electric field magnitude resulting from fluid-particle coupling. In Fig. 3.1, the level of particle clustering can be seen to increase with increasing v_c^* with a more profound effect at low Stokes numbers. The uncharged case shows particles are relatively homogeneously distributed for $\text{St} = 0.1\,\text{St}_{\text{cr}}$. Even as low as $v_c^* = 0.1$, Coulomb interactions are able to overcome fluid drag, causing particles to cross streamlines and organize into clusters. At $v_c^* = 1$ and $\text{St} = 0.1\,\text{St}_{\text{cr}}$, the clusters appear to be larger, and chains of particles form and are advected within the Taylor–Green cells. As St approaches its critical value, increased inertia assists in the clustering process. Charged particles are found to agglomerate into chains between vortices even as low as $v_c^* = 0.1$. When $\text{St} \gg \text{St}_{\text{cr}}$, particles behave ballistically and require sufficient charge to cluster. In this case, clustering does not occur at $\text{St} = 10\,\text{St}_{\text{cr}}$ until $v_c^* = 1.0$. A zoomed-in view of the Taylor–Green flow is shown in Fig. 3.2. At early times ($t/\tau_p = 0.1$), long chains and rings form. The collision force plays an important role in restricting particles from

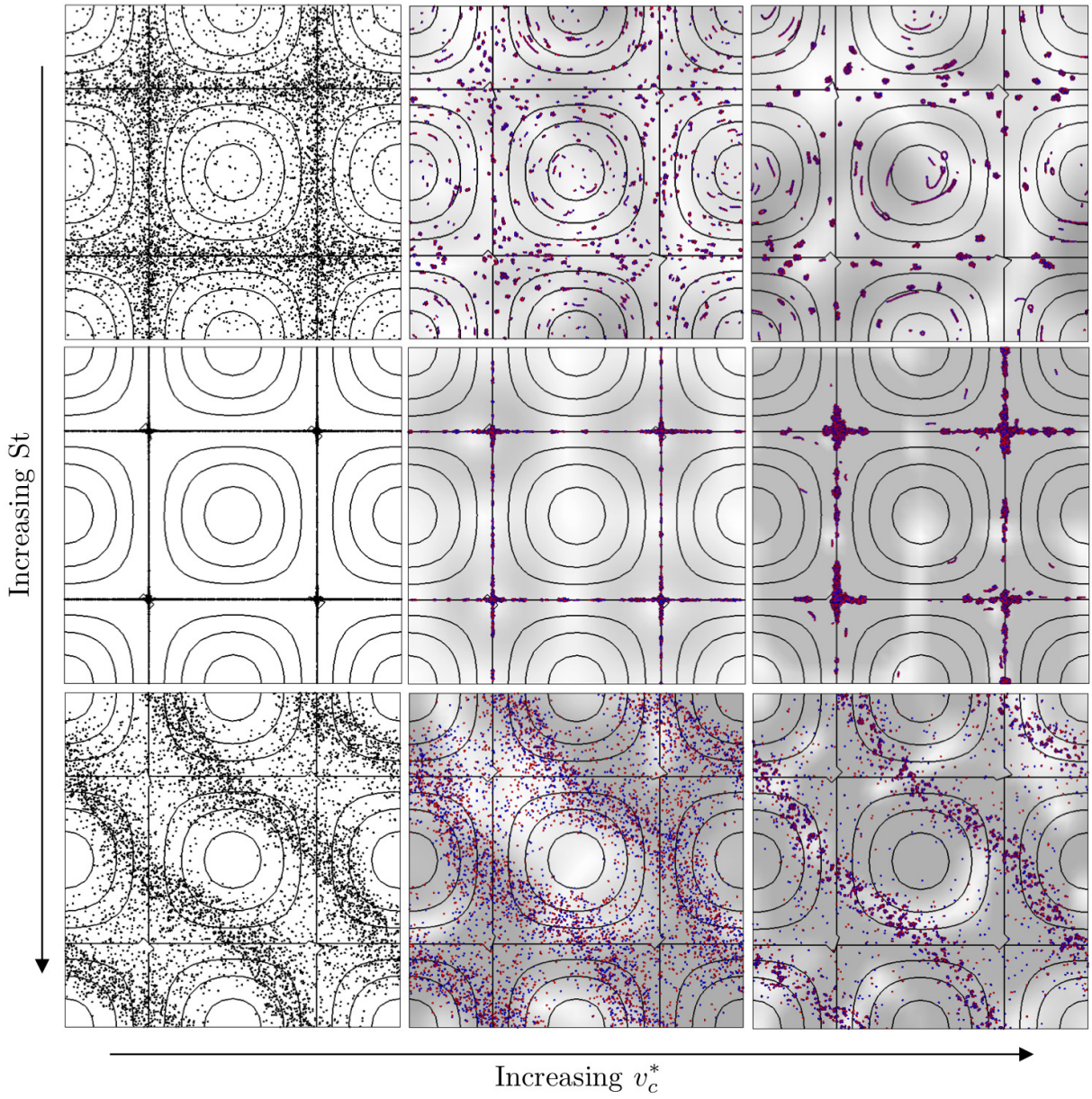

Figure 3.1: Instantaneous particle position in the Taylor Green vortex at $t/\tau_f = 1000$ using P^{3}M. Electric settling velocity $v_c^* = 0$, 0.1, and 1 (increasing from left to right) and $\mathrm{St}/\mathrm{St}_{\mathrm{cr}} = 0.1$, 1, and 100 (increasing from top to bottom). Gray-scale represents the electric field magnitude (ranging from 0 (white) to 10,000 V/m (black)). Particles are colored by their charge: neutral (black), positive (red), and negative (blue).

overlapping as they form these complex structures. The attractive electrostatic force must overcome the rebound effect of colliding particles. Even with a coefficient of restitution of 0.9, the majority of contact is observed to result in stable structures. By the time the flow reaches a statistically stationary state, particles can be seen to self-organize into

large agglomerates that accumulate in high strain regions between vortices.

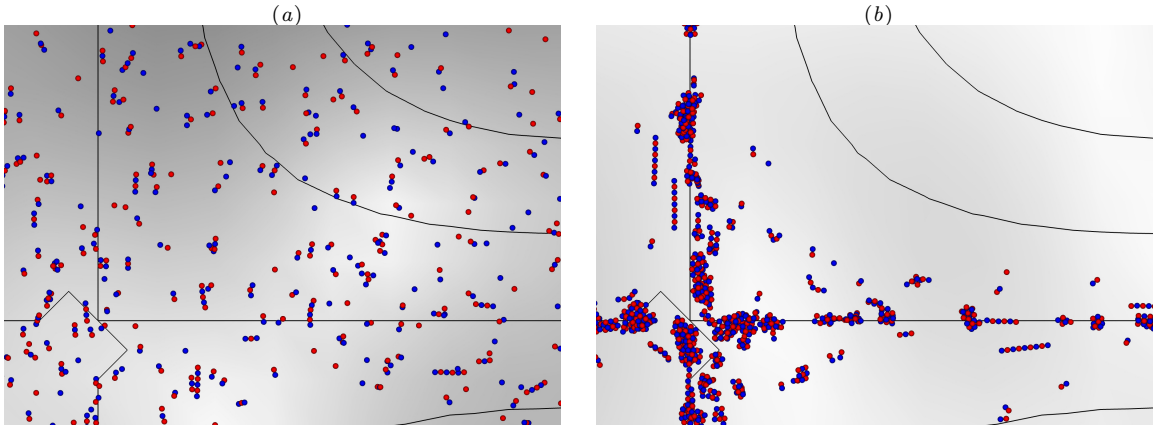

Figure 3.2: Zoomed-in view of the Taylor–Green vortex computed using P^{3}M with $v_c^* = 0.1$ and $\mathrm{St} = \mathrm{St}_{\mathrm{cr}}$. (a) $t/\tau_f = 1$, (b) $t/\tau_f = 10$. Color scheme same as Fig. 3.1.

For comparison, the resulting particle distribution computed using PM is shown in Fig. 3.3. It can be seen that particle clustering is not able to be captured even at the highest charge density ($v_c^* = 1$) for PM, while particle agglomeration is present in all P^{3}M cases. Because the direct pairwise sum is not accounted for in PM, short-range interactions are essentially averaged out when the charge is projected to the mesh. The complex structures observed in the P^{3}M calculations are thus unable to be captured. In the following section, a quantitative comparison between P^{3}M and PM will be made in simulations of homogenous isotropic turbulence.

3.3 Charged particles in homogeneous isotropic turbulence

3.3.1 System configuration

In this section, we consider 10^5 particles suspended in homogeneous isotropic turbulence (HIT) with density ratio $\rho_p/\rho_f = 1000$. The simulation domain is triply periodic with each side of length $L = 2\pi$ m. Particles are initially randomly distributed within the domain. We consider two scenarios: (i) suspensions of likely charged particles (i.e., all particles contain the same charge); and (ii) suspensions of oppositely charged particles

such that half of the particles have each polarity. The Taylor Reynolds number varies between $\mathrm{Re}_\lambda = 25.8$ and 43.5 with $\mathrm{Re}_\lambda = u_{\mathrm{rms}}\lambda/\nu$, where $\lambda = \sqrt{15\nu/\epsilon}\, u_{\mathrm{rms}}$ is the Taylor microscale. The viscous dissipation rate ϵ and rms fluctuating velocity u_{rms} are averaged over the stationary period of the forced HIT. To achieve the desired Re_λ, the linear forcing scheme of Eswaran and Pope [63] is added to the right-hand side of Eq. (2.2). For each

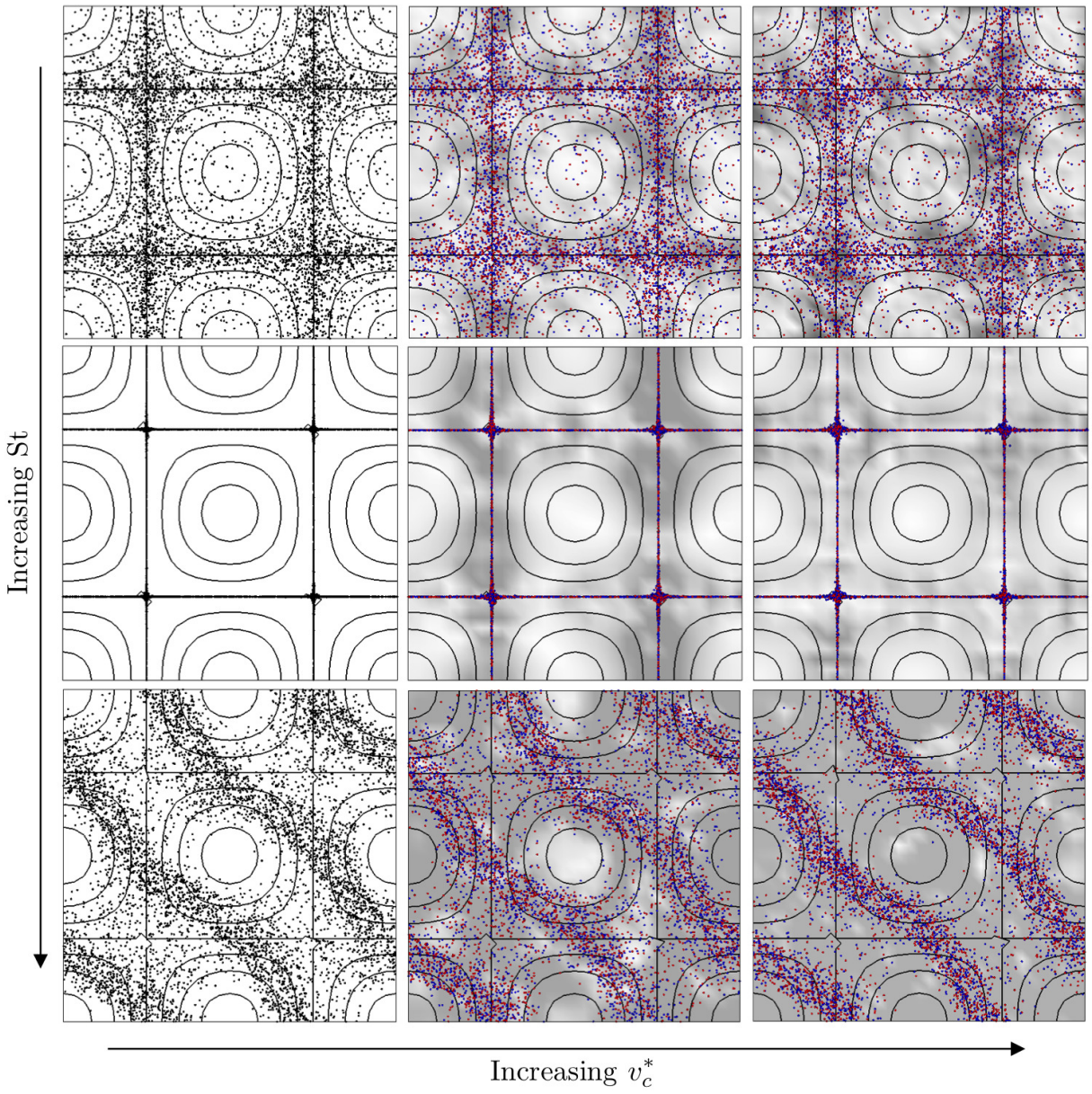

Figure 3.3: Instantaneous particle position in the Taylor Green vortex at $t/\tau_f = 1000$ using PM. Electric settling velocity $v_c^* = 0$, 0.1, and 1 (increasing from left to right) and $\mathrm{St}/\mathrm{St}_{\mathrm{cr}} = 0.1$, 1, and 100 (increasing from top to bottom). Color scheme same as Fig. 3.1.

case, the particle diameter $d_p \ll \eta$, where $\eta = (\nu^3/\epsilon)^{1/4}$ is the Kolmogorov length scale, and the mean volume fraction $\langle \alpha_p \rangle \ll 1$ such that particles do not significantly modify the underlying turbulence and one-way coupling is applicable. In this work, angled brackets denote a volume average. Particle inertia is characterized by a turbulence Stokes number, $\mathrm{St}_\eta = \tau_p/\tau_\eta$, where $\tau_\eta = (\nu/\epsilon)^{1/2}$ is the Kolmogorov time scale. The cutoff radius used in the P^{3}M method was chosen to be $r_{\max} = 4L/N_g$, with N_g the number of grid points in each direction. This was found to be the minimum value that was insensitive to the results reported herein. A list of relevant two-phase flow parameters used in each case is provided in Table 5.1. These parameters correspond to 3.3–25 mm water droplets in air with charge $3 \times 10^{-9} < |q_p| < 60 \times 10^{-9}$ C. It should be noted that for cases with like charge, the Poisson equation used to solve the electric potential (Eq. (4.2) for PM and Eq. (2.25) for P^{3}M) is ill-defined for the triply-periodic system considered here. To that end, a uniform charge density is added to the background flow such that $\langle \rho_m \rangle = 0$.

N_p^3	Re_λ	St_η	$\langle \alpha_p \rangle$	d_p/η
32^3	25.8	0.48	7.86×10^{-5}	0.09
32^3	25.8	0.96	2.22×10^{-4}	0.12
32^3	25.8	6.16	3.63×10^{-3}	0.31
32^3	25.8	24.65	2.89×10^{-2}	0.62
64^3	43.5	0.44	7.56×10^{-6}	0.09
64^3	43.5	0.89	2.14×10^{-5}	0.13
64^3	43.5	7.02	4.85×10^{-4}	0.35
64^3	43.5	27.87	3.84×10^{-3}	0.70

Table 3.1: Parameters used in the HIT simulations.

3.3.2 One-point statistics

To quantify the degree of particle clustering, Eaton and Fessler [57] proposed to measure the deviation of volume fraction from a randomly distributed field of particles by defining a scalar parameter D as a measure for clustering, given by

$$D = \frac{\langle \alpha_p'^2 \rangle^{1/2} - \sigma_p}{\langle \alpha_p \rangle}, \tag{3.4}$$

where σ_p is the standard deviation of a corresponding flow with a random distribution of particles. The probability density function of volume fraction for the corresponding randomly distributed field is given by the discrete Poisson distribution, which is used to compute σ_p.

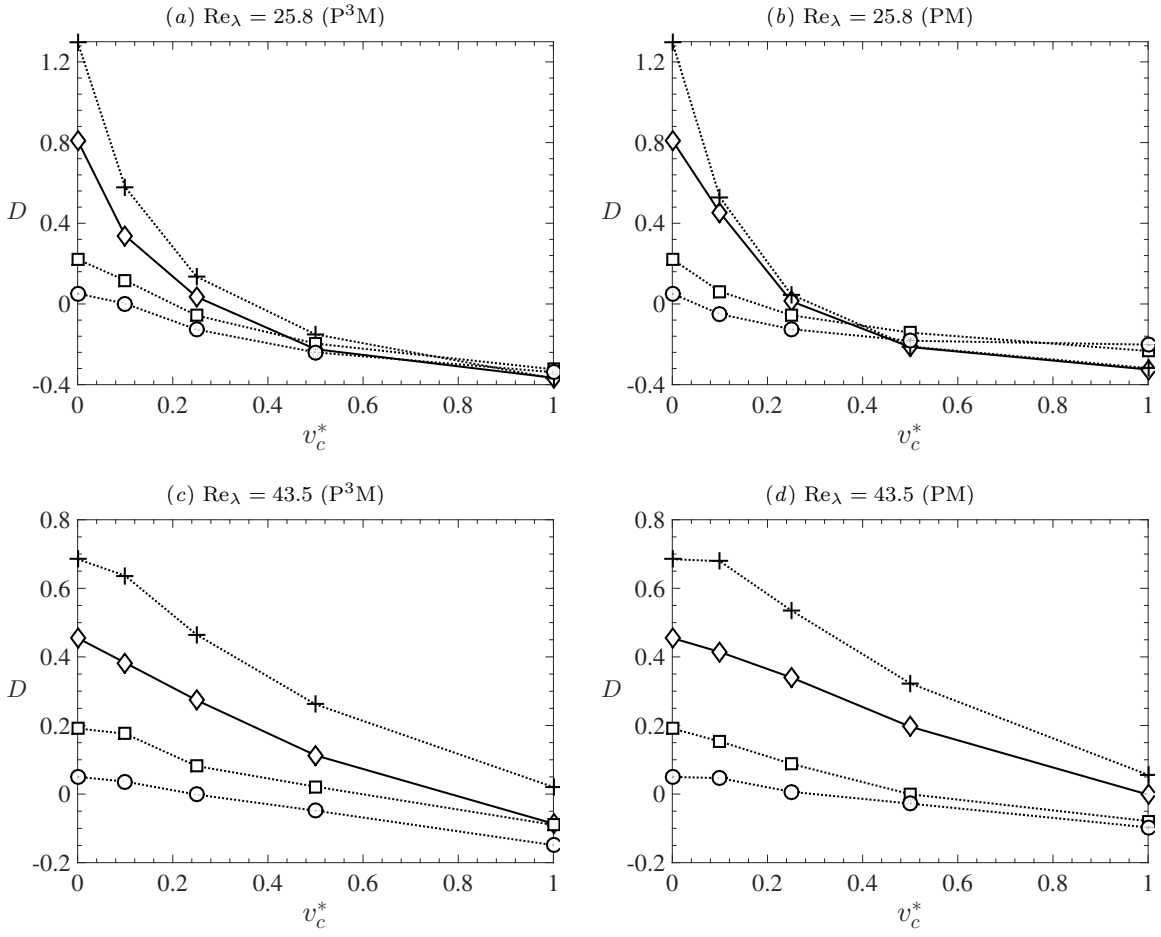

Figure 3.4: Variation of D with non-dimensional Coulomb velocity for like-charged particles. St$_\eta$ = 0.5 (◊), 0.9 (+), 1.0 (+), 6.2 (□), 7.0 (□), 25.0 (◯), and 28.0 (◯).

D is computed for each case and compared in Figs. 3.4–3.5. For the cases with like-charged particles, D follows the same trend as reported by Karnik and Shrimpton [117], that is, the level of clustering decreases with v_c^* for both P^{3}M and PM. At low v_c^*, the Stokes number has more significant effect on D, which is maximum at St$_\eta$ = 1.0 and decreases as St$_\eta$ deviates from unity. As v_c^* increases, however, Coulomb interactions

outcompete the drag force, causing the values of D to collapse with greater effect at lower Reynolds number. Little difference can be observed between P^{3}M and PM in Fig. 3.4, suggesting that for the parameters under consideration, the repulsive Coulomb force is adequately captured without accounting for the direct pairwise sum.

For cases with oppositely charged particles, however, the results of PM and P^{3}M deviate significantly, as seen in Fig. 3.5. Particles become highly clustered in the simulations computed using P^{3}M since the short-range attractive force is accurately represented. For the simulations computed using PM, the level of clustering is not affected by the charge magnitude since the effect of opposite charges are essentially nullified when projecting the charge on the mesh. This discrepancy demonstrates the importance of correctly capturing the short-range interactions when particles contain opposite charges. In general, the level of clustering is maximum when $\mathrm{St}_\eta = 1.0$, and decreases as St_η increases. In Fig. 3.5(a), D varies from 0.72 to 2.84 when v_c^* increases from 0.25 to 0.5 for $\mathrm{Re}_\lambda = 25.8$. At higher Re_λ, however, the level of clustering is not as large due to increased velocity fluctuations causing local drag to overcome the attractive Coulomb forces. A similar effect is seen with variations in v_c^*. In Fig. 3.5(a), D increases by a factor of four when v_c^* changes from 0.25 to 0.5 for $\mathrm{Re}_\lambda = 25.8$, but only increases by a factor of two for $\mathrm{Re}_\lambda = 43.5$.

3.3.3 Two-point statistics

Another important statistical measure of the spatial distribution of particles is the radial distribution function (RDF), defined as the number of particle pairs found at a given separation normalized by the expected number of pairs found in a homogeneous distribution [162]. The RDF, $g(r)$, is calculated by binning particle pairs according to their separation distances within annular shells of thickness Δr, given by

$$g(r) = \frac{P_r/\Delta V_r}{P/V}, \tag{3.5}$$

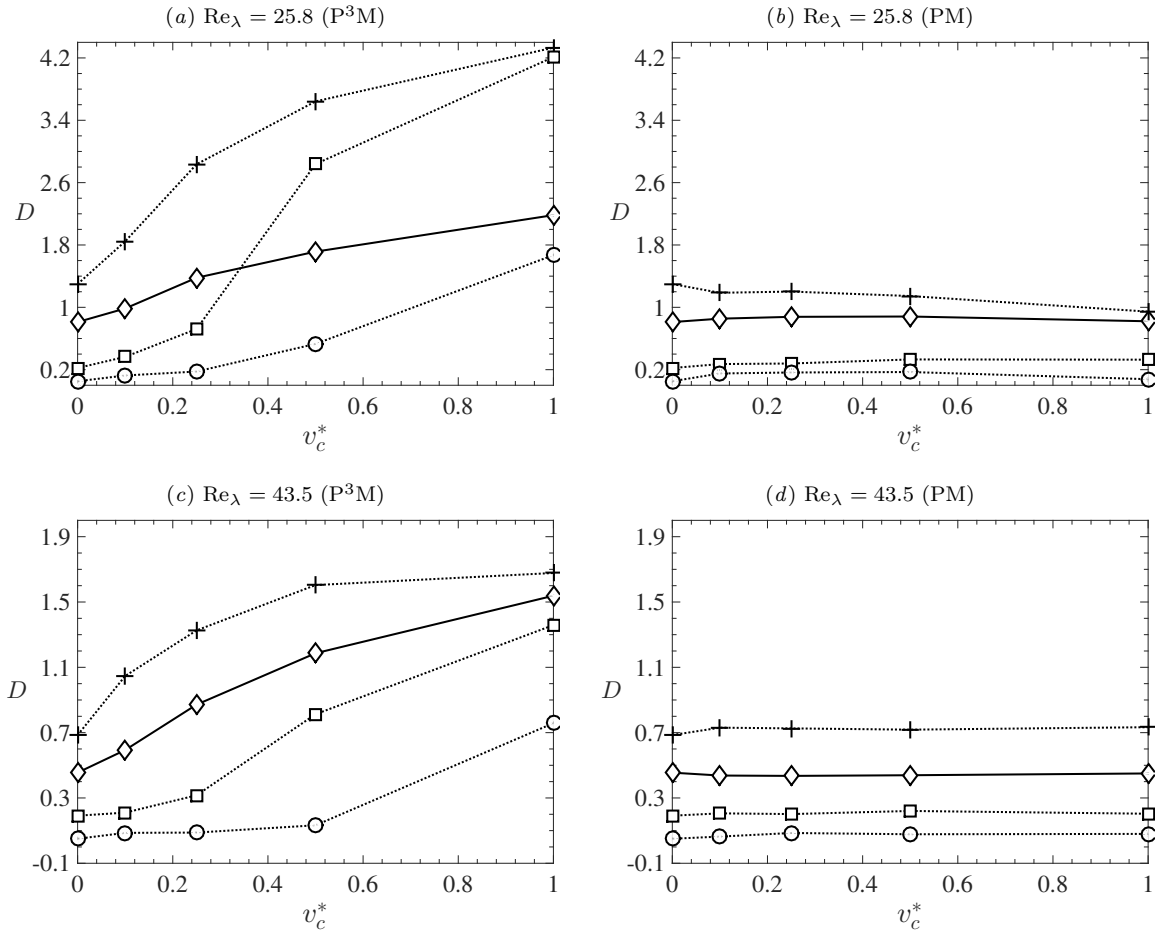

Figure 3.5: Variation of D with non-dimensional Coulomb velocity for oppositely-charged particles. $\mathrm{St}_\eta = 0.5$ (◊), 0.9 (+), 1.0 (+), 6.2 (□), 7.0 (□), 25.0 (◯), and 28.0 (◯).

where P_r is the number of particle pairs separated by a distance $r \pm \Delta r/2$, ΔV_r is the volume of the shell with thickness Δr located at separation r, $P = N_p(N_p - 1)/2$ is the total number of pairs in the simulation, and V is the volume of the sphere with radius $L/2$. With this definition, a value of unity represents a homogeneous distribution and values greater than unity imply clustering.

The RDFs are shown in Fig. 3.6 as a function of v_c^*. For the cases with like-charged particles, the presence of charge is seen to reduce the number of particle pairs up to a pair separation of 10η, which prevents particles from clustering. The result is consistent with what was seen in Fig. 3.4. In addition, for $r/\eta < 2$, the inter-particle electrostatic

repulsive force becomes extremely large, and the RDF rapidly approaches zero. As for the case with oppositely-charged particles, similar to what was observed in the like-charged cases, the RDF remains approximately close to unity for $2 < r/\eta < 10$. For $r/\eta < 2$, the RDF increases rapidly due to particle agglomeration. It was found that such short-range behavior of the two-point statistics were not observed when computed using PM.

The RDF can be seen to be greatly influenced by the Stokes number. Similar to what was observed in Figs. 3.4–3.5, the RDF is maximum when St_η is close to unity. With increasing v_c^*, the effect of charge for both like- and oppositely-charged particles becomes more profound. Figure 3.7 shows the RDF in close contact as a function of St_η, defined as $g^*{=}g(1.5d_p)$. For oppositely-charged particles, g^* is seen to increase with v_c^*, with a peak at $\mathrm{St}_\eta = 1$. Charges increases the peak of g^* by over an order of magnitude. For like-charged particles, an opposite trend is observed, with g^* decreasing as v_c^* increases, and the Stokes number is seen to play less of a role. For $\mathrm{St}_\eta \geq 7$, g^* approaches unity, suggesting the Coulomb repulsive force has a greater influence than preferential concentration from drag, and successfully homogenizes the suspension.

Lu and Shaw [143] recently proposed a model for the influence of charge on the RDF. Their model is based on the assumption that the particle relative velocity arises from dissipation-scale turbulent velocity fluctuations. The modeled RDF is a function of Stokes number and charge magnitude, though it is only valid for sufficiently weak charges such that the influence of Coulomb interactions are restricted to the dissipation scales of turbulence. Their model is able to capture increases in the RDF due to opposite charges and reductions in the RDF for like-charged particles, as was shown herein. However, the flow conditions are restricted to stagnant or low-St_η regimes. The charge density under consideration in their model was also several orders of magnitude smaller than what was used here, and we found it provides poor agreement with the RDFs reported here. This

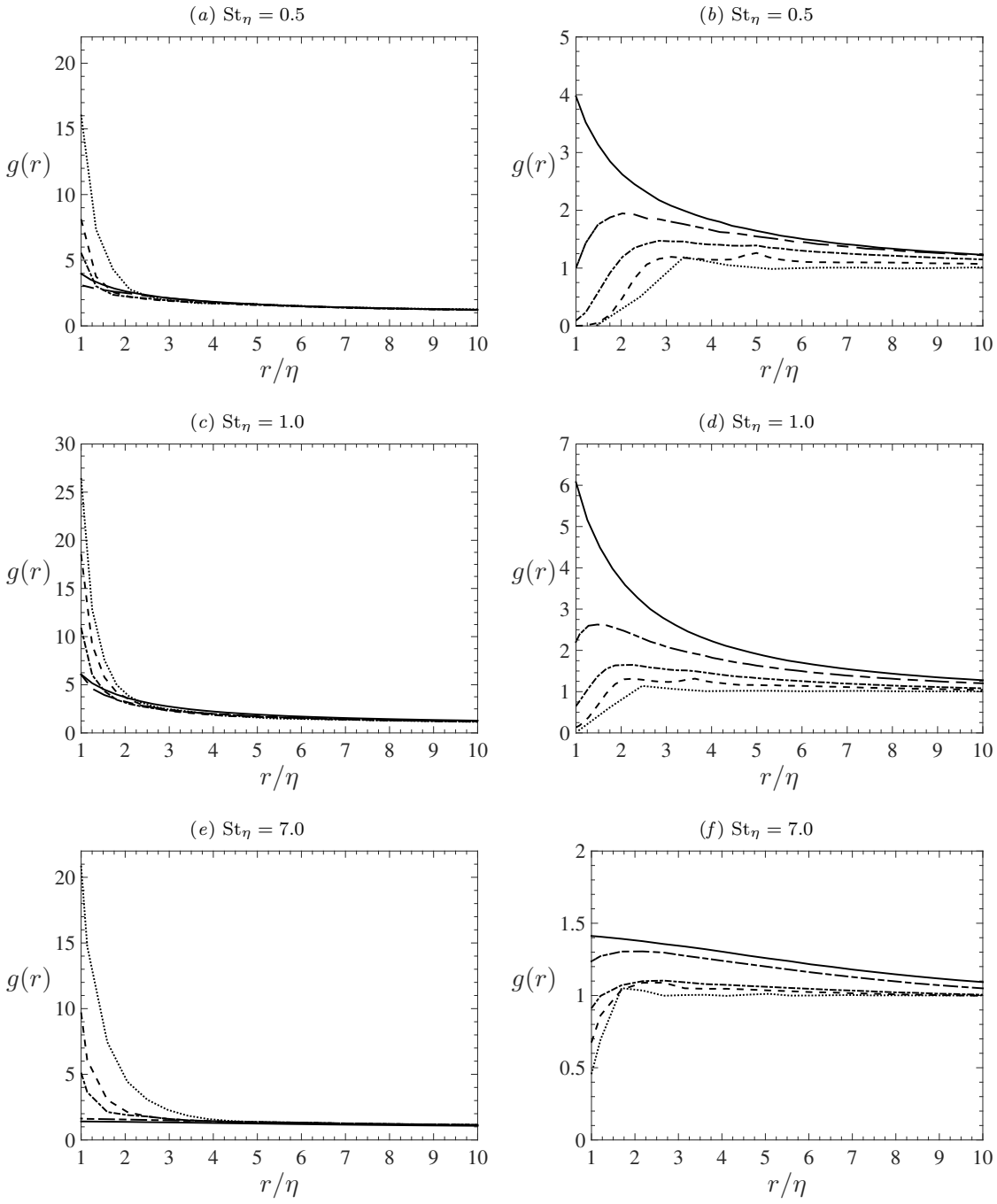

Figure 3.6: Radial distribution functions for $\mathrm{Re}_\lambda = 43.5$ using P^{3}M. $v_c^* = 0$ (−), 0.1 (— –), 0.25 (–·), 0.5 (––), and 1.0 (· · ·). Left: oppositely-charged particles, right: like-charge particles.

is to be expected, as St$_\eta$ approaches unity, particle inertia has a stronger influence on the relative velocity between particles and the fidelity of the model diminishes. Yet, such models are necessary to provide accurate descriptions of the particle distribution without

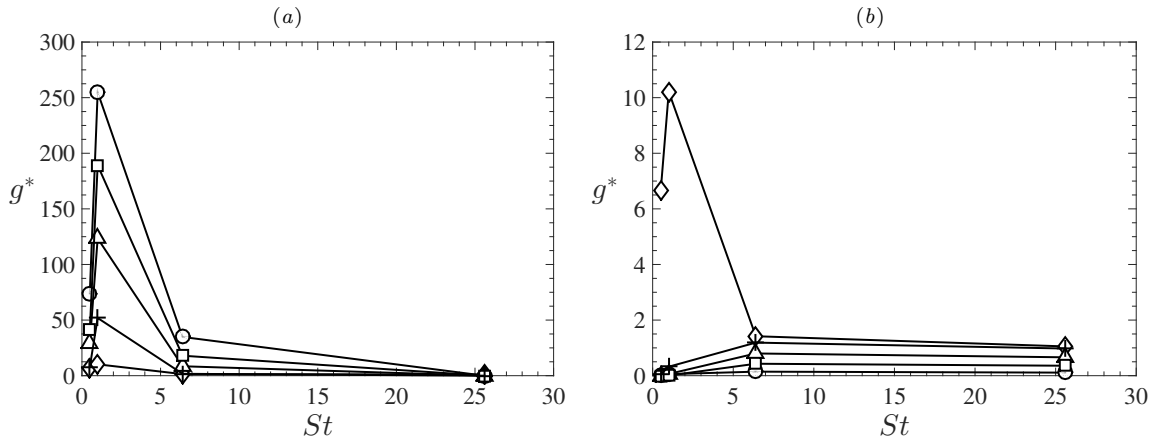

Figure 3.7: Radial distribution function near contact using P^{3}M. $v_c^* = 0$ ($\Diamond$), 0.1 ($+$), 0.25 (Δ), 0.5 ($\Box$), and 1.0 ($\bigcirc$). Left: oppositely-charged particles, right: like-charge particles.

the burden of long simulation run times and the need for supercomputing resources. The method presented in this work can be used in future studies to improve upon such models.

3.4 Charged particles in a fully-developed turbulent pipe flow

In this section, the extended P^{3}M approach as described in Chapter II is combined with an Eulerian–Lagrangian framework to demonstrate its utility in modeling charged particles in turbulent pipe flow. The effect of charge on particle statistics is reported, with an emphasis on both particle-particle interactions using the extended P^{3}M approach and particle-wall interactions due to image charging.

3.4.1 Simulation configuration

The problem under consideration consists of a pipe with inner diameter $D = 20$ mm embedded in a rectangular domain (see Fig. 3.8(a)). The length of the pipe is $L = 10D$ to ensure domain independent results. The domain is discretized on a Cartesian mesh of size $326 \times 256 \times 256$. A conservative cut-cell immersed boundary method is employed to to enforce no-slip and no-penetration boundary conditions in the fluid phase at the pipe wall. Details can be found in as described in Pepiot and Desjardins [181] and Meyer et al. [163].

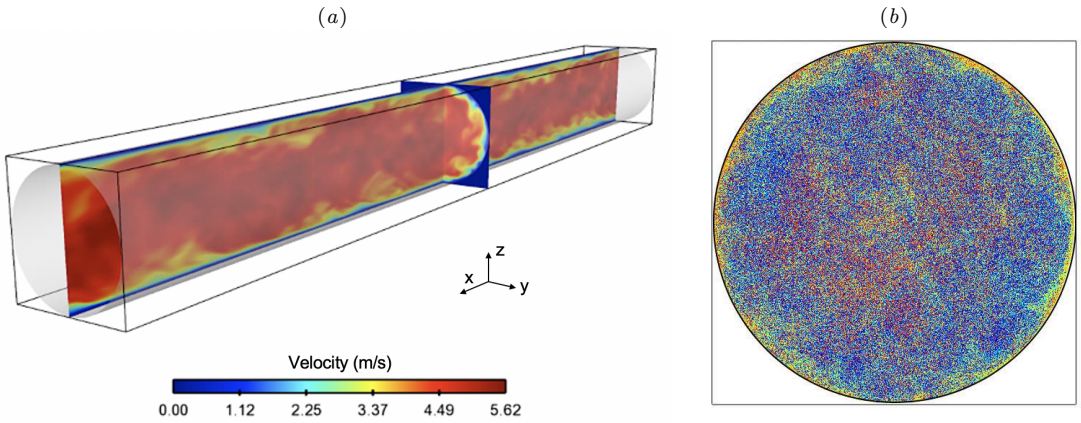

Figure 3.8: Schematic of the turbulent pipe flow with aspect ratio $L/D = 10$ and periodicity enforced in the streamwise (x) direction. (a) The pipe wall is shown as an iso-surface of $\psi = 0$. Color represents the instantaneous fluid velocity magnitude at a statistically stationary state. (b) Particle distribution colored by diameter (blue: 1 µm, red: 10 µm) at a statistically stationary state.

The pipe is periodic in the streamwise (x) direction. The bulk velocity is $U_b = 4.0$ m/s, corresponding to a frictional Reynolds number $\mathrm{Re}_\tau = 180$. The grid spacing is chosen such that $\Delta y^+ = \Delta z^+ = 1.25$ and $\Delta x^+ = 9.8$ to fully resolve the turbulent flow (see Appendix B), where '$+$' denotes the dimensionless wall distance defined as $(\cdot)^+ = u_* (\cdot) / \nu$, where $u_* = \sqrt{\tau_w / \rho}$ is the friction velocity with τ_w the wall shear stress and ρ the fluid density.

Particles are introduced into the flow with random initial locations and zero initial velocities once a statistically stationarity is reached. Polydisperse spherical particles of diameter 1 µm $\leq d_p \leq$ 10 µm and density $\rho_p = 2650$ kg/m^3 are considered, with average particle volume fraction of 6.25×10^{-7}. Due to the low volume fraction considered, particle initialization has negligible effect on statistics at steady state. The size assigned to individual particles is sampled from a random lognormal distribution representative of Arizona road dust (see Fig. 3.9). Particle inertia is again characterized by a turbulence Stokes number $\mathrm{St}_\eta = \tau_p / \tau_\eta$. For the polydisperse distribution of particles considered herein, $\mathrm{St}_\eta \in [0.0148, 1.48]$. Particle velocity statistics and deposition rates are measured

once the particle distribution reaches a statistically stationary state (see Fig. 3.8(b)). Particles are removed from the simulation after impact with the wall.

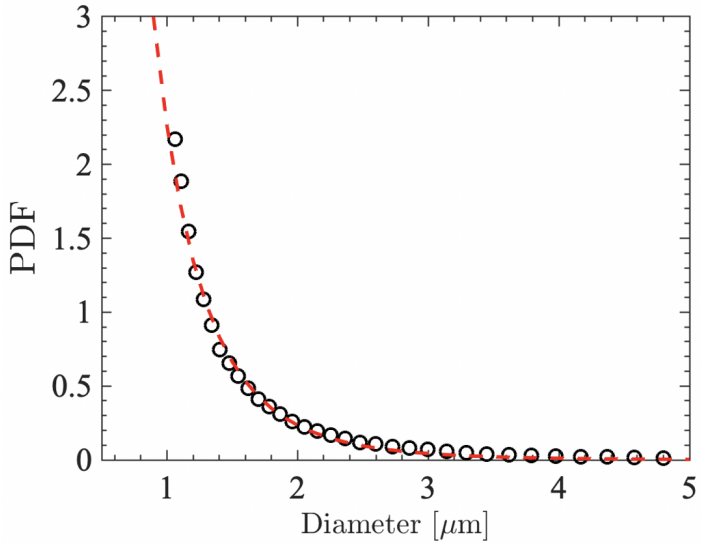

Figure 3.9: Particle size distribution of typical Arizona road dust [261, 259] ($\circ$) and a log-normal fit used in the simulations ($--$) with mean diameter 0.5 µm and standard deviation 0.3 µm. The distribution is truncated between 1 µm and 10 µm.

To investigate the effect of charge on particle dynamics, each particle is assigned a unique value q_p that is proportional to the maximum possible charge $q_{\max}$ according to $q_p = \xi q_{\max}$, with $0 \leq \xi \leq 1$. The maximum charge is given by [106]

$$q_{\max} = 500 \times \left(1.6 \times 10^{-19}\right) \left(d_p/10^{-6}\right)^2 . \tag{3.6}$$

Common airborne dust particles have been measured to have a charge fraction in range of $0.048 \leq \xi \leq 0.23$ [194] . For fly ash particles in turbulent pipe flows with similar Reynolds numbers, ξ is estimated to be 0.105 and 0.077 using the mean charge values measured by Matsusaka et al. [157] and Matsusaka and Masuda [156] respectively. Therefore, $\xi = 0.1$ is chosen in this study as a representative value. Particle statistics for $\xi = 0$ (no charge) and $\xi = 0.1$ will be compared in later sections.

3.4.2 Effect of charge on particle statistics

The simulation is run for 240 D/U_b to reach a statistically stationary state. Figure 3.10 shows the averaged root-mean-square (rms) velocity normalized by the friction velocity, $u^+_{\rm rms} = u_{\rm rms}/u_*$, and averaged streamwise velocity for both phases. Due to the relatively low Stokes number, the majority of the particles closely follow fluid streamline and particle inertia plays little role, except for the largest particles.

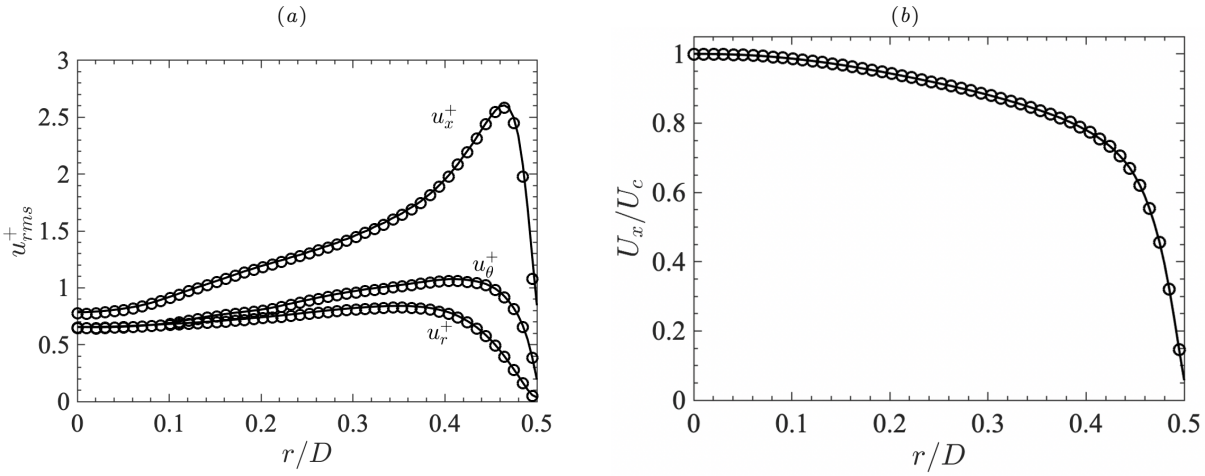

Figure 3.10: Comparison of the mean fluid (–) and particle (∘) streamwise velocities as a function of radial position. (a) Normalized root-mean-square velocity and (b) normalized streamwise velocity.

Figure 3.11 shows the departing and approaching radial velocities of both fluid phase and particles of four different sizes. The departing and approaching radial velocities are defined as $u_r^{\pm}(r) = \pm\langle \boldsymbol{u}(r) \cdot \boldsymbol{n}_r \rangle$ for the fluid and $u_r^{\pm}(r) = \pm\langle \boldsymbol{v}_p(r) \cdot \boldsymbol{n}_r \rangle$ for particles, which quantify the relative motion with respect to the pipe wall. Here $\boldsymbol{n}_r$ denotes the normal vector pointing from the pipe centerline to the location of interest. As shown in Fig. 3.11(a), on average the fluid exhibits outward motion towards the wall for regions close to the wall since $u_r^+(r) > u_r^-(r)$, while the opposite is observed ($u_r^+(r) < u_r^-(r)$) near the centerline of the pipe. Smaller particles ($d_p = 1\mu$m) exhibit similar velocity profiles as the fluid, while the velocities associated with larger particles are observed to deviate from

the fluid due to increased inertia. In addition, the difference between $u_r^+(r)$ and $u_r^-(r)$ increases, indicating larger particles impact the wall with a larger net velocity. Especially very close to the wall, larger particles exhibit larger $u_r^+(r)$ and smaller $u_r^-(r)$.

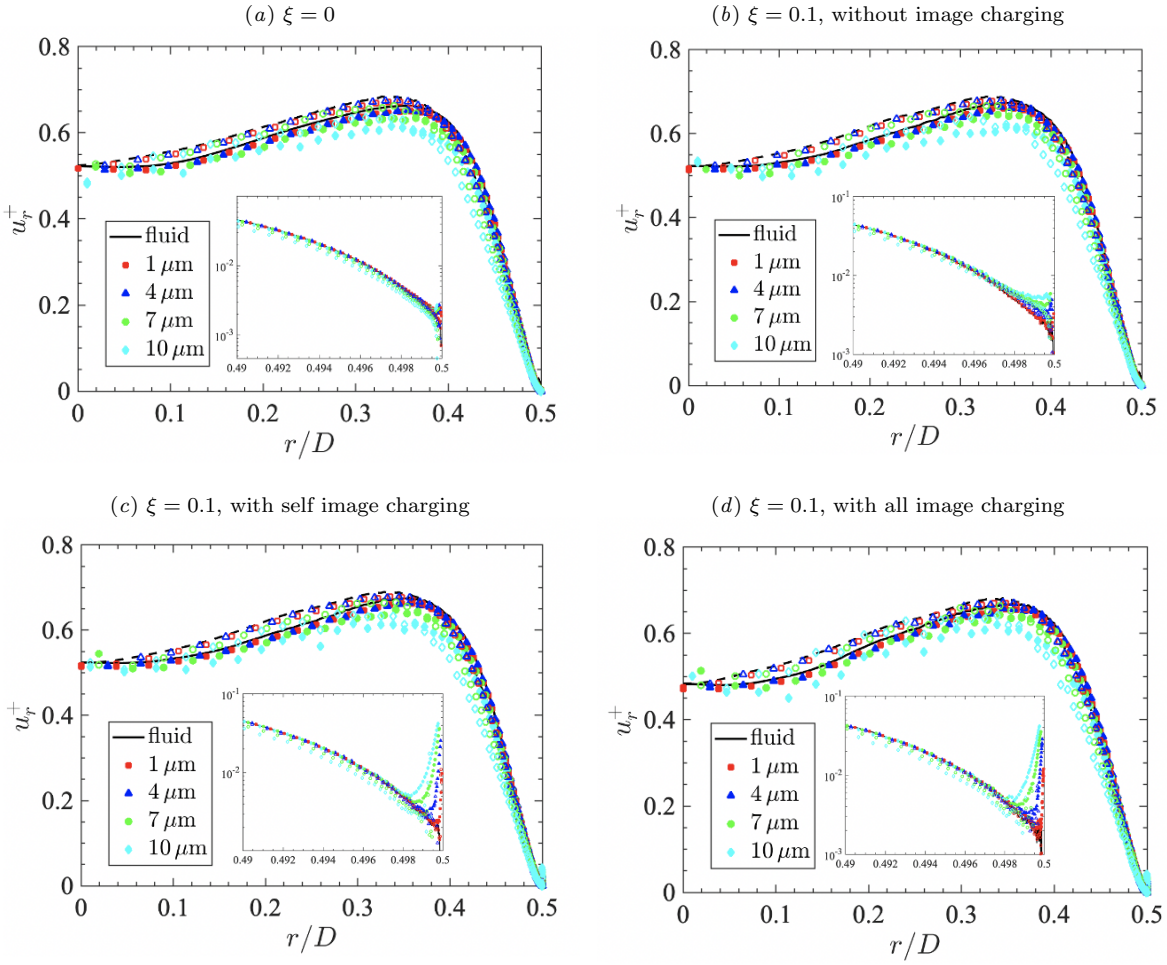

Figure 3.11: The departing (hollow/dashed) and approaching (solid) velocities towards the pipe wall of fluid (line) and particles of four different sizes (symbols). (a) $\xi = 0$, (b) $\xi = 0.1$, (c) $\xi = 0.1$, with self image charging, and (d) $\xi = 0.1$, with image charging of all particles. The inset highlights the difference in particle velocities at regions close to the wall.

Figures 3.11(b)-3.11(d) compare the effect of charge in terms of the particle-particle contribution computed using P^{3}M and the particle-wall contribution computed using image charging. It can be seen that the velocity profiles for both phases are largely unmodified by the presence of charge. However, particle velocities are drastically different close

to the wall. Figure 3.11(b) reveals that the approaching velocity of larger particles are amplified when accounting for particle-particle electrostatic interactions, which leads to larger deposition rates. Particle-wall interactions play an even larger role by enhancing the particle approaching velocities by almost two orders of magnitude while at the same reducing the departing velocities, resulting in larger net radial velocities. Note that by comparing Fig. 3.11(c) and Fig. 3.11(d), the effect of wall images due to the surrounding particles has negligible effect on the particle velocity at the wall, which might be due to the cancellation of the electrical field induced by unlikely charged particles.

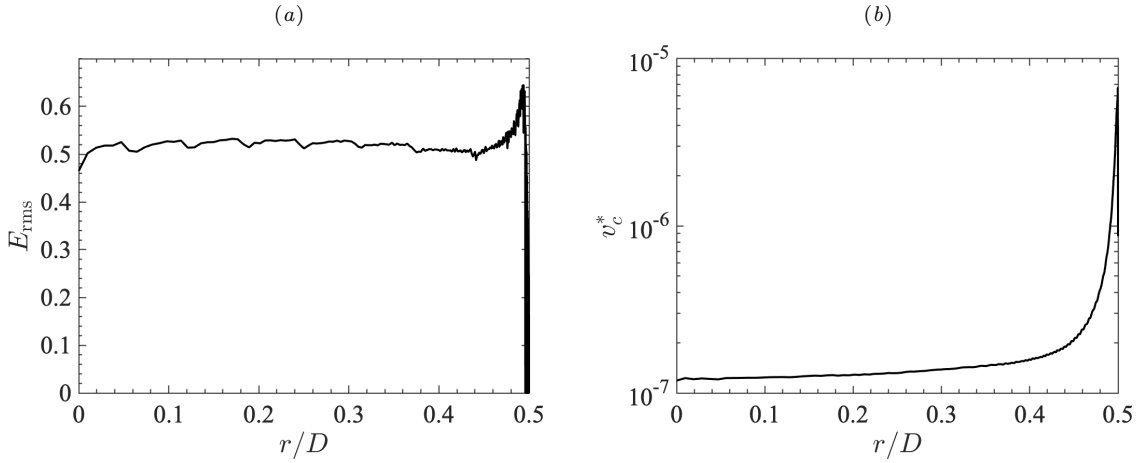

Figure 3.12: (a) Root-mean-square electrical field and (b) nondimensional electric settling velocity as a function of radial position.

The importance of the electrostatic force relative to fluid forces is commonly measured by a non-dimensional electric settling velocity v_c^* defined in Eq. (3.3). Figure 3.12 shows that E_{rms} and v_c^* are approximately constant throughout the flow except very close to the wall. Particles cluster at the wall due to turbophoresis, resulting in a sharp increase in E_{rms} and v_c^*, which is consistent with Fig. 3.11 in which the effect of charge on particle velocities is most significant close to the wall.

Particle clustering close to the wall is a result of two competing effects. Turbophoresis brings particles from the pipe core to the wall, while particles are continuously removed

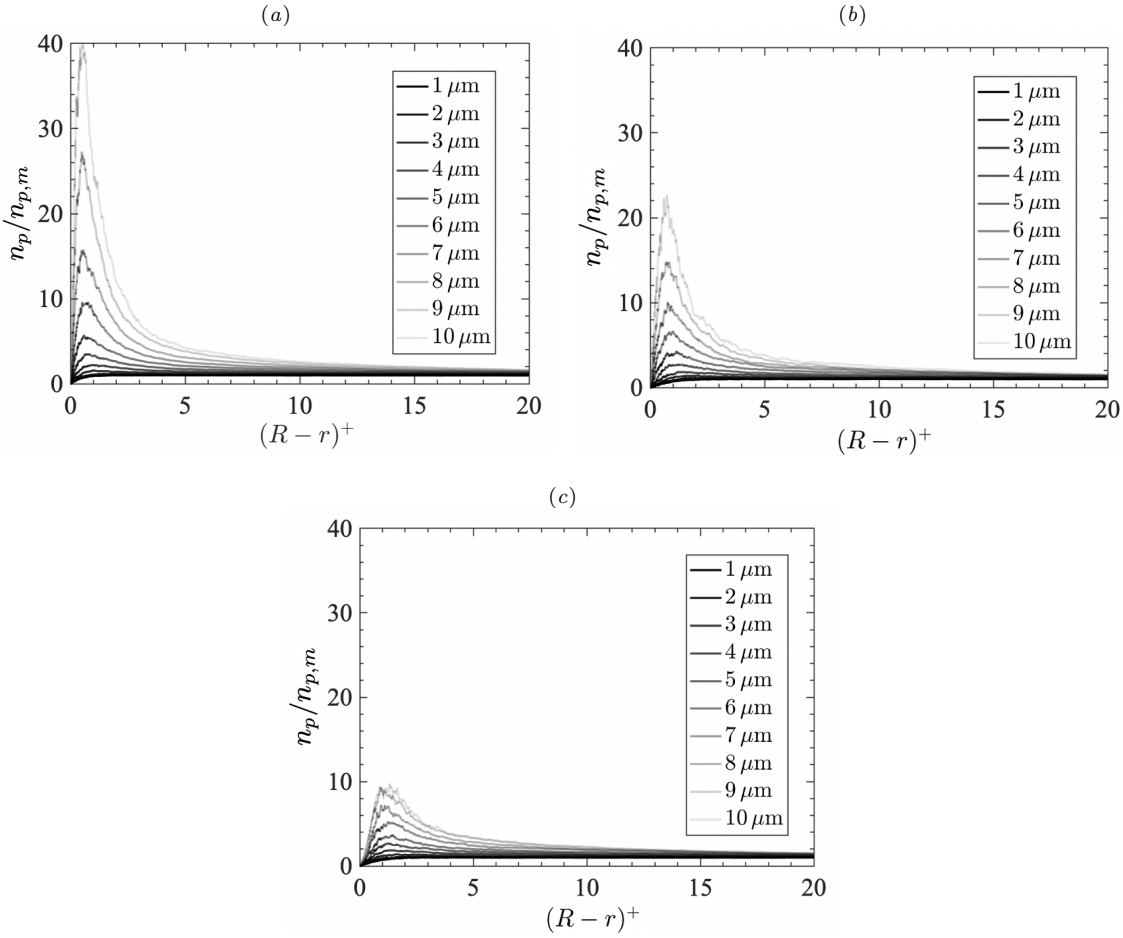

Figure 3.13: Comparison of the particle number density n_p normalized by the mean number density $n_{p,m}$ as a function of distance from the wall for different particle sizes. (a) $\xi = 0$, (b) $\xi = 0.1$ without image charging, and (c) $\xi = 0.1$ with image-charging.

as they deposit on the wall. Electrical charge, due to particle-particle and particle-wall interactions, are shown to enhance deposition and therefore decrease the peak particle number density (see Fig. 3.13). In the absence of charge, the particle number density peaks at $(R - r)^+ = 1$ with R the pipe radius, and increases with increasing particle size (see Fig. 3.13(a)). For 10 μm particles, the peak number density is approximately 40 times larger than the mean number density, which is reduced to about 20 times at $\xi = 0.1$ even without wall image charging, and decreases to less than 10 times when wall image charging is included.

3.5 Conclusions

In the present work, the role of electrostatic charge on particle clustering in turbulent flows was studied using a coupled EL-P^{3}M approach. Special attention was paid to the interplay between fluid coupling (drag) and Coulomb interactions. Results from simulations of a two-dimensional Taylor–Green vortex flow and three-dimensional homogeneous isotropic turbulence (HIT) demonstrated that the Stokes number and electric charge play an important role on the particle dynamics. Despite the low volume fractions considered here, inter-particle collisions were found to be necessary to prevent unphysical overlap that arises via attractive Coulomb interactions. It was found that PM was capable of quantitatively capturing particle segregation for like-charged particles. However, PM was unable to capture particle chain and ring structures observed using P^{3}M for systems with oppositely-charged particles.

The level of particle clustering in HIT was characterized via one- and two-point statistics. These measures were found to be highly influenced by the turbulence Stokes number St_η, Taylor Reynolds number Re_λ, and Coulomb settling velocity v_c^*. Similar to turbulent suspensions of uncharged particles, maximum clustering was observed when St_η approaches unity, and decreased with values deviating from unity. In systems with oppositely-charged particles, the level of clustering was seen to increase at larger values of Re_λ due to the increased influence of drag over the repulsive nature of the Coulomb interactions. The charge magnitude was found to play a dominating role on amplifying or suppressing the level of clustering. In suspensions of like-charged particles, the homogenization of particle distribution increased with increasing v_c^* for both the PM and P^{3}M methods. However, PM was unable to capture enhanced particle segregation in systems with oppositely-charged particles.

The extended P^3M method was then employed to investigate the effect of charge on particle transport in fully-developed turbulent pipe flows. Particles are polydisperse with a lognormal size distribution representative of Arizona road dust. Based on experimental particle charge measurements in pipe flows, each particle was assigned a charge that is 10% of its maximum possible charge based on its size. The wall image charging was shown to have a significant effect on the near-wall particle approaching velocity, especially for larger particles. In addition, particle-particle electrostatic interactions were observed to enhance the near-wall particle approaching velocity, despite it being less signifiant than the particle-wall contribution.

In real systems, neutral particles can acquire charge while highly-charged particles may discharge themselves by capturing ions of the opposite polarity. Such effects were not considered in the present study. Instead, particles were assumed to retain their original charge throughout the duration of each simulation. Because the EL framework explicitly tracks the charge of each particle in addition to particle-particle contact, accounting for such effects can be implemented in a straight forward manner but might result in computationally restrictive time steps. Jin and Marshall [111] recently introduced a probabilistic model for contact electrification that presents a tractable approach to capture such effects, which provides a possible route for future works.

CHAPTER IV

Electrohydrodynamic Generation of Turbulence by Charged Particles

Ionization produced by cosmic rays and atmospheric radioactivity creates charged short life-time aerosols in the upper troposphere. Inhomogeneities in the spatial distribution of aerosols lead to time varying electric fields and space charge, which can often be amplified by more than three orders of magnitude in extreme conditions, such as thunderstorms. The nonlinear coupling between ionized air, charged aerosols, and the background electric field can result in electrohydrodynamic (EHD) body forces that augment atmospheric turbulence. In this chapter, a theoretical and numerical study on the electrohydrodynamic generation of atmospheric turbulence under fair weather and thunderstorm conditions is presented. Linear stability shows that coupling between ionized air and a background electric field acts to increase turbulent kinetic energy (TKE) in the upper troposphere, albeit over long time durations. Direct simulations of charged particles in homogeneous shear flow demonstrate a nonlinear feedback mechanism capable of accelerating the growth rate. Streamwise velocity gradients induce fluctuations in particle concentration and electric potential, resulting in a body force that generates vertical velocity fluctuations. Pressure strain then transfers this energy to turbulent fluctuations in the streamwise direction and the process repeats. This feedback mechanism was found to augment TKE at late stages of the shear layer growth.

4.1 Introduction

Ionization produced by cosmic rays and atmospheric radioactivity creates charged short life-time aerosols that have significant spatial and temporal variations in the troposphere [231, 275, 235, 230]. In extreme conditions, such as thunderstorms, this variability has been observed to amplify the local electric field strength in the atmosphere by more than three orders of magnitude compared to typical fair weather conditions [201, 214]. In the presence of a background electric field, gradients in space charge generate an electrohydrodynamic (EHD) body force if the gas is ionized. The EHD force that arises due to coupling between an electric field, ionized air, and charged aerosols has been shown experimentally to produce instabilities that trigger the onset of turbulent motion in quiescent aerosol clouds [105]. While EHD instabilities are known to induce turbulence in ionized fluids, such as electrolytic cells [28], liquid films [232], and electrostatic precipitators [5], and similar instabilities due to magnetohydrodynamics exist in plasmas [136, 229, 76], its role in augmenting atmospheric turbulence is less established.

Recent studies have shown that detailed interactions between turbulence and aerosol droplets can give rise to preferential concentration of charged particles capable of self-inducing atmospheric electricity [50, 270], which might amplify the aforementioned effects. Depending on the sign and magnitude of the charge each particle carries, these self-induced electrical fields can either mitigate or enhance the level of clustering [118, 144, 270]. Preferential concentration describes the accumulation of inertial (heavy) particles or droplets away from highly vortical regions of the turbulent flow [57, 60, 107, 204, 36]. When the time scale of the particles is on the same order as the turbulent eddies, particles are directed by coherent vortical structures to create non-homogeneities in concentration and the onset of clusters. In the presence of gravity, preferential concentration by turbulence

has been observed to cause particles to accumulate near the downward moving side of vortices where the fluid velocity aligns with the direction of gravity [159, 253, 3]. The gravitational settling of aerosol particles can be enhanced by this preferential sweeping mechanism by as much as 50% [253]. The collision rate between monodisperse particles is also considerably lower when gravity is present [108].

Wind shear (mean velocity gradient) ranging from $\mathcal{O}(10^{-3})$/s to $\mathcal{O}(1)$/s is common in the atmosphere [27, 233, 141]. When particles or droplets are placed within a mean velocity gradient, the anisotropy of the velocity fluctuations induces a preferential orientation of particle clusters and modifies their turbulent transport characteristics [92, 169]. Recently, a new preferential concentration-driven instability has been identified for inertial particles suspended in sheared turbulence [119], showing that two-way coupling between the phases in the presence of mean shear and gravity can lead to the onset of turbulence.

The motivating hypothesis of the present study is that charged aerosols within the atmosphere couple nonlinearly with the background electric field and ionized air, resulting in the production of TKE. We refer to this as a three-way coupling process, whereby velocity fluctuations induce non-homogeneities in droplet concentration, resulting in gradients in electric potential that increase the electric field strength and in turn amplifies the gas-phase velocity fluctuations. We seek to identify under what conditions EHD-induced turbulence is relevant. To this end, a linear stability analysis is performed for sheared flow in the presence of a background electric field to understand the stability criteria, relevant non-dimensional numbers, and time scales associated with EHD-induced turbulence. Then, direct numerical simulations are carried out with relevant atmospheric parameters at 6 km altitude to understand the effect of added nonlinearity by aerosol dynamics on turbulence generation. The TKE budget and growth rate are then reported to assess the significance of EHD for a range of particle loadings.

4.2 Linear stability of the upper troposphere

4.2.1 Governing equations

In this work, the fluid dynamics in the troposphere is modeled according to the incompressible Navier–Stokes equations, given by

$$\frac{\partial \boldsymbol{u}}{\partial t} + \boldsymbol{u} \cdot \nabla \boldsymbol{u} = -\frac{1}{\rho}\nabla p + \nu \nabla^2 \boldsymbol{u} + \frac{1}{\rho}\boldsymbol{F}_e - \Gamma z \frac{\partial \boldsymbol{u}}{\partial x} - \Gamma w \boldsymbol{e}_x, \tag{4.1}$$

where ρ is the gas-phase density, $\boldsymbol{u} = [u\, v\, w]^\mathsf{T}$ is the velocity, p is pressure, ν is the kinematic viscosity, and $\boldsymbol{F}_e$ is an electrohydrodynamic (EHD) body force. The last two terms on the right-hand side of Eq. (4.1) are introduced to account for mean velocity gradients due to wind shear, where Γ is the shear rate, z is the vertical position and $\boldsymbol{e}_x$ is the unit vector in the streamwise direction.

Within the upper troposphere, the electric permittivity is close to the vacuum permittivity ($\epsilon \approx \epsilon_0 = 8.854 \times 10^{-12}\,\mathrm{F/m}$) and can be assumed constant. As a consequence, the EHD body force can be expressed as $\boldsymbol{F}_e = q_f \boldsymbol{E}$, where the electric field, $\boldsymbol{E} = -\nabla\phi$, is determined by solving a Poisson equation for the electric potential ϕ, given by

$$\nabla^2 \phi = -(q_f + q_p)/\epsilon, \tag{4.2}$$

which accounts for both the effect of space charge density in the fluid, q_f, and charge density of aerosol droplets, q_p. In the remainder of this study, the terms aerosols, droplets, and particles will be used interchangeably. Within the first 20 km of the troposphere, there exists a vertical gradient in air conductivity that gives rise to finite space charge density [98, 281], even under fair weather conditions (see Fig. 4.1). We model the transport of space charge as

$$\frac{\partial q_f}{\partial t} + \nabla \cdot (\mu_I q_f \boldsymbol{E} - D_I \nabla q_f + q_f \boldsymbol{u} + q_f \Gamma z \boldsymbol{e}_x) = 0, \tag{4.3}$$

where $\mu_I \approx 10^{-4}\,\mathrm{m^2\,V^{-1}\,s^{-1}}$ is the ion mobility at 6 km altitude based on balloon-borne measurements [197] and $D_I = \mu_I k_B T/e$ is the molecular diffusion coefficient based on the Einstein relation [161]. Here, k_B is the Boltzmann constant, T is temperature, and $e = 1.6 \times 10^{-19}\,\mathrm{C}$ is the elementary charge. Within the first few kilometers of the atmosphere $D_I \approx 2 \times 10^{-6}\ \mathrm{m^2\,s^{-1}}$.

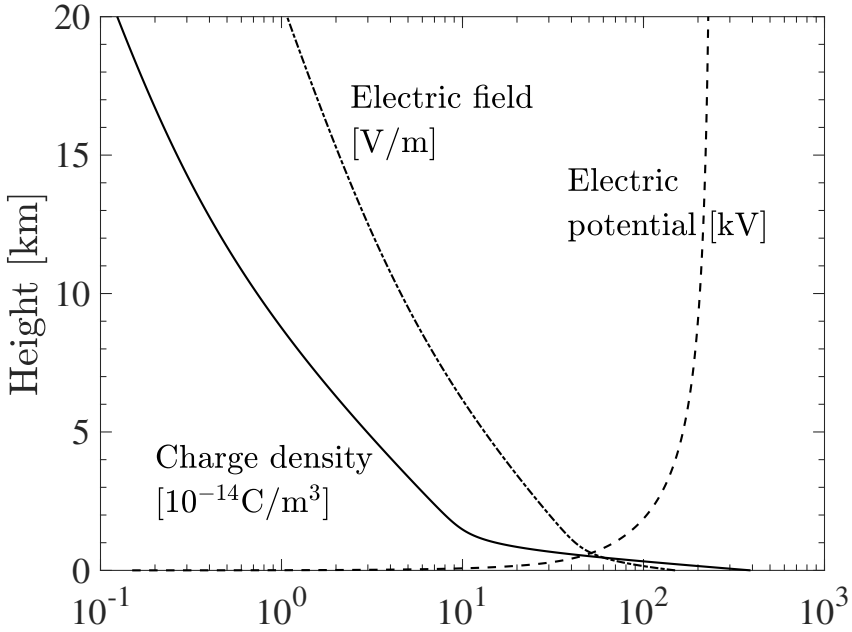

Figure 4.1: Fair weather atmospheric conditions [247] used to define the background state in the stability analysis.

4.2.2 Linear stability analysis

The flow quantities q_f, ϕ, p, $\boldsymbol{u}$ and $\boldsymbol{E}$ can be decomposed into a base state and a fluctuating component as $A = \overline{A} + A'$, where

$$A' = A_0(z)\exp(i\kappa_x x + i\kappa_y y)\exp(\omega\tau), \tag{4.4}$$

with A_0 the fluctuation amplitude, κ_x and κ_y the horizontal wave numbers, ω the growth rate, and $\tau = (\mu_I \overline{\phi}\, t)/L^2$ is the time scale normalized over a vertical span L. Linearizing (4.1)–(4.3) and enforcing $\nabla \cdot \boldsymbol{u} = 0$, the following set of ODEs of total order 7 can

be obtained to find solutions for the non-dimensional fluctuation amplitudes of vertical velocity, $f(z) = w_0(z)L/(\mu_I\overline{\phi}(z))$, and potential, $g(z) = \phi_0(z)/\overline{\phi}(z)$, according to

$$\begin{aligned}\left(\frac{\omega}{\mathrm{Pr}} - (D^2-\alpha^2)\right)(D^2-\alpha^2)f &= -R\frac{\mathrm{d}\overline{q}_f}{\mathrm{d}z}\frac{L^3}{\epsilon\overline{\phi}}\alpha^2 g \\ -R\frac{\overline{E}L}{\overline{\phi}}\left(D^2-\alpha^2\right)\alpha^2 g - S\hat{z}\beta\left(D^2-\alpha^2\right)f &- 2S\beta Df,\end{aligned} \tag{4.5}$$

$$\begin{aligned}-\frac{\epsilon\overline{E}}{L^2}\left(D^2-\alpha^2\right)Dg + \frac{\mathrm{d}\overline{q}_f}{\mathrm{d}z}Dg + \frac{\epsilon\overline{\phi}}{L^3}\omega(D^2-\alpha^2)g \\ + \frac{2\overline{q}_f}{L}(D^2-\alpha^2)g = \frac{\mathrm{d}\overline{q}_f}{\mathrm{d}z}f.\end{aligned} \tag{4.6}$$

Here, $\hat{z} = z/L$, $\beta = L\,\mathrm{d}/\mathrm{d}x$ and $D = L\,\mathrm{d}/\mathrm{d}z$ are the normalized derivative operators and $\alpha = L\sqrt{\kappa_x^2+\kappa_y^2}$ is the normalized wavenumber. This analysis yields the following non-dimensional numbers

$$R = \frac{\epsilon\overline{\phi}}{\mu\mu_I}, \quad \mathrm{Pr} = \frac{\mu}{\rho\overline{\phi}\mu_I}, \quad S = \frac{\rho\Gamma L^2}{\mu} \tag{4.7}$$

that dictate stability and growth rate. Details on the derivation of the linearized equations and associated boundary conditions employed in the analysis are given in Appendix D, and a similar formulation can be found in Schneider and Watson [209] for a charged dielectric liquid film. R is sometimes referred to as the electric Rayleigh number [5] and represents the competition between turbulence production due to charge density fluctuations and dissipation due to viscosity. When R is greater than a critical value R_c, velocity fluctuations will increase with the Coulomb force, and below R_c the EHD-induced turbulence is damped by viscosity. Pr is the electric Prandtl number, a measure of electric time scale to the hydrodynamic time scale [209]. S is the shear Reynolds number that characterizes the importance of mean shear inertial forces to viscous forces over the vertical span L. Note that since $\overline{\phi}$ is also a function of L, all three non-dimensional numbers are functions of L.

4.2.3 Effects of vertical span and shear rate

The ODEs reported in Sec. 4.2.2 are solved numerically using a 4-th order Runge–Kutta scheme for a vertical thickness of the atmosphere $z_0 \leq z \leq z_0 + L$ with a base altitude $z_0 = 6\,\text{km}$. We first consider base state values corresponding to fair weather conditions within the troposphere [247] (see Fig. 4.1). Figure 4.2 shows the minimum values of R_c such that the flow remains stable over all wave numbers, α, as a function of vertical span L. It can immediately be seen that the flow becomes more unstable as the vertical span increases. It is interesting to note that $R \approx 100$ in the troposphere, which corresponds to a vertical span of $L \approx 1\,\text{km}$, consistent with typical cloud thicknesses observed at those elevations [252].

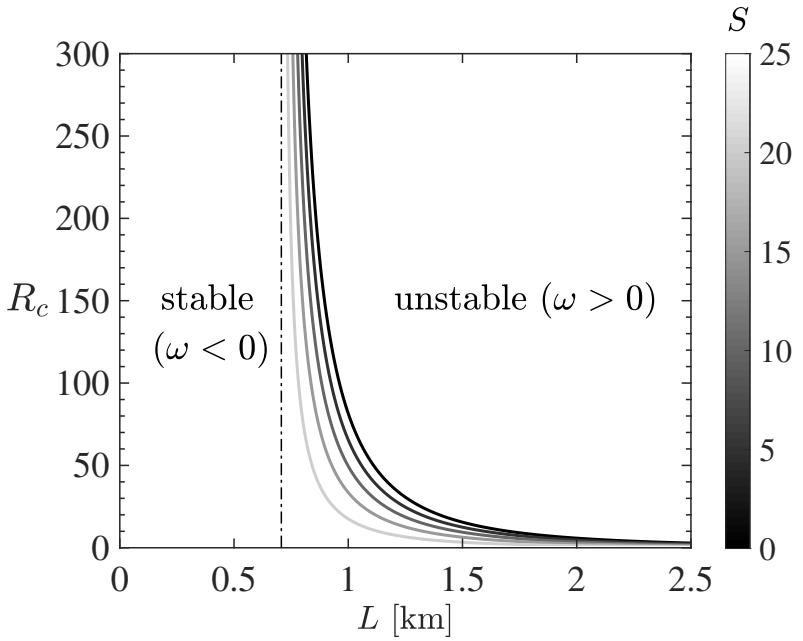

Figure 4.2: Critical value of the electric Rayleigh number as a function of vertical span L for different shear Reynolds numbers S. The system is unconditionally stable when $L \leq 0.707$ km (denoted by the vertical dashed line).

Wind shear is also known to play an important role in atmospheric dynamics, and is responsible for Kelvin-Helmholtz instabilities that influence the turbulence energy budget [266]. Figure 4.2 shows that the system is unconditionally stable for $L \leq 0.707\,\text{km}$

regardless of wind shear, but for $L > 0.707\,\mathrm{km}$, R_c decreases with increasing shear rate, demonstrating shear acts to destabilize the flow, as expected. Even modest values of wind shear, i.e. $\Gamma > 1 \times 10^{-3}\,\mathrm{s}^{-1}$, will lead to values of S significantly larger than those considered in Fig. 4.2, affirming that atmospheric electricity (even in fair weather conditions) is a destabilizing mechanism in the troposphere. We note that the stability analysis neglects gravity, and thus these findings isolate the role of electric body forces on atmospheric stability.

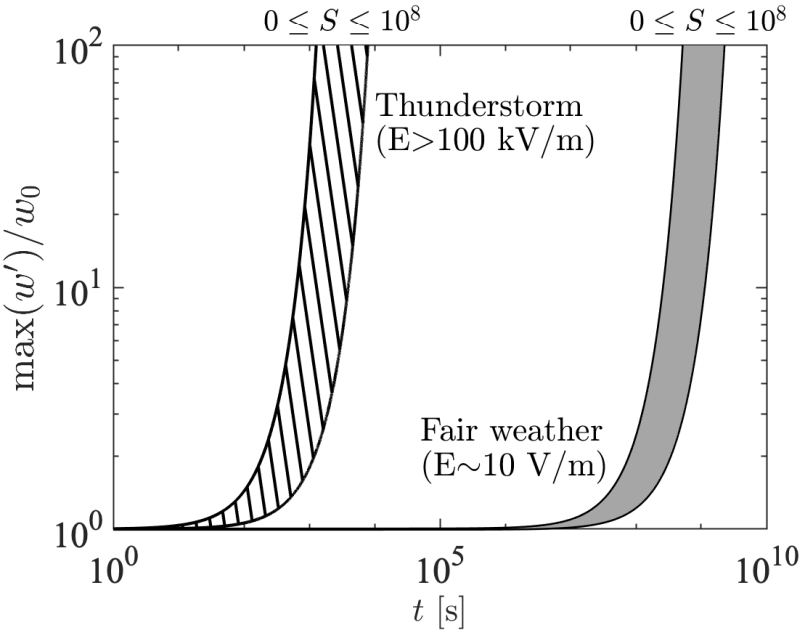

Figure 4.3: Normalized growth of vertical velocity fluctuations under varying shear rates predicted by linear stability analysis under fair weather (solid fill) and thunderstorm (hatch fill) conditions.

Of key interest in the present study is the rate at which small disturbances in the velocity field grow due to EHD. The growth rate, ω, is obtained using prescribed values of α, R and Pr. Using typical fair weather conditions ($\mathrm{Pr} \approx 2.5 \times 10^{-6}$), Fig. 4.3 shows that the maximum growth of vertical velocity fluctuations, w', by EHD is slow, taking approximately $10^9\,\mathrm{s}$ to amplify the fluctuations by two orders of magnitude. Using values relevant to thunderstorm conditions ($\overline{E} = 3 \times 10^5\,\mathrm{V/m}$ and $\overline{\phi} = 2 \times 10^8\,\mathrm{V}$), similar growth is achieved in approximately $10^3\,\mathrm{s}$. However, despite this enhanced growth rate,

the time scales are still relatively slow, even as the shear rate varies by several orders of magnitude. It is important to note that the present linear stability analysis does not take into account detailed aerosol dynamics that are known to be significant in turbulent flows. Numerical simulations that explicitly take these dynamics into account will be presented in the following section.

4.3 Numerical simulations

4.3.1 Simulation configuration

Direct numerical simulations are performed to study the role of nonlinearities associated with aerosol dynamics not accounted for in the linear stability analysis. We consider charged particles suspended in homogeneous shear flow in the presence of a background electric field (see Fig. 4.4). The flow field and space charge are initialized using simple turning wave vectors referred to as Kelvin modes. These wave vectors are initially oriented as upstream waves that rotate as the flow is being sheared and transform into downstream waves. Kelvin modes are known to first experience a transient algebraic growth (a bypass transition) to turbulence and decay after they pass the turning point to downstream waves [122, 120]. Nonlinear effects may couple with the initial transient growth leading to a 'bootstrapping' mechanism [234]. If the electrostatic time scale is significantly smaller than the fluid time scale, heterogeneity in charge distribution may give rise to local EHD body forces during the transient period and prevent or postpone the fluid TKE from decaying.

We consider a triply-periodic domain of length 0.256 m in each direction, discretized using 256^3 grid points. The maximum amount of charge each particle can carry is dictated by the Rayleigh limit, $Q_R = \pi\sqrt{8\epsilon\gamma d_p^3}$, where $\gamma = 0.0738$ N/m is the surface tension coefficient for water droplets and d_p is the particle diameter. The particle charge is taken to be $Q_p = \pm 0.1 Q_R$ and the average particle volume fraction varies between $0 \leq \Phi_v \leq 2\times10^{-3}$,

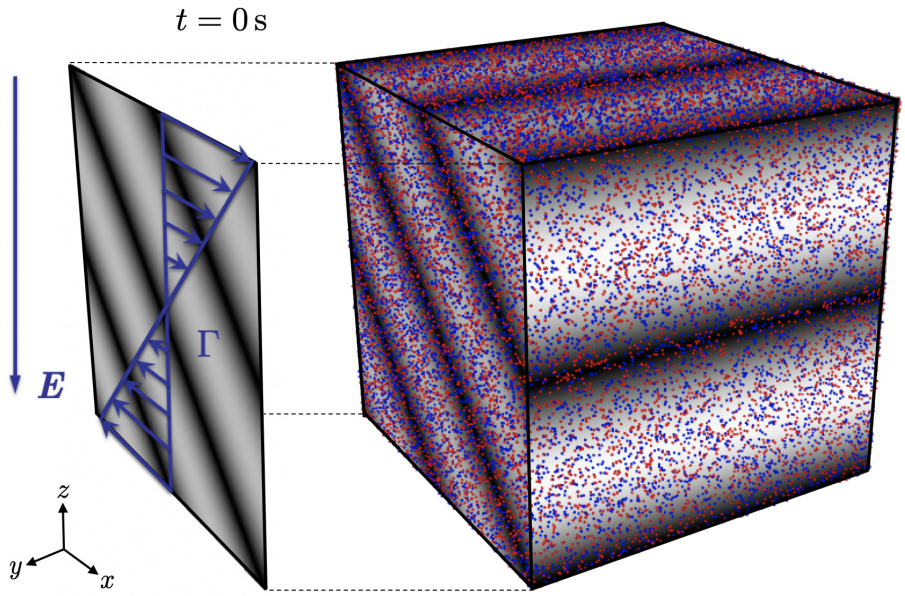

Figure 4.4: Simulation configuration for $\Phi_v = 1 \times 10^{-4}$. Gray scale shows fluid velocity magnitude, ranging from 0 (black) to its maximum value (white). Particles are colored by charge: positive (red) and negative (blue).

corresponding to typical aerosol properties observed in thunderstorm conditions [247, 150]. The root-mean-square EHD fluctuations, $(q_f E)_{\mathrm{rms}} \equiv \sqrt{\langle \left(q_f E - \overline{q}_f \overline{E}\right)^2 \rangle}$, is fixed as the particle loading varies, where angled brackets denote a volume average. Given that $\overline{E}$ is constant and $\overline{q}_f = 0$, $(q_f E)_{\mathrm{rms}} = \langle q_f^2 E'^2 \rangle$. Since the self-induced electric field E' is proportional to the local particle-phase charge density q_p, $(q_f E)_{\mathrm{rms}} \sim \langle q_f^2 q_p^2 \rangle$ is held constant for each simulation. This is done to avoid a trivial solution (e.g., increasing the effect of EHD with increasing volume fraction) and isolate the effect of particle dynamics on TKE production. Therefore, as Φ_v increases, q_f decreases accordingly (see Table 4.1).

4.3.2 Numerics

The fluid-phase equations (4.1)–(4.3) are solved using the numerical framework described in Chapter II. Periodic shear boundary conditions are enforced in the z-direction using a discretely conservative algorithm recently proposed by Kasbaoui et al. [120]. Individual aerosol particles are tracked in a Lagrangian manner [30] governed by Newton's

second law of motion. The electrostatic force is given by

$$\boldsymbol{f}^{(i)}_{\text{coulomb}} = Q_p^{(i)} \boldsymbol{E}[\boldsymbol{x}_p^{(i)}], \tag{4.8}$$

where $Q_p^{(i)}$ is the charge of the i-th particle and $\boldsymbol{E}[\boldsymbol{x}_p^{(i)}]$ is the electric field at the particle position. The particle concentrations are low enough such that direct two-way coupling due to interphase momentum exchange can be neglected. Instead, aerosols affect the gas phase indirectly via their charge distribution. The aerosol charge density, q_p, is obtained by projecting the particle charge to the Eulerian grid. A second-order Runge–Kutta scheme is used for updating each particle's position and velocity. Further details on the numerical implementation can be found in Chapter II.

Because the simulation domain is periodic, q_f and $\boldsymbol{E}$ must be decomposed into mean and fluctuating components and only q_f' and $\boldsymbol{E}'$ are solved for. Equation (4.2) can be rewritten as $\nabla^2\phi' = -(q_f' + q_p)/\epsilon$ and the electric field fluctuation can be solved via $\boldsymbol{E}' = -\nabla\phi'$. We note that particles are assigned equal and opposite charge such that $\langle q_p \rangle = 0$ and the Poisson equation is well posed. The total electric field is then reconstructed as $\boldsymbol{E} = \boldsymbol{E}' + \overline{\boldsymbol{E}}$, and similarly $q_f = q_f' + \overline{q}_f$, with $\overline{\boldsymbol{E}} = [0\,0\,\overline{E}]^\mathsf{T}$. In each simulation, $\overline{q}_f = 0$ and the amplitude of q_f' is prescribed as q_{f_0}. Parameters are chosen to correspond to thunderstorm conditions at an altitude of 6 km as summarized in Table. 4.1.

Φ_v	Mean volume fraction	0	1×10^{-4}	4×10^{-4}	1×10^{-3}	2×10^{-3}
N	Number of particles	0	3.2×10^{6}	1.3×10^{7}	3.2×10^{7}	6.4×10^{7}
q_{f_0} [C/m^3]	Space charge fluctuation	2×10^{-8}	1×10^{-8}	5×10^{-9}	3.2×10^{-9}	2.2×10^{-9}
d_p	Particle diameter			$100\,\mu$m		
Q_p	Particle charge			$\pm\, 7.27 \times 10^{-13}$ C		
ρ_p/ρ	Density ratio			1000		
$\overline{E}$	Background electric field			3.0×10^{5} V/m		

Table 4.1: Parameters used in the homogeneous shear simulations. q_{f_0} is varied with Φ_v such that $(q_f E)_{\text{rms}} \sim \sqrt{\langle q_p^2 q_f^2 \rangle}$ is held constant. All simulations are performed with conditions of $d_p/\Delta x = 0.1$ and $\Gamma = 1.5$.

4.3.3 Evolution and growth of TKE

The aerosol droplets are initially randomly distributed throughout the domain. As shown in Fig. 4.5, horizontal wind shear combined with the background electric field leads to the onset of particle clustering in high strain regions, which eventually generates fluctuations in fluid velocity via coupling with the charge density. Particle clustering arises from a similar mechanism identified by Kasbaoui et al. [119], except here the body force is due to the electric field instead of gravity, and the momentum coupling exists through the charge density instead of the drag force. In the absence of charged droplets, the initial Kelvin modes are rotated and decay without introducing any fluctuations. Gas-phase velocity fluctuations become more intense with increasing droplet loading. To identify the mechanisms responsible for this, we evaluate the evolution of Reynolds stresses, governed by

$$\frac{\mathrm{d}\left\langle u_i' u_j' \right\rangle}{\mathrm{d}t} = \mathcal{P}_{ij} + \mathcal{R}_{ij} - \varepsilon_{ij} + \mathcal{E}_{ij}, \tag{4.9}$$

where $\mathcal{P}_{ij}$, $\mathcal{R}_{ij}$ and ε_{ij} denote mean-gradient production, pressure strain, and viscous dissipation, respectively [188] given by

$$\mathcal{P}_{ij} \equiv -\left\langle u_i' u_k' \right\rangle \frac{\partial \left\langle u_j \right\rangle}{\partial x_k} - \left\langle u_j' u_k' \right\rangle \frac{\partial \left\langle u_i \right\rangle}{\partial x_k}, \tag{4.10}$$

$$\mathcal{R}_{ij} \equiv \left\langle \frac{p'}{\rho} \left(\frac{\partial u_i'}{\partial x_j} + \frac{\partial u_j'}{\partial x_i} \right) \right\rangle, \tag{4.11}$$

$$\varepsilon_{ij} \equiv 2\nu \left\langle \frac{\partial u_i'}{\partial x_k} \frac{\partial u_j'}{\partial x_k} \right\rangle, \tag{4.12}$$

and

$$\rho\mathcal{E}_{ij} = \langle E_j\rangle\langle q_f' u_i'\rangle + \langle E_i\rangle\langle q_f' u_j'\rangle + \langle q_f' E_j' u_i'\rangle + \langle q_f' E_i' u_j'\rangle \tag{4.13}$$

are contributions from EHD. In the present configuration, $\langle E_1\rangle = \langle E_2\rangle = 0$ and $\langle E_3\rangle = \overline{E}$. Also note the last two terms on the right-hand side of Eq. (4.13) containing triply correlations were found to be negligible compare to the first two terms. Taking one-half the trace of (4.9) yields a transport equation for the TKE, defined as $\langle u_i' u_i'\rangle/2$ (repeated indices imply summation). The contributions from EHD, $\mathcal{E}_{ii}/2$, contain two terms. $\mathcal{E}_P{=}\overline{E}\langle q_f' w'\rangle/\rho$ represents production due to the background electric field and correlation between charge density and vertical velocity fluctuations. The second contribution, $\mathcal{E}_T{=}\langle q_f' E_i' u_i'\rangle/\rho$ is found to be negligible in the present study.

The temporal evolution of TKE is shown in Fig. 4.6. All cases exhibit similar algebraic growth at early times. An analytic solution for this early time behavior is provided in Appendix C, which is shown to independent of the aerosol distribution. It can immediately be seen that increasing particle loading enhances TKE post the initial algebraic growth ($t \gtrapprox 1\,\mathrm{s}$). By transferring the charge density from the carrier phase to aerosol particles, the TKE is amplified by as much as a factor of 6 for the highest loading under consideration. It should be noted that the size of the simulation domain is constrained by the high computational cost in tracking $\mathcal{O}(10^8)$ individual particles. Based on the linear stability analysis performed in Sec. 4.2.3, larger domain sizes should result in greater enhancement of TKE. Moreover, a scaling analysis by Di Renzo and Urzay [50] demonstrated that while clustering occurs at the microscale (at the same scale as the smallest turbulent eddies), the self-induced electric field can span much larger scales. Thus, the effects reported here are anticipated to be greater under more relevant length scales.

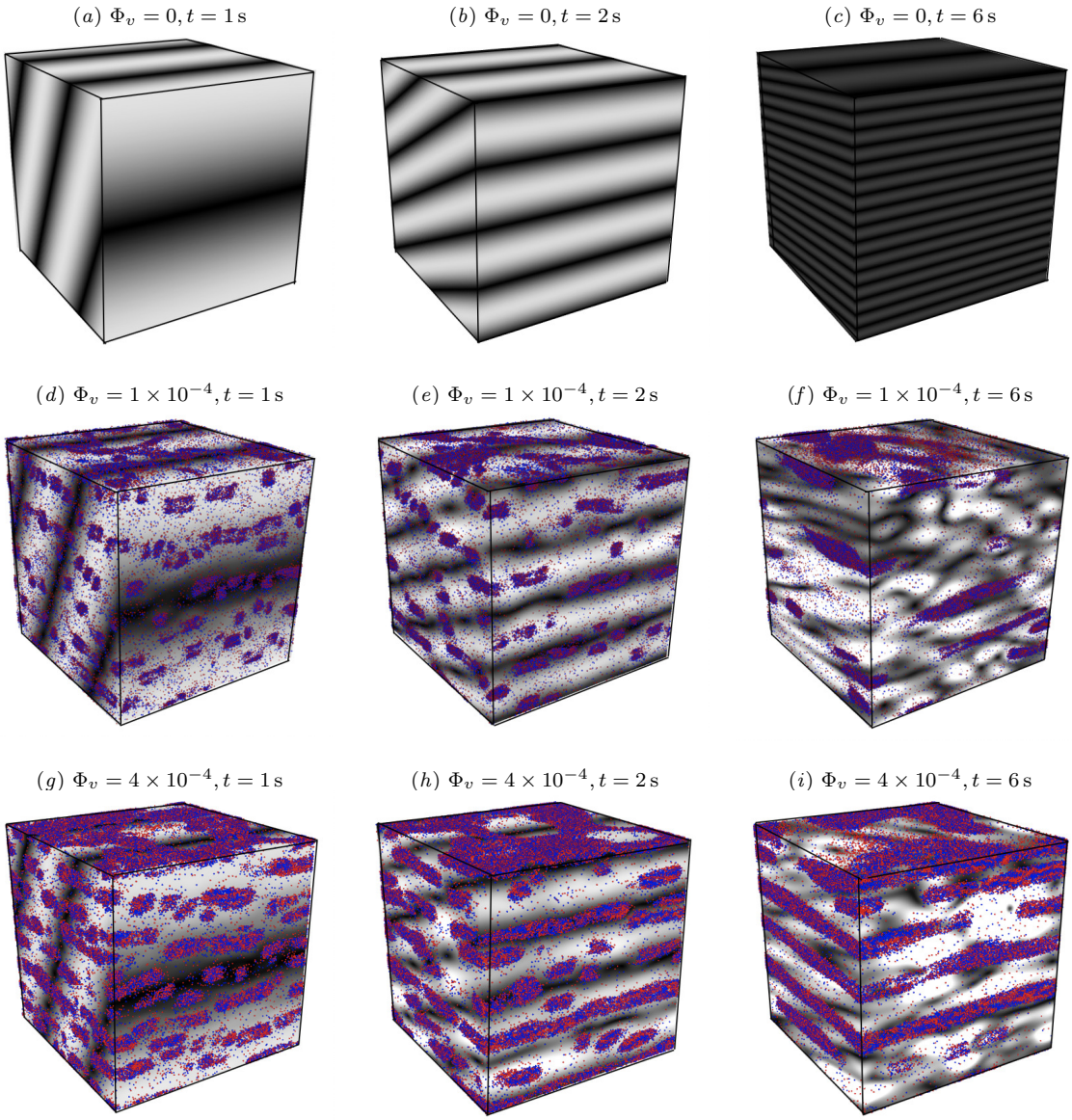

Figure 4.5: Temporal evolution of the gas and particle phases with volume fraction increasing from top to bottom and time increasing from left to right. Color scheme same as Fig. 4.4.

4.3.4 Reynolds stress budget

After the initial algebraic growth is complete, turbulence modulation by charged aerosols is apparent. The temporal evolution of Reynolds stresses are shown in Fig. 4.7. When aerosol particles are absent ($\Phi_v = 0$), the vertical component of Reynolds stress, $\langle w'w' \rangle$, initially grows due to production by EHD ($\mathcal{E}_{33} = 2\overline{E}\langle q_f' w' \rangle / \rho$). This term then

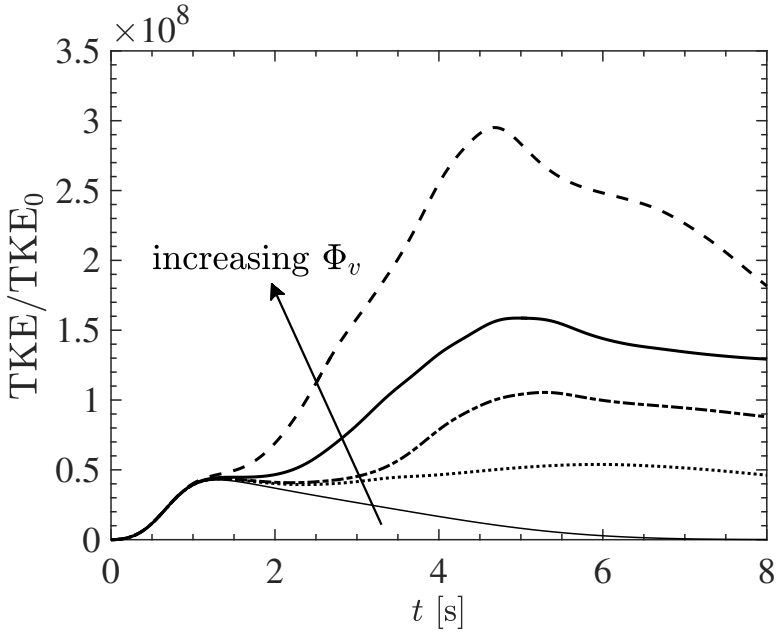

Figure 4.6: Normalized TKE evolution for different particle loadings. $\Phi_v = 0$ (–), 1×10^{-4} ($\cdots$), 4×10^{-4} ($-$ -), 1×10^{-3} ($-$) and 2×10^{-3} (- -).

contributes to mean-gradient production ($\mathcal{P}_{13} = -\langle w'w'\rangle\Gamma$) that increases $\langle u'w'\rangle$. Next, the energy is transferred to the streamwise component $\langle u'u'\rangle$. Because there is no mechanism to sustain TKE when charged aerosol droplets are absent, all three components decay to zero at late times due to viscous dissipation, as shown in Fig. 4.6. When charged droplets are introduced, the Reynolds stresses follow a similar trend at early times and deviate at later times. Only the vertical component $\langle w'w'\rangle$ approaches zero, while $\langle u'w'\rangle$ levels off to a negative value, and the streamwise component, $\langle u'u'\rangle$, is seen to increase. This effect is enhanced with increasing particle volume fraction as shown in Figs. 4.7(b)–4.7(d).

The Reynolds stress budgets are reported for $\Phi_v = 1\times10^{-4}$ in Fig. 4.8 to further understand how energy is transferred between the separate components. We note that the trends reported here are consistent at other values of Φ_v. The initial sinusoidal fluctuation in space charge and vertical velocity together with the background electric field generate a non-zero EHD source $\mathcal{E}_{33} = 2\overline{E}\langle q_f' w'\rangle/\rho$. As a result, the vertical component

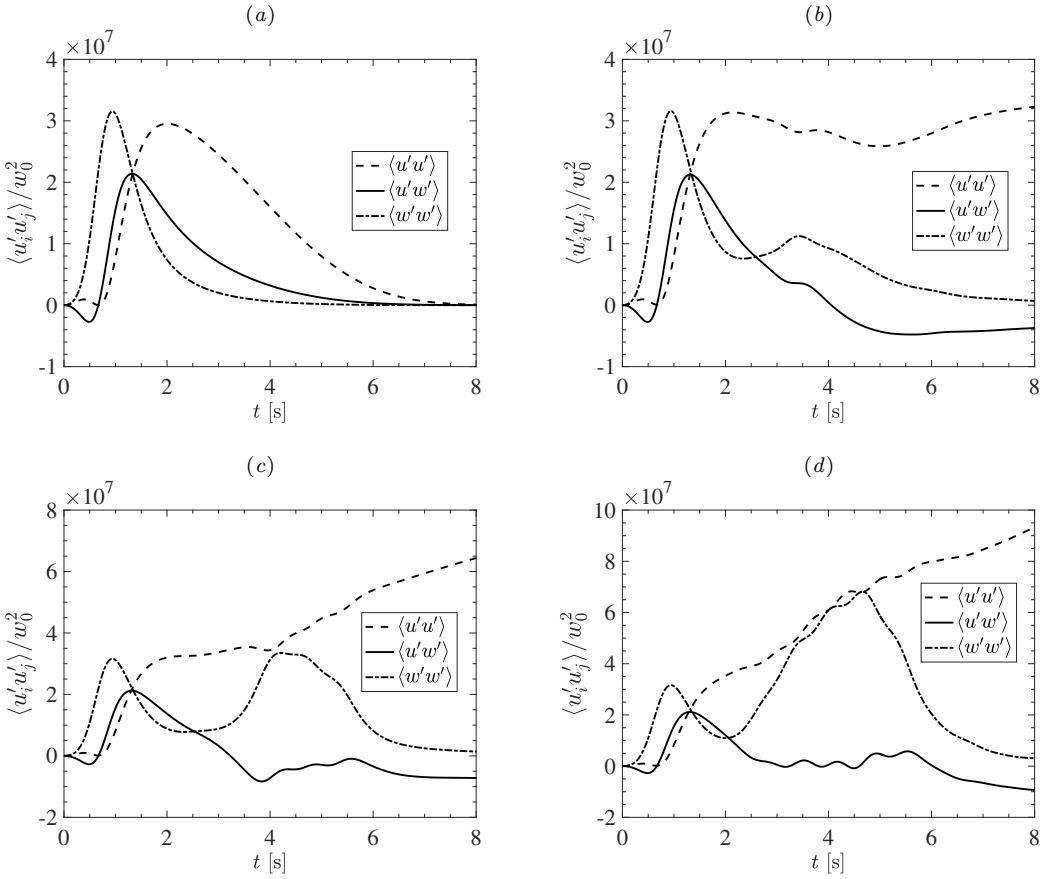

Figure 4.7: Evolution of the Reynolds stresses normalized by w_0^2. (a) $\Phi_v = 0$, (b) 1×10^{-4}, (c) 4×10^{-4} and (d) 1×10^{-3}.

of Reynolds stress, $\langle w'w' \rangle$, grows due to this production terms (see Fig. 4.8(a)). A significant portion of this energy is also transferred to the corresponding pressure strain, $\mathcal{R}_{33} = \langle\, 2p' \left(\partial w'/\partial z\right)/\rho \,\rangle$, and consequently $\langle w'w' \rangle$ decays to zero at late times.

The EHD production term, $\mathcal{E}_{33}$, then decays as a result of diffusion of space charge, at which time pressure strain, $\mathcal{R}_{13} = \langle\, p' \left(\partial u'/\partial z + \partial w'/\partial x\right)/\rho \,\rangle$, acts to redistribute the energy to $\langle u'w' \rangle$. Fig. 4.8(b) reveals that while the streamwise velocity fluctuations increase, a new EHD source term, $\mathcal{E}_{13} = \overline{E}\langle q_f' u' \rangle/\rho$, emerges, further augmenting $\langle u'w' \rangle$. At late time, pressure strain continues to transfer energy from $\langle u'w' \rangle$, similar to $\langle w'w' \rangle$, and the corresponding mean-gradient production, $\mathcal{P}_{13} = -\langle w'w' \rangle \Gamma$, is negative and acts as a sink of $\langle u'w' \rangle$. As a result, $\langle u'w' \rangle$ eventually decays and approaches a negative value

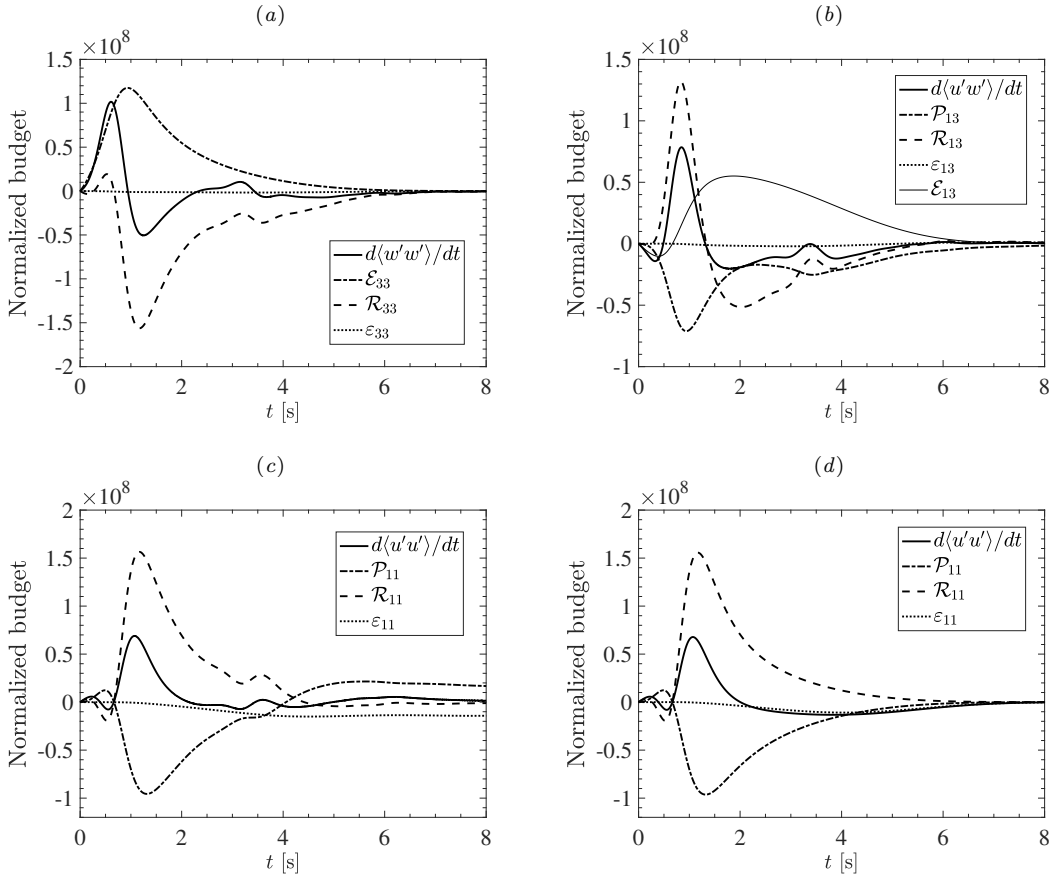

Figure 4.8: Budget of normalized Reynolds stresses. (a) $\langle w'w' \rangle$, (b) $\langle u'w' \rangle$ and (c) $\langle u'u' \rangle$ normalized by Γw_0^2 for $\Phi_v = 1 \times 10^{-4}$. (d) $\langle u'u' \rangle$ normalized by Γw_0^2 in the absence of particles.

when production and dissipation balance.

Fig. 4.8(c) shows the budget for the streamwise component of the Reynolds stress, $\langle u'u' \rangle$. As energy is transferred to the streamwise components, $\langle u'u' \rangle$ is first augmented by the corresponding pressure strain, $\mathcal{R}_{11} = \langle\, 2p' \left(\partial u'/\partial x\right)/\rho \,\rangle$, during the early stage, then mean-gradient production, $\mathcal{P}_{11} = -2\langle u'w' \rangle \Gamma$, acts as a source when $\langle u'w' \rangle$ reaches a negative equilibrium that later sustains $\langle u'u' \rangle$. Note that unlike the other two components of Reynolds stress, the streamwise component always has non-zero production and therefore continues to increase even at late time. Comparing Figs. 4.8(c) and 4.8(d), it can be seen that this non-zero equilibrium state of production ($\mathcal{P}_{11}$) only occurs when charged aerosols are present.

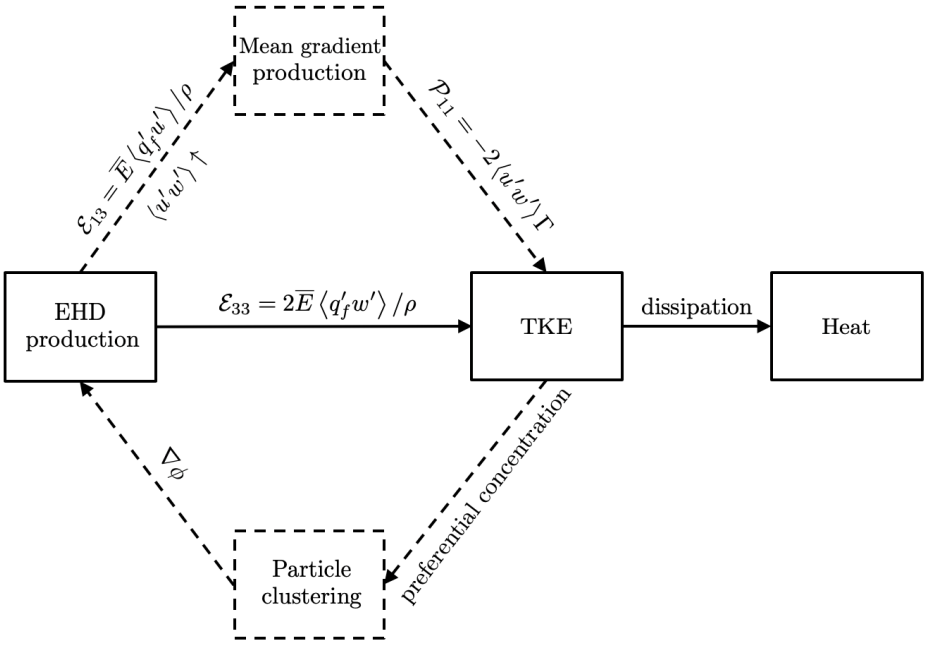

Figure 4.9: Energy transfer due to three-way coupling between turbulence, charged particles, and a background electric field. The dashed lines represent energy transfer when aerosol particles are present. Fluctuations in vertical velocity and space charge give rise to an EHD source term, $\mathcal{E}_{33}$, that produces TKE. In the absence of charged aerosol particles, TKE is eventually dissipated to heat. When particles are present, preferential concentration by the turbulence generates inhomogeneities in particle distribution and consequently gradients in electric potential. This further contributes to the EHD source term $\mathcal{E}_{33}$ in addition to $\mathcal{E}_{13}$ that generates TKE via mean gradient production.

A schematic summarizing the energy transfer is illustrated in Fig. 4.9. As depicted by the solid lines, a background electric field combined with fluctuations in velocity and space charge yields production of TKE that is eventually dissipated into heat. In the absence of charged droplets, no other mechanism exists to further produce TKE. However, when aerosol droplets are present, turbulence can be sustained through two additional processes: (i) turbulence preferentially concentrates charged particles, resulting in fluctuations in electric potential that self-induces an electric field, enhancing $\mathcal{E}_{33}$ and TKE; and (ii) the space charge fluctuation induced by the electric field contributes to another EHD source term, $\mathcal{E}_{13}$, which enhances $\langle u'w' \rangle$, contributing to mean-gradient production ($\mathcal{P}_{11}$) that further augments TKE. This three-way coupling gives rise to a feedback loop that enhances TKE beyond the initial algebraic growth.

4.4 Conclusions

We presented a theoretical and numerical study on the electrohydrodynamic generation of atmospheric turbulence under fair weather and thunderstorm conditions. The focus of this study was on the three-way coupling between turbulence, charged aerosol droplets, and a background electric field. A canonical flow configuration was presented to simulate the upper troposphere, in which a random distribution of charged particles was placed in homogeneous shear flow with a uniform electric field.

Linear stability analysis was performed using base state parameters relevant to fair weather conditions in the upper troposphere. Atmospheric stability was characterized by the electric Rayleigh number, which was found to be a function of vertical span and shear rate. The stability analysis revealed that the atmospheric fluid dynamics are most unstable over a vertical span consistent with typical cloud thicknesses observed at these elevations. The growth rate in velocity fluctuations was estimated using both fair weather and thunderstorm parameters, which was found to be slow even under thunderstorm conditions.

Direct numerical simulations revealed a nonlinear feedback mechanism that acts to accelerate turbulence production under thunderstorm conditions. It was found that horizontal wind shear combined with EHD body forces led to the onset of particle clustering that generated fluctuations in charge density. These fluctuations acted to augment turbulent kinetic energy (TKE) after the initial algebraic growth. TKE was initially produced in the vertical direction and was later transferred to the streamwise (shear) components. The streamwise velocity gradients acted to induce fluctuations in aerosol concentration and consequently generated gradients in electric potential, resulting in an increase in the EHD body force and the process repeated. TKE was enhanced by up to a factor of six

as the particle loading increased.

The present numerical and theoretical analysis demonstrated that charged aerosols in the atmosphere can couple nonlinearly with the background electric field to enhance the onset of TKE. It is important to note that other effects may be at play as well. Particles are capable of transferring charge among each other or acquire charge through triboelectric effects [142, 158, 89, 111]. In addition, the droplet size may vary due to evaporation and condensation. Additional instabilities may also arise when gravity is present, which may add to the TKE augmentation studied here. In the present study, we isolate the effect of charged aerosols on turbulence generation, and therefore these effects were not included. However, the Eulerian–Lagrangian simulation framework can be extended to account for these kinetic processes in TKE augmentation in future work.

CHAPTER V

Breakup of Cohesive Particles by Turbulence

In this chapter, we present a numerical study analysing the breakup of a single cohesive particle aggregate in turbulence. Solid particles with diameters smaller than the Kolmogorov length scale ($d_p < \eta$) are initially aggregated into a spherical 'clump' of diameter $D > \eta$ and placed in homogeneous isotropic turbulence. Parameters are chosen relevant to dust or powder suspended in air such that cohesion due to van der Waals is important. Simulations are performed using an Eulerian–Lagrangian framework that models two-way coupling between the fluid and solid phases and resolves particle-particle interactions. Aggregate breakup is investigated for different Adhesion numbers Ad, Taylor micro-scale Reynolds numbers Re_λ and nondimensional clump sizes D/d_p. The intermittency of turbulence is found to play a key role on the early-stage breakup process, which can be characterized by a turbulent Adhesion number Ad_η that relates the potential energy of the van der Waals force to turbulent shear stresses. A scaling analysis shows that the time rate of breakup for each case collapses when scaled by Ad_η and an aggregate Reynolds number proportional to D. A phenomenological model of the breakup process is proposed that acts as a granular counter-part to the Taylor Analogy Breakup (TAB) model commonly used for droplet breakup. Such a model is useful for predicting particle breakup in coarse-grained simulation frameworks, such as Reynolds-averaged

Navier–Stokes, where relevant spatial and temporal scales are not resolved.

5.1 Introduction

The transport and deposition of tiny (cohesive) particles in turbulent flows play important roles in many engineering, environmental and medical systems. Examples include dry powder inhalers for drug delivery [12, 267, 268], dust ingestion in gas turbine engines [9, 56, 21, 202] and fluidized bed reactors [165, 242, 146, 175]. Micron-sized particles tend to form aggregates due to inter-particle cohesion. The dynamical evolution and morphology of these aggregates involve a complex interplay between turbulent stresses and inter-particle cohesive forces. As a result, particle clumping can arise under various circumstances, which is known to compromise the performance of the aforementioned systems. For example, agglomeration has been shown to significantly deteriorate the delivery efficiency of drug particles [12], accelerate turbine blade erosion in gas turbine engines [87, 97] and defluidize two-phase reactors [165, 37]. Of particular interest to the present study is turbulence-induced breakup of fine particulate aggregates.

Several mechanisms are responsible for particle deagglomeration in a flow field. Breakup can be induced by inertial stresses [129, 101], rotary stresses [220, 110, 67, 68, 276, 167] or turbulent stresses [7, 258, 6, 256]. Several models have recently been developed for deagglomeration due to rotary stress in simple shear flows [54, 199, 246]. The mechanisms responsible for deagglomeration in turbulence, however, are more complicated and less established. Weiler et al. [256] developed a model of critical shear stress for instantaneous breakage as a function of aggregate size and the mean cohesive force. However, aggregates often breakup progressively from the surface, and the critical stress at the vicinity of the aggregate is not always directly available, especially in course-grained simulations where subgrid-scale stresses are not resolved such as in Reynolds-averaged Navier–Stokes

(RANS) frameworks.

The major challenge in numerically investigating the breakage of cohesive particles is properly resolving the wide range of length- and time-scales at play. One common approach is to couple Lagrangian particle tracking with a mean flow field obtained from RANS. The turbulent dispersion of particles is often modeled in a stochastic manner. This approach has been widely used for particle ingestion in gas turbine engines [87, 97, 21]. Despite its low computational cost, Lagrangian particle tracking coupled with RANS has been shown to under-predict turbulent dispersion and deposition of particles compared to experiments [260], especially near boundary layers [200, 72]. On the contrary, particle-resolved direct numerical simulation (PR–DNS) has been applied to fully capture the flow field and particle interactions [239, 248, 249]. While PR–DNS is highly accurate, it is limited to small physical systems due to its high computational cost.

Alternatively, the Eulerian–Lagrangian method tracks individual particles and solves the fluid phase on an Eulerian mesh with grid spacing larger than the particle diameter. It is capable of capturing detailed particle-particle interactions and particle-fluid coupling with moderate computational cost. This approach has been widely applied to study cohesive particles in turbulence [103, 128, 25, 221, 139, 270]. However, most existing studies consider one-way coupling without taking into account influences of drag or volume displacement by particles on the fluid. Such an approach is not appropriate when modeling large particle aggregates as it over-predicts the interphase slip velocity in the vicinity of the particles [53]. Another known deficiency of this method when dealing with cohesive particles is the restrictive time step.

In the present study, an Eulerian–Lagrangian framework is employed where two-way coupling is accounted for via drag and volume displacement effects. The van der Waals force model is modified to allow for soft-sphere contact. A multi-scale time stepping

algorithm is introduced to minimize the computational cost. The numerical framework presented in Chapter II is employed. The relative importance of turbulence and adhesion on breakup dynamics of a single aggregate is analyzed by adjusting the Taylor micro-scale Reynolds number, Re_λ, and the Adhesion number, Ad, that relates the van der Waals surface energy, γ, and the kinetic energy of particles [153]. The Hamaker constant A is varied by 3 orders of magnitude to mimic weakly cohesive particles (e.g. silica) and strongly cohesive materials such as metal oxides. The role of turbulence intermittency on the early-stage deagglomeration is discussed. We then report the temporal evolution of the aggregate, present a breakage regime diagram and a scaling analysis of the breakup rate in § 5.2. Additionally, a phenomenological model of the breakup process is proposed in § 5.3 using a mass-spring-damper analogy, followed by a sensitivity analysis of model parameters in § 5.4. Together with the scaling analysis, the proposed model provides a complete prediction of the deagglomeration process using quantities available in coarse-grained simulations that do not resolve the relevant fluid and particle time scales, such as in RANS.

In the remainder of this chapter, the term 'clump' and 'aggregate' will be used interchangeably.

5.2 Turbulence-induced breakup of a cohesive particle aggregate

5.2.1 Problem setup

In this work, we consider an initially spherical 'clump' of particles suspended in homogeneous isotropic turbulence (see Fig. 5.1). Particles are monodisperse with diameters $d_p = 20$ μm and particle-to-fluid density ratio $\rho_p/\rho = 2200$, corresponding to typical Geldart C-type particles (e.g. dust or powder in air) in which inter-particle cohesion is important [160, 251]. The simulation domain is triply periodic with sides of length $L = 400d_p$. The initial aggregate is formed by randomly distributing particles through-

out the domain and assigning inward-facing normal velocities, commonly referred to as the "centripetal packing method" [138, 268, 199]. First, particles are initially randomly distributed within in a spherical region without overlap. A constant centripetal force is then imposed on each particle to attract the particles towards the center of the domain. Particles undergo collisions and agglomerate in the absence of fluid forces until a single aggregate is formed. The aggregate is then submerged in the flow and held in place until a statistical stationary state is reached. At $t = 0$ the particles are free to evolve, potentially resulting in breakup and the formation of smaller aggregates, sometimes referred to as 'flocs' in liquid suspensions [176, 70, 110, 248, 279].

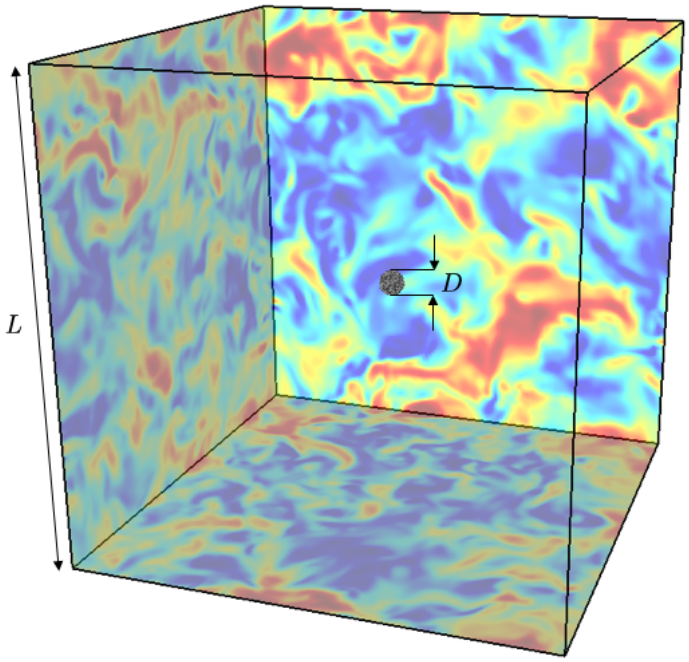

Figure 5.1: Simulation configuration shown with background fluid velocity (blue: low, red: high). Particles are initially close-packed in a spherical aggregate of diameter D. Particles are fixed in place until the flow reach a statistically stationary state prior to deagglomeration.

The competition between turbulent shear stress and inter-particle cohesion on the breakup process is studied by adjusting the initial aggregate diameter D, the Hamaker constant A and Taylor Reynolds number $\mathrm{Re}_\lambda = u_{\mathrm{rms}}\lambda/\nu$ where ν is the kinematic viscosity, u_{rms} is the average root-mean-square velocity and $\lambda = \sqrt{15\nu/\epsilon}\, u_{\mathrm{rms}}$ is the Taylor micro-

scale with ϵ the viscous dissipation rate. The particle Adhesion number is introduced to quantify the effect of van der Waals attraction, defined as $\mathrm{Ad} = 2\gamma/\left(\rho_p u_{\mathrm{rms}}^2 d_p\right)$ where $\gamma = A/(24\pi\delta^2)$ is the potential energy associated with van der Waals force with $\delta = 0.165$ nm [153]. The Hamaker constant A is a material property that indicates the strength of cohesion due to van der Waals [96]. In this study, A is varied between $\mathcal{O}(10^{-21})$ J for weakly cohesive particles (e.g. silica) to $\mathcal{O}(10^{-18})$ J for strongly cohesive materials such as metal oxides [153]. A list of relevant two-phase flow parameters used in each case is provided in Table 5.1.

	Physical parameters			
d_p	Particle diameter	20 µm		
D	Aggregate diameter	200 µm	400 µm	
N	Number of particles	682	5484	
ρ_p	Particle density	2650 kg m^{-3}		
ρ	Fluid density	1.2 kg m^{-3}		
ν	Fluid kinematic viscosity	1.5×10^{-5} m^2 s^{-1}		
e	Coefficient of restitution	0.9		
A	Hamaker constant	[0.4, 300] $\times 10^{-20}$ J		
	Non-dimensional parameters			
N_g^3	Number of grid points	32^3	64^3	128^3
Re_λ	Taylor micro-scale Reynolds number	30	43	64
d_p/η	Normalized particle diameter	0.19	0.42	0.80
D/η	Normalized aggregate size	[1.9, 16]		
Ad	Adhesion number	[0.3, 9.0]		

Table 5.1: Parameters used in the simulations.

A linear forcing term $\boldsymbol{F}_t$ is added to the right-hand-side of the fluid momentum equation (Eq. (2.2)) to enforce statistically stationary turbulence. It is important to note that most standard forcing techniques are not sufficient at maintaining desired turbulence properties (e.g. Re_λ) when two-way coupling is present [149]. In this work, we propose to extend the linear forcing scheme of Lundgren [145], such that the mean interphase exchange contribution is removed and the turbulence statistics remain unaffected by the

presence of particles, given by

$$\boldsymbol{F}_t = Q_t \left(\alpha \boldsymbol{u} - \langle \alpha \boldsymbol{u} \rangle\right) - \langle \boldsymbol{F}_{\text{inter}} \rangle, \tag{5.1}$$

where Q_t is the linear forcing coefficient, and $\langle \cdot \rangle$ denotes the volumetric mean of the quantity within the computational domain.

Due to the large density ratio under consideration ($\rho_p/\rho = 2200$), the effects of fluid torque and lubrication forces on particle motion are neglected. In addition, it is important to note that cohesion due to van der Waals attraction and collisions are treated independently, which implicitly assumes these effects are additive in nature according to the Derjaguin, Muller and Toporov (DMT) theory [45]. The underlying assumption of the DMT theory is that cohesive forces do not modify the surface profile during particle contact. Another popular contact theory proposed by Johnson et al. [114], known as the Johnson, Kendall and Roberts (JKR) theory, assumes that adhesion occurs only within the flattened contact region such that the collision force is nonlinearly coupled with the cohesion force and consequently cannot be treated as additive. As suggested by Johnson and Greenwood [113], the DMT approximation is valid when $\lambda_T \ll 1$ (typically $\lambda_T \lesssim 0.1$) and the JKR model is valid when $\lambda_T \gg 1$ (typically $\lambda_T \gtrsim 10$), with λ_T the dimensionless Tabor parameter defined as

$$\lambda_T = \left(\frac{2 d_p \gamma^2}{E_s^2 \delta^3}\right)^{1/3} \tag{5.2}$$

where E_s is the elastic modulus of particles. For the simulations considered herein, $0.19 \leq \lambda_T \leq 0.98$, and it is therefore not immediately obvious which assumptions readily apply. To this end, a variance-based sensitivity analysis is performed in § 5.4. It is found that the results reported herein are largely unaffected by the choice in contact theory. The results were also found to be insensitive to the restitution coefficient and inclusion of

fluid torque. In the remainder of this work, particle contact mechanics are based on the DMT theory due to the low values of λ_T under consideration and to be consistent with a recently proposed cohesion model that enables larger simulation timesteps [91], which has been discussed in § 2.6.

5.2.2 Flow visualization

Simulations are carried out for three Taylor micro-scale Reynolds numbers and five Adhesion numbers as listed in Table 5.1. The spatial distribution of particles at $t/\tau_p = 4$ is compared in Fig. 5.2. In the absence of van der Waals forces, the aggregate breaks up immediately and particles are dispersed by the background turbulence. It can be observed that particles progressively shed off from the surface of the clump, and gain speed as they are transported away. Particles within the aggregate experience smaller interphase slip velocities due to two-way coupling, resulting in negligible drag forces. It is important to note that the deagglomeration process would be markedly different if two-way coupling were not taken into account. If the simulation was performed with one-way coupling, all of the particles would experience similar drag, resulting in simultaneous breakup throughout the aggregate (see § 5.4).

As Ad increases, inter-particle cohesion eventually overcomes the fluid stresses, preventing breakup from occurring when $\mathrm{Ad} \geq 9$. For the same Ad, the rate of deagglomeration increases with increasing Re_λ due to larger fluid velocity fluctuations. It is clear from Fig. 5.2 that the competition between turbulent stresses acting to disintegrate the particle aggregate and cohesive forces opposing breakup is entirely controlled by Re_λ and Ad. A quantitative assessment of Re_λ and Ad on the evolution of the breakup process will be presented in the following sections.

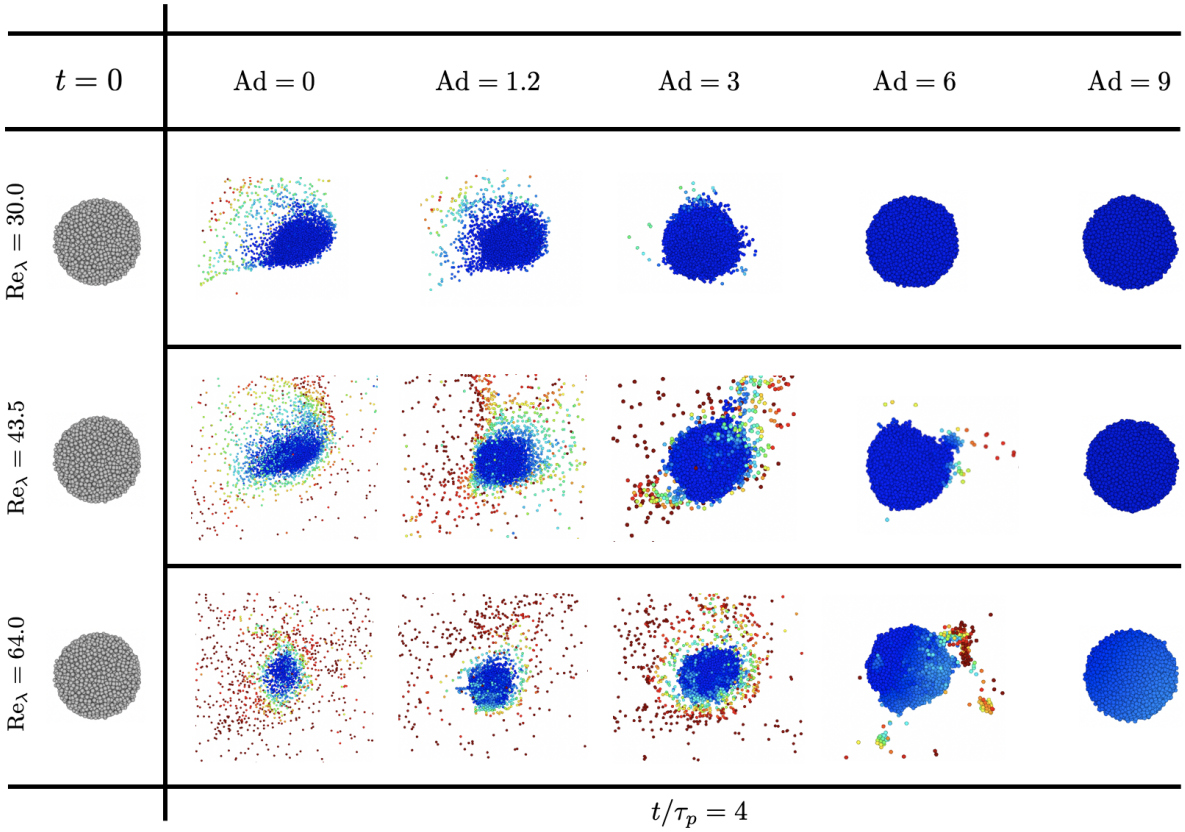

Figure 5.2: Particle position after $t/\tau_p = 4$ colored by their velocity (blue: low, red: high) for different values of Ad and Re_λ. Left ($t = 0$): an initially spherical particle aggregate ($D = 20\,d_p$) suspended in homogeneous isotropic turbulence.

5.2.3 The role of turbulence intermittency on deagglomeration

Fluid stresses exerted on the aggregate surface by turbulence is highly intermittent. Figure 5.3 shows a comparison of the fluid stress at the aggregate surface, defined as $\rho u'^2|_c = \sum_{i=1}^{N} \rho \|\boldsymbol{u}'[\boldsymbol{x}_p^{(i)}]\|^2/N$, with the domain-averaged stress. As can be seen, the instantaneous fluid stress at the vicinity of the aggregate fluctuates by as much as four times the domain-averaged value. The time scales of these fluctuations are significantly smaller than the time required to complete breakup ($\sim 300\tau_f$ for this case), which amplifies the effect of turbulence intermittency on early-stage breakup.

To investigate the effect of turbulence intermittency on the breakup process, particles are held in place until four values of t/τ_f as highlighted in red in Fig. 5.3. The particle

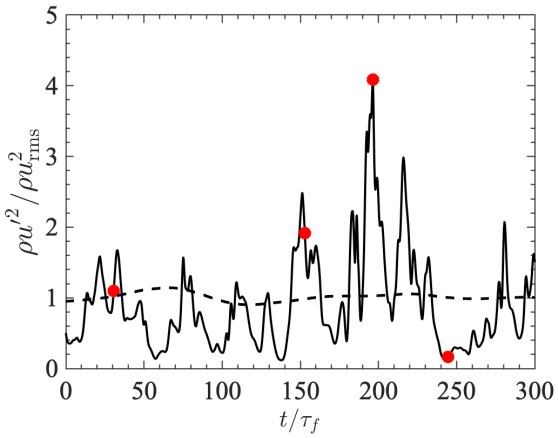

Figure 5.3: Instantaneous fluid stress at the aggregate surface (−) and within the entire domain (−−) normalized by the root-mean-square quantities with $\mathrm{Re}_\lambda = 30$ and $\mathrm{Ad} = 0.3$. Four realizations under consideration (•).

clump is then free to evolve from that particular instant in time. These four realizations contain different fluid stress levels at the vicinity of the clump. In order to quantify its effect on breakup, the gyration radius, R_g, and the fractal dimension, D_f, are computed, which are commonly used to characterize the dynamics and morphology of particle aggregates [74, 199]. The gyration radius is defined as

$$R_g = \sqrt{\frac{1}{N_c}\sum_{i=1}^{N_c}\left\|\boldsymbol{x}_p^{(i)} - \boldsymbol{x}_c\right\|^2}, \tag{5.3}$$

where N_c is the number of particles in the clump, $\boldsymbol{x}_c = \sum_{i=1}^{N_c}\boldsymbol{x}_p^{(i)}/N_c$ is the center of mass of the aggregate. The fractal dimension indicates the compactness of its spatial structure. For a dense spherical aggregate, $D_f \approx 3$. In this work, we follow Ruan et al. [199] and obtain D_f by solving the following nonlinear equation

$$N_c = k_f \left(2R_g/d_p\right)^{D_f}, \tag{5.4}$$

where the fractal pre-factor k_f is

$$k_f = 0.7321 + 0.8612^{\left(\frac{D_f-1}{2}\right)^{1.95}}. \tag{5.5}$$

The initial clump generated by centripetal packing has values $R_g/d_p = 7.625$ and $D_f = 2.94$. The total volume of the clump is defined by $V_c(t) = \{\boldsymbol{x} \in \mathbb{R}^3 : \alpha(\boldsymbol{x}, t) < 0.75\}$, which is evaluated at each simulation timestep in order to quantify the evolution of R_g and D_f. N_c represents the number of particle inside the volume $V_c(t)$.

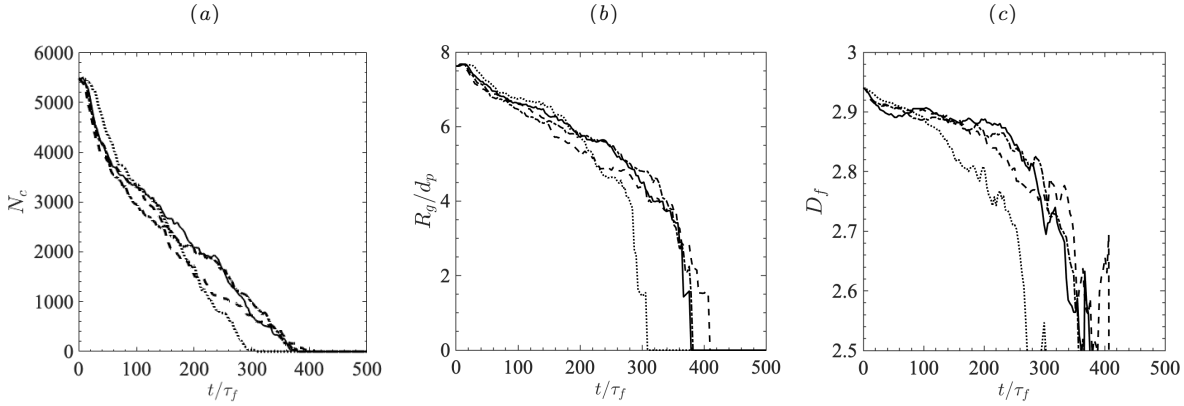

Figure 5.4: Characteristics of the aggregate for four different realizations with $\mathrm{Re}_\lambda = 64$ and $\mathrm{Ad} = 0.3$. (a) Number of particles, (b) normalized Gyration radius and (c) fractal dimension of the particle clump. Line types $-$, $-\cdot$, $--$, and $\cdots$ correspond to red data points from left to right shown in Fig. 5.3.

Figure 5.4 shows the temporal evolution of N_c, R_g and D_f for the four realizations with $\mathrm{Re}_\lambda = 64$ and $\mathrm{Ad} = 0.3$. It can be seen that the breakup statistics change substantially over the different realizations despite Re_λ and Ad being held constant. The cases with higher initial turbulence intensity result in quicker initial breakup yet later time statistics remain relatively unchanged. This can be associated with the time scale of the intermittent fluctuations being significantly smaller than the time it takes for total breakage. Although the aggregate breaks up faster with larger initial surface stress, it is subject to smaller fluctuations on average (see Fig. 5.3) resulting in slower breakage at late times. Despite this intermittency, N_c decays in an approximately linear manner whereas R_g decreases much faster at late time. The fractal dimension D_f decreases from 2.94 to approximately 2.5, indicating significant deformation of the aggregate. Note that the statistics of the fractal dimension D_f becomes noisy when the number of particles

in the aggregate is $N_c \lessapprox 1000$ or equivalently the Gyration radius $R_g \lessapprox 2d_p$ due to the limited sample size. To mitigate the effect of turbulence intermittency on the subsequent results reported herein, all simulations are initialized such that $\rho u'^2|_c$ is approximately equal to the global fluid stress at $t = 0$.

5.2.4 Early-stage deagglomeration

Figure 5.5 shows the temporal evolution of the number of particles N_c and the Gyration radius R_g of the aggregate for $\mathrm{Re}_\lambda = 64$ as a function of Ad. The number of particles within the aggregate decreases linearly as it breaks up. As Ad increases, inter-particle cohesive forces become more significant, resulting in a decreased rate of deagglomeration. It can be seen that the deagglomeration statistics exhibit a stair-step behavior when Ad exceeds a critical value of Ad = 3. This is attributed to the intermittency of turbulent fluctuations, as shown in Fig. 5.6. Particles shed off from the aggregate more rapidly when the clump experiences larger velocity fluctuations. Similar trends are also observed for the Gyration radius, whereas the radius decreases faster during the late stage of deagglomeration, as a direct consequence of the linear decay in N_c, or equivalently linear decay in aggregate volume. Note that when Ad > 3, particles become so cohesive that the clump retains its original shape and size, which were omitted from Fig. 5.5.

Figure 5.6 highlights the effect of fluid stresses at the aggregate surface for Ad = 3 and $\mathrm{Re}_\lambda = 64$. The iso-contour of $\alpha = 0.75$ shown in white is used to visualise the surface of the aggregate. A direct one-to-one correspondance can be observed between the stair-step breakup behavior and instantaneous turbulent velocity fluctuations. The snapshots indicate the abrupt decrease in aggregate size is associated with turbulent eddies interacting with the aggregate resulting in breakup of smaller satellite aggregates. Before breakage, the clump is seen to remain relatively spherical. In the presence of large velocity fluctuations, the aggregate breaks from the side of its surface where the velocity

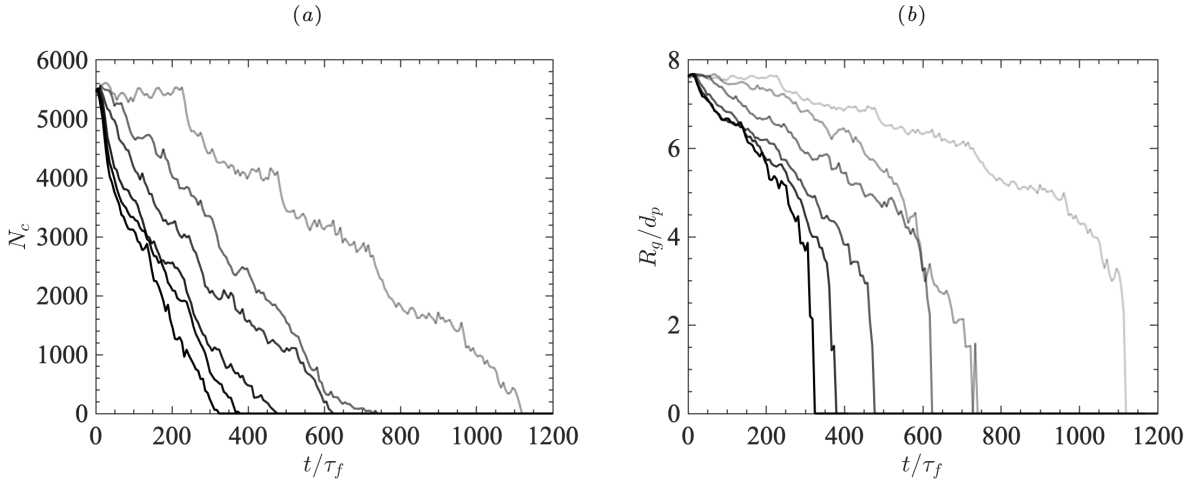

Figure 5.5: Temporal evolution of (a) the number of particles and (b) gyration radius of the aggregate. $\mathrm{Re}_\lambda = 64$ and $\mathrm{Ad} = 0, 0.3, 0.6, 1.2, 1.8, 3$ (from black to light gray).

gradient is high. As the aggregate shrinks, the net effect of cohesion within the aggregate also decreases and consequently breaks up in all directions. Although the surface area is smaller than the original aggregate, particles shed off at higher speeds resulting in the same rate-of-change in N_c. At late time ($t > 1000\tau_f$), D drops below a critical value where turbulent eddies can no longer break the aggregate into smaller pieces, i.e. when $D \sim \eta$.

5.2.5 Scaling analysis

To better understand the role of turbulence and adhesion on the breakup process, the breakage outcome associated with each simulation is plotted in terms of the adhesive stress, γ/η, and the turbulent stress, $\rho_p u_{\mathrm{rms}}^2$. As shown in Fig. 5.7, larger fluid stress results in a transition from a "no breakage" regime to a "breakage" regime at a given γ/η. A simulation is classified as "no breakage" when N_c remains unchanged for $t \geq 1000\,\tau_f$. Similarly, at a given $\rho_p u_{\mathrm{rms}}^2$, the increase of γ/η, either due to enhanced cohesion or smaller η, reduces the likelihood of breakup. The breakup outcome is found to depend on a turbulent Adhesion number $\mathrm{Ad}_{\eta,\mathrm{crit}} = \gamma/\left(\rho_p u_{\mathrm{rms}}^2 \eta\right) = 1.8$ where $\mathrm{Ad}_\eta = \mathrm{Ad}\left(d_p/\eta\right)$. Note

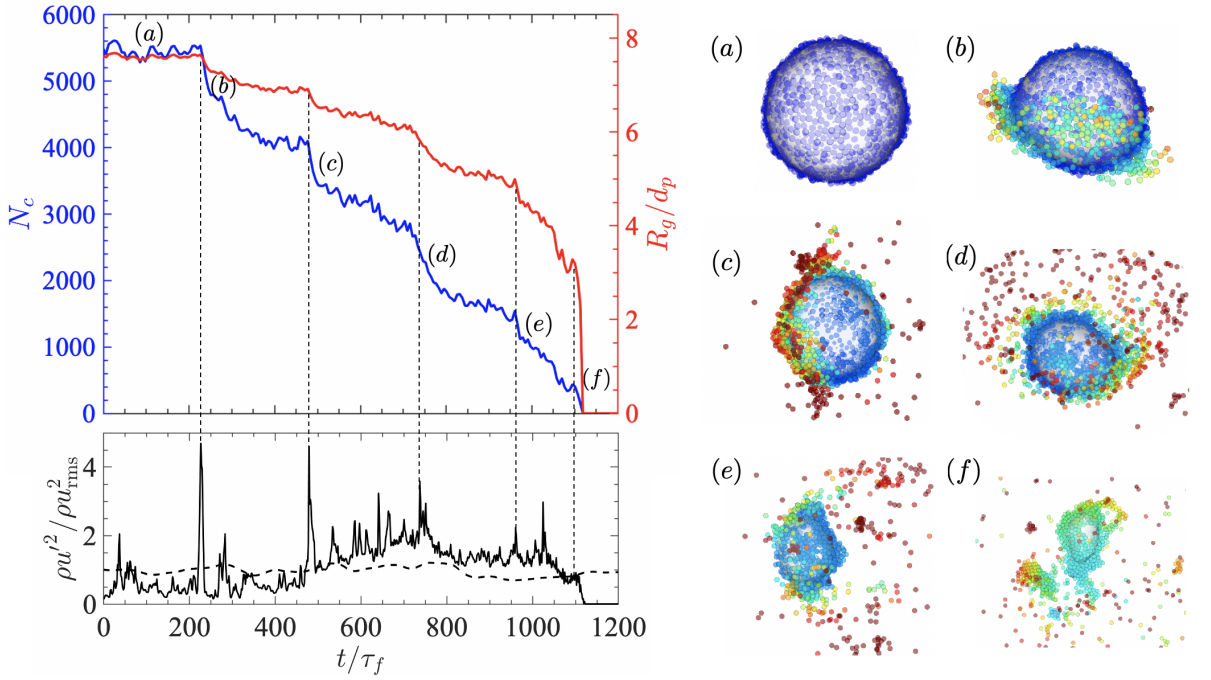

Figure 5.6: Temporal evolution of the number of particles (blue) and Gyration radius (red) of the aggregate and corresponding fluid stress at the aggregate surface for Ad = 3 and $\mathrm{Re}_\lambda = 64$. Left: stair-step behavior is observed in the statistics indicating intermediate breakup occurs when the local fluid stress exceeds a threshold value. Right: corresponding instantaneous snapshots of particle position, with iso-contour of $\alpha = 0.75$ (white) representing the surface of the aggregate. Color scheme same as Fig. 5.2.

that for simple shear flow where η is not well defined, it has been found that the breakage outcome is instead characterized by D [199]. The simulations performed in the present study indicate that the characteristic length scale associated with aggregate breakup is η when $\eta \ll D$. In simple shear flow, particles experience a uniform shear rate within the aggregate, therefore larger aggregates will experience larger velocity differences across the surface. In homogeneous isotropic turbulence, however, turbulent eddies create local regions of high shear of size proportional to η. When $\eta \ll D$, these eddies are agnostic to the clump size D resulting in progressive breakup into smaller clumps, as depicted in Fig. 5.6.

Figure 5.5 shows that the breakup rates ($\dot{N}_c = \mathrm{d}N_c/\mathrm{d}t$) are approximately constant for each case under consideration. The breakup rates are extracted from each simulation and

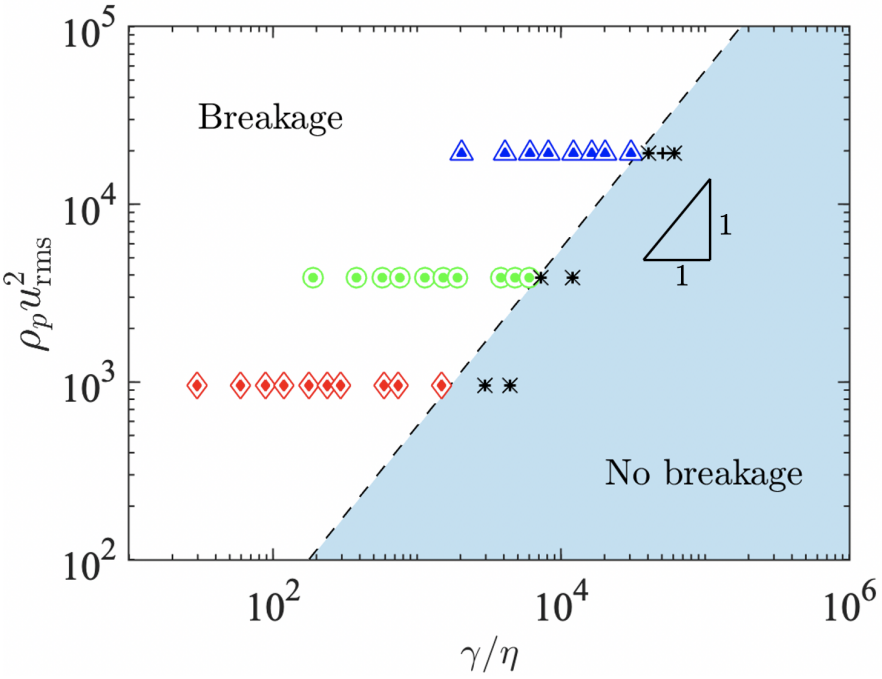

Figure 5.7: Breakage regime diagram for a particle aggregate suspended in homogeneous isotropic turbulence. $\mathrm{Re}_\lambda = 30$(♦), 43(●), 64(▲) and nondimensional clump size $D/d_p = 10\,(\text{solid}), 20\,(\text{hollow})$, with $+$ and $\times$ denoting cases without breakage for $D/d_p = 10$ and 20, respectively. The linear dashed line separating the breakup outcome is given by $\mathrm{Ad}_{\eta,\mathrm{crit}} = \gamma/\left(\rho_p u_{\mathrm{rms}}^2 \eta\right) = 1.8$.

plotted in Fig. 5.8(a). It can immediately be seen that the breakup rate increases with D and Re_λ, but decreases with Ad. The effect of D and Re_λ can be taken into account via an aggregate Reynolds number $\mathrm{Re}_D = u_{\mathrm{rms}} D/\nu$. When $\mathrm{Ad}_\eta = 0$, adhesion has no effect on the breakup rate and consequently $\dot{N}_c \tau_p \sim \mathrm{Re}_D$. When $\mathrm{Ad}_\eta \geq \mathrm{Ad}_{\eta,\mathrm{crit}}$, no breakage will occur according to Fig. 5.7 ($\dot{N}_c \tau_p = 0$). With this, a correction factor $(1 - \mathrm{Ad}_\eta/\mathrm{Ad}_{\eta,\mathrm{crit}})$ can be introduced to account for the effect of cohesion. Based on these observations, the data is rescaled with respect to $\mathrm{Re}_D(1 - \mathrm{Ad}_\eta/\mathrm{Ad}_{\eta,\mathrm{crit}})$. As shown in Fig. 5.8($b$), the breakup rate follows a linear scaling given by $\dot{N}_c \tau_p = 28\,\mathrm{Re}_D(1 - \mathrm{Ad}_\eta/\mathrm{Ad}_{\eta,\mathrm{crit}})$. Note that small deviations are observed at lower Reynolds numbers (e.g. $\mathrm{Re}_\lambda = 30$). For these cases, the eddy size becomes comparable to D, and turbulence must breakup the entire aggregate instead of a piece of it. As a result, the assumption that η is the characteristic length scale for deagglomeraton does not hold at low Reynolds numbers and the breakup

will exhibit dependance of D/d_p instead. Based on the simulation results, the dependence of breakup on η is applicable when $D/\eta \gtrsim 5$.

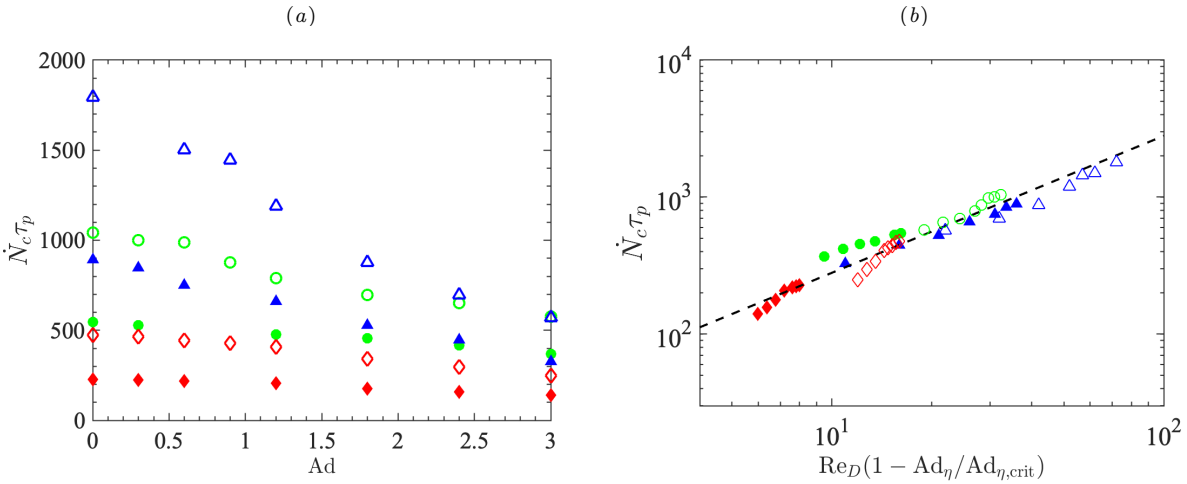

Figure 5.8: Rate of deagglomeration quantified by the time-rate-of-change of number of particles within the aggregate. $\mathrm{Re}_\lambda = 30(\blacklozenge), 43(\bullet), 64(\blacktriangle)$ and aggregate size $D/d_p = 10\,(\text{solid}), 20\,(\text{hollow})$. Rate of deagglomeration plotted as a function of Ad (a) and $\mathrm{Re}_D(1-\mathrm{Ad}_\eta/\mathrm{Ad}_{\eta,\mathrm{crit}})$ (b). $\dot{N}_c\tau_p = 28\,\mathrm{Re}_D(1-\mathrm{Ad}_\eta/\mathrm{Ad}_{\eta,\mathrm{crit}})$ $(--)$.

5.3 Phenomenological model of aggregate breakup

Despite valuable insights provided by the numerical simulations presented herein and many other works using PR–DNS, they are limited to relatively small-scale systems due to the high computational cost needed to resolve the relevant length- and time-scales. Particle transport in large-scale systems is typically modeled without knowledge of the velocity field at the scale of individual particles. However, the breakup of cohesive particles reported in § 5.2.3 and § 5.2.4 are shown to depend strongly on local turbulence statistics such as η and u_{rms}. In addition, the effect of turbulence intermittency is not captured when particles traverse an averaged flow field, such as in the case of RANS. The aim here is to develop a reduced-order model capable of capturing the breakup of cohesive particles in the absence of a resolved turbulent flow field.

The Taylor analogy breakup (TAB) model is widely used in calculating droplet breakup.

This method is based on Taylor's analogy [226] for an oscillating and distorting droplet. The droplet deformation is treated as a mass-spring-damper system, where the surface tension force acts as a restorative force, the force exerted by the surrounding gas phase acts as an external force, and the droplet viscosity acts as a damper. Motivated by the TAB model, we propose a similar mass-spring-damper analogy to model turbulence-induced breakup of cohesive particles. In this case, the van der Waals force is treated as an analog to the droplet surface tension, and friction due to inter-particle contact is treated as an analog to the droplet viscosity. We refer to this model as a Granular Taylor analogy breakup (G-TAB) model.

Assuming the local turbulence statistics are known from a turbulence model such as RANS, Ad_η can be determined to estimate whether or not breakup occurs. As shown in Fig. 5.9, three distinct breakup regimes are observed: $\mathrm{Ad}_\eta \leq 0.5$, the cohesive force is weak compared to turbulent stresses and the aggregate breaks up instantaneously; $0.5 < \mathrm{Ad}_\eta \leq 1.8$, the competition between turbulence and cohesion results in delayed breakage of the aggregate; and when cohesion becomes significant ($\mathrm{Ad}_\eta > 1.8$), turbulence is unable to overcome the attractive forces, resulting in no breakup. The G-TAB model is employed to predict the breakup time as a function of Ad_η when $0.5 < \mathrm{Ad}_\eta \leq 1.8$. The governing equation is given by

$$F - kx - d\frac{\mathrm{d}x}{\mathrm{d}t} = m\frac{\mathrm{d}^2x}{\mathrm{d}t^2}, \tag{5.6}$$

where x is the displacement of the aggregate equator from its spherical (undisturbed) position. The coefficients of this equation are based on Taylor's analogy, given as

$$\text{inertial force due to turbulence:} \qquad \frac{F}{m} = C_F\frac{\rho u_{\mathrm{rms}}^2}{\rho_p \eta}, \tag{5.7}$$

(5.8) restorative force due to adhesion: $$\frac{k}{m} = C_k \frac{\gamma}{\rho_p \eta^3},$$

(5.9) damper due to inter-particle friction: $$\frac{d}{m} = C_d \frac{\mu_p}{\rho_p \eta^2},$$

where μ_p is the effective solids viscosity at random close packing (RCP) and C_F, C_k and C_d are model coefficients that will be determined later.

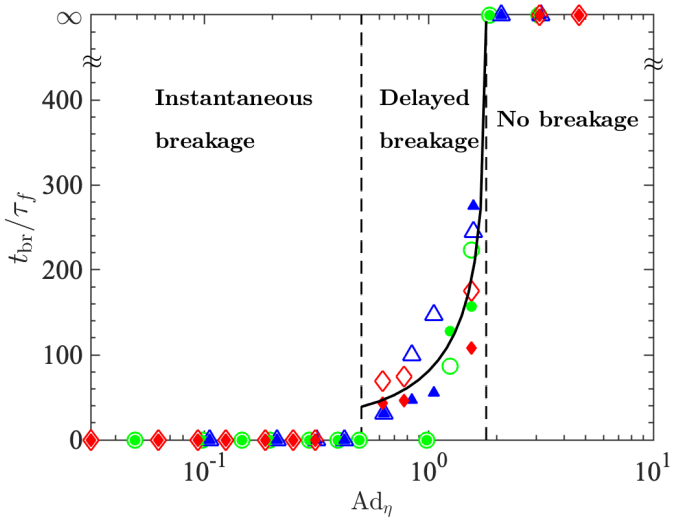

Figure 5.9: Time to initial breakup $t_{\rm br}$ as a function of the turbulent Adhesion number. Symbols are the same as Fig. 5.7. The black line corresponds to Eq. (5.19) with $C_F = 0.8$, $C_k = 2 \times 10^{-4}$, $C_d = 0.3$ and $C_b = 1$. The vertical dashed lines correspond to $\mathrm{Ad}_\eta = 0.5$ and $\mathrm{Ad}_\eta = 1.8$.

For non-cohesive particles, Bocquet et al. [18] gives the solids viscosity as $\mu_p^0 = (m_p\sqrt{\Theta}/d_p^2) g_0^{\beta-1}$ from Kinetic theory, where $\Theta = \langle \boldsymbol{v}_p^{(i)} \cdot \boldsymbol{v}_p^{(i)} \rangle / 3$ is the granular temperature, $g_0 = (1 - n/n_c)^{-1}$ is the radial distribution function at contact with n the local number density and n_c the maximum number density at RCP. $\beta = 1.75$ is a phenomenological constant measured from experiments. For cohesive particles, μ_p increases monotonically with increasing adhesion due to enhanced inter-particle attraction. A linear correction has been introduced by Roy et al. [198] as $\mu_p = \mu_p^0(1 + 1.47\,\mathrm{Bo})$ where $\mathrm{Bo} = F_{\rm vdw}/(p_s d_p^2)$

is the bond number that measures the cohesion strength relative to the compressive force. The solids pressure p_s at RCP is given as $p_s = n_0 g_0 m_p \Theta$ with $n_0 = (1+\mathrm{e})(\pi/3) n_c^2 d_p^3$ [18]. Based on these relations, μ_p is computed as a function of Θ and Bo

$$\mu_p = (m_p \sqrt{\Theta}/d_p^2) g_0^{\beta-1} (1 + 1.47\,\mathrm{Bo}), \tag{5.10}$$

which depends on Re_λ and Ad. Based on the simulation results reported herein, $\Theta/(\Gamma d_p)^2$ is found to scale linearly with Re_D^{-1} (see Fig. 5.10). Therefore, we propose a simple model for the granular temperature of the particles within the aggregate near RCP as

$$\Theta = C_\Theta \mathrm{Re}_D^{-1} (\Gamma d_p)^2, \tag{5.11}$$

where the coefficient $C_\Theta = 0.2$ is determined from the simulations, and the shear rate is approximated as $\Gamma \approx u_{\mathrm{rms}}/D$. A more detailed algebraic expression for Θ is available by Syamlal et al. [223].

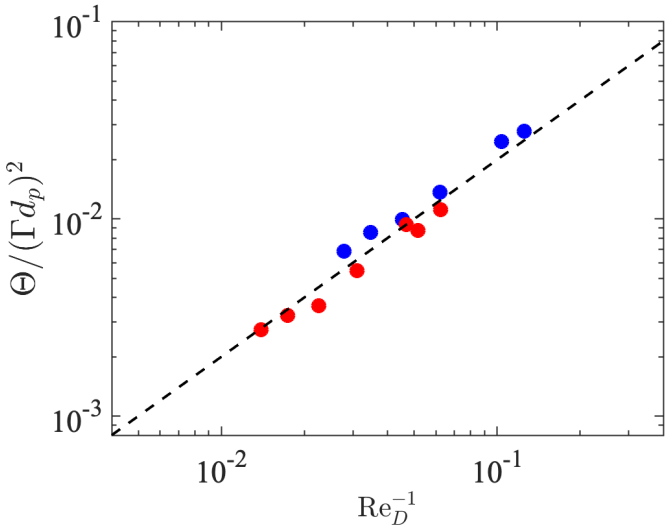

Figure 5.10: Scaling of the mean granular temperature within the aggregate for $D = 10\,d_p$ (blue) and $20\,d_p$ (red). $\Theta/(\Gamma d_p)^2 = 0.2\,\mathrm{Re}_D^{-1}$ (−−).

The aggregate is assumed to breakup if the distortion grows to a critical ratio of the

Kolmogorov length scale. This breakup requirement is given as

$$y = x/\left(C_b\eta\right) > 1. \tag{5.12}$$

Consequently, Eq. (5.7) can be nondimensionalized as

$$\frac{\mathrm{d}^2 y}{\mathrm{d}t^2} = \frac{C_F}{C_b}\frac{\rho}{\rho_p}\frac{u_{\mathrm{rms}}^2}{\eta^2} - \frac{C_k\gamma}{\rho_p\eta^3}y - \frac{C_d\mu_p}{\rho_p\eta^2}\frac{\mathrm{d}y}{\mathrm{d}t}, \tag{5.13}$$

which exhibits the following analytical solution

$$y(t) = \mathrm{Ad}_c\left(1 - e^{-(t/t_d)}\left[\cos(\omega t) + \frac{1}{\omega t_d}\sin(\omega t)\right]\right), \tag{5.14}$$

where

$$\frac{1}{t_d} = \frac{C_d}{2}\frac{\mu_p}{\rho_p\eta^2}, \tag{5.15}$$

$$\mathrm{Ad}_c = \frac{C_F}{C_kC_b}\frac{1}{Ad_\eta}\frac{\rho_f}{\rho_p}, \tag{5.16}$$

and

$$\omega^2 \quad = \quad C_k\frac{\gamma}{\rho_p\eta^3} - \frac{1}{t_d^2}. \tag{5.17}$$

The aggregate is assumed to breakup when the maximum displacement satisfies

$$\max(y) = \mathrm{Ad}_c\left(e^{-\pi/(\omega t_d)} + 1\right) > 1, \tag{5.18}$$

and the corresponding breakup time is uniquely obtained by solving

$$y(t_{\mathrm{br}}) = 1, \quad t_{\mathrm{br}} < \pi/\omega. \tag{5.19}$$

The model coefficients are determined by solving Eqs. (5.15)–(5.17) and Eq. (5.19) using t_{br} extracted from each simulation. The G-TAB model is able to predict t_{br} and

the correct $\mathrm{Ad}_{\eta,\mathrm{crit}}$ as shown in Fig. 5.9 with $C_F = 0.8$, $C_k = 2 \times 10^{-4}$, $C_d = 0.3$ and $C_b = 1$. These coefficients are on the same order as the original TAB model except for C_k, which is significantly smaller, indicative that a larger restorative force is required to prevent breakup compared to that of the surface tension required for liquid droplets. This discrepancy is primarily due to the short-range nature of the van der Waals force which results in non-restorative deformation as inter-particle distances increase beyond the force range. Note that the model is not applied when $\mathrm{Ad}_\eta < 0.5$, resulting in the instantaneous breakage regime where $t_{\mathrm{br}} = 0$.

In summary, for any spherical aggregate of particles with known size ratio D/d_p, Hamaker constant A and local turbulence quantities η and u_{rms}, the nondimensional numbers Ad_η, Bo and Re_D can be calculated. With this, the G-TAB model predicts the time it takes to initiate breakage based on Ad_η and Bo. If an aggregate is predicted to break (i.e. $\mathrm{Ad}_\eta < 1.8$), then the rate of breakup is modeled using the scaling shown in Fig. 5.8 given by

$$\mathrm{d}N_c/\mathrm{d}t = \frac{28\,\mathrm{Re}_D}{\tau_p}(1 - \mathrm{Ad}_\eta/\mathrm{Ad}_{\eta,\mathrm{crit}}). \tag{5.20}$$

This provides a comprehensive prediction of the deagglomeration process of a clump of cohesive particles in turbulence from the onset of breakage to complete fragmentation into primary particles. Because u_{rms} and η are readily available in a RANS calculation, the G-TAB model can readily be incorporated. We note that this model is specifically designed for the breakup of a single dense spherical aggregate in turbulence. While non-spherical or less densely-packed aggregates may require different model coefficients, the mass-spring-damper analogy proposed here is anticipated to hold.

Many efforts have recently been made towards modeling aggregate breakup due to particle interactions. Chen and Li [34] showed that the collision-induced breakage rate scales

exponentially with Ad and aggregate size. van Wachem et al. [245] proposed a discrete fragmentation model (DFM) to simulate the breakup behavior due to aggregate-aggregate and aggregate-wall collisions without tracking each individual primary particle. Unlike these studies, the present work provides a framework that isolates the effect of turbulence on particle breakup using a simple phenomenological model. At present, experimental measurements of particle breakup in turbulence are scarce. While such measurements are challenging to make experimentally, primarily due to the difficulty in seeding an individual aggregate in a controlled manner and due to the opaque nature of the particles, such data would be invaluable to further validate such models.

5.4 Sensitivity of aggregate breakup to modeling parameters

Two key metrics used in the analysis of aggregate breakup and model development in the present study are the time-to-breakup, t_{br}, and breakup rate, $\dot{N}_c$. As summarized in Chapter II, the numerical prediction of breakup depends on a set of parameters for modeling inelastic collisions and cohesion due to van der Waals forces. The purpose of this Appendix is to evaluate the sensitivity of the quantities of interest (QoIs), namely t_{br} and $\dot{N}_c$, to the various modeling parameters employed. Specific attention is paid to the effect of the spring stiffness, k, and restitution coefficient, e, appearing in (2.6), the role of two-way coupling, the relative importance of fluid torque and choice in cohesion model. The simulation configuration outlined in § 5.2.1 is used, with $\mathrm{Re}_\lambda = 64$ and $\mathrm{Ad} = 0.3$ and 3. It should be noted that while Gu et al. [91] previously demonstrated that simulations of gas-fluidization of cohesive particles are insensitive to the particle stiffness using the modified cohesion model employed here, the present study represents the first application of this model to large (with respect to the Kolmogorov length scale) and dense (near close packing) particle aggregates.

		Ad	Spring stiffness, k (N/m)				Restitution coefficient, e			Two-way coupling		Fluid torque	
			10	100	300	7000	0.1	0.3	0.9	w/	w/o	w/	w/o
Gu *et al.* 2016	$\dot{N}_c\tau_p$	0.3	**1523**	1219	1246	1167	1371	1167	**1523**	**1523**	17138	1594	**1523**
		3.0	**570**	577	565	568	576	568	**570**	**570**	10968	593	**570**
	t_{br}/τ_f	0.3	**0**	0	0	0	0	0	**0**	**0**	0	0	**0**
		3.0	**225**	210	280	230	180	210	**225**	**225**	0	225	**225**
Hamaker 1937	$\dot{N}_c\tau_p$	0.3	914	979	997	1167	826	793	914	914	17312	937	914
		3.0	0	0	0	568	0	0	0	0	10765	0	0
	t_{br}/τ_f	0.3	1750	840	800	0	1740	1780	1750	1750	0	1760	1750
		3.0	∞	∞	∞	230	∞	∞	∞	∞	0	∞	∞

Table 5.2: Breakup time (t_{br}) and time rate of breakup ($\dot{N}_c$) for different values of model parameters. Values used in the primary study displayed in bold.

Table 5.2 summarizes the non-dimensional time-rate-of-breakup and breakup time for different model parameters and conditions, with the values used to generate the results reported in § 5.2 highlighted in bold. The modified van der Waals model of Gu et al. [91] is also compared to the original model of Hamaker [96] to demonstrate the reduced dependence of spring stiffness on the QoIs. It can immediately be seen that the QoIs are far more sensitive to the particle stiffness when the original model of Hamaker [96] is used. Taking the 'real' value of particle stiffness to be $k = 7000$ N/m, both models yield the same results when this value is used, albeit with excessively small timesteps. However, as k is reduced to an artifically soft value of 10 N/m, t_{br}/τ_f changes from 0 to 1750 using Hamaker [96] with Ad = 0.3, whereas t_{br}/τ_f predicted using the modified model remains 0. The QoIs are seen to be even less sensitive to k for higher values of Ad with the modified model. Specifically, varying the stiffness from $k = 7000$ to $k = 10$ N/m results in a 23.3% change in breakup rate for Ad = 0.3 and only a 0.9% change for Ad = 3. This is likely due to the increased duration of breakup at higher values of Ad. Similar variations in the breakup rate can also be seen when varying the coefficient of restitution, despite it changing from near-elastic (e = 0.9) to highly inelastic (e = 0.1). Similar trends are observed for the other QoI (t_{br}/τ_f) as well.

The QoIs are found to be much less sensitive to the inclusion of fluid torque. It can be seen that accounting for the fluid torque slightly increases the breakup rate, and has negligible effect on the breakup time. For Ad = 0.3, the non-dimensional breakup rate $\dot{N}_c\tau_p$ varies from 1523 to 1594, and with Ad = 3, it varies from 570 to 593. Meanwhile, it has no noticeable change in the breakup time t_{br}. This is not surprising as fluid torque acting on each particle i, $\boldsymbol{M}_f^{(i)}$, is proportional to the dynamic viscosity μ, which is added to the right-hand-side of Eq. (2.5) according to [35]

$$\boldsymbol{M}_f^{(i)} = -\pi\mu d_p^3 \left(\boldsymbol{\omega}_p^{(i)} - \boldsymbol{\omega}\right), \tag{5.21}$$

where $\boldsymbol{\omega} = \nabla \times \boldsymbol{u}/2$ is the fluid rotation rate vector. While such effects are known to be important for liquid-solid suspensions, the dynamic viscosity is typically two orders of magnitudes smaller in gas-solid flows. Meanwhile, two-way coupling is seen to have substantial effects on the results.

To obtain a quantitative understanding of how sensitive the QoIs are to the modeling parameters, a variance-based sensitivity analysis is performed for parameters listed in Table. 5.2. The total-effect Sobol sensitivity indices [218, 205] are computed, defined as

$$S_{Ti} = \frac{E_{\mathbf{X}_{\sim i}}\left(\mathrm{Var}_{X_i}\left(Y \mid \mathbf{X}_{\sim i}\right)\right)}{\mathrm{Var}(Y)}, \tag{5.22}$$

where Y is the output (QoI), $\mathbf{X}$ is a vector of four independent input parameters (i.e., k, e, two-way coupling, fluid torque), $\mathbf{X}_{\sim i}$ denotes the set of all variables except X_i, and E and Var denote the expectation and variance, respectively. S_{Ti} can be interpreted as a measure of the contribution of X_i's variance to the output variance, including the total variance caused by its interactions with other input variables, normalized by the global output variance of the QoI, Var(Y). Note that for cases in which the aggregate fails to breakup, $t_{\mathrm{br}} = \infty$, which results in ill-defined Sobol indices. To this end, a transformed

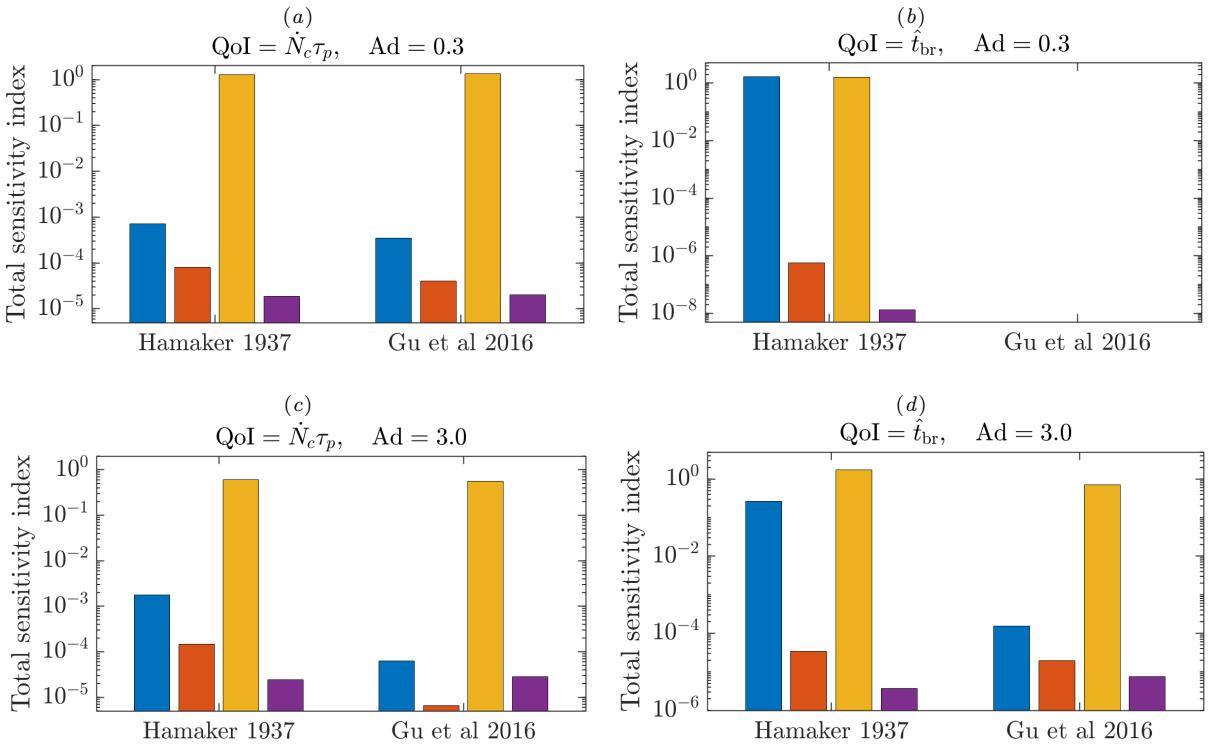

Figure 5.11: Total-effect Sobol sensitivity index of time-to-breakup ((a) and (c)) and breakup rate ((b) and (d)) for Ad = 0.3 and 3.0 normalized by the global variance of each QoI. Particle stiffness k (blue), restitution coefficient e (orange), two-way coupling (yellow) and the fluid torque (purple).

QoI $\hat{t}_{\mathrm{br}}$ is defined to measure the breakup time by monotonically mapping t_{br} to a finite range via

$$\hat{t}_{\mathrm{br}} = (t_{\mathrm{br}}/\overline{t_{\mathrm{br}}})^2/\left((t_{\mathrm{br}}/\overline{t_{\mathrm{br}}})^2+1\right) \tag{5.23}$$

with $\overline{t_{\mathrm{br}}}$ the mean of all finite t_{br} values such that $\hat{t}_{\mathrm{br}} = 0$ when $t_{\mathrm{br}} = 0$ and $\hat{t}_{\mathrm{br}} = 1$ when $t_{\mathrm{br}} = \infty$. We found that S_{Ti} is not sensitive to the specific choice of the mapping function as long as it is a monotonic function such that they have the same physical meaning.

As shown in Fig. 5.11, the modified model of Gu et al. [91] significantly reduces the sensitivity of the particle stiffness on both QoIs. The effect is more profound on $\dot{N}_c\tau_p$ for Ad = 3 than Ad = 0.3 as previously observed in Table 5.2. For $\hat{t}_{\mathrm{br}}$, however, the dependency on these input parameters are completey removed when Ad = 0.3 since

the aggregate breaks up instantaneously (i.e., $\hat{t}_{\mathrm{br}} = 0$). Even when particles are highly cohesive (Ad = 3), the Sobol index of k using the model of Gu et al. [91] is approximately three orders of magnitude smaller than Hamaker's original model, which demonstrates the advantage of using the modified model. Nevertheless, both QoIs are most sensitive to two-way coupling for both values of Ad.

To better illustrate the large discrepancy in QoIs between one-way and two-way coupling, we compare the instantaneous particle distribution and the corresponding flow field at $t/\tau_f = 60$ in Fig. 5.12. When one-way coupling is considered, the local flow remains unmodified by the presence of particles, resulting in relatively large interphase slip velocities and consequently large values in drag. It can be seen that despite the presence of cohesion, strong drag induced by the turbulence results in instantaneously breakup. However, with two-way coupling, the near close-packing distribution of particles is seen to result in a no-slip boundary condition, resulting in null drag for all of the particles except those near the surface of the aggregate. In § 5.2, this was shown to result in fragmentation that occurs progressively from the outer surface where the shear stresses are greatest.

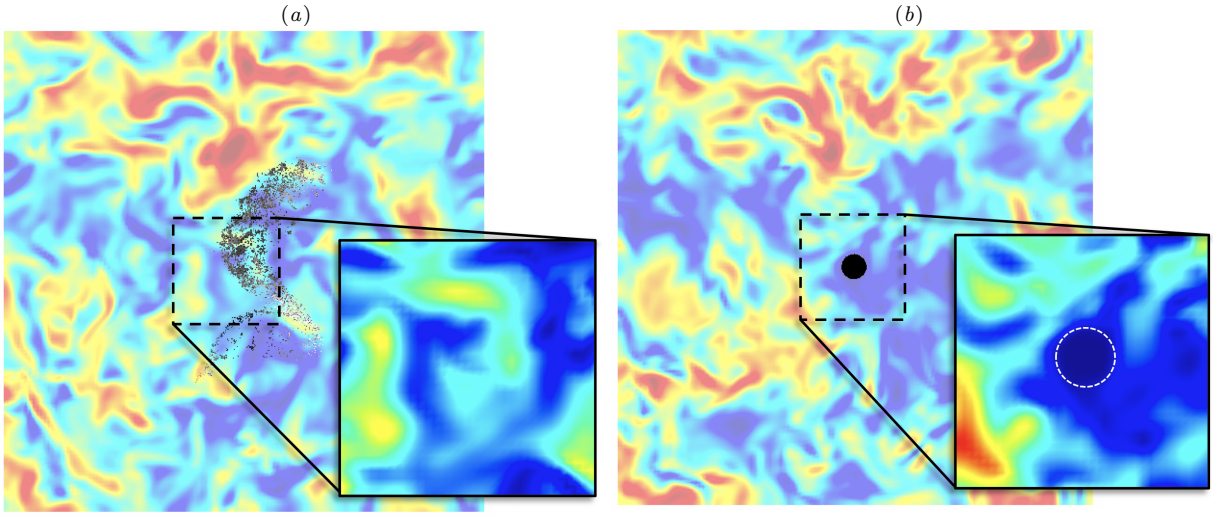

Figure 5.12: Comparison of the velocity field and particle distribution with (a) one-way coupling and (b) two-way coupling for $\mathrm{Re}_\lambda = 64$ and Ad = 3 at $t/\tau_f = 60$. Color scheme same as Fig. 6.4 with white dash line showing the aggregate interface.

Figure 5.13 compares the evolution of aggregate breakup using the van der Waals models of Gu et al. [91] and Hamaker [96]. The time-to-breakup and breakup rate are seen to be relatively similar for both values of Ad as k is adjusted using the Gu *et al.* model. However for the original Hamaker model, larger values of k results in significantly larger breakup time when $\mathrm{Ad} = 0.3$, and fails to predict breakup when $\mathrm{Ad} = 3$, which confirms that the particle dynamics are highly sensitive to particle stiffness using the original Hamaker model. Note that although the dependency of k is not removed completely as shown in Fig. 5.11, the sensitivity is relatively small and the model of breakup proposed herein is anticipated to apply generally for dense spherical aggregates.

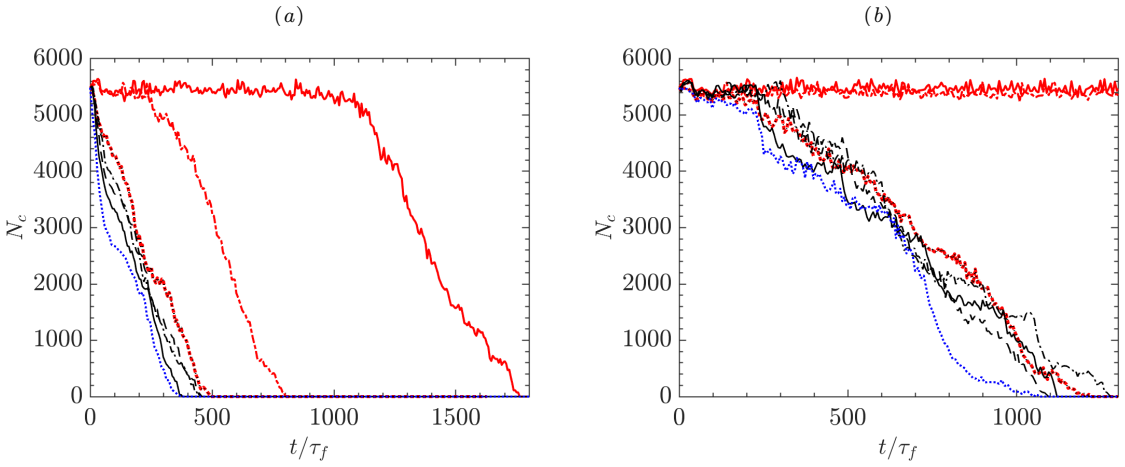

Figure 5.13: Evolution of the number of particles within the aggregate for (a) $\mathrm{Ad} = 0.3$ and (b) $\mathrm{Ad} = 3$ with $\mathrm{Re}_\lambda = 64$. Van der Waals model of Gu *et al.* 2016 (black) and Hamaker 1937 (red) with $k = 10$ $(-)$, 100 $(--)$, 300 $(-\cdot)$ and 7000 $(\cdots)$ N/m. JKR theory (which is independent of k) (blue).

Recall that treating inter-particle collisions and cohesion as additive forces implicitly assumes the surface profile of the particles remain unmodified according to the Derjaguin, Muller and Toporov (DMT) theory [45]. For solid particles in air, this assumption is typically only valid for sub-micron size particles. For larger particles, the Johnson, Kendall and Roberts (JKR) theory might be more appropriate, which assumes that adhesion occurs only within the flattened contact region, and consequently the collision force is

nonlinearly coupled with the adhesion force. The validity of each theory is characterized by the Tabor number (5.2). DMT is most appropriate when $\lambda_T \ll 1$ (typically $\lambda_T \lesssim 0.1$) and the JKR model is valid when $\lambda_T \gg 1$ (typically $\lambda_T \gtrsim 10$). As discussed in § 5.2.1, $0.19 \leq \lambda_T \leq 0.98$, and thus DMT was chosen in the present study. In order to show the applicability of the DMT theory in the cases considered here, the aggregate breakup processes using both theories are compared in Fig. 5.13 for Ad = 0.3 and 3. The DMT theory is analyzed by coupling the soft-sphere collision model with the cohesion model of Gu et al. [91] in addition to the original van der Waals model of Hamaker [96]. The numerical implementation of JKR model is based on Chen et al. [35]. For both values of Ad, the JKR model predicts a slightly larger rate of breakup than the DMT models ($\dot{N}_c\tau_p = 1610$ versus 1523 for Ad = 0.3 and 598 versus 570 for Ad = 3), and the breakup times are in reasonable agreement for all cases ($t_{\mathrm{br}}/\tau_f = 0$ versus 0 for Ad = 0.3 and 220 versus 225 for Ad = 3).

5.5 Conclusions

In the present study, a 'clump' of Geldart C-type particles (e.g. dust or powder in air) was placed in homogeneous isotropic turbulence to study the interplay between turbulence and adhesion on deagglomeration. Numerical simulations were carried out in an Eulerian–Lagrangian framework that resolves particle-particle interactions and models fluid-particle coupling. The adhesion number Ad, Taylor micro-scale Reynolds number Re_λ and nondimensional clump size D/d_p were varied to investigate the breakup criteria and breakup rate of the aggregate.

To fully resolve the wide range of length- and time-scales present in the system, we employed a multi-scale time stepping algorithm that subiterates particles at a smaller time step than the fluid phase. A modified linear-forcing technique was introduced to maintain

statistically stationary turbulence in the presence of particles with two-way coupling. A modified van der Waals model developed for soft-sphere collisions was also adopted to allow for larger simulation time steps while keeping the results insensitive to the choice of particle stiffness. A variance-based sensitivity analysis was performed to quantify the relative importance of the modeling parameters appearing in the particle-phase equations on the time-to-breakup and breakup rate. The simulation results were found to be most sensitive when switching between one-way and two-way coupling. In the absence of two-way coupling, the local flow remains unmodified in the presence of particles, resulting in relatively large interphase slip velocities and consequently instantaneous breakup.

The temporal evolution of the aggregate size and flow visualizations demonstrated that turbulence intermittency plays an important role on the deagglomeration process. It was found that the time rate of breakup is affected substantially by different flow realizations of the same Re_λ. As particles become more cohesive (e.g. $\mathrm{Ad} \geq 3$), a stair-step behavior was observed for the breakup rate due to the presence of large turbulent velocity fluctuations at the vicinity of the aggregate.

The aggregate is shown to breakup progressively into smaller clumps proportional to η. A regime map of fluid stress versus adhesive stress revealed that a critical turbulent Adhesion number, $\mathrm{Ad}_{\eta,\mathrm{crit}} = \gamma/\left(\rho_p u_{\mathrm{rms}}^2 \eta\right) = 1.8$, is capable of predicting the breakup outcome of an aggregate in turbulence. A scaling analysis further demonstrated a linear relation between the time rate of breakup $\dot{N}_c$ and the aggregate Reynolds number Re_D, with a correction due to adhesion $(1 - \mathrm{Ad}_\eta/\mathrm{Ad}_{\eta,\mathrm{crit}})$.

As a direct analog to the Taylor analogy breakup (TAB) model commonly used for droplet breakup in the spray community, the analysis performed herein was used to inform a mass-spring-damper model to predict the breakup time of the aggregate, referred as Granular-TAB (G-TAB). Here, turbulent velocity fluctuations act to deform the ag-

gregate, damped by solid-phase shear stress modeled using a solids viscosity informed by Kinetic theory. The predicted breakup time for a given Ad_η was in good agreement with simulations.

CHAPTER VI

Particle Deposition in Wall-bounded Flows and Uncertainty Quantification

In this chapter, we investigate particle deposition in wall-bounded flows in the presence of electrostatic and van der Waals force. A fully-developed turbulent pipe configuration is considered where the relative importance of cohesive forces are compared using both DNS and a 1D Eulerian model. The uncertainties in deposition due to variations in charge magnitudes and Hamaker constants are quantified using a multi-fidelity approach that optimally manages model evaluations for a given computational budget. Significant speedup is obtained compared to classic Monte Carlo estimation. Both predict charge plays a bigger role in deposition than van der Waals across different particle sizes.

6.1 Introduction

Particles suspended in a fluid are commonly observed to be deposited on solid walls. Measuring, predicting, and understanding the deposition rate are important in many medical [12, 267, 268], environmental [262, 109, 132, 131, 164, 265], and engineering [9, 56, 21, 202, 165, 242, 146, 175, 255] applications. Most of these applications primarily involve Geldart C-type particles for which cohesive forces such as van der Waals attraction and electrostatics become important. Many previous studies provide experimental measurements [137, 73, 210, 257, 211] that classify particle deposition into three distinct regimes

governed by different physics (see Fig. 1.5): (1) turbulent diffusion regime where tiny particles deposit due to turbulent diffusion, (2) diffusion-impaction regime where particles ejected by turbulent eddies directly impact on the wall, and (3) inertia-moderated regime where deposition is moderated as ballistic particles are less responsive to turbulence.

The complex and multi-physical nature of the particle deposition process make the modeling extremely challenging. The most commonly used deposition models, such as free flight [73] and random walk models [84, 116, 44], neglect particle interactions comparing to other effects such as turbulent dispersion or drag. Guha [94] proposed an unified 1D Eulerian model purely derived from conservation laws and compatible with particle forces including Saffman lift, electrostatics, etc. The model predicts the deposition rate for the first two regimes can be amplified by up to two orders of magnitude due to mirror charging at the wall, whereas little effect is observed in the inertia-moderated regime. While incredibly valuable, the model only accounts for particle-wall electrostatic interactions and the particle distribution is assumed to be only a function of wall distance. In reality, however, particle clustering can be significantly modified by particle-particle electrostatic interactions [50, 51, 118]. In addition, particles are known to accumulate along the low-speed streaks, defined as regions of lower-than-mean streamwise velocity [244, 282, 151]. These spatial inhomogeneities can alter particle near-wall deposition and are yet to be fully understood.

Another outstanding modeling challenge is the significant uncertainties associated with cohesive force measurements as well as material properties of tiny particles such as dust. For example, the measurement of the Hamaker constant, which dictates the strength of van der Waals attraction, can span five orders of magnitudes for typical dust particles [249]. It remains an ongoing debate in the literature about how to parametrize and measure cohesive forces accurately [103, 135, 25]. Another key uncertainty of dust in-

gestion in gas turbine engines is the constitution of the ingested particles, which varies significantly with geographic locations [219] or even specific size ranges [217]. These uncertainties are becoming more relevant with aviation growth all round the globe, as well as increasing usage of inertial particle separators for modern helicopter turboshaft engines where large particles are filtered out during engine intakes [41].

As summarized in Table 1.1, particle properties exhibit large variations even at standard atmospheric conditions. There are large uncertainties in particle charge amount and Hamaker constant whose effects on particle deposition models remain elusive, especially when the carrier phase is turbulent. Other effects such as temperature gradients or surface roughness may further amplify these uncertainties [94]. The variations in particulate constitutions, physical properties and flow conditions introduce inevitable measurement errors for experimental deposition studies shown in Fig. 1.5, demonstrating the importance of quantifying how sensitive the particle deposition rate is to these uncertainties. Nevertheless, most of the existing numerical studies consider monodisperse particles with single valued charge [143, 144] and Hamaker constant [103, 99]. Accurately quantifying these uncertainties requires many expensive simulations. Efficient framework for uncertainty quantification and sensitivity analysis is needed to investigate the effects of particle uncertainties on deposition in a tractable manner, which is of prime interest to this work.

Uncertainty quantification typically involves propagating input uncertainties through a system to quantify the distribution of the system outputs, and estimate statistics such as the mean, variance, or sensitivity. It has recently gained popularity in fluid dynamic studies [171, 24, 170, 124]. However, numerical methods for uncertainty propagation are often based on Monte Carlo estimation, which can require large numbers of numerical simulations to obtain estimates with acceptable accuracies [177, 17]. Recently a multi-fidelity Monte Carlo (MFMC) method has been developed that leverages the low-fidelity

models to speed up the uncertainty propagation while guarantees unbiased estimators by occasionally recoursing to the high-fidelity model [179, 180]. The idea is to optimize the work distribution among models of different fidelities such that the error is minimized for a given computational budget. This allows us to efficiently quantify the uncertainties in the particle deposition rate for a given charge, diameter and Hamaker constant of the particle phase. Another advantage of the MFMC framework is that the mean quantity-based optimization admits an analytical solution that can be directly applied for variance and sensitivity estimates as well [190].

In this chapter, analysis of variance-based sensitivity, also known as Sobol indices, is performed for the particle deposition rate in a turbulent pipe flow using the MFMC method. Two deposition models of different fidelities, direct numerical simulations and 1D Eulerian model proposed by Guha [94], are considered to expedite the evaluations. The system configuration, input and output parameters are described in § 6.2. In § 6.3, the relative magnitudes of particles forces are compared. The multi-fidelity framework is introduced in § 6.4, details on modeling approaches are then presented in § 6.5, followed by a comparison of deposition rates predicted by these two models with variations in cohesion strength. Finally, global sensitivity analysis using Sobol indices is discussed in § 6.6 to uncover the relative importance of cohesive forces for three different particle sizes.

6.2 Problem setup – fully-developed pipe configuration

The problem under consideration consists of a cylindrical pipe with inner diameter $D = 20$ mm. The length of the pipe is $L = 10D$ to ensure domain independent results. The pipe is periodic in the streamwise (x) direction. The pipe carries fully-developed turbulent air flow with kinetic viscosity $\nu = 1.5 \times 10^{-5}$ and bulk velocity $U_b = 4.0$ m/s, corresponding to a frictional Reynolds number $\mathrm{Re}_\tau = 180$ and a bulk Reynolds number

Re = 5333. Particles are assumed to be at statistically stationary state where particle mass flux toward the wall is constant in the radial direction. Initial number of particles is set to $N = 10^6$ to ensure enough statistical samples.

To investigate the effect of charge on particle dynamics and deposition, each particle is assigned a unique value q_p that is proportional to the maximum possible charge $q_{\max}$ according to $q_p = \xi q_{\max}$, with $0 \leq \xi \leq 1$. The maximum charge is given by [106]

$$q_{\max} = 500 \times \left(1.6 \times 10^{-19}\right) \left(d_p/10^{-6}\right)^2 . \tag{6.1}$$

In this study, we vary between $\xi = 0$ (no charge) and $\xi = 0.1$, which is representative of charge measurements for common dust particles in turbulent pipe flows [157, 156, 194]. The Hamaker constant A is varied between 10^{-20} J for weakly cohesive particles (e.g. silica) to 10^{-18} J for strongly cohesive materials such as metal oxides [153]. Similarly a non-dimensional parameter $\zeta = A/A_0$ is introduced with $A_0 = 10^{-18}$ J. In this study we consider $0 < \zeta < 1$. The deposition rate is typically characterized using the non-dimensional deposition velocity [116, 240, 155, 151, 184, 282], given by

$$V_{\text{dep}}^{+} \equiv \frac{V_{\text{dep}}}{u_*} = \frac{J_w}{\rho_{pm} u_*} \tag{6.2}$$

where J_w is the particle mass flux to the wall per unit area, ρ_{pm} is the mean particle bulk density in the pipe and $u_* = \sqrt{\tau_w/\rho}$ is the friction velocity with τ_w the wall shear stress. Throughout the rest of this chapter, ζ and ξ are independent random variables used as input parameters, V_{dep}^{+} is the system output or quantity of interest (QoI) for both DNS and 1D Eulerian model. Specifically, uncertainties in the mean, standard deviation, and sensitivity of V_{dep}^{+} will be quantified.

6.3 Particle deposition in a turbulent pipe flow

6.3.1 Relative importance of cohesive forces

Before introducing sensitivity analysis and uncertainty quantifications, it is of prime importance to understand how van der Waals and electrostatic forces compare in terms of magnitudes for wall-bounded systems with different particle loadings. Figure 6.1(a) shows the particle acceleration due to these two forces ($\xi = 0.1$ and $\zeta = 1$) as a function of particle separation distance according to Eq. (2.11) and Eq. (2.41). The van der Waals force is seen to be dominant at short separation ($s < \mathcal{O}(10^{-6})$), but is surpassed by electrostatic forces at longer range. The influence of van der Waals force decays with increasing particle size, whereas the electrostatic force results in higher accelerations for larger particles at long range.

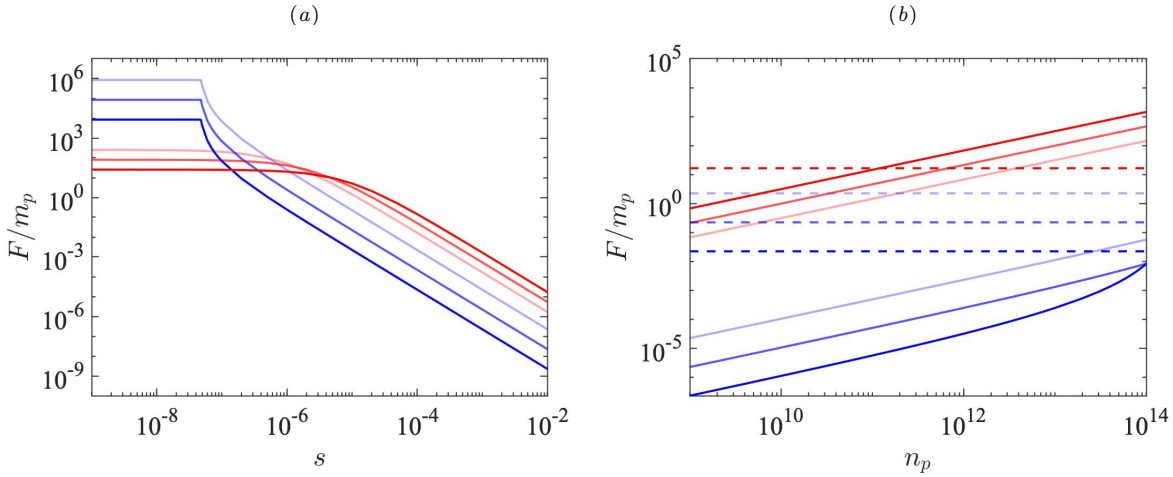

Figure 6.1: Particle acceleration due to electrostatics (−) and van der Waals (−) as a function of (a) separation distance s and (b) particle number density n_p. Larger particles are shown with higher transparency. Particle-wall contributions are shown as dashed lines.

Based on Fig. 6.1(a), the average particle acceleration for a given particle number density n_p can be estimated by assuming random distribution of particles, which gives the average distance between particles $d = (1/n_p)^{1/3}$. Let $F(x)$ denotes the functional forms given by Eq. (2.11) and Eq. (2.41). The domain-averaged particle-particle force

is therefore $F_{\mathrm{p-p}} = F(1/{n_p}^{1/3})$. The domain-averaged particle-wall force is estimated by integrating the force in the radial direction

$$F_{\mathrm{p-w}} = \int_0^{0.5D - r_{\mathrm{cutoff}}} F(x) \frac{8x}{D^2}\, dx, \tag{6.3}$$

where $r_{\mathrm{cutoff}} = s_{\mathrm{min}}$ for van der Waals and $r_{\mathrm{cutoff}} = d_p$ for electrostatics to avoid singularity. The accelerations due to estimated forces are compared in Fig. 6.1(b). It can be seen that domain-averaged particle-particle contributions increase with n_p while particle-wall contributions are insensitive to the particle loading. As a result, the relative importance of these four different forces strongly depends on n_p. For instance, particle-particle electrostatic force surpasses particle-wall image charging when $n_p \gtrsim \mathcal{O}(10^{11})$. Due to the short-range nature of van der Waals, however, the particle-wall contribution is always more dominant than the inter-particle van der Waals attraction. For the system considered herein ($n_p = 1.6 \times 10^{10}$), the relative importance is ranked as particle-wall electrostatics, particle-particle electrostatics, particle-wall van der Waals, and particle-particle van der Waals, which is orders of magnitudes smaller than the former three.

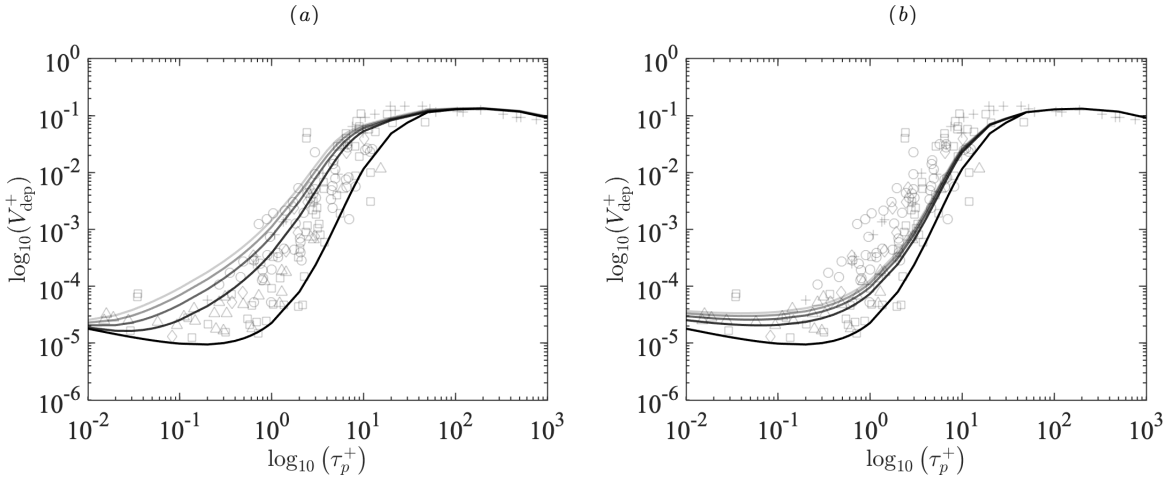

Figure 6.2: Non-dimensional deposition velocities versus the non-dimensional particle response time predicted by the 1D Eulerian model of Guha [94]. (a) Electrostatics due to image charging with $\xi = 0, 0.025, 0.05, 0.075, 0.1$ and (b) van der Waals attraction with $\zeta = 0, 0.25, 0.5, 0.75, 1$. Higher values of ξ and ζ are shown with increasing transparency. Symbols same as Fig. 1.5.

Non-dimensional deposition velocities versus the non-dimensional particle response time predicted by the 1D Eulerian model of Guha [94] are shown in Fig 6.2. For the ranges considered, electrostatic force is seen to have a larger effect on the deposition rate than the van der Waals force across all particles sizes, which is consistent with previous analysis (Fig. 6.1(b)). In addition, the electrostatic force exhibits the largest enhancement for the mid-sized particles (diffusion-impaction regime), for which the charge amount is significant and at the same time particles are most responsive to the turbulent eddies. Van der Waals force, on the other hand, primarily affects the deposition rate of small particles (diffusional deposition regime).

6.3.2 Effect of charge on deposition rate

Previous studies [274, 93, 94] have shown that particle deposition in turbulent pipe flows can be classified into three regimes. For sub-micron particles, Brownian motion dominates and deposition is primarily driven by turbulent diffusion, referred to as the diffusional deposition regime. As the particle size increases, the deposition rate increases dramatically as a result of the interaction between inertial particles and turbulent eddies. This regime is referred to as the diffusion-impaction regime where particles ejected from turbulent eddies directly impact the wall at a relatively high velocity. The third regime is known as the inertia-moderated regime, where particles are so ballistic that the deposition rate decreases with increasing particle size due to their delayed response to turbulence.

In the presence of charge, however, Guha [94] has shown that the deposition rate during the first two regimes can be amplified by up to two orders of magnitude due to mirror charging at the wall alone, while little effect is observed in the inertia-moderated regime. This, along with results from § 3.4, suggest that accurately capturing the pairwise interactions might further enhance the aforementioned effects.

The deposition rate is computed as the non-dimensional deposition velocity V^+_{dep} com-

monly used in Eulerian-Lagrangian studies [116, 240, 155, 151, 184, 282], given by

$$V_{\text{dep}}^{+} = \left(\frac{N_{\text{dep}} D}{4\Delta t \left(N - N_{\text{dep}} \right)} \right) \Big/ u_{*}, \tag{6.4}$$

where N_{dep} is the number of particles deposited on the wall and removed from the original N particle count over a certain time Δt. Note that although the particle statistics do not reach a steady state since they are removed when they hit the wall, a "quasi-equilibrium" state exists where the local particle concentration normalized by the domain-averaged particle concentration no longer varies in the streamwise direction [58]. To this end, ΔN_{dep} is not measured until such "quasi-equilibrium" state is reached such that V_{dep}^{+} is uniquely defined.

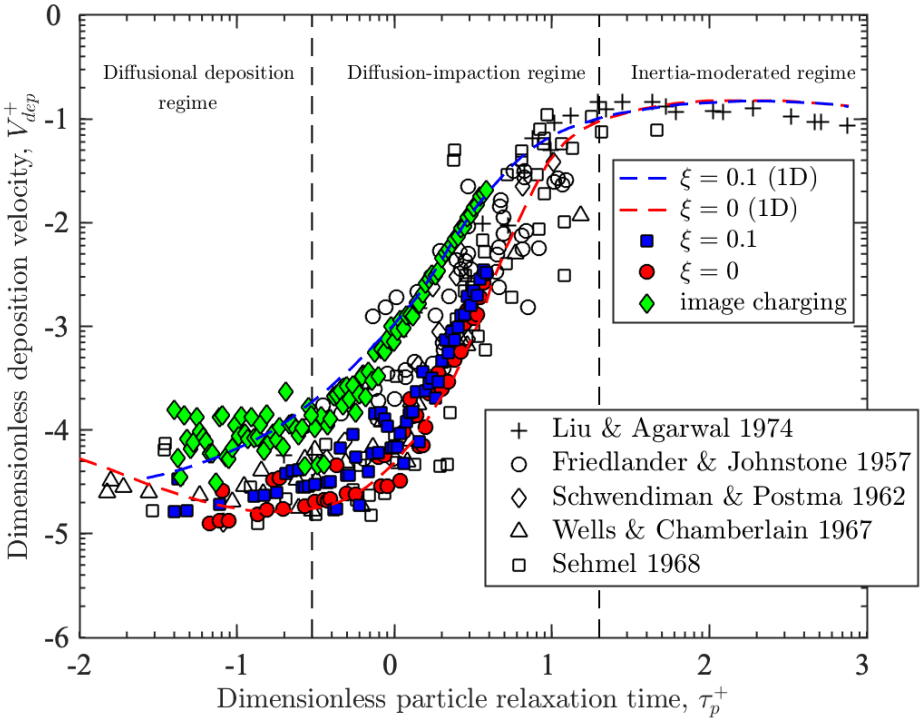

Figure 6.3: Deposition regime diagram that compares experiments (hollow symbols), 1D Eulerian model [94] (dashed lines), and simulation results (solid symbols).

Figure 6.3 shows the deposition regime diagram that compares experiments, a 1D Eulerian model proposed by Guha [94], and the deposition rates computed from the

same setup of periodic pipe flows described in § 3.4. The 1D model treats both the fluid and particle phases in an Eulerian reference frame, and neglects particle-particle interactions. It can be seen that the deposition rates of non-charged and image-charged particles from the simulations are within the range of experiments and also match well with the 1D model. These results reveal that wall image charging at $\xi = 0.1$ significantly enhances particle deposition by approximately an order of magnitude across the spectrum of particle sizes considered. The deposition velocity, in the Eulerian sense, is proportional to the product of particle number density and particle approaching velocity at the wall ($V_{\text{dep}} \sim n_p u_r^+$) [274]. Although the peak n_p of the charged case is four times smaller than the uncharged case as shown in Fig. 3.13, u_r^+ is almost two orders of magnitudes larger than the uncharged case as shown in Fig. 3.11. Therefore, the resulting V_{dep} is still amplified by charge by about one order of magnitude.

The deposition rate at $\xi = 0.1$ without image charging, however, is only marginally higher than the non-charged case, indicating that the electrostatic effect of particle-wall interactions is more important than particle-particle interactions in terms of deposition rate. One reason can be that particle clustering due to electrostatics is not significant at the low particle concentration considered in this study. Nevertheless, particle-particle interactions do have an effect on the deposition rate and other near-wall particle statistics discussed in § 3.4, and is anticipated to be more important for systems with larger particle charge or higher particle concentrations as evidenced by Fig. 6.1(b). In addition, the notable change in deposition rate for $\xi = 0.1$ further motivates the need to quantify the uncertainties in V_{dep}^+ when varying ξ and ζ simultaneously. Accurately quantifying the mean, variance, and sensitivity of V_{dep}^+ requires many expensive DNS simulations. The agreement between DNS and 1D model predictions encourages us to explore the possibility of leveraging both models to expedite this process in the following sections.

6.4 Multi-fidelity uncertainty quantification

Uncertainty quantification is propagating input uncertainties through a system of interest to quantify the uncertainties' effects on the system outputs. However, numerical methods for uncertainty propagation are often based on Monte Carlo (MC) estimation, which can require large numbers of numerical simulations to obtain estimates with acceptable accuracies. In this study, we will employ a multi-fidelity Monte Carlo (MFMC) method, which optimizes the work distribution among models of different fidelities such that the error is minimized for a given computational budget [179, 180]. The MFMC method leverages the low-fidelity models to speed up the uncertainty propagation while guarantees unbiased estimators by occasionally recoursing to the high-fidelity model.

6.4.1 Uncertainty propagation with Monte Carlo estimation

Consider our turbulent pipe DNS simulation as a high-fidelity model given as

$$f^{(1)} : \mathcal{X} \to \mathcal{Y} \tag{6.5}$$

where $\boldsymbol{x} \in \mathcal{X}$ is the input and $y = f^{(1)}(\boldsymbol{x}) \in \mathcal{Y}$ is the output. In our case, the input parameters $\xi \in [0, 0.1]$ and $\zeta \in [0, 1]$ are considered to be a random variable X. The output $y = V^{+}_{\text{dep}} = f^{(1)}(X)$. Our goal is to estimate statistics of $f^{(1)}(X)$ for the high-fidelity model $f^{(1)}$ and a given input random variable X. In the following, we restrict the discussion to estimating the expected value but will show later that this strategy generally applies to other statistical metrics. Consider a system whose output has an expected value s:

$$s = \mathbb{E}[f^{(1)}(X)]. \tag{6.6}$$

A Monte Carlo estimator of the expected value s of $f^{(1)}(X)$ is the average of m realizations of X $(\boldsymbol{x}_1, \ldots, \boldsymbol{x}_m)$

$$\overline{y}_m = \frac{1}{m} \sum_{i=1}^{m} f^{(1)}(\boldsymbol{x}_i) \tag{6.7}$$

The Monte Carlo estimator $\overline{y}_m$ is an unbiased estimator of s in terms of expectation

$$\mathbb{E}[\overline{y}_m] = s \tag{6.8}$$

We are interested in minimizing the mean-squared error (MSE) of $\overline{y}_m$ defined as

$$e(\overline{y}_m) = \mathbb{E}\left[(\overline{y}_m - s)^2\right] = \frac{\mathrm{Var}[f^{(1)}(X)]}{m} \tag{6.9}$$

The computational cost of the Monte Carlo estimator $\overline{y}_m$ is therefore

$$c(\overline{y}_m) = wm \tag{6.10}$$

where w is the cost of each high-fidelity evaluation. Depending on the variance $\mathrm{Var}[f^{(1)}(X)]$ of the output random variable, a large number of high-fidelity model evaluations can be necessary to obtain a Monte Carlo estimate of s with an acceptable MSE. If the high-fidelity model is expensive to evaluate, then Monte Carlo estimation will become computationally intractable.

6.4.2 Multi-fidelity Monte Carlo estimation for uncertainty propagation

Multi-fidelity Monte Carlo (MFMC) estimation makes use of low-fidelity models to speed up the uncertainty quantification process, it optimizes the number of evaluations on each model for a given computational budget in order to minimize the total MSE. Suppose we have k models of different level of fidelity $f^{(1)}, \ldots, f^{(k)}$, each one evaluated

m_k times ($0 < m_1 \leq m_2 \leq \cdots \leq m_k$), then their Monte Carlo estimators are defined as

$$\overline{y}_{m_1} = \frac{1}{m_1} \sum_{j=1}^{m} f^{(1)}\left(\boldsymbol{x}_j\right), \quad \overline{y}_{m_i}^{(i)} = \frac{1}{m_i} \sum_{j=1}^{m_i} f^{(i)}\left(\boldsymbol{x}_j\right), \quad \overline{y}_{m_{i-1}}^{(i)} = \frac{1}{m_{i-1}} \sum_{j=1}^{m_{i-1}} f^{(i)}\left(\boldsymbol{x}_j\right) \tag{6.11}$$

The MFMC estimator is defined as a linear combination of the Monte Carlo estimators

$$\hat{s} = \overline{y}_{m_1} + \sum_{i=2}^{k} \alpha_i \left(\overline{y}_{m_i}^{(i)} - \overline{y}_{m_{i-1}}^{(i)}\right) \tag{6.12}$$

The goal of the MFMC method is to find the optimal set of coefficients α_i and number of evaluations m_i at a given computational budget p such that the total cost

$$c(\hat{s}) = \sum_{i=1}^{k} m_i w_i \leq p, \tag{6.13}$$

where w_i is the cost of model $f^{(i)}$. The optimization requires the correlation coefficients between the low-fidelity models and the high-fidelity model given by

$$\rho_{1,i} = \frac{\operatorname{Cov}\left[f^{(1)}(X), f^{(i)}(X)\right]}{\sqrt{\operatorname{Var}\left[f^{(1)}(X)\right] \operatorname{Var}\left[f^{(i)}(X)\right]}}, \quad i = 2, \ldots, k \tag{6.14}$$

Then an analytical solution of this optimization yields for $i = 2, \ldots, k$

$$\alpha_i^* = \frac{\rho_{1,i}\sigma_1}{\sigma_i} \tag{6.15}$$

$$r_i^* = \sqrt{\frac{w_1\left(\rho_{1,i}^2 - \rho_{1,i+1}^2\right)}{w_i\left(1 - \rho_{1,2}^2\right)}} \tag{6.16}$$

$$m_i^* = m_1^* r_i^* \tag{6.17}$$

where $m_1^* = p/(\boldsymbol{w}^T \boldsymbol{r}^*)$ and $\sigma_i = \sqrt{\mathrm{Var}\left[f^{(i)}(X)\right]}$ is the standard deviation of model $f^{(i)}$. A mild precondition on the model costs is required for this analytical solution to exist:

$$\frac{w_{i-1}}{w_i} > \frac{\rho_{1,i-1}^2 - \rho_{1,i}^2}{\rho_{1,i}^2 - \rho_{1,i+1}^2} \tag{6.18}$$

for $i = 2, \ldots, k$ with $\rho_{1,k+1} = 1$. We will show in § 6.6 that Eq. (6.18) can be easily satisfied for our purposes.

6.4.3 Multi-fidelity Monte Carlo estimation for global sensitivity analysis

One of the most popular way of measuring sensitivity is known as the variance-based sensitivity analysis, also referred to as the Sobol method or Sobol indices [218, 205]. It provides a quantitative measure of how uncertainty in a model input contributes to uncertainty in the model output. A direct measure of sensitivity based on variance information is commonly referred to as main-effect index, which for input i is defined as

$$s_i \equiv \frac{V_i}{\mathrm{Var}(Y)} = \frac{\mathrm{Var}_{X_i}\left(E_{\mathbf{X}_{\sim i}}\left(Y \mid X_i\right)\right)}{\mathrm{Var}(Y)}, \tag{6.19}$$

where Y is the output (QoI), $\mathbf{X}$ is a vector of all input parameters, $\mathbf{X}_{\sim i}$ denotes the set of all input variables except X_i. Higher-order interaction indices s_{ij}, s_{ijk} and so on can be formed using variance caused by several inputs combined. Therefore, when the number of variables is large, the number of model evaluations increase exponentially. To this end, the total-effect index can be used to measure the contribution to the output variance of X_i, including all variance caused by its interactions with any other input variables, given by

$$s_i^t \equiv \frac{T_i}{\mathrm{Var}(Y)} = \frac{E_{\mathbf{X}_{\sim i}}\left(\mathrm{Var}_{X_i}\left(Y \mid \mathbf{X}_{\sim i}\right)\right)}{\mathrm{Var}(Y)} \tag{6.20}$$

However, Sobol index is typically evaluated using Monte Carlo estimation which is computationally intractable when the models are expensive or the parameter space is large.

Similar to the MFMC estimator defined for the model output (Eq. (6.12)), a MFMC estimator of the Sobol index is given by Qian et al. [190] as $s_i = \hat{V}_{i,\mathrm{mf}}/\mathrm{Var}(Y)$ and $s_i^t = \hat{T}_{i,\mathrm{mf}}/\mathrm{Var}(Y)$, where

$$\hat{V}_{i,\mathrm{mf}} = \hat{V}_{i,m_1}^{(1)} + \sum_{j=2}^{k} \alpha_j \left(\hat{V}_{i,m_j}^{(j)} - \hat{V}_{i,m_{j-1}}^{(j)} \right) \tag{6.21}$$

and

$$\hat{T}_{i,\mathrm{mf}} = \hat{T}_{i,m_1}^{(1)} + \sum_{j=2}^{k} \alpha_j \left(\hat{T}_{i,m_j}^{(j)} - \hat{T}_{i,m_{j-1}}^{(j)} \right). \tag{6.22}$$

Here, an unbiased Monte Carlo estimator of V_i and T_i proposed by Owen [174] is used given as

$$\hat{V}_i = \frac{2m}{2m-1} \left(\frac{1}{m} \sum_{j=1}^{m} f\left(\boldsymbol{x}_j\right) f\left(y_j^{(i)}\right) - \left(\frac{\hat{E} + \hat{E}'}{2} \right)^2 + \frac{\hat{V} + \hat{V}'}{4m} \right) \tag{6.23}$$

and

$$\hat{T}_i = \frac{1}{2m} \sum_{j=1}^{m} \left(f\left(\boldsymbol{x}_j'\right) - f\left(y_j^{(i)}\right) \right)^2, \tag{6.24}$$

where $\hat{E}$, $\hat{E}'$ and $\hat{V}$, $\hat{V}'$are the sample means and variances estimated using two sets of m independent realizations of input X respectively ($\boldsymbol{x}_1, \ldots, \boldsymbol{x}_m$ and $\boldsymbol{x}_1', \ldots, \boldsymbol{x}_m'$).

Although the MFMC estimators of the Sobol indices are formulated differently with the MFMC estimator of the mean QoI described in § 6.4.2, Qian et al. [190] have shown that the same optimization procedures (Eq. (6.15)–(6.17)) can be used to estimate the variance and Sobol indices without sacrificing the performance of the algorithm.

6.5 Modeling approaches

For our current deposition study, two models of different fidelity are considered ($k = 2$): direct numerical simulation coupled with Lagrangian particle tracking as high-fidelity

model $f^{(1)}$, and 1D Eulerian model proposed by Guha [94] as low-fidelity model $f^{(2)}$. Details of each model are described in the following.

6.5.1 High-fidelity model – 3D DNS simulations

Direct numerical simulations for particle-laden pipe are performed in the Euler-Lagrangian framework described in Chapter II. The domain is discretized on a Cartesian mesh of size $326 \times 256 \times 256$. A conservative cut-cell immersed boundary method is employed to to enforce no-slip and no-penetration boundary conditions in the fluid phase at the pipe wall. Details can be found in as described in Pepiot and Desjardins [181] and Meyer et al. [163]. The grid spacing is chosen such that $\Delta y^+ = \Delta z^+ = 1.25$ and $\Delta x^+ = 9.8$ to fully resolve the turbulent flow (see Appendix B), where '$^+$' denotes the dimensionless wall distance defined as $(\cdot)^+ = u_* (\cdot) / \nu$, where $u_* = \sqrt{\tau_w / \rho}$ is the friction velocity with τ_w the wall shear stress and ρ the fluid density.

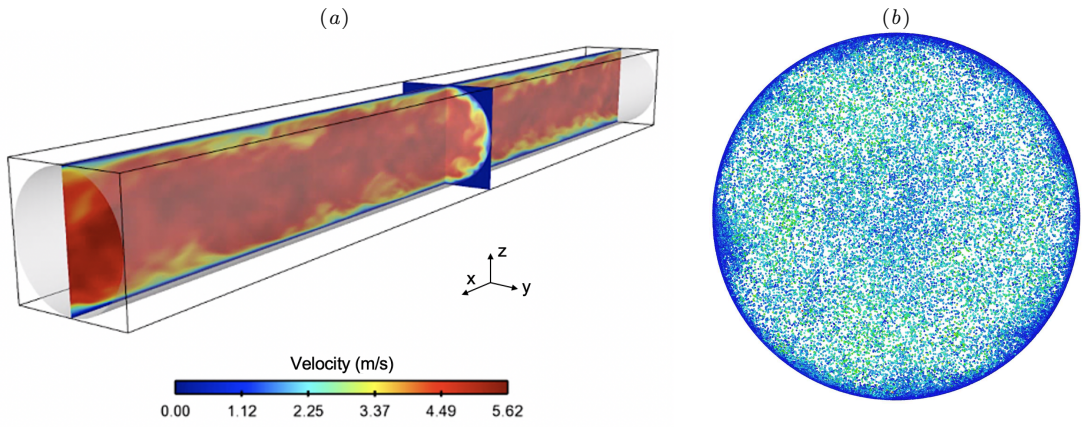

Figure 6.4: Schematic of the turbulent pipe flow with aspect ratio $L/D = 10$ and periodicity enforced in the streamwise (x) direction. (a) The pipe wall is shown as an iso-surface of $\psi = 0$. Color represents the instantaneous fluid velocity magnitude at a statistically stationary state. (b) Particle distribution colored by radial velocity (blue: 0, red: 1 m/s) for $\tau_p^+ = 10$ at a statistically stationary state.

Particles are introduced into the flow once a statistically stationarity is reached. Monodisperse spherical particles of three different diameters $d_p = 1.6$ µm, 5 µm and 16 µm and density $\rho_p = 2650$ kg/m^3 are considered, with initial number of particles $N = 10^6$. The

maximum particle volume fraction is below 3.4×10^{-5} so that one-way coupling assumption is valid. Particle inertia is characterized by a non-dimensional particle response time $\tau_p^+ = \tau_p/\tau_f$, where $\tau_p = \rho_p d_p^2/(18\rho\nu)$ is the particle response time and $\tau_f = \nu/u_*^2$ is the frictional time scale. The three particle sizes correspond to $\tau_p^+ = 0.1, 1, \text{and } 10$ respectively. Particle cohesion is turned on and deposition rates (V_{dep}^+) are measured after the simulation is run for $240\, D/U_b$, at which the particle distribution reaches a statistically stationary state (see Fig. 6.4(b)). Particles are removed from the simulation after impact with the wall.

6.5.2 Low-fidelity model – 1D Eulerian deposition model

Guha (1997) has established, by deriving from the fundamental Eulerian conservation equations of mass and momentum for the particles, a unified advection-diffusion theory in which turbophoresis arises naturally. The theory includes molecular and turbulent diffusion, thermophoresis, shear-induced lift force, electrical forces, and gravity. The predicted deposition rates by this one-dimensional model have been shown to be comparable to Lagrangian calculations in § 6.3.2 and is therefore ideal for multi-fidelity uncertainty quantification. Here we present a model formulation based on Guha [93] while incorporating boundary conditions derived from kinetic theory [274]. The model is also modified to include additional source terms due to cohesion in the momentum equation.

The model consider non-dimensionalized deposition velocity and particle response time defined as

$$V_{\text{dep}}^+ \equiv \frac{V_{\text{dep}}}{u_*} = \frac{J_w}{\rho_{pm} u_*} \tag{6.25}$$

$$\tau_p^+ \equiv \frac{\tau_p u_*^2}{\nu} = \frac{1}{18}\left(\frac{\rho_p^0}{\rho}\right)\frac{d_p^2 u_*^2}{\nu^2} \tag{6.26}$$

where J_w is the particle mass flux to the wall per unit area, ρ_{pm} is the mean particle density in the pipe, and ρ_p^0 is the particle material density.

The non-dimensionalized particle momentum and continuity equations are given by

$$\overline{V}_{py}^{+}\frac{\partial \overline{V}_{py}^{+}}{\partial y^{+}} + \frac{\overline{V}_{py}^{+}}{\tau_1^{+}} = -\frac{\partial}{\partial y^{+}}(\mathfrak{R}\overline{V_{fy}'^{+2}}) \tag{6.27}$$

$$\partial V_{dep}^{+}/\partial y^{+} = 0, \quad V_{dep}^{+} = -\left(\frac{D_{\mathrm{B}}}{\nu} + \frac{\varepsilon}{\nu}\right)\frac{\partial \rho_p^{+}}{\partial y^{+}} - \rho_p^{+} D_{\mathrm{T}}^{+}\frac{\partial \ln T}{\partial y^{+}} + \rho_p^{+}\overline{V}_{py}^{+} \tag{6.28}$$

where $\overline{V}_{py}^{+} = \overline{V}_{py}/u_*$, $\rho_p^{+} = \overline{\rho}_p/\rho_{p_0}$, $V_{fy}'^{+} = V_{fy}'/u_*$, $D_T^{+} = D_T/\nu$. Here $y^{+} = y\,u_*/\nu$ is the dimensionless wall unit and ρ_{p_0} is the particle density at the pipe centerline. Equations are solved numerically with grid refinement close to wall, the drag term is treated implicitly to assure numerical stability. The boundary condition is derived from kinetic theory by Young and Leeming [274]

$$-\left(\frac{D_{\mathrm{B}}}{\nu} + \frac{\varepsilon}{\nu}\right)\frac{\partial \rho_{p_w}^{+}}{\partial y^{+}} = \rho_{p_w}^{+}\overline{V}_{py}^{+}\left(\frac{\exp\left(-M_r^2\right)}{2\sqrt{\pi}M_r} - \frac{1-\mathrm{erf}(M_r)}{2}\right) \tag{6.29}$$

where ρ_{p_w} is the particle density at the pipe wall. Details on the empirical closures for $\mathfrak{R}$, V_{fy}', D_B, D_T, ε are described in Guha [93, 94].

In the presence of van der Waals and electrostatic forces, the Reynolds-averaged particle momentum equations (Eq. (6.27)) is modified to include these two additional source terms given as

$$\overline{V}_{py}^{+}\frac{\partial \overline{V}_{py}^{+}}{\partial y^{+}} + \frac{\overline{V}_{py}^{+}}{\tau_1^{+}} = -\frac{\partial}{\partial y^{+}}(\mathfrak{R}\overline{V_{fy}'^{+2}}) + F_{\mathrm{elec}}^{+} + F_{\mathrm{vdw}}^{+}, \tag{6.30}$$

where the electrostatic force and van der Waals force are non-dimensionalized as $F_{\mathrm{elec}}^{+} = F_{\mathrm{elec}}\,\nu/u_*^3$ and $F_{\mathrm{vdw}}^{+} = F_{\mathrm{vdw}}\,\nu/u_*^3$ respectively. The charged particle is assumed to experience an attractive force due to induced charges on the wall, which is modeled as image

charging given as

$$F_{\text{elec}} = -\frac{3q_p^2}{8\pi^2\varepsilon_0\rho_{\text{p}}^0\, d_p^3\, y^2}. \tag{6.31}$$

The van der Waals force between a spherical particle and wall is given as

$$F_{\text{vdw}} = -\frac{A\, d_p}{12m_p\,(y - 0.5d_p)^2}. \tag{6.32}$$

Note that when particles are in contact with the wall, $y = 0.5d_p$ and F_{vdw} becomes infinity. To avoid this singularity, a cutoff distance 10^{-12} m is used when solving Eq. (6.30) numerically, which was found to be the maximum value that was insensitive to the predicted deposition rates.

6.5.3 A comparison of high- and low-fidelity models

A hundred simulation runs are performed for both high- and low-fidelity models by uniformly sampling the parameter space shown in Fig. 6.5. Three particle sizes ($\tau_p^+ = 0.1, 1, \text{and } 10$) are considered from each deposition regime.

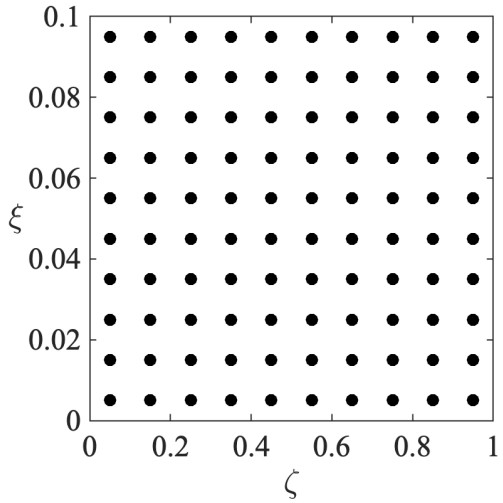

Figure 6.5: Uniform sampling of 100 pairs of input parameters (ζ, ξ) in range $\zeta \in (0, 1)$ and $\xi \in (0, 0.1)$.

The deposition rates from DNS simulations are measured from the rates at which the number of deposited particles N_{dep} increases in time. As shown in Fig. 6.6(a)-6.6(c), N_{dep}

evolves linearly in time after a short initial transient ($t/\tau_f < 10$), beyond which the deposition rate can be uniquely determined. The van der Waals is seen to have comparable effects on the deposition rate to the electrostatic force for smallest particles ($\tau_p^+ = 0.1$), resulting in a wide spread of the deposition curves. However as the electrostatic contribution quickly surpasses the van der Waals for larger particles, the variation in van der Waals strength (ζ) exhibits little effect on the deposition unless when ξ is close to zero.

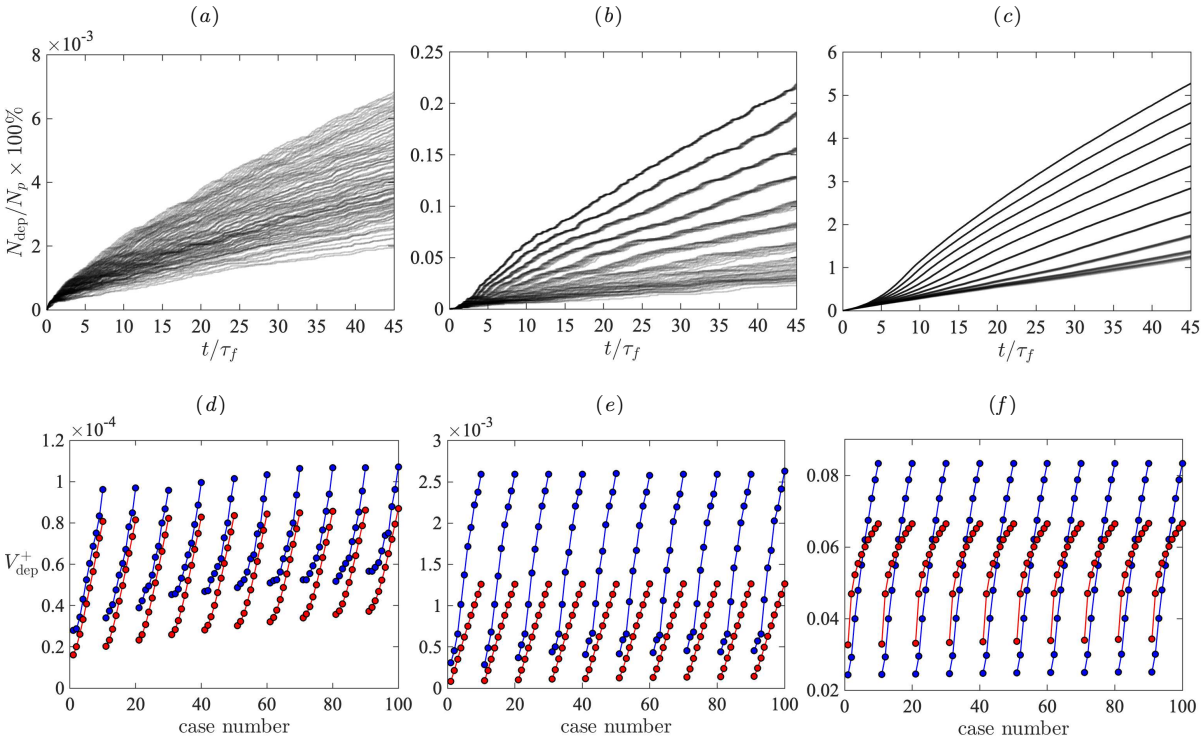

Figure 6.6: (a)-(c) Temporal evolution of total particles deposited in percentage from 100 DNS simulations, with lines shown in transparency. The slopes are used to determine the deposition rates. (d)-(f) Non-dimensional deposition velocities predicted by DNS simulations (−●−) and the 1D Eulerian model (−●−) for 100 runs. Each line spans the range of ξ with increasing ζ from left to right.

The computed deposition rate in terms of non-dimensional deposition velocity V^+_{dep} is then compared with the 1D Eulerian model predictions in Fig. 6.6(d)-6.6(f). The 1D model is seen to under-predict V^+_{dep} for all three particle sizes, especially for mid-size particles for which clustering due to turbulence is expected to be the most significant. Recall that the 1D model only accounts for particle-wall interactions and the particle

distribution is assumed to be only a function of wall distance, spatial inhomogeneities due to preferential concentration and low-speed streak regions along the wall are neglected. However, these inhomogeneities amplify particle-particle interactions and collision rates, which may potentially contribute particle deposition. Nevertheless, the general trends of V_{dep}^{+} predicted by the 1D model and 3D DNS are in decent agreement, which results in a high correlation coefficient (ρ_{12}) that is essential for the MFMC sensitivity analysis presented in the following section.

6.6 Uncertainty quantification and sensitivity analysis of the deposition rate

The model prediction results from both models are then leveraged to estimate the global sensitivity of the deposition rate in terms of main-effect Sobol indices. The goal is to minimize variance of predicted Sobol indices for a given computational budget p, or equivalently, use minimal computational resource to achieve certain error requirements. The computational costs, model statistics and correlations are tabulated in Table. 6.1. For demonstration purpose, these model statistics are computed using all 100 runs before

τ_p^+	Model	μ_k	σ_k	ρ_{1k}	w_k
0.1	$f^{(1)}$ = DNS	6.73×10^{-5}	1.91×10^{-5}	1	1
	$f^{(2)}$ = 1D Eulerian	5.28×10^{-5}	1.88×10^{-5}	0.989	1/2880
1	$f^{(1)}$ = DNS	1.52×10^{-3}	7.63×10^{-4}	1	1
	$f^{(2)}$ = 1D Eulerian	7.02×10^{-4}	3.72×10^{-4}	0.995	1/2880
10	$f^{(1)}$ = DNS	5.74×10^{-2}	1.96×10^{-2}	1	1
	$f^{(2)}$ = 1D Eulerian	5.68×10^{-2}	1.01×10^{-2}	0.937	1/2880

Table 6.1: Prior estimates of V_{dep}^{+} mean (μ_k), standard deviation (σ_k), correlation coefficients (ρ_{1k}), and model costs (w_k) used for multi-fidelity sensitivity analysis for three different particle sizes.

being fed into the multi-fidelity optimization (Eq. (6.15)-(6.17)). Note that in practice, however, a pilot run with a small number of input samples is needed to estimate these statistics. Peherstorfer et al. [179] has demonstrated that the model arrangements are insensitive to the these prior estimates of model statistics. Furthermore, data from pilot

runs can be reused when evaluating variances or sensitivities of QoIs and therefore results in no additional cost. Unlike mean or variance estimates, Sobol index estimates require $(d+2)$ model evaluations for each Monte Carlo sample, an effective budget $p_{\text{eff}} = p/(d+2)$ introduced by Qian et al. [190] is used for the optimization instead of p.

The computational budget is measured in terms of CPU hours and is normalized such that the cost of one well-converged DNS run is unity, which is estimated to be 256 CPU hours. The average cost of each 1D model is only 1/2880. As shown in Table 6.1, the mean (μ_k) and standard deviation (σ_k) of V_{dep}^+ are comparable between these two models, resulting in high correlation coefficients (ρ_{12}) for all three cases. It is interesting to note that the ρ_{12} for $\tau_p^+ = 1$ is the highest despite relatively large discrepancy between its DNS and 1D model statistics. This is because by definition, ρ_{12} only reflects the similarity of model prediction trends and is agnostic to the absolute values of mean or standard deviation. Difference in these model statistics is later compensated by the control variate coefficients α_k.

It is important to note that the multi-fidelity approach is not guaranteed to work for any models of any correlations. To assess the performance of an estimator, the mean-squared error (MSE) is typically used, which is defined as

$$\text{MSE}\left(\hat{s}\right) = \frac{1}{m}\sum_{i=1}^{m}\left(s_i - \hat{s}\right)^2, \tag{6.33}$$

where s_i and $\hat{s}$ are the observed values and estimator prediction respectively. In the case of two models, Peherstorfer et al. [179] derived an analytical estimate of the variance reduction achieved by the MFMC estimator compared to the classic MC estimator given as

$$\gamma \equiv \frac{\text{MSE}\left(\hat{s}_{\text{mf}}\right)}{\text{MSE}\left(\hat{s}_{\text{mc}}\right)} = \left(\sqrt{1-\rho_{12}^2} + \rho_{12}\sqrt{w_2/w_1}\right)^2 \tag{6.34}$$

where γ is the variance reduction ratio, $\hat{s}_{\text{mf}}$ and $\hat{s}_{\text{mc}}$ denote the MFMC estimator and the classic MC estimator respectively.

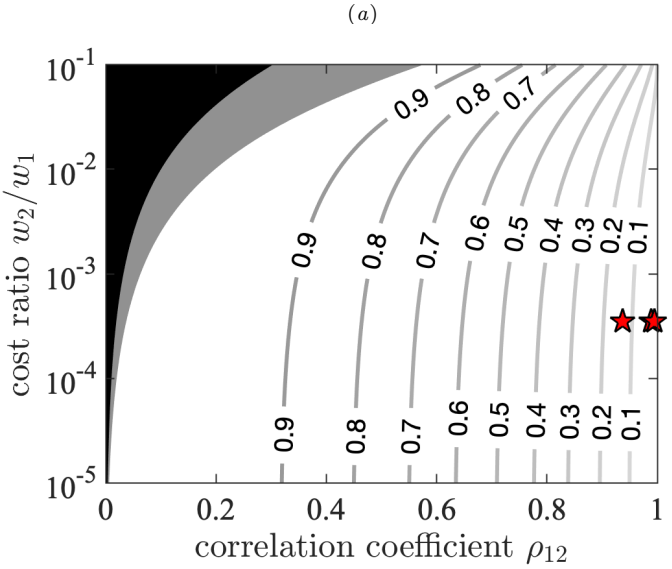

Figure 6.7: Contours of variance reduction ratio γ as a function of model cost ratio w_2/w_1 and correlation coefficient ρ_{12}. The black region shows where the precondition (Eq. (6.18)) is violated. The gray region represents where the MFMC estimators fail to reduce the variance of our QoIs compared to classic MC (i.e., $\gamma > 1$). $\gamma = 0.028, 0.014$, and 0.135 for $\tau_p^+ = 0.1, 1$, and 10 respectively, shown here as pentagrams.

Figure 6.7 shows the contour plot of γ for $\rho_{12} \in [0, 1]$ and $w_2/w_1 \in [10^{-5}, 10^{-1}]$. The multi-fidelity approach fails when $\gamma > 1$ or the precondition (Eq. (6.18)) is not met. However, it only happens for extreme cases, either highly uncorrelated models (e.g., $\rho_{12} < 0.3$) or expensive low-order models (e.g., $w_2/w_1 > 10^{-2}$). The values in Table 6.1 yield $\gamma = 0.028, 0.014$, and 0.135 for $\tau_p^+ = 0.1, 1$, and 10 respectively, confirming that the MFMC estimator will significantly improve MSE using these two models.

Using these model statistics, the effective budget p_{eff} is then distributed among our two models of consideration. Table. 6.2 summarizes the number of evaluations m_k and the control variate coefficients α_k assigned by the multi-fidelity approach for $p = 36$ and 72. The same set of m_k and α_k is then used to estimate the mean, variance, and sensitivity indices. As is expected, more evaluations are done for the 1D model when it is better correlated with the DNS predictions (e.g., $\tau_p^+ = 1$), and a higher coefficient α_k is required

when the 1D model under-predicts σ_k (e.g., $\tau_p^+ = 1$ and 10). The classic MC method using only high-fidelity (DNS) and only low-fidelity (1D Eulerian) models are also included here for later comparisons.

τ_p^+	Model	MC ($p = 36$)		MF ($p = 36$)		MC ($p = 72$)		MF ($p = 72$)	
		m_k		m_k	α_k	m_k		m_k	α_k
0.1	$f^{(1)}$	9	–	8	1	18	–	16	1
	$f^{(2)}$	–	25920	2861	1.005	–	51840	5488	1.005
1	$f^{(1)}$	9	–	7	1	18	–	15	1
	$f^{(2)}$	–	25920	3932	2.040	–	51840	7726	2.040
10	$f^{(1)}$	9	–	8	1	18	–	17	1
	$f^{(2)}$	–	25920	1237	1.816	–	51840	2487	1.816

Table 6.2: Number of evaluations m_k and control variate coefficients α_k per model for MC and MF approaches with a given computational budget of $p = 36$ and $p = 72$.

Figure 6.8 quantifies the uncertainties in mean and standard deviation of V_{dep}^+ predicted by MC estimators (using only DNS or 1D models) and multi-fidelity approach with same budget $p = 72$. Data statistics of 100 estimate replicates are shown as box plots in which the central mark indicates the median, and the bottom and top edges of the box mark the 25th and 75th percentiles, respectively. The whiskers extend to the lower and upper bounds of the dataset. The MF estimators admit notably smaller variances in the both predicted mean and standard deviation compared to the high-fidelity MC estimators. Although the variance predicted by low-fidelity MC estimator is the smallest due to a larger number of evaluations, it suffers inevitable bias embedded in the model itself and therefore deviates from the "true" solutions, which is taken from a well-converged MC estimates using $p = 50000$ by randomly sampling from 100 DNS data.

The distribution of mean and standard deviation estimates from 100 replicates of MFMC and MC estimators are shown in Fig. 6.9 for $p = 72$ and $\tau_p^+ = 0.1$ as an example. The variations in both mean and standard deviation are significantly reduced using the multi-fidelity approach as indicated by the narrower distributions. The distribution is not noticeably skewed which makes standard deviation a sufficient statistical metric. Similar

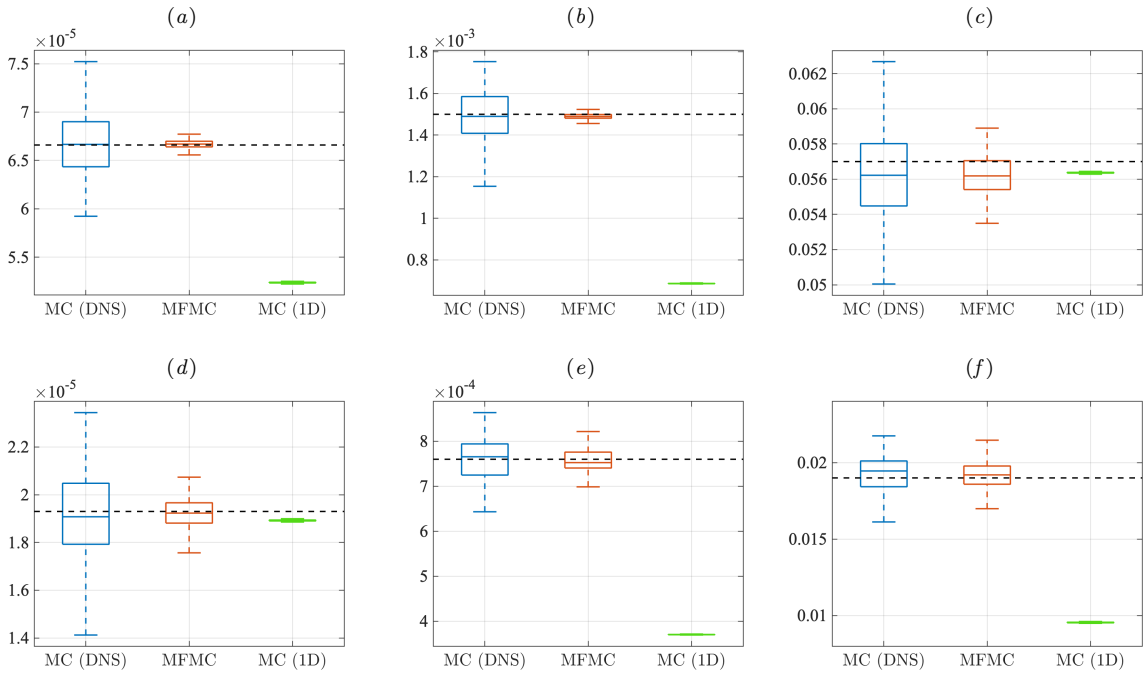

Figure 6.8: Box plots of 100 mean (top) and standard deviation (bottom) estimate replicates for V_{dep}^{+} with $\tau_p^{+} = 0.1, 1,$ and 1 from left to right. Predictions from DNS only, multi-fidelity approach, and 1D model only are shown in blue, red, and green respectively. Results reported for same budget $p = 72$. Dashed line represents "true" values from well-converged estimates.

reduction in estimator variations is observed for other particle sizes and computational budgets considered in Fig. 6.8. Note here the MFMC estimator is not biased toward the low-fidelity model for which the expected values of these statistics are different from DNS.

Figure 6.10 presents the estimated global sensitivity of V_{dep}^{+} using both high-fidelity MC and the MFMC estimators. Data statistics of 100 estimate replicates are shown as box plots. Similar to the mean and standard deviation, the MF estimators admit smaller variance in the predicted Sobol indices compared to the classic MC estimators, allowing definitive ranking of input parameters (i.e., ζ and ξ) with $p = 36$, while Monte Carlo barely achieves this at $p = 72$. For instance, the variation in MF s_m^1 with $p = 36$ is smaller than MC s_m^1 with a higher budget $p = 72$ across all three particle sizes.

To more quantitatively assess the benefit of multi-fidelity method, the estimated MSE is plotted in Fig. 6.11 using MFMC estimator, MC estimator with only DNS, and MC

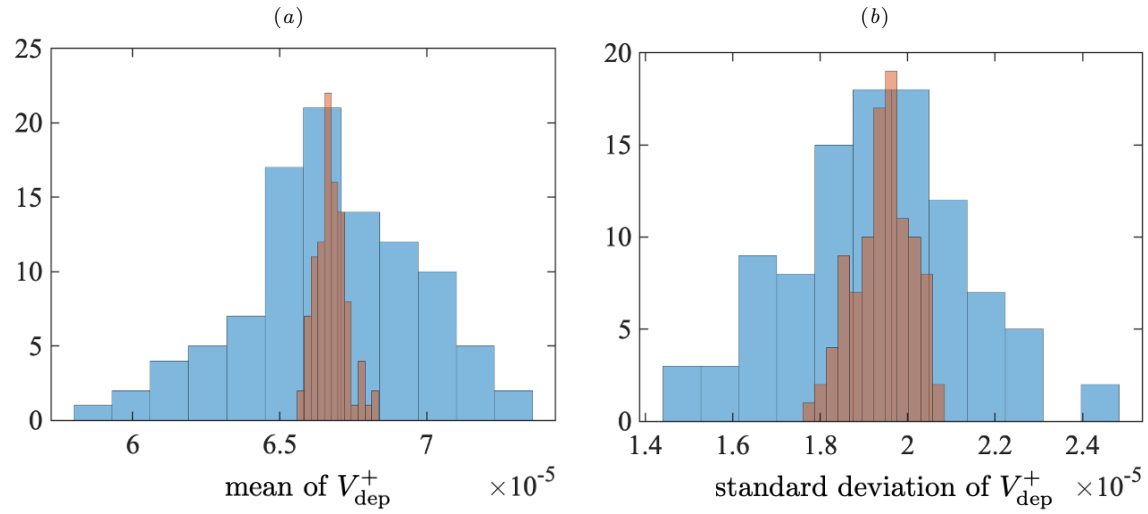

Figure 6.9: Distribution of (a) mean and (b) standard deviation predicted by 100 replicates of MFMC (red) and MC (blue) estimators with $p = 72$ and $\tau_p^+ = 0.1$.

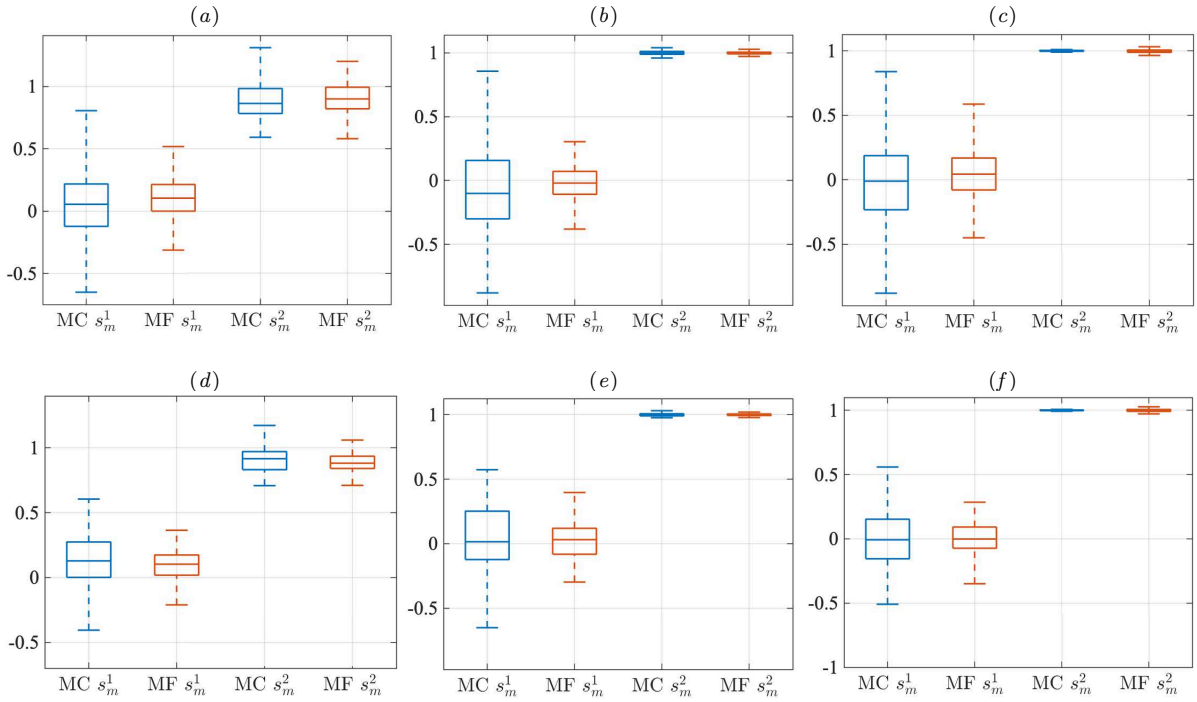

Figure 6.10: Box plots of 100 main-effect sensitivity estimate replicates for non-dimensional deposition velocity with (a)-(c) $p = 36$ and (d)-(f) $p = 72$. $\tau_p^+ = 0.1, 1$ and 1 from left to right. Classic Monte Carlo (MC) and multi-fidelity (MF) predictions are shown in blue and red respectively. s_m^1 and s_m^2 are main Sobol index for ζ and ξ respectively.

estimator with only 1D model. MSE is computed via Eq. (6.33) with $\hat{s}$ taken from a well-converged estimates using $p = 50,000$ by randomly sampling from 100 DNS data.

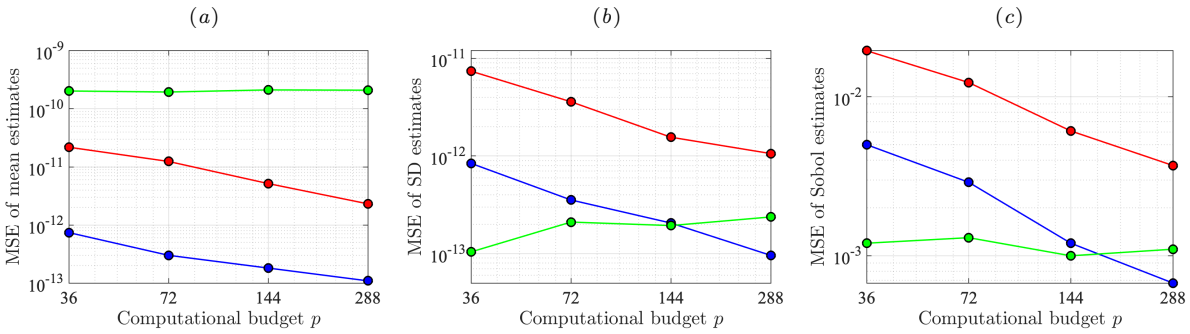

Figure 6.11: The estimated MSE of MFMC estimator (blue), MC estimator with only DNS (red), and MC estimator with only 1D mode (green) for $\tau_p^+ = 0.1$ and four different budgets. QoIs are (a) mean and (b) standard deviation of V_{dep}^+, and (c) Sobol index of V_{dep}^+ to van der Waals.

The MFMC estimator with $p = 36$ achieves the same level of MSE compared to the classic MC estimator using only DNS data with $p = 288$, which translates to at least 8 times speedup. Such cost saving is seen for estimation of all three quantities: mean, standard deviation, and Sobol index of V_{dep}^+. Note that although using the low-fidelity model alone to estimate sensitivities exhibit small variation when the budget is small, it converges to a wrong solution as shown in Fig. 6.11(b) and 6.11(c) due to the inevitable bias embedded in the model. The bias in 1D model prediction is also seen in Fig. 6.11(a) where the error in predicted mean of V_{dep}^+ is orders of magnitudes larger than the MFMC estimator.

τ_p^+	d_p (μm)	mean	standard deviation	s_m^1	s_m^2
0.1	1.6	6.66×10^{-5}	1.93×10^{-5} (29.0%)	0.072	0.903
1	5	1.50×10^{-3}	7.65×10^{-4} (51.0%)	0.001	0.998
10	16	5.70×10^{-2}	1.90×10^{-2} (33.3%)	0.014	1.000

Table 6.3: Estimation of mean, standard deviation (with its percentage of the mean in brackets), main-effect Sobol indices of V_{dep}^+ using multi-fidelity approach for three different particle sizes with $p = 288$.

Finally, the predicted statistics of V_{dep}^+ using MFMC estimator with $p = 288$ are tabulated in Table. 6.3. In terms of uncertainties, the deposition rate of mid-sized particles ($\tau_p^+ = 1$ or $d_p = 5\,\mu\text{m}$) exhibits the largest standard deviation given the same variations in electrical charge and Hamaker constant, which is primarily due to these particles being most responsive to the turbulent eddies. Nevertheless, notable variations in V_{dep}^+ are

observed for all three particle sizes ($29\% - 51\%$), highlighting the importance of cohesion on particle deposition rate. Therefore, special attention should be paid on accurately computing electrostatics and van der Waals for deposition studies that involve Geldart-C particles. Pretreatments using pressurized declumper or charge neutralizer can be leveraged to reduce these uncertainties in experimental investigations.

In terms of sensitivity, van der Waals force has almost negligible effect on the deposition rates ($s_m^1 \approx 0$) for $\tau_p^+ = 1$ and 10, namely deposition is much more sensitive to electrostatics compared to van der Waals. This is expected because electrostatics is non-negligible on particle statistics over a much wider range. Nevertheless, van der Waals force does play a bigger role for the smallest particles ($\tau_p^+ = 1$ or $d_p = 1.6\,\mu\text{m}$). Such sensitivity information provides insights about when to neglect van der Waals force for a given particle size (in this case $d_p \gtrsim 1.6\,\mu\text{m}$). Note that Sobol index estimations depend on the distribution and range considered for the input parameters. In this study we consider uniform distribution of ζ and ξ within typical experiment-measured ranges, which allows us to isolate the uncertainties due to electrostatics and van der Waals and compare their relative importance. While accurately measuring their distribution in common dust samples experimentally are extremely difficult and therefore scarce, such data would be invaluable to provide more insights on the sensitivity analysis.

6.7 Conclusions

In this chapter, deposition of fine particulates in wall-bounded turbulent flows was investigated with variations in particle cohesion strength. Relative importance of cohesive forces was compared analytically in a cylindrical pipe as a function of particle number density. Particle-wall contributions was found to be dominant whereas particle-particle interactions due to van der Waals are negligible in dilute suspensions. In addition, wall

image charging was observed to significantly enhance deposition whereas particle-particle interactions play much less of a role. Deposition predicted by the 1D Eulerian model was seen to be systematically lower than DNS simulations, while both exhibit very similar trends when varying charge amounts and Hamaker constants. A multi-fidelity approach was employed to optimally estimate mean, variance, and sensitivity of the deposition rate by exploiting the high correlations between DNS and the 1D Eulerian model. The global sensitivity analysis using the multi-fidelity approach admits eight times speedup compared to classic Monte Carlo methods. Deposition was found to be more sensitive to electrostatics than van der Waals across all particle sizes. The effect of van der Waals on deposition was seen to decay rapidly with increasing particle size.

CHAPTER VII

Conclusions

7.1 Summary of achievements

A key contribution from this work involves the development of an Eulerian–Lagrangian framework capable of accurately predicting transport and deposition of fine particulates in the presence of turbulence and cohesive forces. Efficient algorithms were developed to accurately resolve particle-particle interactions (both long- and short-range) and particle-fluid coupling in periodic and wall-bounded geometries. The numerical framework has been employed to understand the effects of van der Waals and electrostatics on particle transport, (de)agglomeration, and deposition in turbulent flows. Short-range electrostatic interactions are found to play a key role in particle clustering even in dilute particle suspensions. A new turbulence generation mechanism is identified via three-way coupling between an electric field, charged particles, and ionized air. A phenomenological model was developed based on the scaling analysis and mass-spring-damper analogy to predict the turbulence-induced breakup of a particle aggregate in the absence of a resolved flow field. Sensitivities of deposition on cohesive forces are efficiently quantified by leveraging both DNS and low-fidelity models. Further details on the contributions made throughout the dissertation are outlined below.

1. In Chapter II, an Eulerian–Lagrangian strategy for simulating particle-laden flows

capable of accurately resolving particle interactions in the presence of attractive forces was developed.

(a) The P^{3}M method was coupled with EL framework and nearest neighbor search algorithm for the first time to simulate charged particle-laden flows. The particle electrostatic force is separated into short-range and long-range contributions such that it admits high accuracy while avoiding $\mathcal{O}(N^2)$ operations.

(b) The original P^{3}M requires FFT evaluations and therefore is limited to periodic domains. A scaled-mapping treatment was proposed to extend P^{3}M to non-periodic geometries while retaining its high accuracy and cost savings.

(c) The accuracy of state-of-the-art electrostatic algorithms were assessed and compared for the first time with various model parameters and interpolation orders.

(d) A levelset distance function is coupled with image charging to efficiently impose iso-potential boundary conditions for conducting walls.

(e) In order to properly resolve the wide range of time scales at play in a tractable manner, a multi-scale time stepping framework was employed where the particle equations are solved on a separate time scale from the fluid, allowing for simultaneously resolving a wide range of scales efficiently.

2. In Chapter III, a numerical study on charged particle transport in turbulence was presented, quantifying the relative importance of electrostatic and fluid drag on particle transport. Correctly capturing the short-range interaction was shown to be important even in dilute suspensions.

(a) A benchmarking study of charged particles in a Taylor-Green vortex showed that P^{3}M is capable of capturing particle clustering while PM fails, demonstrating the importance of short-range interactions even in dilute suspensions.

(b) Oppositely-charged particles were shown to form chain and ring structures when transporting in homogeneous isotropic turbulence, while preferential concentration was completely mitigated for the case with likely-charged particles.

(c) In wall-bounded flows, particle-wall interactions were found to be notably more significant than particle-particle interactions for charged particle near-wall statistics, while both have negligible effects away from the wall.

3. In Chapter IV, linear stability analysis and direct numerical simulations of charged aerosols in ionized air reveal a non-linear feedback mechanism capable of generating atmospheric turbulence under extreme weather conditions.

   (a) Linear stability shows that coupling between ionized air and a background electric field acts to increase turbulent kinetic energy (TKE) in the upper troposphere, albeit over long time durations.

   (b) Critical stability conditions of the upper troposphere, dictated by an electric Rayleigh number, are determined as a function of vertical span and shear rate. The atmospheric fluid dynamics are found to be most unstable over a vertical span consistent with typical cloud thicknesses observed at these elevations.

   (c) Direct simulations of charged droplets in homogeneous shear flow demonstrate a new nonlinear feedback mechanism capable of accelerating this unstable growth and augmenting TKE by up to a factor of six.

4. In Chapter V, turbulence-induced breakup of a spherical 'clump' of cohesive particles were investigated using the aforementioned numerical framework. Deformation of the particle aggregate is modeled using a mass-spring-damper analogy.

   (a) A new linear-forcing scheme was developed to maintain statistically stationary turbulence in the presence of particles with two-way coupling.

(b) The time-rate of aggregate breakup was found to vary substantially for different realizations of the same turbulence. The local fluid stress seen by the aggregate can reach four times the domain-averaged values, resulting in intermittent breakup of aggregate in turbulence.

(c) A turbulent Adhesion number based on the Kolmogorov length scale and adhesive potential was introduced for the first time to characterize the breakup process. A critical turbulent Adhesion number was identified that well predicts the breakup and non-breakup regimes.

(d) As a direct analog to the Taylor analogy breakup (TAB) model commonly used for droplet breakup in the spray community, the analysis performed herein was used to inform a mass-spring-damper model to predict the breakup time of the aggregate, referred as Granular-TAB (G-TAB). The predicted breakup time for a given Ad_η was in good agreement with simulations and is useful for predicting aggregate breakup in coarse-grained simulations such as RANS.

(e) A variance-based sensitivity analysis was performed to quantify the relative importance of the modeling parameters on the aggregate breakup. The simulation results were found to be most sensitive to two-way coupling, the absence of which results in unphysical interphase slip velocities and instantaneous breakup.

5. In Chapter VI, deposition of fine particulates in wall-bounded turbulent flows are investigated. We characterize and quantify the effects of charge and van der Waals using both DNS and a 1D Eulerian model, followed by a global sensitivity analysis on deposition by leveraging models of different fidelities.

(a) Relative importance of cohesive forces are compared analytically in a cylindrical pipe as a function of particle number density. Particle-wall contributions are

found to be dominant whereas particle-particle interactions due to van der Waals are negligible in dilute suspensions.

(b) Deposition predicted by the 1D Eulerian model was found to be systematically lower than DNS, highlighting the importance of particle clustering on deposition.

(c) A multi-fidelity approach was employed to optimally estimate mean, variance, and sensitivity of the QoI (deposition rate). Cheap 1D models were evaluated to reduce the cost while retaining accuracy guarantees of expensive DNS.

(d) Deposition was found to be more sensitive to electrostatics than van der Waals across all particle sizes. The effect of van der Waals on deposition was seen to decay rapidly with increasing particle size.

The above contributions are also presented in the following publications:

- **Yao, Y.**, Capecelatro, J. (2021) An accurate particle-mesh method for simulating charged particles in wall-bounded flows, *Powder Technology*. 387, 239-250.
- **Yao, Y.**, Capecelatro, J. (2021) Deagglomeration of cohesive particles by turbulence, *Journal of Fluid Mechanics*. 911, A10.
- **Yao, Y.**, Capecelatro, J. (2019) Electrohydrodynamic generation of atmospheric turbulence, *Physical Review Fluids*. 4, 1-19.
- **Yao, Y.**, Capecelatro, J. (2018) Competition between drag and Coulomb interactions in turbulent particle-laden flows using a coupled-fluid-Ewald-summation approach, *Physical Review Fluids*. 3, 1–20.

The following papers, delivered during my Ph.D. research, also contribute to advancing existing numerical methods and physical understanding in the area of particle-laden flows despite not being presented in this dissertation:

- Monroe, K., **Yao, Y.**, Lattanzi, A., Raghav, V., Capecelatro, J. (2021) Role of Pulsatility on Particle Dispersion in Expiratory Flows, *Physics of Fluids*. 33, 4.
- **Yao, Y.**, Shallcross, G., Ni. R, Kim, T., Mehta, M., Rabinovitch, J., Capecelatro, J. (2020) The dynamics of inertial particles in under-expanded jets: A numerical study, in *AIAA Scitech 2020 Forum* (p. 1327).
- Kim, T., Ni, R., Capecelatro, J., **Yao, Y.**, Shallcross, G., Mehta, M., Rabinovitch, J. (2020) The dynamics of inertial particles in under-expanded jets: An experimental study, in *AIAA Scitech 2020 Forum* (p. 1326).

7.2 Future perspectives

7.2.1 A roadmap to improve particle stochastic models in RANS using DNS simulations

Reliable, physics-based models for the transport and deposition of dust in turbulent flows is a key step towards enabling next generation turbomachinery. The numerical framework developed in this dissertation is highly accurate but still computationally expensive for simulating systems such as gas turbine engines. In fact, RANS coupled with Lagrangian particle tracking remains the workhorse for the simulation of turbomachinery. Stochastic particle models such as random walk (RW) models are typically employed to account for turbulence dispersion of the particles in RANS as the local fluid velocity at the particle location is not resolved. Despite being computationally efficient, this approach has been shown to significantly overpredict deposition [83]. An accurate deposition prediction using RANS coupled with RW models requires at a very minimum: (1) accurate flow solution (mean and fluctuations), (2) good turbulent dispersion model, and (3) valid impact/rebound model or assumptions. While RW models have been shown mathematically to resemble turbulent dispersion at least at large time scales, and 'all-stick' assumption can be made at high engine operating temperatures above the particle

melting points, RANS in wall-bounded flows is known to inevitably exhibit large errors, especially in near-wall regions where off-diagonal terms in Reynolds stress tensor are mis-predicted [124]. Two-phase statistics generated by our high-fidelity simulations can be leveraged to isolate errors in flow solution obtained from RANS in addition to errors associated with turbulent dispersion using existing RW models, which provides a pathway to improve their accuracy. An example is described in Appendix E where direct one-to-one comparisons between DNS, RANS coupled with RW, and experimental measurements of particle deposition under realistic engine operating conditions are performed, followed by preliminary results of particle statistics and deposition rates.

7.2.2 Uncertainty quantification of deposition rates by varying dust constituents

A key simplification made in the sensitivity analysis of Chapter VI is that the input parameters (i.e., charge amount and Hamaker constant) are uniformly sampled from a prescribed lower and upper bound while keeping all other parameters such as particle density, restitution coefficients constant. In addition, 'all-stick' assumption is made and therefore uncertainties due to impact/rebound process is omitted. Although these simplifications are necessary to isolate the sensitivities of cohesive forces, uncertainties due to rebound model, particle density, restitution coefficients, and melting temperatures are of prime importance for a comprehensive understanding of deposition physics.

One attractive way to tackle these additional uncertainties is to vary the mass fraction of dust constituents given by real dust sample measurements (e.g., Fig. 1.7). The aforementioned properties of the dust mixture can be then determined as a linear combination or functional form of the properties of each constituents. Variations therefore naturally arise within their physical limits. Furthermore, physics-based rebound models exist that predict restitution coefficients as a function of cohesion strength and melting temperature [21, 187], which allow us to move away from 'all-stick' assumption. The MFMC

approach described in Chapter VI can be performed to efficiently assess the sensitivity of each input parameters via a prior run of fewer samples, followed by a dimensionality reduction that eliminates the low-sensitivity input parameters. Finally, uncertainty propagation can be performed on reduced input parameter space such that it is tractable computationally.

APPENDIX A

Additional algorithms for computing electrostatics

A.1 Ewald summation

While the PM approach avoids $\mathcal{O}(N^2)$ calculation, it requires that the length scale used to resolve the spatial gradients of electric potential are greater than the spacing between the particles. Due to non-trivial interactions between the phases in turbulent flows, particles may preferentially concentrate in certain regions, and thus in general this assumption does not hold. Ewald summation separates the long-range and short-range forces to efficiently compute the electrostatic force in periodic boxes with quick convergence. Consider a system of N_p particles with charges $q_p^{(i)}$ at positions $\boldsymbol{x}_p^{(i)}$ in a cubic box of length L with triply periodic boundary conditions. The Ewald summation approach separates the total force of particle i into three components

$$\boldsymbol{F}^{(i)}_{\text{coulomb}} = \boldsymbol{F}^{(i)}_r + \boldsymbol{F}^{(i)}_k + \boldsymbol{F}^{(i)}_d, \tag{A.1}$$

where $\boldsymbol{F}^{(i)}_r$ and $\boldsymbol{F}^{(i)}_k$ represent contributions from real space and Fourier space, respectively, and $\boldsymbol{F}^{(i)}_d$ is the dipole correction term to avoid double counting. These separate contributions are expressed as

$$\boldsymbol{F}^{(i)}_r = q_p^{(i)} \sum_j q_p^{(j)} \sum_{\boldsymbol{m}\in\boldsymbol{Z}^3}{}' \Big(\frac{2\alpha}{\sqrt{\pi}} \exp(-\alpha^2 |\boldsymbol{r}_{ij} + \boldsymbol{m}L|^2) + \frac{\operatorname{erfc}(\alpha|\boldsymbol{r}_{ij} + \boldsymbol{m}L|)}{|\boldsymbol{r}_{ij} + \boldsymbol{m}L|} \Big) \frac{\boldsymbol{r}_{ij} + \boldsymbol{m}L}{|\boldsymbol{r}_{ij} + \boldsymbol{m}L|^2}, \tag{A.2}$$

$$\boldsymbol{F}_k^{(i)} = \frac{q_p^{(i)}}{L^3} \sum_j q_p^{(j)} \sum_{\boldsymbol{k}\neq 0} \frac{4\pi \boldsymbol{k}}{k^2} \exp\Big(-\frac{k^2}{4\alpha^2} \Big) \sin(\boldsymbol{k} \cdot \boldsymbol{r}_{ij}), \tag{A.3}$$

and

$$\boldsymbol{F}_d^{(i)} = -\frac{4\pi q_p^{(i)}}{(1+2\epsilon')L^3} \sum_j q_p^{(j)} \boldsymbol{x}_p^{(j)}, \tag{A.4}$$

where erfc is the complementary error function, $\boldsymbol{m}$ and $\boldsymbol{k}$ represent the number of iterations over periodic boxes in real and Fourier space, respectively, which are distinguished using a cutoff radius $r_{\max}$, and ϵ' is the dielectric constant, which in the case of a vacuum is $\epsilon' = 1$. The inverse length α, referred to as the Ewald parameter, tunes the relative weight of the real space and the reciprocal space contribution. Since long-range interactions converge significantly faster in Fourier space, the Ewald summation will converge after only a few iterations for both $\boldsymbol{m}$ and $\boldsymbol{k}$. As a result, the computational cost scales as $\mathcal{O}\left(N^{3/2}\right)$ with an optimal choice of α. A well converged Ewald summation will give the exact solution for an electrostatic field with periodic boundary conditions. It also acts as the foundation of P^{3}M method.

A.2 Hybrid method

One drawback of the classic P^{3}M method is that it relies on Fourier transforms, and therefore must be solved in periodic domains. However, many applications involving suspensions of charged particles in turbulence are wall bounded. Kolehmainen et al. [126] recently proposed a hybrid method that combines the truncated pairwise summation approach for the short-range potential and an injection method for the long-range contribution. The electric field is given by

$$\boldsymbol{E}^{(i)}(\boldsymbol{x}_p) = \boldsymbol{E}_s^{(i)}(\boldsymbol{x}_p) + \boldsymbol{E}_l[\boldsymbol{x}_{\text{cell}}^{(i)}] + \boldsymbol{E}_c^{(i)}(\boldsymbol{x}_p), \tag{A.5}$$

where $\boldsymbol{E}_l[\boldsymbol{x}_{\text{cell}}^{(i)}]$ is the long-range electric force at $\boldsymbol{x}_{\text{cell}}^{(i)}$, the center of the cell that particle i belongs to. The short-range contribution is obtained by summing all pairwise electrostatic interactions within the cutoff radius,

$$\boldsymbol{E}_s^{(i)}(\boldsymbol{x}_p) = \frac{1}{4\pi\epsilon_0} \sum_{0<r_{ij}<r_{\max}} q_p^{(j)} \frac{(\boldsymbol{x}_p^{(i)} - \boldsymbol{x}_p^{(j)})}{\left|\boldsymbol{x}_p^{(i)} - \boldsymbol{x}_p^{(j)}\right|^3}, \tag{A.6}$$

and the long-range contribution is found by

$$\boldsymbol{E}_l[\boldsymbol{x}_{\text{cell}}^{(i)}] = -\nabla\phi[\boldsymbol{x}_{\text{cell}}^{(i)}]. \tag{A.7}$$

Here, the electric potential, ϕ, is obtained by solving a Poisson equation for the cell-averaged value via

$$\nabla^2\phi = -\frac{\rho_v}{\epsilon}, \tag{A.8}$$

with the cell-averaged charge density given by

$$\rho_v = \frac{1}{V_k} \sum_{\boldsymbol{x}_p^{(j)} \in V_k} q_p^{(i)}, \tag{A.9}$$

where V_k is the volume of the local cell that particle j belongs to. The final term, $\boldsymbol{E}_c(\boldsymbol{x}_p^{(i)})$, is the contribution to be removed to avoid double counting, given by

$$\boldsymbol{E}_c^{(i)}(\boldsymbol{x}_p) = -\sum_{0<r_{ij}<r_{\max}} \begin{cases} 0, & \text{if } \boldsymbol{x}_p^{(i)} \text{ and } \boldsymbol{x}_p^{(j)} \text{ in the same cell} \\ \frac{1}{4\pi\epsilon} \frac{q_p^{(j)}(\boldsymbol{x}_{\text{cell}}^{(i)} - \boldsymbol{x}_{\text{cell}}^{(j)})}{\left|\boldsymbol{x}_{\text{cell}}^{(i)} - \boldsymbol{x}_{\text{cell}}^{(j)}\right|^3}, & \text{otherwise.} \end{cases} \tag{A.10}$$

While the Hybrid method does not rely on Fourier transform and thus can be applied to complex geometries, compared to P^{3}M, its accuracy is limited by the correction term that is of the order of the spatial discretization. For P^{3}M, however, the truncation error is compensated using an optimized influence function, and thus its accuracy is expected to be significantly greater than the Hybrid method.

APPENDIX B

Validation of DNS turbulent pipe flows

To fully resolve the fluid phase dynamics, direct numerical simulation (DNS) of a single-phase turbulent pipe flow is performed. The pipe diameter $D = 0.02\,\mathrm{m}$ is chosen to be the same as a companion experimental study by our collaborators Gnanaselvam et al. [83]. The bulk velocity $U_b = 4\,\mathrm{m/s}$ which yields $\eta^+ = 1.6$ and $\mathrm{Re}_\tau = 180$. The fluid-phase equations are discretized on a Cartesian mesh, and a conservative immersed boundary (IB) method is employed to model the cylindrical pipe geometry without requiring a body-fitted mesh. The method is based on a cut-cell formulation that requires rescaling of the convective and viscous fluxes in these cells, and provides discrete conservation of mass and momentum [163, 181].

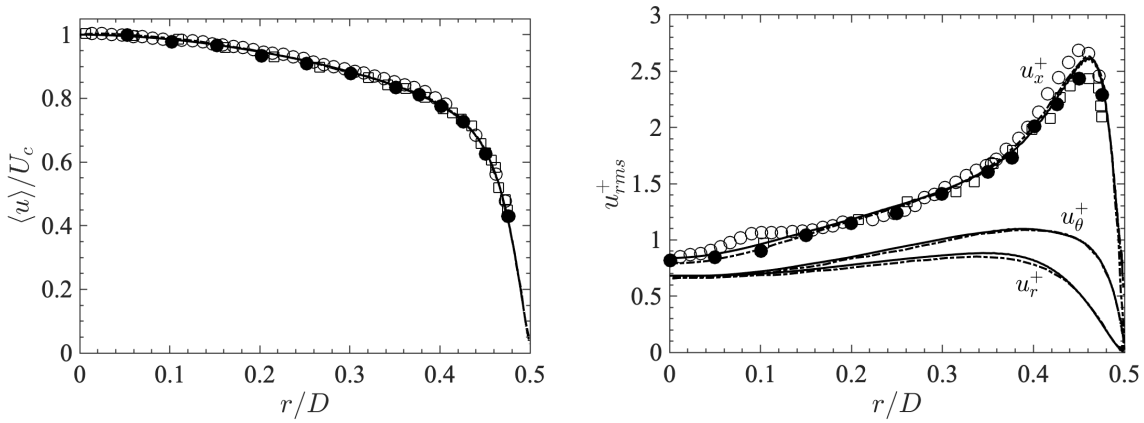

Figure B.1: Mean fluid velocity profiles in fully developed turbulent pipe flow. (a) Mean streamwise velocity normalized by the centerline value U_c and (b) normalized root-mean-square velocity. Current study (−), DNS (−·) and experiments (PIV: ○, LDA: ●, HWA: □) by Eggels et al. [58].

We consider a domain of size $10D \times D \times D$, discretized using $326 \times 256 \times 256$ grid points

(see Fig. 3.8(a)). The grid spacing is chosen such that $\Delta y^+ = \Delta z^+ = 1.25$ and $\Delta x^+ = 9.8$ to satisfy the resolution criteria of DNS for pipe flows [185, 151, 58] proposed by Grötzbach [90], which requires (i) $\Delta^+ = (\Delta x^+ \, \Delta y^+ \, \Delta z^+)^{1/3} \leq \pi \eta^+$ and (ii) at least three grid points in wall buffer region ($y^+ \leq 5$). Periodic boundary conditions are applied in the streamwise direction. A uniform source term resembling a mean pressure gradient, $\boldsymbol{F}_{\mathrm{mfr}}$, is added to the right-hand side of Eq. (2.2) and adjusted dynamically to maintain the desired flow rate. The flow is initialized with $10\% \, U_b$ sinusoidal fluctuations to accelerate the transient process. A statistical stationary state is reached after $240 \, D/U_b$. A comparison of the velocity statistics against DNS and experimental data of the same pipe configuration from Eggels et al. [58] is provided in Fig. B.1. Excellent agreement is seen for both mean streamwise velocity and root-mean-square fluctuations in all three directions.

APPENDIX C

Analytical solution of the initial algebraic growth

In homogeneous shear flows, the initial algebraic growth is known to sustain large amplification of perturbation energy that may introduce nonlinear effects and lead to onset of turbulence [79, 208, 78, 203, 148]. Because conventional linear stability analysis fails to accurately predict the transient growth, other techniques, such as non-normal modal analysis [29, 234, 207], or the Wentzel–Kramers–Brillouin (WKB) method [102, 15], have been used in the past. In the present analysis, we consider the method of characteristics. By neglecting the particle phase, Eqs. (4.1) and (4.3) are rewritten along characteristics in Fourier space, together with the wavevector characteristic equations, resulting in the following three coupled ODEs

$$\begin{aligned} \frac{\mathrm{d}\boldsymbol{\kappa}}{\mathrm{d}t} &= -\nabla \mathbf{u}_b^T \cdot \boldsymbol{\kappa} \\ \frac{\mathrm{d}\hat{q}_f}{\mathrm{d}t} &= -i\mu_I \overline{E} \kappa_3 \hat{q}_f - D_I \kappa^2 \hat{q}_f \\ \frac{\mathrm{d}\hat{w}}{\mathrm{d}t} &= \frac{2\Gamma \kappa_1 \kappa_3}{\kappa^2}\hat{w} - \nu\kappa^2 \hat{w} + \left(1 - \frac{\kappa_3^2}{\kappa^2}\right)\frac{\hat{q}_f \overline{E}}{\rho}, \end{aligned} \tag{C.1}$$

where the hat denotes the Fourier transform of a quantity, $\boldsymbol{\kappa} = [\kappa_1\, \kappa_2\, \kappa_3]^\mathsf{T}$ is the wavevector, and $\nabla \mathbf{u}_b = \Gamma \mathbf{e}_1 \mathbf{e}_3^\mathsf{T}$ is the base state velocity gradient tensor. The vertical velocity can be determined by assuming $w'(t, \boldsymbol{x}) = \hat{w}(t) \exp(i\boldsymbol{\kappa}(t) \cdot \boldsymbol{x})$. The remaining velocity components can be obtained by enforcing continuity. As shown in Fig. C.1, the second-order algebraic growth closely matches the numerical simulations from Sec. 4.3, confirming that charged aerosols do not affect the initial algebraic growth rate.

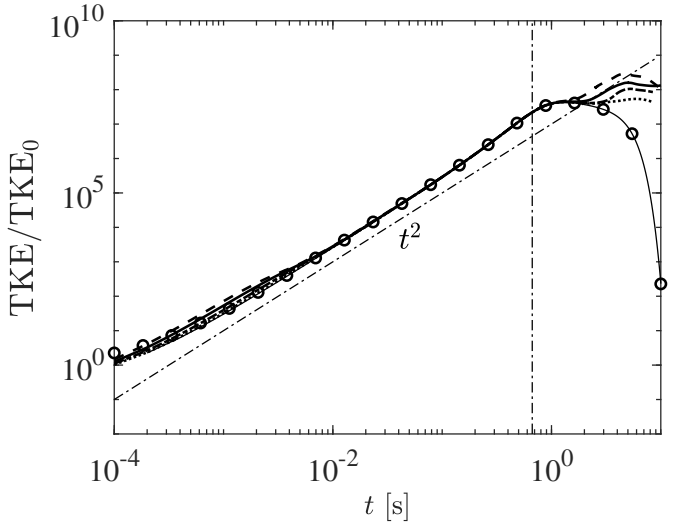

Figure C.1: Normalized TKE evolution for particle loading $\Phi_v = 0$ (–), 1×10^{-4} ($\cdots$), 4×10^{-4} (— -), 1×10^{-3} (—), and 2×10^{-3} (- -). Theoretical solution obtained from Eq. (C.1) ($\circ$) are shown for comparison. The vertical dashed line indicates the turning point from upstream and downstream waves.

The second-order algebraic initial growth rate can be approximated analytically from Eq. (C.1). Solving the wavevector characteristic equation yields $\kappa_1 = \kappa_0 = 2\pi/L$ and $\kappa_3 = (1 - \Gamma t)\,\kappa_0$. With this, the magnitude of $\hat{q}_f$ can easily be obtained by solving the first-order linear ODE in Eq. (C.1)

$$\hat{q}_f(t) = \hat{q}_{f0} \exp\left(-\frac{1}{3} D_I \kappa_0^2 t \left(\Gamma^2 t^2 - 3\Gamma t + 6\right)\right). \tag{C.2}$$

Solving $\hat{q}_f$, the third ODE for velocity results in a first-order linear equation and can be approximated via a Taylor series expansion according to

$$\begin{aligned} \frac{\mathrm{d}\hat{w}}{\mathrm{d}t} &= \frac{1}{1 + (1 - \Gamma t)^2} \frac{\hat{q}_{f0}\overline{E}}{\rho} \exp\left(-\frac{1}{3} D_I \kappa_0^2 t \left(\Gamma^2 t^2 - 3\Gamma t + 6\right)\right) \\ &\approx \frac{1}{1 + (1 - \Gamma t)^2} \frac{\hat{q}_{f0}\overline{E}}{\rho} \left(1 - 2 D_I \kappa_0^2\, t + D_I \kappa_0^2 (\Gamma + 2 D_I \kappa_0^2)\, t^2\right). \end{aligned} \tag{C.3}$$

The first two terms on the right-hand-side can be neglected since they are orders of

magnitude smaller than the last term. Integrating Eq. (C.3) yields

$$\begin{aligned}\hat{w}(t) &= \hat{w}_0 - \frac{\hat{q}_{f0}\overline{E}}{\rho\Gamma^2}(\Gamma - 2D_I\kappa_0^2)\left(\tan^{-1}(1-\Gamma t) - \frac{\pi}{4}\right) \\ &\approx \hat{w}_0 + \frac{\hat{q}_{f0}\overline{E}}{2\rho\Gamma}(\Gamma - 2D_I\kappa_0^2)\, t.\end{aligned} \tag{C.4}$$

By applying continuity, the streamwise velocity can be expressed as

$$\hat{u}(t) = -\frac{\hat{w}(t)\kappa_3}{\kappa_1} = -\hat{w}_0(1-\Gamma t) - \frac{\hat{q}_{f0}\overline{E}}{2\rho\Gamma}(\Gamma - 2D_I\kappa_0^2)\,(1-\Gamma t)t. \tag{C.5}$$

With this, the TKE can be approximated by

$$\mathrm{TKE}(t) = \frac{1}{2}\left(\hat{w}^2 + \hat{u}^2\right) \approx \mathrm{TKE}_0 + \frac{\hat{q}_{f0}^2\overline{E}^2}{2\rho^2\Gamma^2}(\Gamma - 2D_I\kappa_0^2)^2\, t^2 = \mathcal{O}(t^2), \tag{C.6}$$

which implies when t is small, the initial growth of TKE is second-order. This growth rate is also consistent with the well-known quadratic-scaling law for the transient energy growth in uniform shear flow [148, 147].

APPENDIX D

Linearization and non-dimensionalization of the governing equations

We start with the governing equations (4.1) and (4.3) and neglect the convective term in the momentum equation and diffusion term in the charge transport equation due to their relatively small magnitudes

$$\left(\rho\frac{\partial}{\partial t}-\mu\nabla^2\right)\boldsymbol{u}=q_f\boldsymbol{E}-\nabla p-\rho\Gamma z\frac{\partial \boldsymbol{u}}{\partial x}-\rho\Gamma w\boldsymbol{e}_x, \tag{D.1}$$

$$\frac{\partial q_f}{\partial t}+\nabla\cdot(\mu_I q_f\boldsymbol{E}+q_f\boldsymbol{u}+q_f\Gamma z\boldsymbol{e}_x)=0. \tag{D.2}$$

The flow quantities q_f, ϕ, p, $\boldsymbol{u}$ and $\boldsymbol{E}$ are decomposed into a base state and a fluctuating component as $A=\overline{A}+A'$, where

$$A'=A_0(z)\exp(i\kappa_x x+i\kappa_y y)\exp(\omega\tau), \tag{D.3}$$

with A_0 the fluctuation amplitude, κ_x and κ_y the horizontal wave numbers, ω the growth rate, and $\tau=(\mu_I\overline{\phi}\,t)/L^2$ is the time scale normalized over a vertical span L. Consider (D.1) first at a base case where $\overline{\boldsymbol{u}}=[\overline{u}\,\overline{v}\,\overline{w}]^{\mathsf{T}}=0$, then (D.1) reduces to

$$\overline{q}_f\overline{\boldsymbol{E}}=\nabla\overline{p}, \tag{D.4}$$

by subtracting (D.1) by (D.4), we have

$$\left(\rho\frac{\partial}{\partial t}-\mu\nabla^2\right)\boldsymbol{u}=(q_f\boldsymbol{E})'-\nabla p'-\rho\Gamma z\frac{\partial \boldsymbol{u}}{\partial x}-\rho\Gamma w\boldsymbol{e}_x, \tag{D.5}$$

for incompressible flow, we can take divergence of (D.5) and apply $\nabla\cdot\boldsymbol{u}=0$ to arrive

$$\nabla^2 p'=\nabla\cdot(q_f\boldsymbol{E})'. \tag{D.6}$$

Now consider the vertical component of (D.5)

$$\left(\rho\frac{\partial}{\partial t}-\mu\nabla^2\right)w'=(q_fE_3)'-\frac{\partial}{\partial z}p'-\rho\Gamma z\frac{\partial w'}{\partial x}, \tag{D.7}$$

we can take the Laplacian of (D.7) and incorporate (D.6)

$$\left(\rho\frac{\partial}{\partial t}-\mu\nabla^2\right)\nabla^2 w'=\nabla^2(q_fE_3)'-\frac{\partial}{\partial z}\left(\nabla\cdot(q_f\boldsymbol{E})'\right)-\rho\Gamma\nabla^2\left(z\frac{\partial w'}{\partial x}\right), \tag{D.8}$$

where

$$\begin{aligned}\frac{\partial}{\partial z}\left(\nabla\cdot(q_f\boldsymbol{E})'\right)&=\frac{\partial}{\partial z}\left(\nabla\cdot\left({q_f}'\overline{\boldsymbol{E}}\right)+\nabla\cdot\left(\overline{q}_f\boldsymbol{E}'\right)\right)\\&=\overline{E}\,\frac{\partial^2 q_f'}{\partial z^2}+\frac{d^2\overline{q}_f}{dz^2}E_3'+\frac{d\overline{q}_f}{dz}\frac{\partial E_3'}{\partial z}+2\,\frac{q_f'}{\epsilon}\frac{d\overline{q}_f}{dz}+3\,\frac{\overline{q}_f}{\epsilon}\frac{\partial q_f'}{\partial z},\end{aligned} \tag{D.9}$$

$$\begin{aligned}\nabla^2(q_fE_3)'&=\nabla^2\left(q_f'\overline{E}\right)+\nabla^2\left(\overline{q}_fE_3'\right)\\&=\overline{E}\,\nabla^2 q_f'+\frac{q_f'}{\epsilon}\frac{d\overline{q}_f}{dz}+2\,\frac{dq_f'}{dz}\frac{d\overline{E}}{dz}+\overline{q}_f\nabla^2E_3'+E_3'\frac{d^2\overline{q}_f}{dz^2}+2\,\frac{d\overline{q}_f}{dz}\frac{dE_3'}{dz},\end{aligned} \tag{D.10}$$

and

$$\rho\Gamma\nabla^2\left(z\frac{\partial w'}{\partial x}\right)=\rho\Gamma z\frac{\partial}{\partial x}\left(\nabla^2w'\right)+2\rho\Gamma\frac{\partial}{\partial x}\left(\frac{\partial w'}{\partial z}\right). \tag{D.11}$$

Combining (D.8)-(D.11) gives

$$\begin{aligned}\left(\rho\frac{\partial}{\partial t}-\mu\nabla^2\right)\nabla^2w'=&\frac{\partial^2q_f'}{\partial z^2}\overline{E}-\frac{q_f'}{\epsilon}\frac{d\overline{q}_f}{dz}+\frac{\overline{q}_f}{\epsilon}\frac{\partial q_f'}{\partial z}+\overline{q}_f\nabla^2E_3'+\frac{d\overline{q}_f}{dz}\frac{\partial E_3'}{\partial z}+\overline{E}\nabla^2q_f'\\&-\rho\Gamma z\frac{\partial}{\partial x}\left(\nabla^2w'\right)-2\rho\Gamma\frac{\partial}{\partial x}\left(\frac{\partial w'}{\partial z}\right).\end{aligned} \tag{D.12}$$

Using $q_f' = -\epsilon\nabla^2\phi'$ and $E_3' = -d\phi'/dz$, (D.12) can be rewritten in terms of potential

$$\left(\rho\frac{\partial}{\partial t} - \mu\nabla^2\right)\nabla^2 w' = \epsilon\overline{E}\nabla^2\nabla_1^2\phi' + \frac{d\overline{q}_f}{dz}\nabla_1^2\phi' - \rho\Gamma z\frac{\partial}{\partial x}\left(\nabla^2 w'\right) - 2\rho\Gamma\frac{\partial}{\partial x}\left(\frac{\partial w'}{\partial z}\right), \tag{D.13}$$

where $\nabla_1^2 = \partial^2/\partial x^2 + \partial^2/\partial y^2$. Similarly (D.2) can be linearized the same way in the vertical direction to obtain

$$-\epsilon\bar{E}\frac{\partial}{\partial z}\nabla^2\phi' + \frac{\mathrm{d}\bar{q}_f}{\mathrm{d}z}\frac{\partial\phi'}{\partial z} + \frac{\epsilon}{\mu_I}\frac{\partial}{\partial t}\nabla^2\phi' + 2\bar{q}_f\nabla^2\phi' = \frac{1}{\mu_I}\frac{\mathrm{d}\bar{q}_f}{\mathrm{d}z}w'. \tag{D.14}$$

Recall that $\phi' = \phi_0(z)\exp(i\kappa_x x + i\kappa_y y)\exp(\omega\tau)$ and $w' = w_0(z)\exp(i\kappa_x x + i\kappa_y y)\exp(\omega\tau)$, so $\nabla^2\phi' = \left(-(\kappa_x^2+\kappa_y^2) + (\mathrm{d}/\mathrm{d}z)^2\right)\phi'$ and $\nabla^2 w' = \left(-(\kappa_x^2+\kappa_y^2) + (\mathrm{d}/\mathrm{d}z)^2\right)w'$, therefore the equations can be non-dimensionalized with $\nabla^2 = \left(D^2-\alpha^2\right)/L^2$, $\nabla_1^2 = -\alpha^2/L^2$ where $\alpha = L\sqrt{\kappa_x^2+\kappa_y^2}$ and $D = L\mathrm{d}/\mathrm{d}z$, $\partial/\partial t = \partial/\partial\tau\ \left(\mu_I\overline{\phi}/L^2\right) = \omega\ \left(\mu_I\overline{\phi}/L^2\right)$, $\partial/\partial x = \beta/L$, $z = \hat{z}L$, $f(z) = w_0(z)L/(\mu_I\overline{\phi}(z))$, $g(z) = \phi_0(z)/\overline{\phi}(z)$. All the exponential terms eventually cancel out, and we arrive at

$$\begin{aligned}\left(\frac{\omega}{\mathrm{Pr}} - (D^2-\alpha^2)\right)(D^2-\alpha^2)f = -R\frac{\mathrm{d}\overline{q}_f}{\mathrm{d}z}\frac{L^3}{\epsilon\overline{\phi}}\alpha^2 g \\ -R\frac{\overline{E}L}{\overline{\phi}}\left(D^2-\alpha^2\right)\alpha^2 g - S\hat{z}\beta\left(D^2-\alpha^2\right)f - 2S\beta Df,\end{aligned} \tag{D.15}$$

$$\begin{aligned}-\frac{\epsilon\overline{E}}{L^2}\left(D^2-\alpha^2\right)Dg + \frac{\mathrm{d}\overline{q}_f}{\mathrm{d}z}Dg + \frac{\epsilon\overline{\phi}}{L^3}\omega(D^2-\alpha^2)g \\ + \frac{2\overline{q}_f}{L}(D^2-\alpha^2)g = \frac{\mathrm{d}\overline{q}_f}{\mathrm{d}z}f,\end{aligned} \tag{D.16}$$

where

$$R = \frac{\epsilon\bar{\phi}}{\mu\mu_I}, \quad \mathrm{Pr} = \frac{\mu}{\rho\bar{\phi}\mu_I}, \quad S = \frac{\rho\Gamma L^2}{\mu}. \tag{D.17}$$

Equations (D.15) and (D.16) are linear equations of order four and three, respectively. Therefore, four boundary conditions for the initial velocity fluctuation, $w_0(z)$, and three boundary conditions for the initial potential fluctuation, $\phi_0(z)$, are required to obtain a

unique solution. For the velocity fluctuation, we impose $w_0(z_0) = \partial w_0(z_0)/\partial z = 0$ and $w_0(z_0 + L) = \partial w_0(z_0 + L)/\partial z = 0$ based on no-slip boundary conditions and incompressibility of the fluid. For the potential fluctuation, it is assumed that the initial electric field fluctuations at the upper and lower boundaries are zero such that it is not violating Gauss's law, i.e. $\partial\phi_0(z_0)/\partial z = \partial\phi_0(z_0+L)/\partial z = 0$. The last boundary condition is determined by recognizing that the electrical conductivity decreases significantly with altitude in the lower atmosphere [247], and therefore we assume the lower boundary has much larger electrical conductivity than the upper boundary such that relatively the initial potential fluctuation at the lower boundary is negligible, i.e. $\phi_0(z_0) = 0$.

The boundary conditions are then transformed into the final dimensionless form: $f(z_0) = f'(z_0) = g(z_0) = g'(z_0) = 0$ for the lower boundary and $f(z_0 + L) = f'(z_0 + L) = g'(z_0 + L) = 0$ for the upper boundary. To ensure numerical stability, we follow Appendix A in Schneider and Watson [209] to solve the ODEs numerically with these boundary conditions using a shooting method. We also observed that changing boundary conditions for the potential (e.g., employing a Neumann condition for the electric field $g''(z_0) = g''(z_0 + L) = 0$) has little effect on the critical Rayleigh number.

APPENDIX E

Direct comparison of particle deposition in turbulent pipe flows with RANS and experiments

E.1 Problem setup

The system under consideration is the High Temperature Deposition Facility (see Fig. E.1(a)) in collaboration with Jeffery Bons et al at the Ohio State University (OSU). After declumping pretreatment, dust is injected at a 60° angle to a heated turbulent pipe flow at relevant engine operation conditions ($1375-1730\,\mathrm{K}$, $150-300\,\mathrm{m/s}$). Deposition is measured along the pipe as capture efficiency (CE), which is defined as the ratio of total mass deposited and total mass injected. The same experimental conditions are specified in our DNS simulations (see Fig. E.2) and RW models by OSU.

Two different RW models, the Discrete Random Walk (DRW) model proposed by Gosman and Loannides [84] and the Continuous Random Walk (CRW) model proposed by Dehbi [44], are considered. In the DRW model, turbulent dispersion is modeled as discrete interactions between a particle and a turbulent eddy where fluid fluctuation is independently sampled from a random Gaussian process for each eddy. CRW model improves upon DRW by continuously solving for the fluid fluctuation using a Langevin equation. Details on DRW and CRW models can be found in Gnanaselvam et al. [83]. However, as shown in Fig. E.1(b), DRW and CRW both significantly overpredict CE compared to experiments. DNS simulations are performed using the numerical framework described

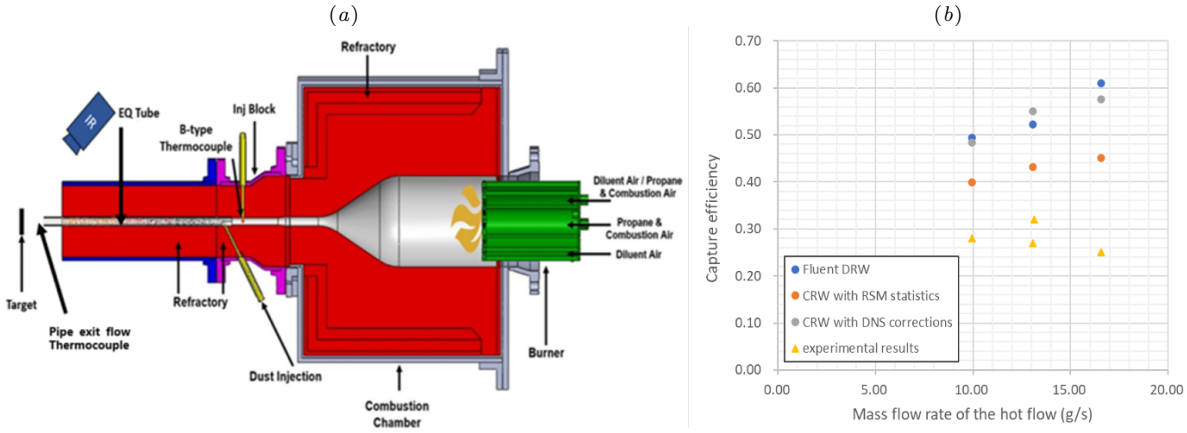

Figure E.1: (a) Experimental setup of the High Temperature Deposition Facility in collaboration with Jeffery Bons et al the Ohio State University. Dust is injected to a heated turbulent pipe flow at relevant engine operation conditions (1677 K, 150 m/s). Deposition is measured along the pipe as capture efficiency. (b) The measured capture efficiencies from experiments are significantly lower than both continuous and discrete random walk models (CRW and DRW) coupled with RANS. Figures adapted from Gnanaselvam et al. [83] with permission.

in Chapter II to uncover the major errors contributing to this discrepancy, with a grid resolution of $326 \times 280 \times 280$ to fully resolve the turbulence (1677K, 150m/s). 'All-stick' assumption is used, namely particles are counted as deposited and removed from the simulation once they collide with the wall, which is appropriate as the flow temperature is above the melting point of injected dust (ARD). The cut-cell immersed boundary method is used to model pipe walls. Scalar transport is modified to impose isothermal conditions at the immersed boundaries. Statistics are not computed until a statistically stationarity is reached for both phases.

E.2 Particle statistics

In our DNS simulations, particles are injected at same velocity, mass flow rate, and density as the OSU experiments (34.5 m/s, 0.01667 g/s, 2727 kg/m^3). The diameters span 1 to 10 µm with a truncated lognormal distribution same as Fig. 3.9 representative of Arizona road dust (ARD). The time-averaged root-mean-square velocity and streamwise velocity at $x/D = 10$ from the injection point are compared between fluid and particles

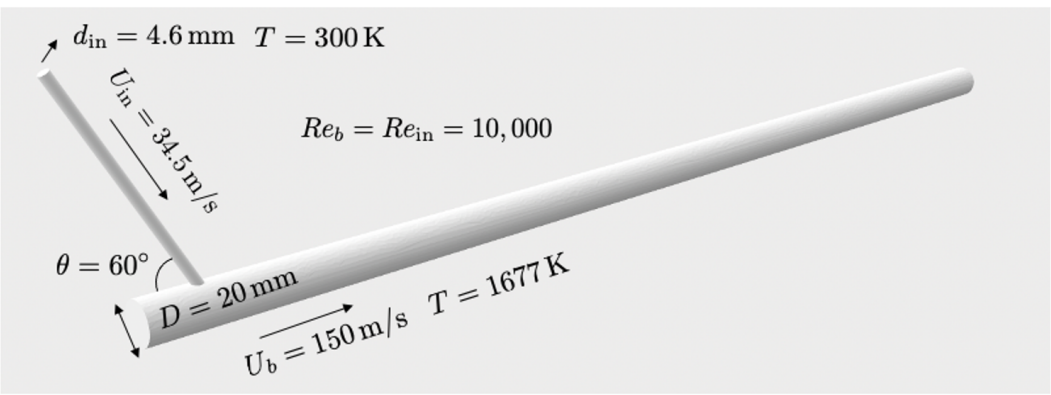

Figure E.2: Parameters and geometry used in the DNS simulations which are the same as OSU experiments [83].

in Fig. E.3. It can be seen that particles are lagging the fluid phase due to their relatively low injection velocities and large Stokes number $(0.57 - 57)$.

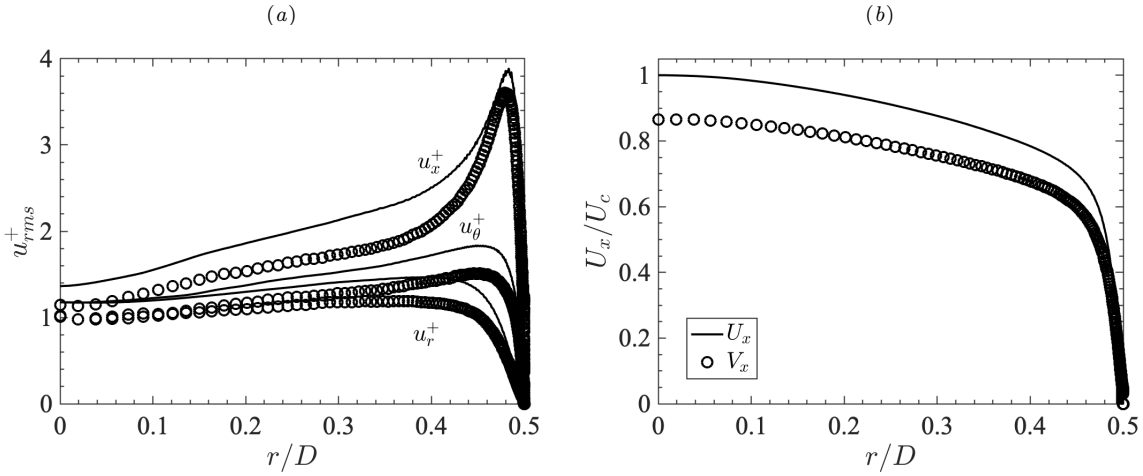

Figure E.3: Comparison of the mean fluid (–) and particle (∘) streamwise velocities at $x/D = 10$ as a function of radial position. (a) Normalized root-mean-square velocity and (b) normalized streamwise velocity.

Figure E.4 shows the departing and approaching radial velocities ($u_r^-(r)$ and $u_r^+(r)$) defined in § 3.4.2 of both fluid phase and particles of four different sizes. As shown in Fig. E.4(a), on average the fluid exhibits zero net radial motion across the pipe ($u_r^+(r) \approx u_r^-(r)$). Smaller particles ($d_p = 1\mu\text{m}$) follow similar velocity profiles as the fluid, while the velocities associated with larger particles are observed to deviate from the fluid due to

increased inertia. In addition, the difference between $u_r^+(r)$ and $u_r^-(r)$ increases drastically, indicating larger particles impact the wall at a notably higher speed. Especially very close to the wall (see Fig. E.4(b)), larger particles possess larger $u_r^+(r)$ and smaller $u_r^-(r)$. Note that $u_r^-(r) = 0$ for 10 µm particles when $r/D > 0.497$, meaning all of them are rapidly impacting the wall when they reach this near-wall region.

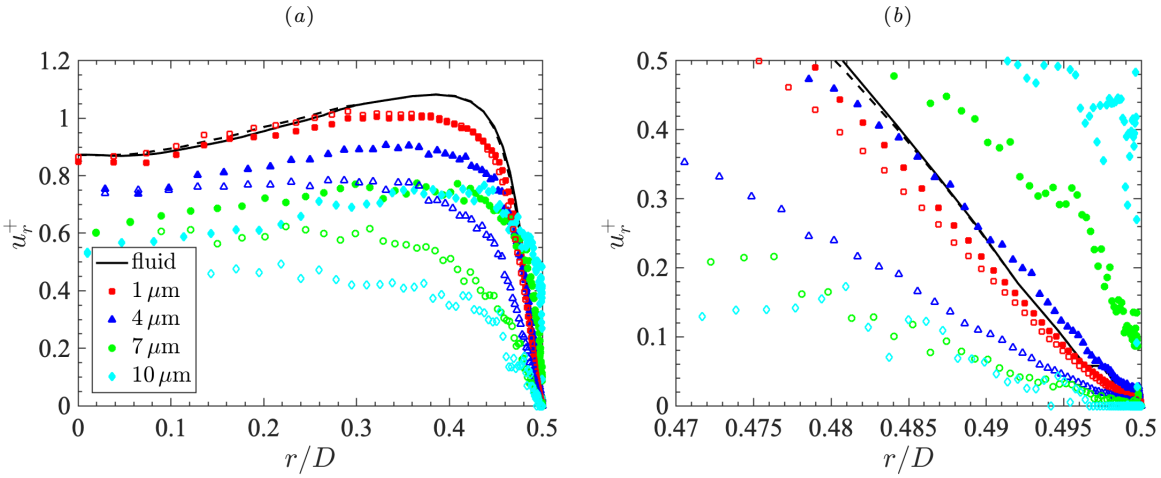

Figure E.4: The departing (hollow/dashed) and approaching (solid) velocities towards the pipe wall of fluid (line) and particles of four different sizes (symbols) over (a) the entire pipe and (b) near-wall region at $x/D = 10$. Line and symbol types same as Fig. 3.11.

E.3 Particle deposition

Even though the net radial velocities of particles are monotonically correlated with particle size, it does not directly translate to the same trend for deposition rates. Particles of the same size under these conditions (1677K, 150m/s) have Stokes numbers or τ_p^+ more than 10 times larger than those in cold pipe flows (298K, 4m/s) descibed in Chapter VI. As a result, a portion of larger particles now belongs to the inertia-moderated regime where particle deposition decays with increasing particle size. Direct comparison of deposition rates predicted by RW, DNS, and experiments under these realistic conditions provides a roadmap where errors in existing RW models can be identified or even mitigated by leveraging two-phase turbulence statistics from DNS.

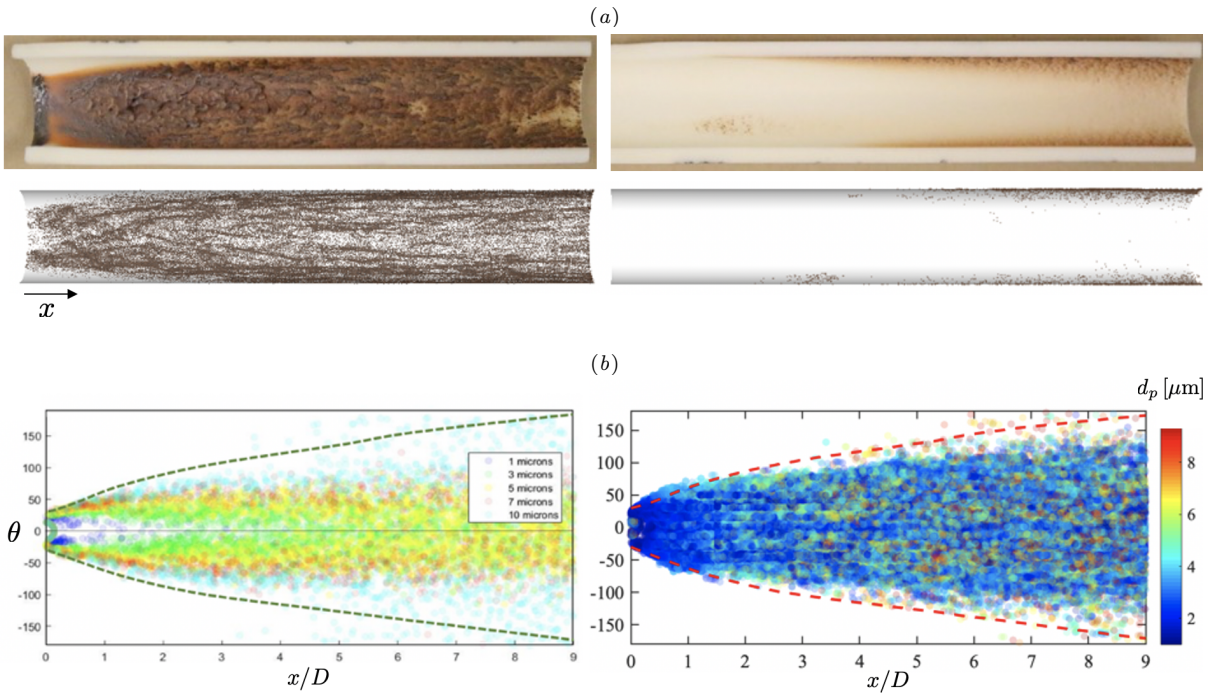

Figure E.5: (a) Qualitative comparison of DNS results (bottom) and OSU experiments (top) at 1669K and 200 m/s. Left and right are cross-sectional views at $\theta = 90°$ and $-90°$ respectively. (b) Azimuthal distribution of deposited particles as a function of downstream locations predicted by CRW model (left) and DNS (right). Dashed red lines represent experimental measurements. A fully-deposited pipe cross-section has θ span $-180°$ to $180°$. Figures showing experiments and CRW predictions are adapted from Gnanaselvam et al. [83] with permission.

Qualitative comparison of deposition patterns from DNS and OSU experiments is shown in Fig. E.5(a). Similar streak-like patterns are observed in both simulations and experiments which is primarily due to particle clustering in low-speed streak regions of wall-bounded flows [244, 282, 151]. It should be noted that dust accumulation and morphology changes observed in the experiments is not captured in the DNS simulations. Nevertheless, the azimuthal distributions of deposited particles measured by the angle to the injection point (θ) are in good agreement with experiments as shown in Fig. E.5(b). The CRW model, on the other hand, underpredicts particle spreading downstream, which again highlights the importance of correctly predicting turbulent dispersion.

Instantaneous distributions of small ($1 - 3\,\mu$m), mid-sized ($4 - 6\,\mu$m), and large ($8 - 10\,\mu$m) particles are shown in Fig. E.6(a). Small particles are seen to preferentially dis-

tribute on the injection side of the pipe whereas large particles penetrate further from the wall due to their large inertia. It is the mid-sized particles that accumulate in the low-speed streak regions, which can potentially lead to enhanced deposition. To confirm this, the capture efficiency for different particle sizes is shown in Fig. E.6(b) that compares DNS with CRW and DRW. Mid-sized particles exhibit the highest capture efficiency as expected. Furthermore, both random walk models are in decent agreement with DNS predictions for small and large particles but deviate for mid-sized particles, which again might be associated with the particle clustering observed in Fig. E.6(a) that is not captured by RW models. The overall CE predicted by DNS is estimated to be 20 %.

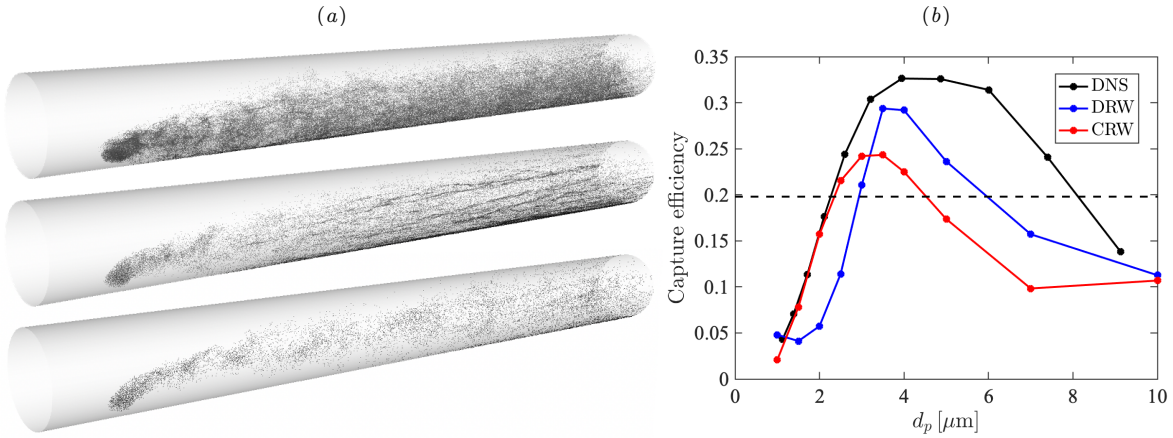

Figure E.6: (a) Instantaneous particle distribution for $d_p \in [1, 3]$ µm (top), $[4, 6]$ µm (middle), and $[8, 10]$ µm (bottom) from DNS. (b) Capture efficiency predicted by DNS, DRW, and CRW with the dashed line showing the overall capture efficiency 20% estimated by DNS. Data of CRW and DRW provided by Gnanaselvam et al. [83].

Figure E.7 compares the deposited particle mass per length normalized by total injected particle mass from DNS, experiments, and RANS coupled with CRW model. The DNS prediction is in good agreement with the experiments, confirming that the 'all-stick' assumption is appropriate when fluid temperature is above the melting temperature of dust. The CRW model is seen to underpredict deposition for $x/D < 10$, but overpredict deposition for $x/D > 15$. Such error can be either from RANS fluid solver especially in the

near-wall regions where anisotropy is not accounted for, or from dispersion predicted by RW models. One-to-one comparisons between DNS and RANS provides route for model improvement. Two-phase turbulence statistics from DNS will be leveraged to quantify errors in existing RW and RANS models and provide needed inputs. For exmaple, non-zero components of Reynolds stress tensor from DNS will be directly fed into RW models in place of RANS, which enable us to isolate errors introduced by RW models.

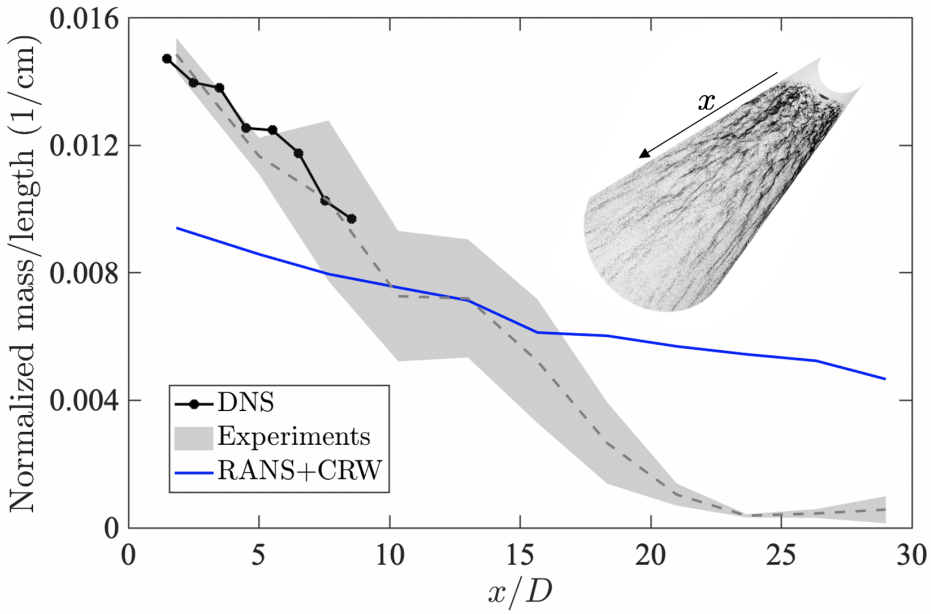

Figure E.7: Normalized deposited mass per unit length as a function of streamwise locations. The grey dashed line represents the mean experimental measurements. Data of CRW and experiments provided by Gnanaselvam et al. [83].

BIBLIOGRAPHY

[1] *Large-scale Atomic/Molecular Massively Parallel Simulator, LAMMPS user manual.* AIREBO description, Sandia Corporation, USA, 2012.

[2] S. Aboud, D. Marreiro, M. Saraniti, and R. Eisenberg. A poisson P^3M force field scheme for particle-based simulations of ionic liquids. *Journal of Computational Electronics*, 3(2):117–133, 2004.

[3] A. Aliseda, A. Cartellier, F. Hainaux, and J. C. Lasheras. Effect of preferential concentration on the settling velocity of heavy particles in homogeneous isotropic turbulence. *Journal of Fluid Mechanics*, 468:77–105, 2002.

[4] T. B. Anderson and R. Jackson. Fluid mechanical description of fluidized beds. Equations of motion. *Industrial & Engineering Chemistry Fundamentals*, 6(4):527–539, 1967.

[5] P. Atten, F. M. J. McCluskey, and A. C. Lahjomri. The electrohydrodynamic origin of turbulence in electrostatic precipitators. *IEEE Transactions on Industry Applications*, (4):705–711, 1987.

[6] M. U. Bäbler, M. Morbidelli, and J. Baldyga. Modelling the breakup of solid aggregates in turbulent flows. *Journal of Fluid Mechanics*, 612:261–289, 2008.

[7] D. H. Bache. Floc rupture and turbulence: a framework for analysis. *Chemical Engineering Science*, 59(12):2521–2534, 2004.

[8] S. Balachandar and J. K. Eaton. Turbulent dispersed multiphase flow. *Annual Review of Fluid Mechanics*, 42:111–133, 2010.

[9] P. F. Batcho, J. C. Moller, C. Padova, and M. G. Dunn. Interpretation of gas turbine response due to dust ingestion. 1987.

[10] S. K. Beal. Deposition of particles in turbulent flow on channel or pipe walls. *Nuclear science and engineering*, 40(1):1–11, 1970.

[11] N. N. Beams, L. N. Olson, and J. B. Freund. A finite element based pˆ3m method for n-body problems. *SIAM Journal on Scientific Computing*, 38(3):A1538–A1560, 2016.

[12] P. Begat, D. A. V. Morton, J. N. Staniforth, and R. Price. The cohesive-adhesive balances in dry powder inhaler formulations II: influence on fine particle delivery characteristics. *Pharmaceutical Research*, 21(10):1826–1833, 2004.

[13] J. Bellan. A new approach to soot control in diesel engines by fuel-drop charging. *Combustion and Flame*, 51:117–119, 1983.

[14] J. Bellan and K. Harstad. Electrostatic dispersions and evaporation of clusters of drops of high-energy fuel for soot control. In *Symposium (International) on Combustion*, volume 26, pages 1713–1722. Elsevier, 1996.

[15] C. M. Bender and S. A. Orszag. *Advanced mathematical methods for scientists and engineers I: Asymptotic methods and perturbation theory.* Springer Science, 2013.

[16] L. Bergström. Hamaker constants of inorganic materials. *Advances in Colloid and Interface Science*, 70:125–169, 1997.

[17] H. Bijl, D. Lucor, S. Mishra, and C. Schwab. *Uncertainty quantification in computational fluid dynamics*, volume 92. Springer Science & Business Media, 2013.

[18] L. Bocquet, W. Losert, D. Schalk, T. C. Lubensky, and J. P. Gollub. Granular shear flow dynamics and forces: Experiment and continuum theory. *Physical Review E*, 65(1):011307, 2001.

[19] N. Bojdo and A. Filippone. A simple model to assess the role of dust composition and size on deposition in rotorcraft engines. *Aerospace*, 6(4):44, 2019.

[20] T. C. Bond, S. J. Doherty, D. W. Fahey, P. M. Forster, T. Berntsen, B. J. DeAngelo, M. G. Flanner, S. Ghan, B. Kärcher, D. Koch, et al. Bounding the role of black carbon in the climate system: A scientific assessment. *Journal of Geophysical Research: Atmospheres*, 118(11):5380–5552, 2013.

[21] J. Bons, R. Prenter, and S. Whitaker. A simple physics-based model for particle rebound and deposition in turbomachinery. *Journal of Turbomachinery*, 139(8), 2017.

[22] L. Bourouiba. Turbulent gas clouds and respiratory pathogen emissions: potential implications for reducing transmission of covid-19. *Jama*, 323(18):1837–1838, 2020.

[23] L. Bourouiba, E. Dehandschoewercker, and J. W. Bush. Violent expiratory events: on coughing and sneezing. *Journal of Fluid Mechanics*, 745:537–563, 2014.

[24] L. G. Bravo, M. Murugan, A. Ghoshal, S. Su, R. Koneru, N. Jain, P. Khare, and A. Flatau. Uncertainty quantification in large eddy simulations of cmas attack and deposition in gas turbine engines. In *AIAA Scitech 2021 Forum*, page 0766, 2021.

[25] M. Breuer and N. Almohammed. Modeling and simulation of particle agglomeration in turbulent flows using a hard-sphere model with deterministic collision detection and enhanced structure models. *International Journal of Multiphase Flow*, 73:171–206, 2015.

[26] J. W. Brooke, T. Hanratty, and J. McLaughlin. Free-flight mixing and deposition of aerosols. *Physics of Fluids*, 6(10):3404–3415, 1994.

[27] K. A. Browning, T. W. Harrold, and J. R. Starr. Richardson number limited shear zones in the free atmosphere. *Quarterly Journal of the Royal Meteorological Society*, 96(407):40–49, 1970.

[28] R. Bruinsma and S. Alexander. Theory of electrohydrodynamic instabilities in electrolytic cells. *The Journal of Chemical Physics*, 92(5):3074–3085, 1990.

[29] K. M. Butler and B. F. Farrell. Three-dimensional optimal perturbations in viscous shear flow. *Physics of Fluids*, 4(8):1637–1650, 1992.

[30] J. Capecelatro and O. Desjardins. An Euler–Lagrange strategy for simulating particle-laden flows. *Journal of Computational Physics*, 238:1–31, 2013.

[31] J. Capecelatro, P. Pepiot, and O. Desjardins. Numerical characterization and modeling of particle clustering in wall-bounded vertical risers. *Chemical Engineering Journal*, 245:295–310, 2014.

[32] L. Ceresiat, H. Grosshans, and M. V. Papalexandris. Powder electrification during pneumatic transport: The role of the particle properties and flow rates. *Journal of Loss Prevention in the Process Industries*, 58:60–69, 2019.

[33] J. Chabadová, Š. Papučík, and R. Nosek. Particle emissions from biomass combustion. In *AIP Conference Proceedings*, volume 1608, pages 67–70. American Institute of Physics, 2014.

[34] S. Chen and S. Li. Collision-induced breakage of agglomerates in homogenous isotropic turbulence laden with adhesive particles. *arXiv preprint arXiv:2004.09726*, 2020.

[35] S. Chen, S. Li, and J. S. Marshall. Exponential scaling in early-stage agglomeration of adhesive particles in turbulence. *Physical Review Fluids*, 4(2):024304, 2019.

[36] J. Chun, D. L. Koch, S. L. Rani, A. Ahluwalia, and L. R. Collins. Clustering of aerosol particles in isotropic turbulence. *Journal of Fluid Mechanics*, 536:219–251, 2005.

[37] R. Cocco, F. Shaffer, R. Hays, S. R. Karri, and T. Knowlton. Particle clusters in and above fluidized beds. *Powder Technology*, 203(1):3–11, 2010.

[38] R. Cocco, S. R. Karri, T. Knowlton, et al. Introduction to fluidization. *Chem. Eng. Prog*, 110(11): 21–29, 2014.

[39] H. Couchman. Mesh-refined P3M-A fast adaptive N-body algorithm. *The Astrophysical Journal*, 368:L23–L26, 1991.

[40] J. M. Crosby, S. Lewis, J. P. Bons, W. Ai, and T. H. Fletcher. Effects of particle size, gas temperature and metal temperature on high pressure turbine deposition in land based gas turbines from various synfuels. In *ASME Turbo Expo 2007: Power for Land, Sea, and Air*, pages 1365–1376. American Society of Mechanical Engineers Digital Collection, 2007.

[41] E. D. Crowe and J. P. Bons. Effects of dust composition on particle deposition in an effusion cooling geometry. In *Turbo Expo: Power for Land, Sea, and Air*, volume 58585, page V02DT47A011. American Society of Mechanical Engineers, 2019.

[42] P. A. Cundall and O. D. L. Strack. A discrete numerical model for granular assemblies. *Geotechnique*, 29(1):47–65, 1979.

[43] C. Davies. Deposition of aerosols from turbulent flow through pipes. *Proceedings of the Royal Society of London. Series A. Mathematical and Physical Sciences*, 289(1417):235–246, 1966.

[44] A. Dehbi. Turbulent particle dispersion in arbitrary wall-bounded geometries: A coupled cfd-langevin-equation based approach. *International Journal of Multiphase Flow*, 34(9):819–828, 2008.

[45] B. V. Derjaguin, V. M. Muller, and Y. P. Toporov. Effect of contact deformations on the adhesion of particles. *Journal of Colloid and Interface Science*, 53(2):314–326, 1975.

[46] M. Deserno and C. Holm. How to mesh up Ewald sums. I. A theoretical and numerical comparison of various particle mesh routines. *Journal of Chemical Physics*, 109(18):7678–7693, 1998.

[47] M. Deserno and C. Holm. How to mesh up Ewald sums. II. An accurate error estimate for the particle–particle–particle-mesh algorithm. *Journal of Chemical Physics*, 109(18):7694–7701, 1998.

[48] O. Desjardins, G. Blanquart, G. Balarac, and H. Pitsch. High order conservative finite difference scheme for variable density low Mach number turbulent flows. *Journal of Computational Physics*, 227(15):7125–7159, 2008.

[49] O. Desjardins, R. O. Fox, and P. Villedieu. A quadrature-based moment method for dilute fluid-particle flows. *Journal of Computational Physics*, 227(4):2514–2539, 2008.

[50] M. Di Renzo and J. Urzay. Aerodynamic generation of electric fields in turbulence laden with charged inertial particles. *Nature Communications*, 9(1):1676, 2018.

[51] M. Di Renzo, P. Johnson, M. Bassenne, L. Villafañe, and J. Urzay. Mitigation of turbophoresis in particle-laden turbulent channel flows by using incident electric fields. *Physical Review Fluids*, 4 (12):124303, 2019.

[52] J. P. Díaz Téllez. *Adhesion enhancement of a biomimetic dry adhesive by means of an increase to the Hamaker constant via nanocomposite formation.* PhD thesis, Applied Sciences: School of Engineering Science, 2013.

[53] F. F. Dizaji and J. S. Marshall. On the significance of two-way coupling in simulation of turbulent particle agglomeration. *Powder Technology*, 318:83–94, 2017.

[54] F. F. Dizaji, J. S. Marshall, and J. R. Grant. Collision and breakup of fractal particle agglomerates in a shear flow. *Journal of Fluid Mechanics*, 862:592–623, 2019.

[55] M. Dong, S. Li, J. Xie, and J. Han. Experimental studies on the normal impact of fly ash particles with planar surfaces. *Energies*, 6(7):3245–3262, 2013.

[56] M. G. Dunn, A. J. Baran, and J. Miatech. Operation of gas turbine engines in volcanic ash clouds. 1996.

[57] J. K. Eaton and J. R. Fessler. Preferential concentration of particles by turbulence. *International Journal of Multiphase Flow*, 20:169–209, 1994.

[58] J. Eggels, F. Unger, M. Weiss, J. Westerweel, R. Adrian, R. Friedrich, and F. Nieuwstadt. Fully developed turbulent pipe flow: a comparison between direct numerical simulation and experiment. *Journal of Fluid Mechanics*, 268:175–210, 1994.

[59] S. Elghobashi. On predicting particle-laden turbulent flows. *Applied scientific research*, 52(4): 309–329, 1994.

[60] S. Elghobashi and G. C. Truesdell. Direct simulation of particle dispersion in a decaying isotropic turbulence. *Journal of Fluid Mechanics*, 242:655–700, 1992.

[61] J. P. Engelbrecht, E. V. McDonald, J. A. Gillies, and A. W. Gertler. Department of defense enhanced particulate matter surveillance program (epmsp). Technical report, DESERT RESEARCH INST RENO NV, 2008.

[62] F. Esposito, R. Molinaro, C. I. Popa, C. Molfese, F. Cozzolino, L. Marty, K. Taj-Eddine, G. Di Achille, G. Franzese, S. Silvestro, and G. G. Ori. The role of the atmospheric electric field in the dust-lifting process. *Geophysical Research Letters*, 43(10):5501–5508, 2016.

[63] V. Eswaran and S. B. Pope. An examination of forcing in direct numerical simulations of turbulence. *Computers & Fluids*, 16(3):257–278, 1988.

[64] P. P. Ewald. The calculation of optical and electrostatic grid potential. *Annual Physics*, 64(3): 253–287, 1921.

[65] J. Exner, M. Hahn, M. Schubert, D. Hanft, P. Fuierer, and R. Moos. Powder requirements for aerosol deposition of alumina films. *Advanced Powder Technology*, 26(4):1143–1151, 2015.

[66] R. D. Falgout and U. M. Yang. hypre: A library of high performance preconditioners. In *International Conference on Computational Science*, pages 632–641. Springer, 2002.

[67] M. Fanelli, D. L. Feke, and I. Manas-Zloczower. Prediction of the dispersion of particle clusters in the nano-scale—part i: Steady shearing responses. *Chemical Engineering Science*, 61(2):473–488, 2006.

[68] M. Fanelli, D. L. Feke, and I. Manas-Zloczower. Prediction of the dispersion of particle clusters in the nano-scale–Part II, unsteady shearing responses. *Chemical Engineering Science*, 61(15): 4944–4956, 2006.

[69] B. Faure, G. Salazar-Alvarez, and L. Bergström. Hamaker constants of iron oxide nanoparticles. *Langmuir*, 27(14):8659–8664, 2011.

[70] J. C. Flesch, P. T. Spicer, and S. E. Pratsinis. Laminar and turbulent shear-induced flocculation of fractal aggregates. *AIChE Journal*, 45(5):1114–1124, 1999.

[71] B. Forsyth, B. Y. Liu, and F. J. Romay. Particle charge distribution measurement for commonly generated laboratory aerosols. *Aerosol Science and Technology*, 28(6):489–501, 1998.

[72] P. R. Forsyth, D. R. H. Gillespie, and M. McGilvray. Development and applications of a coupled particle deposition–dynamic mesh morphing approach for the numerical simulation of gas turbine flows. *Journal of Engineering for Gas Turbines and Power*, 140(2), 2018.

[73] S. Friedlander and H. Johnstone. Deposition of suspended particles from turbulent gas streams. *Industrial & Engineering Chemistry*, 49(7):1151–1156, 1957.

[74] S. K. Friedlander. *Smoke, dust, and haze*, volume 198. Oxford University Press New York, 2000.

[75] K. C. Galbreath, D. L. Toman, and C. J. Zygarlicke. Reducing power production costs by utilizing petroleum coke. Technical report, University of North Dakota (US), 1999.

[76] A. A. Galeev, S. S. Moiseev, and R. Z. Sagdeev. The theory of the stability of non-uniform plasma and anomalous diffusion. *Journal of Nuclear Energy. Part C, Plasma Physics, Accelerators, Thermonuclear Research*, 6(6):645, 1964.

[77] R. Gargallo, P. H. Hünenberger, F. X. Avilés, and B. Oliva. Molecular dynamics simulation of highly charged proteins: Comparison of the particle-particle particle-mesh and reaction field methods for the calculation of electrostatic interactions. *Protein Science*, 12(10):2161–2172, 2003.

[78] B. Gayen and M. Alam. Algebraic and exponential instabilities in a sheared micropolar granular fluid. *Journal of Fluid Mechanics*, 567:195–233, 2006.

[79] T. Gebhardt and S. Grossmann. Chaos transition despite linear stability. *Physical Review E*, 50 (5):3705, 1994.

[80] D. Geldart. Types of gas fluidization. *Powder Technology*, 7(5):285–292, 1973.

[81] D. Gidaspow. *Multiphase flow and fluidization: continuum and kinetic theory descriptions*. Academic Pr, 1994.

[82] J. S. Gilbert, S. J. Lane, R. S. J. Sparks, and T. Koyaguchi. Charge measurements on particle fallout from a volcanic plume. *Nature*, 349(6310):598, 1991.

[83] P. Gnanaselvam, C. H. Lo, J. Han, and J. P. Bons. Turbulent dispersion and deposition of micron-sized particles in a turbulent pipe flow at high temperatures. In *AIAA Scitech 2021 Forum*, page 0850, 2021.

[84] A. Gosman and E. Loannides. Aspects of computer simulation of liquid-fueled combustors. *Journal of energy*, 7(6):482–490, 1983.

[85] M. Goudarzy, M. M. Rahman, D. König, and T. Schanz. Influence of non-plastic fines content on maximum shear modulus of granular materials. *Soils and Foundations*, 56(6):973–983, 2016.

[86] T. J. Grahame and R. B. Schlesinger. Cardiovascular health and particulate vehicular emissions: a critical evaluation of the evidence. *Air Quality, Atmosphere & Health*, 3(1):3–27, 2010.

[87] G. Grant and W. Tabakoff. Erosion prediction in turbomachinery resulting from environmental solid particles. *Journal of Aircraft*, 12(5):471–478, 1975.

[88] H. Grosshans and M. V. Papalexandris. On the accuracy of the numerical computation of the electrostatic forces between charged particles. *Powder Technology*, 322:185–194, 2017.

[89] H. Grosshans and M. V. Papalexandris. Direct numerical simulation of triboelectric charging in particle-laden turbulent channel flows. *Journal of Fluid Mechanics*, 818:465–491, 2017.

[90] G. Grötzbach. Spatial resolution requirements for direct numerical simulation of the rayleigh-bénard convection. *Journal of computational physics*, 49(2):241–264, 1983.

[91] Y. Gu, A. Ozel, and S. Sundaresan. A modified cohesion model for CFD–DEM simulations of fluidization. *Powder Technology*, 296:17–28, 2016.

[92] P. Gualtieri, F. Picano, and C. M. Casciola. Anisotropic clustering of inertial particles in homogeneous shear flow. *Journal of Fluid Mechanics*, 629:25–39, 2009.

[93] A. Guha. A unified eulerian theory of turbulent deposition to smooth and rough surfaces. *Journal of Aerosol Science*, 28(8):1517–1537, 1997.

[94] A. Guha. Transport and deposition of particles in turbulent and laminar flow. *Annual Review of Fluid Mechanics*, 40:311–341, 2008.

[95] J. Hærvig. On the adhesive behaviour of micron-sized particles in turbulent flow. 2017.

[96] H. C. Hamaker. The london—van der Waals attraction between spherical particles. *Physica*, 4(10): 1058–1072, 1937.

[97] A. Hamed, W. C. Tabakoff, and R. V. Wenglarz. Erosion and deposition in turbomachinery. *Journal of Propulsion and Power*, 22(2):350–360, 2006.

[98] R. G. Harrison and M. H. P. Ambaum. Enhancement of cloud formation by droplet charging. *Proceedings of the Royal Society of London A*, 464(2098):2561–2573, 2008.

[99] P. A. Hartley, G. D. Parfitt, and L. B. Pollack. The role of the van der Waals force in the agglomeration of powders containing submicron particles. *Powder Technology*, 42(1):35–46, 1985.

[100] G. Hendrickson. Electrostatics and gas phase fluidized bed polymerization reactor wall sheeting. *Chemical Engineering Science*, 61(4):1041–1064, 2006.

[101] K. Higashitani, K. Iimura, and H. Sanda. Simulation of deformation and breakup of large aggregates in flows of viscous fluids. *Chemical Engineering Science*, 56(9):2927–2938, 2001.

[102] E. J. Hinch. *Perturbation methods*. Cambridge University Press, 1991.

[103] C. A. Ho and M. Sommerfeld. Modelling of micro-particle agglomeration in turbulent flows. *Chemical Engineering Science*, 57(15):3073–3084, 2002.

[104] R. W. Hockney and J. W. Eastwood. *Computer simulation using particles*. CRC Press, 1988.

[105] W. A. Hoppel and S. G. Gathman. Charge transport through an aerosol cloud. *Journal of Applied Physics*, 41(5):1971–1977, 1970.

[106] E. Howard and P. Hesketh. Fine particles in gaseous media. *Ann Arbor Science Publishers Inc., Michigan, USA*, 1977.

[107] P. J. Ireland, A. D. Bragg, and L. R. Collins. The effect of Reynolds number on inertial particle dynamics in isotropic turbulence. Part 1. Simulations without gravitational effects. *Journal of Fluid Mechanics*, 796:617–658, 2016.

[108] P. J. Ireland, A. D. Bragg, and L. R. Collins. The effect of Reynolds number on inertial particle dynamics in isotropic turbulence. Part 2. Simulations with gravitational effects. *Journal of Fluid Mechanics*, 796:659–711, 2016.

[109] S. Janhäll. Review on urban vegetation and particle air pollution–deposition and dispersion. *Atmospheric environment*, 105:130–137, 2015.

[110] P. Jarvis, B. Jefferson, J. Gregory, and S. A. Parsons. A review of floc strength and breakage. *Water Research*, 39(14):3121–3137, 2005.

[111] X. Jin and J. S. Marshall. The role of fluid turbulence on contact electrification of suspended particles. *Journal of Electrostatics*, 87:217–227, 2017.

[112] S. Johansen. The deposition of particles on vertical walls. *International Journal of Multiphase Flow*, 17(3):355–376, 1991.

[113] K. L. Johnson and J. A. Greenwood. An adhesion map for the contact of elastic spheres. *Journal of Colloid and Interface Science*, 192(2):326–333, 1997.

[114] K. L. Johnson, K. Kendall, and A. D. Roberts. Surface energy and the contact of elastic solids. *Proceedings of the royal society of London. A. mathematical and physical sciences*, 324(1558):301–313, 1971.

[115] R. M. Jones and L. M. Brosseau. Aerosol transmission of infectious disease. *Journal of Occupational and Environmental Medicine*, 57(5):501–508, 2015.

[116] G. Kallio and M. Reeks. A numerical simulation of particle deposition in turbulent boundary layers. *International Journal of Multiphase Flow*, 15(3):433–446, 1989.

[117] A. U. Karnik and J. S. Shrimpton. Mitigation of preferential concentration of small inertial particles in stationary isotropic turbulence using electrical and gravitational body forces. *Physics of Fluids*, 24(7):073301, 2012.

[118] A. U. Karnik and J. S. Shrimpton. Mitigation of preferential concentration of small inertial particles in stationary isotropic turbulence using electrical and gravitational body forces. *Physics of Fluids*, 24(7):073301, 2012.

[119] M. H. Kasbaoui, D. L. Koch, G. Subramanian, and O. Desjardins. Preferential concentration driven instability of sheared gas–solid suspensions. *Journal of Fluid Mechanics*, 770:85–123, 2015.

[120] M. H. Kasbaoui, R. G. Patel, D. L. Koch, and O. Desjardins. An algorithm for solving the Navier–Stokes equations with shear-periodic boundary conditions and its application to homogeneously sheared turbulence. *Journal of Fluid Mechanics*, 833:687–716, 2017.

[121] R. Kasper, J. Turnow, and N. Kornev. Numerical modeling and simulation of particulate fouling of structured heat transfer surfaces using a multiphase euler-lagrange approach. *International Journal of Heat and Mass Transfer*, 115:932–945, 2017.

[122] L. Kelvin. Stability of fluid motion: rectilinear motion of viscous fluid between two parallel plates. *Philosophical Magazine*, 24(5):188–196, 1887.

[123] I. M. Kennedy. The health effects of combustion-generated aerosols. *Proceedings of the Combustion Institute*, 31(2):2757–2770, 2007.

[124] K. S. Klemmer and M. E. Mueller. Implied models approach for turbulence model form physics-based uncertainty quantification. *Phys. Rev. Fluids*, 6:044606, Apr 2021. doi: 10.1103/PhysRevFluids.6.044606. URL `https://link.aps.org/doi/10.1103/PhysRevFluids.6.044606`.

[125] J. F. Kok and N. O. Renno. The effects of electric forces on dust lifting: Preliminary studies with a numerical model. In *Journal of Physics: Conference Series*, volume 142, page 012047. IOP Publishing, 2008.

[126] J. Kolehmainen, A. Ozel, C. M. Boyce, and S. Sundaresan. A hybrid approach to computing electrostatic forces in fluidized beds of charged particles. *AIChE Journal*, 62(7):2282–2295, 2016.

[127] A. Koper, K. Prałat, J. Ciemnicka, and K. Buczkowska. Influence of the calcination temperature of synthetic gypsum on the particle size distribution and setting time of modified building materials. *Energies*, 13(21):5759, 2020.

[128] P. Kosinski and A. C. Hoffmann. An extension of the hard-sphere particle–particle collision model to study agglomeration. *Chemical Engineering Science*, 65(10):3231–3239, 2010.

[129] Y. Kousaka, K. Okuyama, A. Shimizu, and T. Yoshida. Dispersion mechanism of aggregate particles in air. *Journal of Chemical Engineering of Japan*, 12(2):152–159, 1979.

[130] W. B. Kunkel. The static electrification of dust particles on dispersion into a cloud. *Journal of Applied Physics*, 21(8):820–832, 1950.

[131] A. Lai. Particle deposition indoors: a review. *Indoor air*, 12(4):211–214, 2002.

[132] A. C. Lai and W. W. Nazaroff. Modeling indoor particle deposition from turbulent flow onto smooth surfaces. *Journal of aerosol science*, 31(4):463–476, 2000.

[133] G. Lefevre and A. Jolivet. Calculation of hamaker constants applied to the deposition of metallic oxide particles at high temperature. In *Proceedings of International Conference on Heat Exchanger Fouling and Cleaning*, volume 8, pages 120–24, 2009.

[134] S. Li, J. Xie, M. Dong, and L. Bai. Rebound characteristics for the impact of sio2 particle onto a flat surface at different temperatures. *Powder Technology*, 284:418–428, 2015.

[135] W. Lick, L. Jin, and J. Gailani. Initiation of movement of quartz particles. *Journal of Hydraulic Engineering*, 130(8):755–761, 2004.

[136] E. M. Lifschitz and L. P. Pitajewski. Physical kinetics. In *Textbook of Theoretical Physics. 10.* 1983.

[137] B. Y. Liu and J. K. Agarwal. Experimental observation of aerosol deposition in turbulent flow. *Journal of Aerosol Science*, 5(2):145–155, 1974.

[138] L. F. Liu, Z. P. Zhang, and A. B. Yu. Dynamic simulation of the centripetal packing of mono-sized spheres. *Physica A: Statistical Mechanics and its Applications*, 268(3-4):433–453, 1999.

[139] P. Liu and C. M. Hrenya. Cluster-induced deagglomeration in dilute gravity-driven gas-solid flows of cohesive grains. *Physical Review Letters*, 121(23):238001, 2018.

[140] X. Liu, J. Kolehmainen, I. Nwogbaga, A. Ozel, and S. Sundaresan. Effect of particle size on tribocharging. *Powder Technology*, 375:199–209, 2020.

[141] K. H. Lloyd, C. H. Low, and R. A. Vincent. Turbulence, billows and gravity waves in a high shear region of the upper atmosphere. *Planetary and Space Science*, 21(4):653–661, 1973.

[142] J. Lowell and A. C. Rose-Innes. Contact electrification. *Advances in Physics*, 29(6):947–1023, 1980.

[143] J. Lu and R. A. Shaw. Charged particle dynamics in turbulence: Theory and direct numerical simulations. *Physics of Fluids*, 27(6):065111, 2015.

[144] J. Lu, H. Nordsiek, E. W. Saw, and R. A. Shaw. Clustering of charged inertial particles in turbulence. *Physical Review Letters*, 104(18):184505, 2010.

[145] T. S. Lundgren. Linearly forces isotropic turbulence. Technical report, Center for Turbulence Research, 2003.

[146] A. Mahecha-Botero, J. R. Grace, S. Elnashaie, and C. J. Lim. Advances in modeling of fluidized-bed catalytic reactors: a comprehensive review. *Chemical Engineering Communications*, 196(11): 1375–1405, 2009.

[147] M. Malik, M. Alam, and J. Dey. Nonmodal energy growth and optimal perturbations in compressible plane Couette flow. *Physics of Fluids*, 18(3):034103, 2006.

[148] M. Malik, J. Dey, and M. Alam. Linear stability, transient energy growth, and the role of viscosity stratification in compressible plane Couette flow. *Physical Review E*, 77(3):036322, 2008.

[149] G. Mallouppas, W. K. George, and B. G. M. van Wachem. New forcing scheme to sustain particle-laden homogeneous and isotropic turbulence. *Physics of Fluids*, 25(8):083304, 2013.

[150] E. R. Mansell and C. L. Ziegler. Aerosol effects on simulated storm electrification and precipitation in a two-moment bulk microphysics model. *Journal of the Atmospheric Sciences*, 70(7):2032–2050, 2013.

[151] C. Marchioli, A. Giusti, M. V. Salvetti, and A. Soldati. Direct numerical simulation of particle wall transfer and deposition in upward turbulent pipe flow. *International Journal of Multiphase Flow*, 29(6):1017–1038, 2003.

[152] J. S. Marshall. Discrete-element modeling of particulate aerosol flows. *Journal of Computational Physics*, 228(5):1541–1561, 2009.

[153] J. S. Marshall and S. Li. *Adhesive particle flow*. Cambridge University Press, 2014.

[154] M. Massot. Eulerian multi-fluid models for polydisperse evaporating sprays. In *Multiphase reacting flows: modelling and simulation*, pages 79–123. Springer, 2007.

[155] E. A. Matida, K. Nishino, and K. Torii. Statistical simulation of particle deposition on the wall from turbulent dispersed pipe flow. *International Journal of Heat and Fluid Flow*, 21(4):389–402, 2000.

[156] S. Matsusaka and H. Masuda. Simultaneous measurement of mass flow rate and charge-to-mass ratio of particles in gas–solids pipe flow. *Chemical Engineering Science*, 61(7):2254–2261, 2006.

[157] S. Matsusaka, H. Umemoto, M. Nishitani, and H. Masuda. Electrostatic charge distribution of particles in gas–solids pipe flow. *Journal of Electrostatics*, 55(1):81–96, 2002.

[158] S. Matsusaka, H. Maruyama, T. Matsuyama, and M. Ghadiri. Triboelectric charging of powders: A review. *Chemical Engineering Science*, 65(22):5781–5807, 2010.

[159] M. R. Maxey. The gravitational settling of aerosol particles in homogeneous turbulence and random flow fields. *Journal of Fluid Mechanics*, 174:441–465, 1987.

[160] I. N. McCave. Erosion, transport and deposition of fine-grained marine sediments. *Geological Society, London, Special Publications*, 15(1):35–69, 1984.

[161] E. W. McDaniel and E. A. Mason. *The mobility and diffusion of ions in gases*. Wiley, 1973.

[162] D. A. McQuarrie. *Statistical Mechanics*. Harper and Row, 1976.

[163] M. Meyer, A. Devesa, S. Hickel, X. Hu, and N. A. Adams. A conservative immersed interface method for large-eddy simulation of incompressible flows. *Journal of Computational Physics*, 229 (18):6300–6317, 2010.

[164] G. V. Middleton and M. A. Hampton. Part i. sediment gravity flows: mechanics of flow and deposition. 1973.

[165] T. Mikami, H. Kamiya, and M. Horio. Numerical simulation of cohesive powder behavior in a fluidized bed. *Chemical Engineering Science*, 53(10):1927–1940, 1998.

[166] K. Monroe, Y. Yao, A. Lattanzi, V. Raghav, and J. Capecelatro. Role of pulsatility on particle dispersion in expiratory flows. *arXiv preprint arXiv:2103.00581*, 2021.

[167] J. A. Mousel and J. S. Marshall. Aggregate growth and breakup in particulate suspension flow through a micro-nozzle. *Microfluidics and Nanofluidics*, 8(2):171–186, 2010.

[168] H. R. Moutinho, C.-S. Jiang, B. To, C. Perkins, M. Muller, M. M. Al-Jassim, and L. Simpson. Investigation of adhesion forces between dust particles and solar glass. In *2017 IEEE 44th Photovoltaic Specialist Conference (PVSC)*, pages 2280–2284. IEEE, 2017.

[169] C. Nicolai, B. Jacob, and R. Piva. On the spatial distribution of small heavy particles in homogeneous shear turbulence. *Physics of Fluids*, 25(8):083301, 2013.

[170] S. Nili, C. Park, N. H. Kim, R. T. Haftka, and S. Balachandar. Prioritizing possible force models error in multiphase flow using global sensitivity analysis. *AIAA Journal*, pages 1–11, 2021.

[171] T. A. Oliver and R. D. Moser. Bayesian uncertainty quantification applied to rans turbulence models. In *Journal of Physics: Conference Series*, volume 318, page 042032. IOP Publishing, 2011.

[172] A. Ontiveros-Ortega, J. A. Moleon, I. Plaza, and C. Guillén. Effect of interfacial properties on mechanical stability of ash deposit. *Journal of Rock Mechanics and Geotechnical Engineering*, 8 (2):187–197, 2016.

[173] H. Ounis, G. Ahmadi, and J. B. McLaughlin. Brownian particle deposition in a directly simulated turbulent channel flow. *Physics of Fluids A: Fluid Dynamics*, 5(6):1427–1432, 1993.

[174] A. B. Owen. Variance components and generalized sobol'indices. *SIAM/ASA Journal on Uncertainty Quantification*, 1(1):19–41, 2013.

[175] H. Pan, X.-Z. Chen, X.-F. Liang, L.-T. Zhu, and Z.-H. Luo. Cfd simulations of gas–liquid–solid flow in fluidized bed reactors—a review. *Powder Technology*, 299:235–258, 2016.

[176] J. D. Pandya and L. A. Spielman. Floc breakage in agitated suspensions: effect of agitation rate. *Chemical Engineering Science*, 38(12), 1983.

[177] C. E. Papadopoulos and H. Yeung. Uncertainty estimation and monte carlo simulation method. *Flow Measurement and Instrumentation*, 12(4):291–298, 2001.

[178] P. Papavergos and A. Hedley. Particle deposition behaviour from turbulent flows. *Chemical engineering research & design*, 62(5):275–295, 1984.

[179] B. Peherstorfer, K. Willcox, and M. Gunzburger. Optimal model management for multifidelity monte carlo estimation. *SIAM Journal on Scientific Computing*, 38(5):A3163–A3194, 2016.

[180] B. Peherstorfer, K. Willcox, and M. Gunzburger. Survey of multifidelity methods in uncertainty propagation, inference, and optimization. *Siam Review*, 60(3):550–591, 2018.

[181] P. Pepiot and O. Desjardins. Direct numerical simulation of dense particle-laden flows using a conservative immersed boundary technique. In *Proceedings of the Summer Program*, page 323. Citeseer, 2010.

[182] J. W. Perram, H. G. Petersen, and S. W. De Leeuw. An algorithm for the simulation of condensed matter which grows as the 3/2 power of the number of particles. *Molecular Physics*, 65(4):875–893, 1988.

[183] H. G. Petersen. Accuracy and efficiency of the particle mesh ewald method. *The Journal of chemical physics*, 103(9):3668–3679, 1995.

[184] D. J. Phares and G. Sharma. A dns study of aerosol deposition in a turbulent square duct flow. *Aerosol Science and Technology*, 40(11):1016–1024, 2006.

[185] F. Picano, G. Sardina, and C. M. Casciola. Spatial development of particle-laden turbulent pipe flow. *Physics of Fluids*, 21(9):093305, 2009.

[186] C. D. Pierce. *Progress-variable approach for large-eddy simulation of turbulent combustion.* PhD thesis, Citeseer, 2001.

[187] N. Plewacki, P. Gnanaselvam, and J. P. Bons. The effect of elevated temperatures on airborne particle deposition and rebounds. In *AIAA Scitech 2020 Forum*, page 1576, 2020.

[188] S. B. Pope. *Turbulent flows.* Cambridge University Press, 2000.

[189] W. H. Press, S. A. Teukolsky, W. T. Vetterling, and B. P. Flannery. *Numerical recipies in C.* Cambridge University Press Cambridge, 1992.

[190] E. Qian, B. Peherstorfer, D. O'Malley, V. V. Vesselinov, and K. Willcox. Multifidelity monte carlo estimation of variance and sensitivity indices. *SIAM/ASA Journal on Uncertainty Quantification*, 6(2):683–706, 2018.

[191] C. J. Reagle, J. M. Delimont, W. F. Ng, S. V. Ekkad, and V. Rajendran. Measuring the coefficient of restitution of high speed microparticle impacts using a ptv and cfd hybrid technique. *Measurement science and technology*, 24(10):105303, 2013.

[192] N. O. Renno, J. F. Kok, H. Kirkham, and S. Rogacki. A miniature sensor for electrical field measurements in dusty planetary atmospheres. In *Journal of Physics: Conference Series*, volume 142, page 012075. IOP Publishing, 2008.

[193] A. C. Resurreccion, P. Moldrup, M. Tuller, T. Ferré, K. Kawamoto, T. Komatsu, and L. W. De Jonge. Relationship between specific surface area and the dry end of the water retention curve for soils with varying clay and organic carbon contents. *Water Resources Research*, 47(6), 2011.

[194] M. Rodrigues, W. Marra Jr, R. Almeida, and J. Coury. Measurement of the electrostatic charge in airborne particles: Ii-particle charge distribution of different aerosols. *Brazilian Journal of Chemical Engineering*, 23(1):125–133, 2006.

[195] R. G. Rokkam, R. O. Fox, and M. E. Muhle. Computational fluid dynamics and electrostatic modeling of polymerization fluidized-bed reactors. *Powder Technology*, 203(2):109–124, 2010.

[196] R. G. Rokkam, A. Sowinski, R. O. Fox, P. Mehrani, and M. E. Muhle. Computational and experimental study of electrostatics in gas–solid polymerization fluidized beds. *Chemical Engineering Science*, 92:146–156, 2013.

[197] J. M. Rosen, D. J. Hofmann, and W. Gringel. Measurements of ion mobility to 30 km. *Journal of Geophysical Research: Atmospheres*, 90(D4):5876–5884, 1985.

[198] S. Roy, S. Luding, and T. Weinhart. A general (ized) local rheology for wet granular materials. *New Journal of Physics*, 19(4):043014, 2017.

[199] X. Ruan, S. Chen, and S. Li. Structural evolution and breakage of dense agglomerates in shear flow and Taylor-Green vortex. *Chemical Engineering Science*, 211:115261, 2020.

[200] M. Rybalko, E. Loth, and D. Lankford. A lagrangian particle random walk model for hybrid rans/les turbulent flows. *Powder Technology*, 221:105–113, 2012.

[201] M. J. Rycroft, S. Israelsson, and C. Price. The global atmospheric electric circuit, solar activity and climate change. *Journal of Atmospheric and Solar-Terrestrial Physics*, 62(17-18):1563–1576, 2000.

[202] C. Sacco, C. Bowen, R. Lundgreen, J. P. Bons, E. Ruggiero, J. Allen, and J. Bailey. Dynamic similarity in turbine deposition testing and the role of pressure. *Journal of Engineering for Gas Turbines and Power*, 140(10):102605, 2018.

[203] P. Sagaut and C. Cambon. *Homogeneous turbulence dynamics*, volume 10. Springer, 2008.

[204] J. P. L. C. Salazar, J. De Jong, L. Cao, S. H. Woodward, H. Meng, and L. R. Collins. Experimental and numerical investigation of inertial particle clustering in isotropic turbulence. *Journal of Fluid Mechanics*, 600:245–256, 2008.

[205] A. Saltelli, M. Ratto, T. Andres, F. Campolongo, J. Cariboni, D. Gatelli, M. Saisana, and S. Tarantola. *Global sensitivity analysis: the primer*. John Wiley & Sons, 2008.

[206] C. S. Sandeep, K. Senetakis, D. Cheung, C. E. Choi, Y. Wang, M. Coop, and C. W. W. Ng. Experimental study on the coefficient of restitution of grain against block interfaces for natural and engineered materials. *Canadian Geotechnical Journal*, 58(1):35–48, 2021.

[207] P. J. Schmid. Nonmodal stability theory. *Annual Review of Fluid Mechanics*, 39:129–162, 2007.

[208] A. Schmiegel and B. Eckhardt. Fractal stability border in plane Couette flow. *Physical Review Letters*, 79(26):5250, 1997.

[209] J. M. Schneider and P. K. Watson. Electrohydrodynamic stability of space-charge-limited currents in dielectric liquids. I. Theoretical study. *Physics of Fluids*, 13(8):1948–1954, 1970.

[210] L. Schwendiman and A. Postma. Turbulent deposition in sampling lines. *Rapport technique Tech. Inf. Div. TID-7628, USAEC*, 118, 1962.

[211] G. A. Sehmel. Aerosol deposition from turbulent airstreams in vertical conduits. Technical report, Battelle-Northwest, Richland, Wash. Pacific Northwest Lab., 1968.

[212] Y. Shan, J. L. Klepeis, M. P. Eastwood, R. O. Dror, and D. E. Shaw. Gaussian split Ewald: A fast Ewald mesh method for molecular simulation. *The Journal of Chemical Physics*, 122(5):054101, 2005.

[213] J. S. Shrimpton and A. J. Yule. Characterisation of charged hydrocarbon sprays for application in combustion systems. *Experiments in Fluids*, 26(5):460–469, 1999.

[214] D. Siingh, V. Gopalakrishnan, R. P. Singh, A. K. Kamra, S. Singh, V. Pant, R. Singh, and A. K. Singh. The atmospheric global electric circuit: an overview. *Atmospheric Research*, 84(2):91–110, 2007.

[215] S. Singh and D. Tafti. Predicting the coefficient of restitution for particle wall collisions in gas turbine components. In *ASME Turbo Expo 2013: Turbine Technical Conference and Exposition*. American Society of Mechanical Engineers Digital Collection, 2013.

[216] P. Sippola, J. Kolehmainen, A. Ozel, X. Liu, P. Saarenrinne, and S. Sundaresan. Experimental and numerical study of wall layer development in a tribocharged fluidized bed. *Journal of Fluid Mechanics*, 849:860–884, 2018.

[217] J. L. Smialek, F. A. Archer, and R. G. Garlick. Turbine airfoil degradation in the persian gulf war. *JOM*, 46(12):39–41, 1994.

[218] I. M. Sobol. Sensitivity analysis for non-linear mathematical models. *Mathematical modelling and computational experiment*, 1:407–414, 1993.

[219] W. Song, Y. Lavallée, K.-U. Hess, U. Kueppers, C. Cimarelli, and D. B. Dingwell. Volcanic ash melting under conditions relevant to ash turbine interactions. *Nature communications*, 7(1):1–10, 2016.

[220] R. C. Sonntag and W. B. Russel. Structure and breakup of flocs subjected to fluid stresses: Ii. theory. *Journal of Colloid and Interface Science*, 115(2):378–389, 1987.

[221] R. Sun, H. Xiao, and H. Sun. Investigating the settling dynamics of cohesive silt particles with particle-resolving simulations. *Advances in Water Resources*, 111:406–422, 2018.

[222] S. Sundaram and L. R. Collins. Collision statistics in an isotropic particle-laden turbulent suspension. part 1. direct numerical simulations. *Journal of Fluid Mechanics*, 335:75–109, 1997.

[223] M. Syamlal, W. Rogers, and T. J. O'Brien. Mfix documentation theory guide. Technical report, USDOE Morgantown Energy Technology Center, WV (United States), 1993.

[224] W. Tabakoff, A. Hamed, and M. Metwally. Effect of particle size distribution on particle dynamics and blade erosion in axial flow turbines. *Journal of Engineering for Gas Turbines and Power*, 113 (4):607–615, 1991.

[225] I. Tanaka, M. Koishi, and K. Shinohara. A study on the process for formation of spherical cement through an examination of the changes of powder properties and electrical charges of the cement and its constituent materials during surface modification. *Cement and concrete research*, 32(1): 57–64, 2002.

[226] G. I. Taylor. The shape and acceleration of a drop in a high speed air stream, 1963.

[227] S. Tenneti and S. Subramaniam. Particle-resolved direct numerical simulation for gas-solid flow model development. *Annual Review of Fluid Mechanics*, 46:199–230, 2014.

[228] S. Tenneti, R. Garg, and S. Subramaniam. Drag law for monodisperse gas–solid systems using particle-resolved direct numerical simulation of flow past fixed assemblies of spheres. *International Journal of Multiphase Flow*, 37(9):1072–1092, 2011.

[229] A. V. Timofeev and B. N. Shvilkin. Drift-dissipative instability of an inhomogeneous plasma in a magnetic field. *Soviet Physics Uspekhi*, 19(2):149, 1976.

[230] B. A. Tinsley. Scavenging of condensation nuclei in clouds: dependence of sign of electroscavenging effect on droplet and CCN sizes. In *Proceedings, International Conference on Clouds and Precipitation*, page 248, 2004.

[231] B. A. Tinsley, R. P. Rohrbaugh, M. Hei, and K. V. Beard. Effects of image charges on the scavenging of aerosol particles by cloud droplets and on droplet charging and possible ice nucleation processes. *Journal of the Atmospheric Sciences*, 57(13):2118–2134, 2000.

[232] G. Tomar, V. Shankar, A. Sharma, and G. Biswas. Electrohydrodynamic instability of a confined viscoelastic liquid film. *Journal of Non-newtonian Fluid Mechanics*, 143(2-3):120–130, 2007.

[233] A. A. Townsend. Excitation of internal waves in a stably-stratified atmosphere with considerable wind-shear. *Journal of Fluid Mechanics*, 32(1):145–171, 1968.

[234] L. N. Trefethen, A. E. Trefethen, S. C. Reddy, and T. A. Driscoll. Hydrodynamic stability without eigenvalues. *Science*, 261(5121):578–584, 1993.

[235] S. N. Tripathi and R. G. Harrison. Enhancement of contact nucleation by scavenging of charged aerosol particles. *Atmospheric Research*, 62(1-2):57–70, 2002.

[236] C.-J. Tsai, D. Y. Pui, and B. Y. Liu. Elastic flattening and particle adhesion. *Aerosol Science and Technology*, 15(4):239–255, 1991.

[237] P. Tsou. Silica aerogel captures cosmic dust intact. *Journal of Non-Crystalline Solids*, 186:415–427, 1995.

[238] Y. Tsuji, T. Kawaguchi, and T. Tanaka. Discrete particle simulation of two-dimensional fluidized bed. *Powder Technology*, 77(1):79–87, 1993.

[239] M. Uhlmann. Interface-resolved direct numerical simulation of vertical particulate channel flow in the turbulent regime. *Physics of Fluids*, 20(5):053305, 2008.

[240] W. Uijttewaal and R. Oliemans. Particle dispersion and deposition in direct numerical and large eddy simulations of vertical pipe flows. *Physics of Fluids*, 8(10):2590–2604, 1996.

[241] V. Valmacco, M. Elzbieciak-Wodka, C. Besnard, P. Maroni, G. Trefalt, and M. Borkovec. Dispersion forces acting between silica particles across water: Influence of nanoscale roughness. *Nanoscale Horizons*, 1(4):325–330, 2016.

[242] M. A. van der Hoef, M. van Sint Annaland, N. G. Deen, and J. Kuipers. Numerical simulation of dense gas-solid fluidized beds: a multiscale modeling strategy. *Annual Review of Fluid Mechanics*, 40:47–70, 2008.

[243] H. A. Van der Vorst. *Iterative Krylov methods for large linear systems*, volume 13. Cambridge University Press, 2003.

[244] B. van Haarlem, B. J. Boersma, and F. T. Nieuwstadt. Direct numerical simulation of particle deposition onto a free-slip and no-slip surface. *Physics of Fluids*, 10(10):2608–2620, 1998.

[245] B. van Wachem, K. Thalberg, D. Nguyen, L. M. de Juan, J. Remmelgas, and I. Niklasson-Bjorn. Analysis, modelling and simulation of the fragmentation of agglomerates. *Chemical Engineering Science*, page 115944, 2020.

[246] T.-T. Vo, P. Mutabaruka, S. Nezamabadi, J.-Y. Delenne, and F. Radjai. Evolution of wet agglomerates inside inertial shear flow of dry granular materials. *Physical Review E*, 101:032906, Mar 2020. doi: 10.1103/PhysRevE.101.032906. URL `https://link.aps.org/doi/10.1103/PhysRevE.101.032906`.

[247] H. Volland. *Atmospheric electrodynamics*, volume 11. Springer Science & Business Media, 2013.

[248] B. Vowinckel, E. Biegert, P. Luzzatto-Fegiz, and E. Meiburg. Consolidation of freshly deposited cohesive and noncohesive sediment: Particle-resolved simulations. *Physical Review Fluids*, 4(7): 074305, 2019.

[249] B. Vowinckel, J. Withers, P. Luzzatto-Fegiz, and E. Meiburg. Settling of cohesive sediment: particle-resolved simulations. *Journal of Fluid Mechanics*, 858:5–44, 2019.

[250] J. H. Walther, R. Jaffe, T. Halicioglu, and P. Koumoutsakos. Molecular dynamics simulations of carbon nanotubes in water. In *Proceedings of the summer program*, page 5, 2000.

[251] F.-J. Wang, J.-X. Zhu, and J. M. Beeckmans. Pressure gradient and particle adhesion in the pneumatic transport of cohesive fine powders. *International Journal of Multiphase Flow*, 26(2): 245–265, 2000.

[252] J. Wang, W. B. Rossow, and Y. Zhang. Cloud vertical structure and its variations from a 20-yr global rawinsonde dataset. *Journal of Climate*, 13(17):3041–3056, 2000.

[253] L. P. Wang and M. R. Maxey. Settling velocity and concentration distribution of heavy particles in homogeneous isotropic turbulence. *Journal of Fluid Mechanics*, 256:27–68, 1993.

[254] Q. Wang and K. D. Squires. Large eddy simulation of particle-laden turbulent channel flow. *Physics of Fluids*, 8(5):1207–1223, 1996.

[255] A. P. Watkinson. Deposition from crude oils in heat exchangers. *Heat transfer engineering*, 28(3): 177–184, 2007.

[256] C. Weiler, M. Wolkenhauer, M. Trunk, and P. Langguth. New model describing the total dispersion of dry powder agglomerates. *Powder Technology*, 203(2):248–253, 2010.

[257] A. Wells and A. Chamberlain. Transport of small particles to vertical surfaces. *British Journal of Applied Physics*, 18(12):1793, 1967.

[258] R. Wengeler and H. Nirschl. Turbulent hydrodynamic stress induced dispersion and fragmentation of nanoscale agglomerates. *Journal of Colloid and Interface Science*, 306(2):262–273, 2007.

[259] S. M. Whitaker and J. P. Bons. An improved particle impact model by accounting for rate of strain and stochastic rebound. In *Turbo Expo: Power for Land, Sea, and Air*, volume 51029, page V02DT47A016. American Society of Mechanical Engineers, 2018.

[260] S. M. Whitaker, R. Prenter, and J. P. Bons. The effect of freestream turbulence on deposition for nozzle guide vanes. *Journal of Turbomachinery*, 137(12), 2015.

[261] S. M. Whitaker, B. Peterson, A. F. Miller, and J. P. Bons. The effect of particle loading, size, and temperature on deposition in a vane leading edge impingement cooling geometry. In *Turbo Expo: Power for Land, Sea, and Air*, volume 49798, page V05BT16A013. American Society of Mechanical Engineers, 2016.

[262] M. Williams. Atmospheric dispersal of pollutants and the modelling of air pollution. *Pollution, causes, effects and control*, pages 225–43, 1990.

[263] R. Wing and I. McGill. The protection of gas turbine blades. *Aircraft Engineering and Aerospace Technology*, 1981.

[264] N. Wood. A simple method for the calculation of turbulent deposition to smooth and rough surfaces. *Journal of aerosol Science*, 12(3):275–290, 1981.

[265] L. Wright. Sediment transport and deposition at river mouths: a synthesis. *Geological Society of America Bulletin*, 88(6):857–868, 1977.

[266] J. C. Wyngaard and O. R. Coté. The budgets of turbulent kinetic energy and temperature variance in the atmospheric surface layer. *Journal of the Atmospheric Sciences*, 28(2):190–201, 1971.

[267] J. Yang, C.-Y. Wu, and M. Adams. Dem analysis of particle adhesion during powder mixing for dry powder inhaler formulation development. *Granular Matter*, 15(4):417–426, 2013.

[268] J. Yang, C.-Y. Wu, and M. Adams. Numerical modelling of agglomeration and deagglomeration in dry powder inhalers: a review. *Current Pharmaceutical Design*, 21(40):5915–5922, 2015.

[269] J. Yao, H. Han, Y. Hou, E. Gong, and W. Yin. A method of calculating the interaction energy between particles in minerals flotation. *Mathematical Problems in Engineering*, 2016, 2016.

[270] Y. Yao and J. Capecelatro. Competition between drag and Coulomb interactions in turbulent particle-laden flows using a coupled-fluid–Ewald-summation based approach. *Physical Review Fluids*, 3(3):034301, 2018.

[271] Y. Yao and J. Capecelatro. Electrohydrodynamic generation of atmospheric turbulence. *Physical Review Fluids*, 4(12):123701, 2019.

[272] Y. Yao and J. Capecelatro. An accurate particle-mesh method for simulating charged particles in wall-bounded flows. *Powder Technology*, 387:239–250, 2021.

[273] Y. Yao and J. Capecelatro. Deagglomeration of cohesive particles by turbulence. *Journal of Fluid Mechanics*, 911, 2021.

[274] J. Young and A. Leeming. A theory of particle deposition in turbulent pipe flow. *Journal of Fluid Mechanics*, 340:129–159, 1997.

[275] F. Yu and R. P. Turco. From molecular clusters to nanoparticles: Role of ambient ionization in tropospheric aerosol formation. *Journal of Geophysical Research: Atmospheres*, 106(D5):4797–4814, 2001.

[276] M. Zeidan, B. H. Xu, X. Jia, and R. A. Williams. Simulation of aggregate deformation and breakup in simple shear flows using a combined continuum and discrete model. *Chemical Engineering Research and Design*, 85(12):1645–1654, 2007.

[277] D. Z. Zhang and A. Prosperetti. Averaged equations for inviscid disperse two-phase flow. *Journal of Fluid Mechanics*, 267:185–220, 1994.

[278] Q. Zhang, H. Liu, Z. Ma, and Z. Xiao. Preferential concentration of heavy particles in compressible isotropic turbulence. *Physics of Fluids*, 28(5):055104, 2016.

[279] K. Zhao, B. Vowinckel, T.-J. Hsu, T. Köllner, B. Bai, and E. Meiburg. An efficient cellular flow model for cohesive particle flocculation in turbulence. *Journal of Fluid Mechanics*, 889:R3, 2020. doi: 10.1017/jfm.2020.79.

[280] L. Zhou and B. A. Tinsley. Production of space charge at the boundaries of layer clouds. *Journal of Geophysical Research: Atmospheres*, 112(D11), 2007.

[281] L. Zhou and B. A. Tinsley. Production of space charge at the boundaries of layer clouds. *Journal of Geophysical Research: Atmospheres*, 112(D11), 2007.

[282] F. Zonta, C. Marchioli, and A. Soldati. Particle and droplet deposition in turbulent swirled pipe flow. *International Journal of Multiphase Flow*, 56:172–183, 2013.